THE UNIVERSITY *of* EDINBURGH

The development of functionalised porous carbon materials for the separation of carbon dioxide from gas mixtures

THE UNIVERSITY
of EDINBURGH

J A Arran Gibson

Doctor of Philosophy

2016

Abstract

This work concerns the functionalisation of a variety of carbon materials for the selective adsorption of carbon dioxide. A key challenge in post-combustion capture from gas fired power plants is related to the low CO_2 concentration in the flue gas (4-8%). Therefore highly selective adsorbents have the potential to improve the efficiency of the separation of carbon dioxide from gas mixtures.

The study was performed in conjunction with the EPSRC funded project 'Adsorption Materials and Processes for Carbon Capture from Gas-Fired Power Plants – AMPGas'. The carbon materials investigated included multi-walled carbon nanotubes, a microporous activated carbon, two types of mesoporous activated carbon and multi-walled carbon nanotube/polyvinyl alcohol composite aerogels. The uptake of carbon dioxide by these materials was enhanced through the addition of basic amine groups to the materials.

The adsorption properties of the samples were tested by the zero-length column technique, thermal gravimetric analysis and breakthrough experiments. The materials were generally tested at conditions representative of those found in the flue gas of a fossil fuel power plant: 0.1 bar partial pressure of CO_2.

Two approaches were adopted for the chemical functionalization of the solid carbon supports. First, amine groups were covalently grafted directly to the surface and secondly amine molecules were physically adsorbed within the porous structure of the material by wet impregnation. It was seen that wet impregnation enabled the incorporation of a greater number of amine groups and the CO_2 capacity of the materials was investigated with respect to the carbon support structure, the type of amine and the amount of amine loading. Larger pore volume mesoporous carbon materials were seen to provide a more efficient support for the amine to interact with the CO_2. A greater than 12-fold increase in the CO_2 capacity was observed when the amine impregnated carbon material was compared to the raw starting material.

The extended zero-length column was introduced and fully characterized as a novel breakthrough experiment. It requires a small sample mass (~50 mg) and it allows binary selectivities to be calculated. It was shown, through multiple experiments and simulations that the breakthrough experiments were conducted under close to isothermal conditions which greatly simplifies the analysis of the breakthrough curves. In addition, a new zero-length column model was proposed to account for the reaction between the amine and the CO_2 in the adsorbed phase and fitted to experimental data. An interesting double curvature was observed in the concentration profile during the desorption step which was attributed to the kinetics of the amine-CO_2 reaction.

A brief investigation was carried out into the binary separation of biogas (45% CO_2: 55% CH_4) by zeolite 13X, activated carbon and an amine impregnated activated carbon.

Finally, initial investigations into the properties of low density carbon nanotube aerogels which have a large accessible pore volume, were carried out. Their potential as highly efficient supports for amine impregnation was investigated.

It was found that amine functionalized carbons strongly interact with carbon dioxide and have the potential to be integrated as an adsorbent in a rapid temperature swing process that separates carbon dioxide from dilute gas streams.

Lay Summary

The 2008 Climate Change Act sets the UK government a legally binding target of an 80% reduction in carbon dioxide emissions by 2050. To meet this target a variety of emerging technologies will have to be adopted. The implementation of carbon capture and storage (CCS), where the carbon dioxide is separated (captured) from the power station's flue gas and then stored in geological formations would significantly reduce the UKs carbon dioxide emissions to the atmosphere. Post-combustion capture has been identified as an attractive option as a CCS plant can be retrofitted to existing power generation infrastructure. Approximately two thirds of the cost of a CCS plant is associated with the separation of the CO_2 and it is at this stage that there is the greatest opportunity for savings.

Gas-fired power plants play a key role in the generation of energy in the UK, currently accounting for ~46% of electricity generation and ~35% of emissions. The key challenge in carbon capture from a gas fired power plant lies in the low CO_2 concentration in the flue gas (4-8%). Therefore, a conventional amine process will have a large energy penalty. Novel adsorbent materials combined with an optimized separation process have the potential to significantly reduce the cost of carbon capture. In this work, new carbon materials are developed that are highly selective towards carbon dioxide with a good capture capacity at the concentrations of interest. The novel carbon adsorbents are functionalised with amine groups that improve their affinity to CO_2. Due to the large volumes of gas that have to be treated, a process with a short cycle time is desirable to reduce the size and cost of the carbon capture plant. The functionalised materials developed in this work are ideally suited to a rapid temperature swing process where the CO_2 is captured by the material and then subsequently removed at elevated temperature for long term storage. The material can then be reused in the next cycle to capture additional CO_2.

A variety of different carbon-based materials were synthesised and ranked with regards to their ability to capture CO_2. Further experiments and simulations were then

conducted to fully characterise the promising materials and assess whether the materials could be utilized in an efficient carbon capture process.

Declaration

I hereby certify that I have composed this thesis and that the work presented is my own except where indicated. In addition, the work has not been previously submitted for any other degree or professional qualification.

J. A. Arran Gibson

Publications

J. A. Arran Gibson, Andrei V. Gromov, Stefano Brandani and Eleanor E.B. Campbell, *The effect of pore structure on the CO_2 adsorption efficiency of polyamine impregnated porous carbons,* Microporous and Mesoporous Materials, **208**, (2015) 129-139

J. A. Arran Gibson, Enzo Mangano, Elenica Shiko, Alex G. Greenaway, Andrei V. Gromov, Magdalena M. Lozinska, Daniel Friedrich, Eleanor E. B. Campbell, Paul A. Wright and Stefano Brandani, *Adsorption Materials and Processes for Carbon Capture from Gas-Fired Power Plants – AMPGas,* Ind. Eng. Chem. Res., **55**, (2016) 3840-3851

The work presented in this thesis is my own, however the contribution of several people should be noted. The material synthetic work, presented in this thesis, has been carried out in close collaboration with Dr. Andrei Gromov. In addition, various master's students have contributed to the project's success. Hannah Levene was involved in the work that covalently functionalized the surface of the CNTs that is presented in Chapter 4. Ben Hunter and Ellen Wick, together with myself, carried out the electrical resistance measurements on the functionalized carbon nanotubes (Section 4.2.3). Rachel Rayne was involved in the synthesis of the third mesoporous carbon (meso-AC2) that is presented in section 5.2.5.

All the experimental adsorption measurements, the simulations and the subsequent analysis of the data was carried out by the author.

Acknowledgements

I would like to acknowledge the funding for this work from the University of Edinburgh and the EPSRC through the grant for the project ‘Adsorption materials and processes for Carbon Capture from Gas-Fired Power Plants- AMPGas’ (EP/J02077X/1), without which the work would not have been possible. I would like to thank my two supervisors Prof. Stefano Brandani and Prof. Eleanor Campbell for initially providing me with the opportunity to carry out my PhD studies under their tutelage. The depth of knowledge and enthusiasm they both have for their fields has been an inspiration. In addition, I would like to thank them for their ongoing support, guidance, expertise and encouragement throughout my studies.

The academic discussions, advice and friendships from all members of the Campbell group past and present have been invaluable throughout the project. In particular, the project has been carried out in partnership with Dr. Andrei Gromov whose hard work, knowledge and expertise have been vital to the success of the work. I would like to thank him for his advice, training and friendship over the past three years.

The close knit working environment of the carbon capture group at the University of Edinburgh has been the perfect place to carry out my studies. I would like to thank all members of the group for their friendships and support over the years. In particular, all the guidance and help in the lab from Dr. Enzo Mangano and Dr. Eleni Shiko was greatly appreciated.

I would like to acknowledge the assistance received from the members of the technical staff in both the School of Chemistry and the School of Engineering that was critical to ensure that the required experimental work was carried out in a timely manner.

I would also like to thank my Mum, Dad, Rory and Caitlin for their support and encouragement throughout my studies. Finally, but not least, I would like to thank Rebecca for her patience, support and encouragement as I worked to complete my degree.

Contents

1 Introduction – Carbon Capture and Storage

Anthropogenic carbon dioxide emissions have been steadily increasing since the start of the industrial revolution in the 18th century. Over the past couple of decades the levels of CO_2 and other greenhouse gases present in our atmosphere have become a major area of concern within the scientific community. The concentration of CO_2 in our atmosphere measured by the National Oceanic and Atmospheric Administration has increased from an average of 318 ppm in July 1960 to 401 ppm in July 2015[1] with the current general upward trend showing no sign of abating. If this upward trend is allowed to continue then the levels of greenhouse gases in the atmosphere will lead to further global warming resulting in irreversible damage to our planet's natural cycles. In the UK, the 2008 climate change act set the UK government the target of reducing CO_2 emissions by 80% when compared to the 1990s baseline level. To meet this ambitious target whilst continuing to satisfy our growing energy demands, a variety of different technologies will have to be implemented.

The Department of Energy and Climate Change have reported that the UK's greenhouse gas emissions are dominated by CO_2 (82%)[2]. The generation of energy is responsible for producing 33%[2] of the UK's total greenhouse gas emissions and it is in this sector that there is the greatest potential to reduce emissions. Renewable technologies, such as wind farms, hydroelectric plants and solar energy have important roles to play in generating clean green energy, however, to satisfy energy demand and account for the intermittent nature of certain renewable technologies, fossil fuels will remain an important part of energy generation for many years to come. Therefore to reduce CO_2 emissions from large fossil fuel power stations, and meet the UK government's commitment by 2050, it will be necessary to implement carbon capture and storage (CCS).

The principle of CCS involves the separation and purification of carbon dioxide from the flue gas, before it is released into the atmosphere. The CO_2 can then be transported via pipeline or tanker to a variety of geological sites, such as depleted oil wells or

saline formations, for long term storage. To improve the economic case for CCS in certain cases the CO_2 can be utilized for enhanced oil recovery (EOR) to remove additional oil from depleted reserves.[3] Alternatively, carbon capture and utilization (CCU) could be implemented where the captured CO_2 is used as the feedstock in a biological or chemical process to produce a chemical or fuel.[4] However, the current scale of the emissions is such, that only a small percentage could be used to produce viable products.[5] Therefore, to tackle climate change CCS is required.

Typically the concentration of CO_2 in the flue gas ranges from 4% for a gas fueled power station, to up to 16 % for a coal fired power plant.[6] For viable economical long term storage the CO_2 must be separated from the other components of the flue gas, predominately nitrogen (80%), and concentrated to a purity > 95%.

To implement CCS several different approaches have been proposed. These include:

(1) Pre-combustion capture
(2) Oxy-fuel combustion
(3) Post-combustion capture

The first method, pre-combustion capture, involves the gasification of fuel to form syngas, from which the carbon dioxide and carbon monoxide is separated from the hydrogen. The hydrogen is then combusted to produce energy with water as a by-product. Advantages of pre-combustion are that multiple different fuels can be used and hydrogen is produced as a versatile product.[7]

The principle of the second method, oxy-fuel combustion, is to separate the oxygen from the nitrogen in air prior to combustion. The fuel is then burned in a stream of oxygen and recycled flue gas, resulting in an effluent stream with a concentration of CO_2 typically greater than 90 %.[8] Disadvantages at present include the energy penalty of separating oxygen and nitrogen by cryogenic distillation along with the high operating temperatures.[7]

The third method, post-combustion capture, requires the direct separation and purification of CO_2 from the flue gas. The major attraction of post combustion capture is that a carbon capture plant could easily be fitted to an existing power plant, reducing the required capital expenditure. A number of technologies have been proposed to separate the CO_2 at this stage. These include a liquid amine absorption process, adsorption on porous solids or a membrane separation.[9]

The liquid amine absorption process is a mature technology that has been used for many years in natural gas processing plants and petrochemical refineries. However, the process does have limitations, including a high equipment corrosion rate and a high energy penalty when regenerating the solvents. As an alternative competing technology, separation by adsorption on porous solids has been proposed. A wide variety of novel adsorbents have been proposed and developed for the separation of CO_2/N_2, including zeolites, metal organic frameworks (MOFs), silicas and activated carbons. The various attributes of these different materials are detailed in section 2.

There have been several different adsorption separation processes proposed for carbon capture. A recent review by Abanades et al.[9] discusses in detail the applicability of the various process configurations to specific separation conditions. A few examples of separation technologies include pressure swing adsorption (PSA), vacuum pressure swing adsorption (VPSA), temperature swing adsorption (TSA) and electric swing adsorption (ESA). In a PSA process, the adsorbent selectively adsorbs the component that strongly interacts with the surface whilst allowing the majority of the weakly adsorbed components to pass through the adsorption bed. The adsorbent is then regenerated by removing the strongly adsorbed component at low pressure. To achieve a high purity product stream, multiple stages may be required. PSA systems have been widely documented and are used in a variety of separation processes on an industrial scale.[10, 11] Optimization of a PSA process can result in a very efficient separation of gases and PSA technology has been used in a variety of industrial applications to date including air drying and the separation of CO_2 and methane from landfill gas.[11] VPSA works on a similar basis to PSA except the adsorbent is regenerated at a pressure below atmospheric. A post combustion capture process involving pressure swing, would have

to be a VPSA process as the cost of compressing all the flue gas to high pressure is too great.

TSA involves selective adsorption of one component at low temperature followed by a second step where there is a rapid temperature rise of the adsorbent, increasing the mole fraction of the adsorbed component in the gas phase, and hence purifying the product stream.[12] A combination of a PSA and TSA process can be implemented to achieve an efficient separation. In order to capture CO_2 from dilute gas streams (4-8%), strong highly selective adsorbents are required. Such adsorbents have a very steep isotherm profile in the low pressure region. As a result, in order to remove the adsorbed CO_2 via a pressure swing adsorption process, very low vacuum pressures are required which have a significant associated cost. To achieve the target of 90+ % recovery and 95+% purity of CO_2 from the capture process is not feasible by VPSA in the case of dilute CO_2 gas streams.[9] Through a temperature swing process the adsorbent can be regenerated at elevated temperature which can result in adsorbents with significant working capacities. To minimise the size of the adsorption unit a rapid temperature swing adsorption process (RTSA), where the adsorbent can be rapidly cycled through adsorption, regeneration and cooling steps, is required. A rotary wheel adsorber can deliver on the requirements of a rapid temperature swing adsorption process and was therefore fully investigated as part of the AMPGas project.[13]

The principle of a rotating adsorption unit has been commercialised by Seibu Giken Co. Ltd. in the form of a honeycomb rotor for the dehumidification of air.[14] Since a large volume of gas must be treated for carbon capture, an industrial rotary wheel adsorber would be similar in design to a rotary wheel heat exchanger. The adaption of this familiar technology would enable an efficient separation of CO_2 via RTSA. Inventys have proposed the VeloxoTherm™ process for carbon capture based on this technology.[15]

An ESA process can rely on an increase in temperature of the packed bed by joule heating of the adsorbent as a result of applying a potential difference across it, which in turn results in the desorption of the adsorbed component.[16] This is of particular

interest for carbon materials due to their interesting electrical properties.[17] The choice of adsorbent is critical in determining the optimum process to implement for a particular scenario and establishing the lifetime cost of the process.

The separation of CO_2 from nitrogen during the capture stage of CCS can be responsible for 70% or more of the energy penalty of CCS.[7] It is therefore at the capture stage that the greatest potential for cost savings lies. The area of focus in this work was to design strong highly selective adsorbents that can capture CO_2 from dilute flue gas streams. In a gas-fired power plant, with turbines operating under standard conditions, the CO_2 concentration in the flue gas is approximately 4%. However, if a percentage of the flue gas is recirculated back through the turbines, the CO_2 partial pressure at the outlet can be increased to approximately 8% without detrimentally affecting the efficiency of the turbines.[6, 18, 19] As the CO_2 concentration is higher, the adsorbent will adsorb a greater quantity of CO_2 and therefore the required size of the separation unit, the energy penalty and hence the cost of the carbon capture process can be reduced.[18] The development of new novel adsorbents has the potential to reduce the energy penalty of CO_2 separation and along with an optimised separation process, provide a viable economical process that could be implemented to reduce anthropogenic emissions.

The work in this thesis was carried out as part of the EPSRC funded project 'Adsorption Materials and Processes for Carbon Capture from Gas Fired Power Plants – AMPGas' which included The University of Edinburgh (coordinator), University of St Andrews and Heriot Watt University. With AMPGas, a variety of different materials including zeolites, metal-organic frameworks, amine impregnated silicas and amine functionalized carbons and carbon nanotubes were designed, characterized and tested. The primary aim of the project was to design materials specifically for CO_2 capture from dilute gas streams (4-8%) that could be utilized in a rapid temperature swing process, such as the rotary wheel adsorber that was under development as part of the project.

The motivation of the work was to design and characterise highly selective materials that could be used as viable adsorbents in a carbon capture unit. When ranking and selecting potential adsorbent materials for a carbon capture process several different parameters must be considered, including: CO_2 capacity, cyclic stability, material cost, kinetics and selectivity. The focus of this work was carbon based adsorbents because of several key attributes. Porous carbons are generally cheap to produce and they have a surface that can be functionalized to enhance selectivity. Carbon materials have interesting electrical properties which make them viable candidates for a joule heating or ESA regeneration process. In addition, amine functionalized carbon materials continue to selectively adsorb CO_2 in the presence of water vapour.

In this dissertation the synthesis and characterisation of a variety of different novel functionalized carbon adsorbents is discussed. The materials were first ranked with regard to their overall uptake of CO_2 and then further tests and studies were carried out on promising materials to determine their structural and kinetic properties. The thesis is arranged as follows:

- **Chapter 2:** The background and recent developments with regard to competitive adsorbents that have been reported in the literature is discussed.
- **Chapter 3:** The background and theory of the experimental techniques used within the project to characterise and rank the adsorbents including the zero-length column technique, thermal gravimetric analysis and volumetric experiments
- **Chapter 4:** The covalent grafting of amine moieties to multi-walled carbon nanotubes and activated carbons for selective uptake of CO_2.
- **Chapter 5:** The wet impregnation of different amine molecules into activated carbon with different average pore sizes was investigated. The effect of the amine impregnation on the accessible pore volume and the efficiency of the CO_2 interaction with the amine groups is discussed.
- **Chapter 6:** A kinetic study into the reaction of CO_2 with the amine groups via the ZLC and E-ZLC technique. A novel E-ZLC experiment with a thermocouple in the adsorption bed is also reported.

- **Chapter 7:** The results of an investigation into the potential for upgrading Biogas (45% CO_2, 55% CH_4) by zeolite 13X, activated carbon and amine impregnated activated carbon are discussed.
- **Chapter 8:** Novel carbon nanotube aerogels were designed and produced with a large pore volume, suitable for amine impregnation. The mechanical strength and adsorption properties of the aerogels was investigated.
- **Chapter 9:** Conclusions

The two highlights of the work can be found in chapter 6 and 8. In chapter 6 a novel kinetic model is proposed that can be used to simulate the reaction between CO_2 and amine in the adsorbed phase of an adsorbent. After further validation, the model could be used to model the potential performance of an adsorbent in a carbon capture process. In chapter 8, a novel low density crosslinked carbon nanotube/polyvinyl alcohol aerogel is proposed as support for amine impregnation. The large pore volume aerogels enable the incorporation of a large weight percentage of amine and hence promising CO_2 capacities.

2 Introduction – Adsorbent materials

Over the years, several different types of materials have been proposed and investigated for the separation of CO_2 from dilute gas streams. These include zeolites, metal-organic frameworks and amine modified activated carbons and silicas. There are several recent comprehensive reviews that compare the attributes of different solid adsorbents for carbon capture.[9, 20, 21] It is clear that an adsorbent is required to have a high affinity and selectivity for CO_2 at low partial pressures to be economically viable. Adsorbents have found applications in areas including separations, purifications, decontaminations and catalysis.

An overview of the attributes along with some recent developments within each of the main classes of material is presented below.

2.1 Zeolites

Zeolites can be of both a natural and synthetic origin and are microporous materials consisting of aluminosilicate. A large number of different cations can be incorporated in the microporous structure to tune the properties of the material. In general, the cations are loosely bound and can be readily exchanged in solution. Different cations fine tune the pore size and the adsorption characteristics by affecting the strength of the interaction between the zeolite and the adsorbate. A wide variety of different cations have been used, including Na^+, Li^+ and K^+ [22, 23]; the positive charge is balanced by the AlO_4^- tetrahedral structure within the zeolite framework. The CO_2 molecule with its large quadrupole moment (-14.29 X 10^{-40} C m^2) has a strong interaction with the electric field generated by the cations within the zeolite structure.[20] In general, zeolites are classical physisorbents with an increase in the amount of CO_2 adsorbed at reduce temperature and increased pressure. The heat of adsorption for CO_2 on zeolites is typically between 24 and 50 kJ mol^{-1}.[9]

Zeolites have been widely used as adsorbents because they are very stable and have strong physical adsorption sites. Zeolites can selectively separate CO_2 by a kinetic and/or equilibrium mechanism. For example, natural zeolites (e.g. mordenite clinoptilolite and chabazite) and synthetic zeolites (e.g. 13X, 4A and 5A) have all been shown to preferentially adsorb carbon dioxide over nitrogen.[20, 24]

There are a large number of reports in the literature detailing the different zeolite structures, the effect of pore size and the type of cation on the CO_2 adsorption. For example, a series of reports investigated the CO_2 adsorption properties of univalent cation forms of zeolite Rho ($M_{9.8}Al_{9.8}Si_{38.2}O_{96,}$ M = H, Li, Na, K, NH_4, Cs)[22]. The CO_2 uptake at low partial pressure of CO_2 follows the trend of $Li^+ > Na^+ > K^+ > Cs^+$.[22, 23] The highest CO_2 uptake was obtained on the Li-Rho zeolite (3.4 mmol g^{-1} at 0.1 bar, 298 K), however due to a high affinity to water and the higher price of lithium the majority of the further investigations were carried out on Na-Rho (3.07 mmol g^{-1} at 0.1 bar, 298 K) which only had a marginally lower CO_2 capacity. These zeolites exhibited interesting adsorption properties with a cation gating mechanism used to explain the selective transport of CO_2 through the windows of the zeolite into the cages. The position of the cation within the cages was observed to be dependent on the pressure of CO_2 and the size of the cation.[23] The postulated gating mechanism is shown in Figure 2.1. At low loadings the diffusivity of the CO_2 from the pores was relatively low, potentially limiting their viability in an industrial scale capture process.

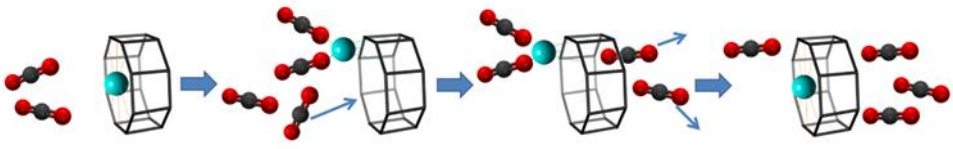

Figure 2.1: Cation gating mechanism provides additional selectivity, equilibrium and kinetic[25]

The related synthetic paulingite (Na,H-ECR-18) has also been investigated, upon dehydration it was observed that there was a change in symmetry and the structure distorted to afford closer coordination of the Na^+ atoms to the O atoms in the 8-membered rings.[25] The location of the Na^+ ions again resulted in CO_2 adsorption occurring via the 'trapdoor' mechanism, which permits separation of the different gas molecules with respect to the strength of the interaction with the cation as opposed to a separation with respect to molecular size.[25]

A recent report by Guo et al. detailed a method to predict the structure of zeolites of increasing complexity and subsequently synthesise them.[26] Three new zeolite structures ZSM-25, PST-20 and PST-25 were structurally resolved and synthesised. These three zeolites have the largest unit cell volume of any zeolites reported to date. Na^+ exchanged derivatives of ZSM-25 and PST-20 showed selective uptake of CO_2 over both nitrogen and methane. Although the new materials had a lower overall CO_2 capacity than the previously reported Na-Rho they exhibited significantly faster kinetics. This was particularly interesting from a process point of view with the large zeolites having a time constant of a few minutes compared to the Na-Rho which had a time constant of several hours. The faster kinetics would result in shorter process cycle times which could result in a reduction in the required size of the capture plant.

Zeolites exhibit a strong affinity for water, and the amount of CO_2 adsorbed by a zeolite has been shown to greatly reduce in the presence of a low partial pressure of water.[27] As a result a carbon capture process that uses zeolite as an adsorbent would require the flue gas to be pre-dried prior to the CO_2 separation process. A small amount of water in the flue gas could be tolerated because the adsorption separation is a dynamic process. If a countercurrent regeneration step is used, the penetration of the adsorbed water front along the adsorption bed can be controlled, enabling zeolites to be used as the adsorbent.[9]

The commercial zeolite 13 X was used as a benchmark material in this project. It has a cage structure with 12 membered oxygen rings with a diameter of approximately 7.4

Å. Na^+ cations are present in the cages which have a strong interaction with CO_2. 13X has a reported CO_2 capacity of up to 3.03 mmol g^{-1} at 35 °C and 0.1 bar CO_2.[28]

The studies detailed above are just a few examples from the large area of research into the development of zeolites as promising adsorbents for carbon capture. Details of further zeolites that show promise for carbon capture can be found in several reviews.[9, 20, 24] In conclusion zeolites show a large amount of promise as CO_2 physisorbents with the possibility of high working capacities being achieved by an optimized process. The diverse number of possible structures enables the zeolite's structure to be fine-tuned to have optimum capacity and kinetics for a given carbon capture process.

2.2 Metal-Organic Frameworks (MOFs)

In contrast to zeolites, the structure of a metal-organic framework (MOF) can be designed, produced and more easily tailored to a specific application. MOFs are a 3D structure consisting of metal centres that are coordinated in a regular crystalline structure by organic linkers. Both the organic linker and the metal centre can be varied to tailor the MOF to have the desired properties. The metal centres and organic linkers are bound through strong coordination bonds and the removal of the guest species (solvent) often results in a stable pore structure. MOFs can either have stable rigid pore structures or have flexible/dynamic structures.[29] Rigid MOFs have permanent porosity whereas the structure of the flexible MOFs can be affected by changes in conditions such as temperature and pressure.[29] The properties of the MOFs can also be further tuned by post-synthesis treatment, where further functional groups are introduced to modify the surface.

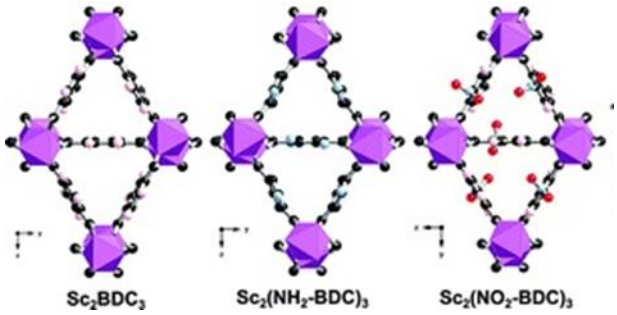

Figure 2.2: Small pore scandium MOFs with amino and nitro functionalised derivatives[30]

Small pore scandium-based metal organic frameworks have exhibited interesting properties for carbon capture (Figure 2.2).[31, 32] The MOF-Sc_2BDC_3 (BDC = 1,4-benzenedicarboxylate) was synthesised with a variety of different functional groups on the organic linkers (NO_2, NH_2). The highest selectivity with respect to CO_2 was observed with the amine modified MOF.[30] Further investigations into MOF $Sc_2(BDC\text{-}NH_2)_3$ utilised a new synchrotron radiation FTIR technique to investigate the adsorption sites and kinetics under dynamic flow. Through the use of polarised light it was shown that adsorbed CO_2 orientates itself along the pore channel during adsorption.[31] A study by Yazaydin et al. directly compared the CO_2 uptake of 14 MOFs at low pressure, they found a maximum uptake of ~5.9 mmol g^{-1} at 293 K, 0.1 bar for Mg/DDBDC.[33] A good correlation between the experimentally measured capacities and the capacities predicted by molecular simulation was also reported. The density and the accessibility of the metal centres along with the pore structure have all been found to directly influence the CO_2 uptake capacity of the MOFs.[29, 33]

MOFs have been proposed as suitable materials for application in areas such as gas storage[34] (hydrogen) gas separation[35], catalysis[36] and sensors[37]. A large number of different MOFs have been proposed and tested for application in a carbon capture process. CO_2 capacities ranging from 0.2 up to 5.96 mmol g^{-1} have been reported at conditions suitable for a post combustion capture process (low pressure and temperature)[9]. Recent reviews provide details on the full range of MOFs that have been developed for carbon capture.[20, 29, 38]

2.3 Amine modified materials

The introduction of basic amine groups to porous materials is a popular method to enhance the CO_2 uptake and selectivity of adsorbents. The basic NH groups selectively interact with the acidic CO_2 in the flue gas to form a carbamate or bicarbamate in the presence of water. The reaction of CO_2 and amine is a strong chemisorption process that greatly enhances the affinity of the material to CO_2. The two generally accepted reactions are shown in Figure 2.3.

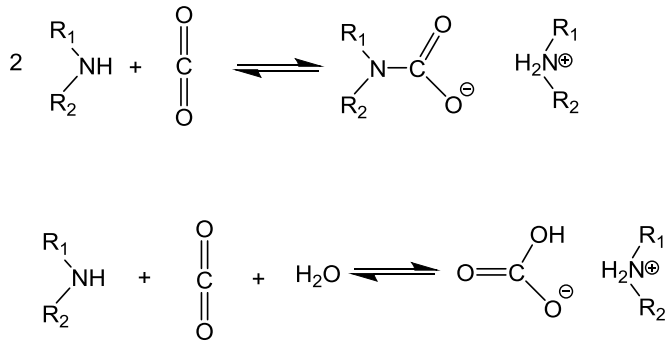

Figure 2.3: Mechanism of interaction of CO_2 with basic NH groups. Top: without water present, bottom: with water present[20]

The majority of work on amine modified porous adsorbents can be split into two main classes of material, mesoporous silicas and carbon adsorbents. A few examples from the literature of each class of material are discussed below.

2.3.1 Mesoporous silicas

Mesoporous silicas that are functionalized with amines have received a lot of attention in the literature as adsorbents for carbon capture. [20, 39-47] Advantages of using a silica support include tunable ordered hierarchical pore structures, high thermal stability and a tunable surface. In the literature, two main approaches have been adopted to functionalise the silica surface; covalent anchoring of amine functionalities and wet impregnation of amine molecules.

Xu et al. first reported the impregnation of polyethylenimine (PEI) onto mesoporous silicas for carbon capture in 2002. [43, 48] The CO_2 capacity was 24 times larger than for the raw MCM-41 and the term 'molecular basket' was coined to describe the incorporation of PEI into the porous structure.[48] A vast number of publications have followed where the loading and type of amine have been varied [49-52] along with the pore structure of the silica support [39, 53-55] in order to optimise the CO_2 capacity and stability of the materials for carbon capture. Over recent years there has been a general trend towards silica materials with a larger total pore volume to enable the incorporation of a greater number of amine groups and hence a higher CO_2 capacity per unit mass.[56-58] Impregnation of low molecular weight amines into silicas has been extensively investigated and although in general their affinity for CO_2 is promising it has been shown that due to the volatility of the amines their stability over several adsorption/desorption cycles is generally poor.[59] High molecular weight polyamines have emerged as the amine of choice for impregnated materials.[56] The degradation of the amine performance over multiple adsorption cycles has been attributed to the irreversible formation of urea that deactivates the reactivity of the sites towards CO_2. In 2010 Sayari et al. reported that the formation of urea linkages could be prevented by the presence of water vapour in the flue gas.[60, 61] As a result amine impregnated sorbents could in principle be reused over multiple adsorption cycles without a drop off in performance.

The second approach to silica functionalization is to graft amine groups directly to the silica surface. The advantages include higher thermal stability as the amines cannot leach from the substrate and potentially fast kinetics, if the CO_2 can access the active sites through the available pore volume. The majority of approaches involve a silanol condensation reaction to graft amine groups to the silanol groups on the surface.[62-64] However, in general the reported uptake capacities are lower than for impregnated materials due to limitations over the number of amine groups that can be grafted directly to the surface.[20, 56]

Amine functionalized silicas can effectively adsorb CO_2 at low CO_2 partial pressures and working capacities have been reported in excess of 4 mmol g^{-1}.[20] The silica based

materials could be used as viable adsorbents in a rapid temperature swing adsorption process for carbon capture.

2.3.2 Amine functionalized carbons and carbon nanotubes

Activated carbon is a versatile adsorbent material widely used in gas adsorption/separation as well as for waste water treatment.[65-68] Due to its highly developed surface (micro/mesoporous structure) and availability, activated carbon is considered as a relatively low-cost solid adsorbent in CO_2 capture and separation applications. However, the selectivity of CO_2/N_2 separation is fairly moderate[21] and therefore it is considered to be practical only for CO_2 rich gas mixtures (i.e. pre-combustion capture)[69, 70]. Surface modification of activated carbon with impregnated organic basic moieties was reported to improve the selectivity of activated carbon and improve the total capacity with respect to CO_2 due to the change of the adsorption mechanism from physisorption to chemisorption[56, 71-74]. This should ensure CO_2 uptake even from CO_2 dilute gas mixtures (i.e flue gas). However, literature results vary significantly depending on the amine/carbon substrate and the conditions and procedure used to calculate the CO_2 capacity. The majority of the work, to date, on this approach is covered in a few comprehensive reviews on the properties of solid sorbents for carbon capture[20, 21, 56].

The alternative solid support material to porous carbons is mesoporous silica. There are a large number of promising reports in the literature on the potential of silicas loaded with a variety of amines as detailed in section 2.3.1. A recent paper by Wang et al. [55] compared different mesoporous silicas and emphasized the importance of pore structure for efficient utilization of amine on the support. However, there is a difference in terms of the loading of the amine onto the carbon support, as the cohesive properties of the silica and carbon surfaces will vary.[65, 75, 76] One advantage of carbon supports over the related silica materials is the potential of thermal regeneration of the adsorbent bed through ohmic heating.[77]

In spite of the plethora of studies, there is still a lack of information concerning the effect of surface impregnation on the porosity and surface structure of the activated carbon materials. There have been some suggestions in the literature concerning the optimum level of impregnation required to achieve the highest CO_2 capacity[20, 73], however, the value appears to be highly dependent on the nature and structure of the support. In some cases difficulties were reported in loading more than a small weight percentage of amine onto the support. [74, 78] This however appears to be a result of the choice of the material and it would seem that the success of the impregnation depends on the morphology of the support. There have been conflicting reports on how large an effect impregnating activated carbon with amine has on the CO_2 capacity of the adsorbent. For example, Arou et al [78] impregnated a microporous carbon with PEI and observed that a weight loading of PEI greater than 0.26 wt% had a detrimental effect on the CO_2 capacity. In contrast, a study by Lee et al[71] into the use of sterically hindered amines impregnated (~ 40 wt%) on palm shell derived activated carbon reported a significant (88%) increase in the enhancement in the CO_2 capacity despite a large reduction in the accessible surface area. In chapter 5, the influence of amine loading and the pore structure of the activated carbon on the CO_2 capacity was investigated. Recent publications from Wang et al. have reported PEI impregnation on mesoporous carbon with an impressive uptake capacity of 2.25 mmol g^{-1} at 400 ppm CO_2 at ambient temperature.[79, 80] In addition, they reported that the inclusion of an additional polymer as a diffusion additive could alleviate diffusion limitations through the impregnated PEI. The kinetics of reaction of amine and CO_2 is of critical importance to the design of a separation process for carbon capture. The kinetics of reaction in PEI impregnated mesoporous carbons was investigated in chapter 6.

One major limitation of solid supports impregnated with low molecular weight amine derivatives is their low stability and performance over repeated adsorption and desorption cycles.[71, 81] Grafting of amines to the surface of a solid support has been suggested as a viable, more stable alternative to physical impregnation of amines. [40, 82-85] Two such works include the grafting of halogenated amines on the surface of a microporous carbon by Houshmand et al.[86] and the modification of carbon powders

with aminophenyl and aryl-aliphatic amine groups by Grondein et al.[82] In chapter 4, amine moieties are directly grafted to the surface of multi-walled carbon nanotubes and a mesoporous carbon and the influence of the functionalization on the adsorbents' affinity to CO_2 was investigated.

Carbon materials were of interest in this project due to their tunable surface chemistry and, in the case of activated carbons, low cost. For a rapid temperature swing process, functionalized carbon materials have promising characteristics. Their electronic properties make them candidates for regeneration through ohmic heating and alternatively the tolerance of the amine functionalities to water vapour opens up the possibility of using waste heat in the form of steam to regenerate the adsorbent bed.[9]

2.4 Summary of performance of literature adsorbents

As has been discussed in the previous sections, numerous adsorbents have been proposed as candidates for use in a carbon capture process. In general, the performance of the materials in the literature are ranked in terms of CO_2 capacity. However, each research study and laboratory tests the materials under different conditions and with different techniques. This can make it challenging to directly compare the performance of the materials reported by different research groups. In Table 2.1 the CO_2 capacities, the method used for the measurement and the conditions of the experiment for selected literature materials is reported. For a direct comparison, selected materials prepared in this work are also included.

Table 2.1: Summary table of literature adsorbents

material	amine	temperature (°C)	CO_2 (%)	q (mmol g^{-1})	measurement technique	Ref
CNTs	APTES[b]	20	15	0.98	breakthrough	[87]
CNT	APTES[b]	50	15	2.45[a]	breakthrough	[88]
AC	EDA[b]	30	100	1.25	TGA	[89]
AC	PEI	75	80	5.0	breakthrough	[73]
AC	MEA	30	100	1.55	TGA	[72]
MCN[d]	PEI	75	100	1.97	TGA	[90]
MCS[e]	PEI	75	15	3.71	breakthrough	[91]
MCF[f]	PEI	75	10	3.94	TGA	[92]
MCM-41	PEI	75	10	2.05	TGA	[48]
SBA-15	TEPA	75	5	3.23	TGA	[93]
13X	-	35	10	2.8	volumetric	[b]
micro-AC	-	35	10	0.28	TGA	[b]
meso-AC2	PEI	75	10	2.07	TGA	[b]
CNT/PVA aerogel	PEI	75	10	2.67	ZLC	[b]

[a] humid conditions; [b] grafted; [c] this work; [d] mesoporous carbon nanospheres; [e]mesoporous carbon spheres, [f] mesoporous cellular foams

In Table 2.1 it can be seen that the materials prepared in this work compare favorably to the functionalized carbon materials reported in the literature that were tested at a low CO_2 partial pressure. There are a large number of studies reporting novel materials with enhanced capacities, however it is also important to consider the kinetics of the chemisorption process and this is addressed through the introduction of a kinetic model in chapter 6. More detailed comparisons of the novel adsorbent reported in the literature can be found in several comprehensive reviews.[9, 20, 21, 94]

3 Background theory and experimental techniques

Throughout this project a series of adsorbent materials were first synthesised and then characterised with a wide variety of techniques. First, the two types of commercial carbon materials, microporous activated carbon provided by Calgon® and multi-walled carbon nanotubes from Thomas Swan & Co. Ltd. were fully characterised. The properties of these commercial materials were then used as the benchmark to assess the performance of the new functionalised materials. For the functionalisation and development of the novel adsorbents the general methodology was as follows: First, the materials were synthesised and functionalised with a variety of wet chemistry synthetic techniques. Second the chemical structure and composition of the materials was established by IR, Raman, X-ray photoelectron spectroscopy (XPS), mass spectrometry and scanning electron microscopy (SEM). Thirdly, the adsorption properties were investigated by the zero-length column experiment, breakthrough experiment, thermal gravimetric analysis and volumetric adsorption studies. Finally the results of the ZLC and breakthrough experiments of promising adsorbents were modelled to fully assess the potential of the adsorbents for CCS. Background theory and experimental details of the wide variety of techniques that were utilised is detailed below.

3.1 Thermal gravimetric analysis

Thermal gravimetric analysis (TGA) is a powerful technique used to monitor the change in a sample's mass as a function of the temperature or a function of time. Measurements throughout this project were carried out on a commercial Setaram Sensys Evo TGDSC instrument as shown in Figure 3.1.

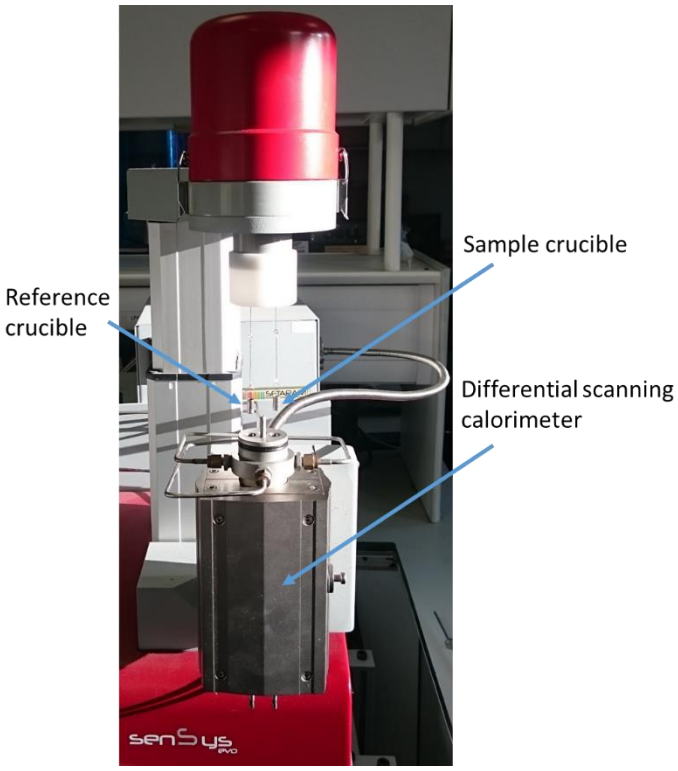

Figure 3.1: Thermogravimetric system showing platinum crucibles

The system consists of two chambers each with a platinum sample crucible. One crucible is packed with 20-60 mg of sample whilst the other is counterbalanced with an equivalent mass of lead balls. The counterbalanced nature of the set-up minimises any buoyancy effects that occur due to any change in the density of the gas during the measurement. The composition of the gas environment can be controlled by two mass flow controllers on the purge and auxiliary gas lines. The inputs are located at the rear of the instrument and there is an adequate mixing volume prior to the sample chamber to ensure the gases are well mixed. Experiments were carried out at a variety of temperatures and typically at a CO_2 partial pressure of 0.1 bar with helium as a carrier.

The system allows the regeneration of the samples under helium flow at an appropriate temperature prior to measurement.

During a typical measurement the sample was first regenerated under helium flow at elevated temperature (100 °C) for a period of time (~5 hrs). The sample was then cooled to the temperature of interest and the microbalance was allowed to stabilise. The helium flow (50 cm^3 min^{-1}) was then switched to a mixture of helium (45 cm^3 min^{-1}) and CO_2 (5 cm^3 min^{-1}). The change in mass of the sample was monitored with respect to time, and corresponded to the uptake of CO_2 by the sample. After the sample was saturated the flow was switched to pure helium (50 cm^3 min^{-1}) and the desorption of the CO_2 from the sample was monitored. The total flow rate was maintained at 50 cm^3 min^{-1} throughout the measurements. A baseline subtraction was applied prior to data analysis.

Simultaneously, during the measurement the Seteram system monitors the heat flow to and from the sample via differential scanning calorimetry (DSC). The heat of adsorption (ΔH) can then be calculated by integrating the heatflow curve using equation 3.1

$$\Delta H = \frac{\int_{t0}^{t} heat\ flow}{m_t - m_{t_0}} dt \qquad (3.1)$$

In which *m* is the adsorbed amount of CO_2 in moles per gram and *t* is time in seconds. Processes with values of ΔH that are less than 50 kJ mol^{-1} are considered to be physisorption whilst values that are greater than 50 kJ mol^{-1} are considered to be chemisorption.[20]

The TGA is a powerful tool for measuring the CO_2 capacity, stability with regards to temperature, and the heat of adsorption of the adsorbent. However, this system does have limitations, including the following. Due to the large mixing volume of the system it is challenging to investigate the kinetics of adsorption. Additionally, without the incorporation of a mass spectrometer, multicomponent mixtures cannot be

investigated along with the performance of a sample in the presence of water. In this regard the zero-length column technique can be utilized to provide further information on a sample's adsorption properties.

3.2 Zero length column technique

The zero-length column (ZLC) technique was first introduced by Eic and Ruthven in 1988[95]. The basic method involves saturating an adsorbent with a known concentration of the component of interest. The flow over the adsorbent is then switched to an inert carrier gas (N_2, Ar, He) to remove the adsorbed species. The concentration profile of the adsorbed species in the gas phase is monitored with respect to time by a detector (e.g. mass-spectrometer, thermal conductivity detector, flame ionisation detector). By conducting the experiment under varied conditions (temperature, flow rate, type of carrier gas) various adsorption parameters can be extracted.

3.2.1 Basic theory and background

Due to the small quantity of sample required in a classical ZLC experiment (2-15 mg) packed in monolayers of crystals, the column can be treated as a well-mixed cell which allows external mass and heat transfer effects to be neglected. These assumptions significantly simplify the models required to fully interpret the ZLC experiments. The mass balance of the system is given by equation 3.2.

$$V_s \frac{\mathrm{d}q}{\mathrm{d}t} + V_g \frac{\mathrm{d}c}{\mathrm{d}t} + Fc = 0 \tag{3.2}$$

Where q is the adsorbed phase concentration, c is the gas phase concentration and F is the inlet flowrate. V_s and V_g are the volume of the solid and gas respectively. The analytical solution to the model was presented by Brandani and Ruthven in 1995[96]:

$$\frac{c(t)}{c_0} = \sum_{n=1}^{\infty} \frac{2L}{\beta_n^2 + (L-1-\gamma\beta_n^2)^2 + L - 1 + \gamma\beta_n^2} \exp\left(-\frac{\beta_n^2 D t}{R^2}\right) \tag{3.3}$$

Where β_n is found from the roots of equation 3.4:

$$\beta_n cot\beta_n + L - 1 - \gamma\beta_n^2 = 0 \tag{3.4}$$

L is defined by equation 3.5:

$$L = \frac{FR^2}{3KV_sD} \tag{3.5}$$

And γ is given by

$$\gamma = \frac{V_g}{3KV_s} \tag{3.6}$$

K is the henry law constant, R is the radius of the particle and D is the diffusivity. In this case it was assumed that the particles of the adsorbent were uniform and spherical. The parameter L defines whether the system is under kinetic or equilibrium control. It is a ratio between the time constant of removing the adsorbed species under equilibrium conditions ($\frac{KV_s}{F}$) and the kinetic diffusional time constant ($\frac{R^2}{D}$). In general, a low value of L (< 1) indicates that desorption of the adsorbate is under equilibrium control ($\frac{KV_s}{F} \gg \frac{R^2}{D}$), whereas L (>>1) indicates that the kinetics are the controlling mechanism ($\frac{KV_s}{F} < \frac{R^2}{D}$).[97, 98] In gas phase experiments the hold up in the fluid phase (γ) is negligible and can generally be neglected.[96]

The ZLC can be used to rapidly rank the uptake capacity of different novel materials. From the area under the concentration response curve the amount adsorbed can be calculated. In the long-time region, at low concentration, noise from the baseline can influence the calculation of the capacity. For this reason, typically an exponential decay of the form ($a$exp(-bt)) is fitted in the long-time region and used to calculate the capacity.

$$q = \frac{F\left[\int_0^{t_0} \frac{c}{c_0}\,\mathrm{d}t + \int_{t_0}^{\infty} a\exp(-bt)\mathrm{d}t\right] - V_b}{V_s} \tag{3.7}$$

Where V_b is the volume of the blank system response with no adsorbent present, t_0 is the time at which the response becomes a pure exponential decay and F is the inlet flow rate. The flow rate is not constant during desorption and a flow rate correction can be applied when the step change in concentration is small to more accurately calculate the capacity, see section 3.2.3. ZLC measurements are always carried out at multiple flow rates in order to validate the extracted material parameters. In this work, the capacity of the material was calculated at a minimum of two flow rates. The average discrepancy in the calculated capacity between flow rates was typically less than 0.1 mmol g^{-1}.

3.2.2 Kinetic analysis

The experiment must be run at multiple flow rates in order to determine the controlling mechanism. Typically when the experiment is carried out at low flow rate the material will be under equilibrium control where the washout of the gas phase is slow enough that the concentration of the adsorbed species on the solid remains at equilibrium with the gas phase throughout the desorption step. If the experimental data ($\frac{c}{c_0}$) is plotted *vs* the product of flow rate and time (Ft) and the desorption plots overlap it is an indicator of equilibrium control.

Under kinetic control, the majority of the information is contained in the long time region. Equation 3.3 reduces to equation 3.8[96, 98] as the higher order terms can be neglected.

$$\frac{c}{c_0} = \frac{2L}{\beta_n^2 + L(L-1)} \exp\left(-\frac{\beta_n^2 Dt}{R^2}\right) \qquad (3.8)$$

From equation 3.8 it can be seen that in the long time region the response becomes a simple exponential decay, which in a semi-log plot is a straight line. From the intercept and the slope of the straight line the L value and $\frac{D}{R^2}$ can be extracted, respectively. The L value is flow rate dependent, whereas under kinetic control the slope in the long time

region should be independent of flow rate. It is essential when determining kinetic parameters (to ensure that the system is operating in the kinetic region) that curves at multiple flow rates are fitted to prevent erroneous calculations of the diffusivity.[97]

There have been numerous studies in the literature where the ZLC technique has been used to determine the kinetic parameters of various materials.[99-101] The technique has also been used to differentiate between a surface barrier diffusion and an intracrystalline diffusion mechanism.[102, 103] In the case of pellets, whether the system is under micro or macro diffusion control can be determined by varying the carrier gas (i.e. N_2 or He) or by changing the radius of the pellet.[99] Establishing which mechanism is the controlling mechanism is of great importance when designing and optimising processes for gas separations. For example, Hu et al. used the ZLC technique to prove that CO_2 adsorption on 13X pellets was under macropore diffusion control.[99] If an adsorbent is under micropore diffusion control then the size of the pellets can be optimized to lower the pressure drop along the adsorption column and hence lower the energy penalty of the process. [99] If a system is under macropore diffusion control a compromise needs to be made between the transport kinetics and the pressure drop along the column.

In addition, the partial loading experiment can be used as an essential tool to determine the adsorption mechanism. The partial loading experiment was proposed in 1996 by Brandani and Ruthven.[102] The method validates the kinetic analysis of the fully saturated ZLC desorption curves. In the experiment the adsorbent is exposed to the feed gas for less time than is required to reach saturation. The flow is then switched to the purge and the response of the material is monitored. It was shown that by conducting the experiment in such a manner there was minimal error in the calculated diffusion time constant from the long-time asymptote but the error in calculating L will be large. A model has been derived to predict the desorption curve at partial saturation (eq. 3.9)[102]

$$\frac{c}{c_0} = \frac{\sum_{n=1}^{\infty} \frac{2L}{\beta_n^2 + L(L-1)} \left[1 - \exp\left(-\beta_n^2 \frac{D}{R^2}\tau\right)\right] \exp\left(-\beta_n^2 \frac{D}{R^2} t\right)}{1 - \sum_{n=1}^{\infty} \frac{2L}{\beta_n^2 + L(L-1)} \exp\left(-\beta_n^2 \frac{D}{R^2}\tau\right)} \quad (3.9)$$

where τ is the time the adsorbent was exposed to the feed mixture. If the partial loading experimental response can be predicted by the model then the calculated equilibrium parameters (L) and kinetic parameters ($\frac{D}{R^2}$) from the fully saturated experiment can be validated. The partial loading experiment can also be used to distinguish between a surface barrier or intracrystalline diffusion controlling mechanism[102].

In further modification of the traditional ZLC experiment, tracer ZLC, is able to measure the self-diffusivity of a material.[104] The versatility of the ZLC technique allows a wide variety of kinetic parameters to be tested and validated.

3.2.3 Equilibrium isotherm

In the case of equilibrium control the slope in the long time region yields the henry law constant. The experiment is typically done at low flow rate. In the case of a linear isotherm, assuming initial conditions:

$$t = 0,\ q = q_0 = Kc_0$$

with

$$q^* = Kc$$

where q^* is the adsorbed phase concentration at equilibrium. The equation of the concentration response curve can be derived from equation 3.2.[105]

$$\ln\left(\frac{c}{c_0}\right) = \frac{-Ft}{KV_s + V_g} \quad (3.10)$$

From the slope of the plot of $ln\left(\frac{c}{c_0}\right)$ vs time, the henry law constant K can be extracted. The value of V_g can be calculated by carrying out a blank experiment, however for a component that is strongly adsorbed $KV_s >> V_g$ so V_g can be neglected. Similar analysis can be applied for an adsorbent with a Langmuir isotherm (eq. 3.11):

$$\frac{q^*}{q_s} = \frac{bc}{1+bc} \tag{3.11}$$

Equation 3.2 can then be integrated under equilibrium conditions to yield the equation for the response curve:[105]

$$\ln\left(\frac{c}{c_0}\right) = \frac{-Ft}{KV_s+V_g} - \frac{KV_s}{KV_s+V_g}\left[\frac{1}{1+bc} - \frac{1}{1+bc_0} + \ln\left(\frac{1+bc_0}{1+bc}\right)\right] \tag{3.12}$$

This equation accounts for the influence of the isotherm shape on the shape of the concentration response of the ZLC. In the long-time region of a plot of $\ln\left(\frac{c}{c_0}\right)$ *vs* time *c* tends to zero and the response becomes linear. The henry law constant *K* can be extracted from the slope providing the adsorbate does not adsorb so strongly that the tail of the desorption response is lost in the baseline.

When the adsorbent is under equilibrium control every point throughout the desorption can be used as an equilibrium point at the respective CO_2 partial pressure in the gas phase (*c*). The previous analysis regards the desorption flow rate as constant throughout the experiment. This is a valid approximation for low concentrations of adsorbate, however at higher concentrations as a significant volume of the adsorbed component is being desorbed the flow rate at the outlet will be higher than the flow rate at the inlet.[105, 106] Equation 3.2 can be modified to give eq. 3.13 to account for the variable flow rate.

$$FC\frac{y}{1-y} = -V_s\frac{\mathrm{d}q^*}{\mathrm{d}t} - V_gC\frac{\mathrm{d}y}{\mathrm{d}t} \tag{3.13}$$

where *y* is the mole fraction of adsorbate in the gas phase and *C* is the total molecular density. It can then be integrated from t=0, $y = y_0$ to give eq. 3.14.[105]

$$q^* = \frac{FC}{V_s}\int_0^\infty \frac{y}{1-y}\mathrm{d}t - \frac{FC}{V_s}\int_0^t \frac{y}{1-y}\mathrm{d}t - V_gc_0\frac{y}{y_0} \tag{3.14}$$

The first term represents the total adsorbed phase concentration at equilibrium. The second integral accounts for the amount desorbed from the sample at time, *t*. The final term accounts for the volume of the blank system. Therefore, assuming that the response is under equilibrium control, it is possible to calculate the adsorbed concentration at different adsorbate partial pressures. By integrating the ZLC response in this manner the equilibrium isotherm can be extracted up to the partial pressure of the feed stream. A similar approach can be utilized to quantify separation parameters for binary mixtures. The equilibrium isotherm of one component can be determined in the presence of another adsorbate.[107]

3.2.4 Experimental set-up

In this work three different ZLC systems have been used. Each of the systems has a slightly different design as they were built at different times and with each iteration improvements have been made. However, the fundamentals of each system are the same, therefore the set-up of the newest of the systems (ARIC ZLC) will be presented in detail. The minor differences that are present in the other systems will be reported. A ZLC system consists of three main sections; they are the dosing system, the ZLC oven and the detector.

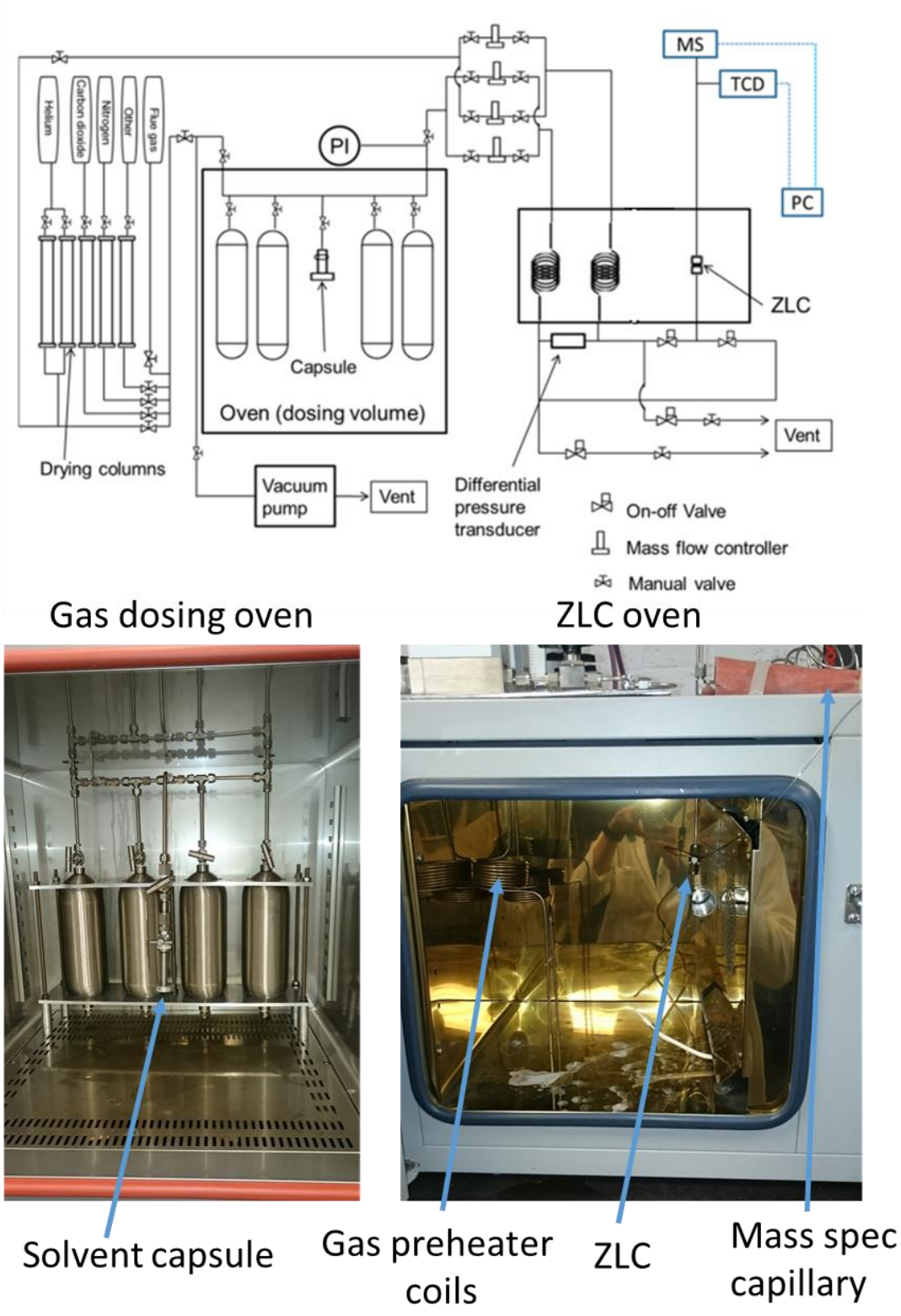

Figure 3.2: Zero-length column experimental set up. Schematic adapted from Hu et al.[108]

3.2.4.1 Gas system

The dosing system consists of a set of 4 connected gas cylinders enclosed inside an oven, with a pressure transducer. There is a gas input connected via a serious of valves to various gas cylinders and a vacuum pump. All gases are pre-dried by drying columns filled with silica gel and zeolite. Mixtures can be created by first pulling a vacuum and then dosing the adsorbate gas to a specific pressure. The cylinders can then be topped up with a carrier gas (N_2, He) in order that the adsorbate gas is present at the partial pressure of interest. For example, to create a 5 bar mixture with a composition of 10% CO_2, 90% He, 0.5 bar of CO_2 would first be added followed by 4.5 bar of helium. The mixture is then left for a minimum of three hours to ensure it is well mixed.

The oven also includes an input where a small capsule containing a solvent can be attached (Figure 3.2). This enables vapour from volatile solvents (including water) to be added to the gas phase. The capsule is first weighed prior to attachment to the system, then the solvent is typically evaporated into the gas phase at elevated temperature and reduced pressure. The required conditions are dependent on the phase diagram of the solvent of interest which can be found on the NIST website.[109] The system is then sealed, the capsule removed, cooled and reweighed. From the mass difference it is possible to exactly determine the number of moles of solvent in the gas phase and then add carrier gas to achieve the desired partial pressure of solvent. Care must be taken at all times to ensure no liquid condenses in the system. For this reason all lines in the system are heated.

3.2.4.2 Lines and mass flow controllers

The system has two primary lines. The purge line which carries the carrier gas for regeneration and desorption and the adsorption line which carriers the adsorbate. The adsorption line is heated to prevent any vapour condensing in the lines. The flow rate is controlled by mass flow controllers, each line has both a low (0-5 cc min^{-1}) and a

high flow (0-250 cc min^{-1}) rate controller. The low flow rate controllers are typically used for equilibrium studies, and the high flow rate controllers are used for kinetic studies. After the mass flow controllers, the gas enters the oven and passes through a preheater coil in the lines. This ensures the gas is preheated and at the temperature of the experiment. During a given experiment the flow rate in each line is the same. Each line splits and is connected to two valves (Figure 3.2). The two valves control whether the gas flows to the ZLC or to the vent. Under normal operation one line is flowing to the vent and one to the ZLC. By simultaneous opening and closing the valves on both lines, the gas can be rapidly switched from adsorption to the purge. After the valves, efforts are made to minimise the dead volume of the system to ensure the volume of the blank response of the ZLC is as small as possible. Gas is continuously flowing through both lines to prevent a build-up of pressure and prevent a back flow of air into the system.

3.2.4.3 Zero-length column

The ZLC is inserted into the oven. The ZLC is a 1/8" Swagelok union. The sample is inserted between two sintered discs that seal the sample within the column (Figure 3.3). The sintered disc is a 1/8" diameter stainless steel disc with a pore size of 0.5 μm and 0.09 mm thickness. Glass wool is inserted on top of the sintered disc followed by a thin layer of sample, then another layer of glass wool. Up to four layers of sample were added (2-15mg). A diagrammatic representation of a packed column is shown in Figure 3.3. The column is then sealed with another sintered disc. The sample is then placed in the ZLC oven and regenerated at elevated temperature over-night, to remove any adsorbed species. The regeneration temperature is highly dependent on the stability of the sample and can vary from (50-400 °C).

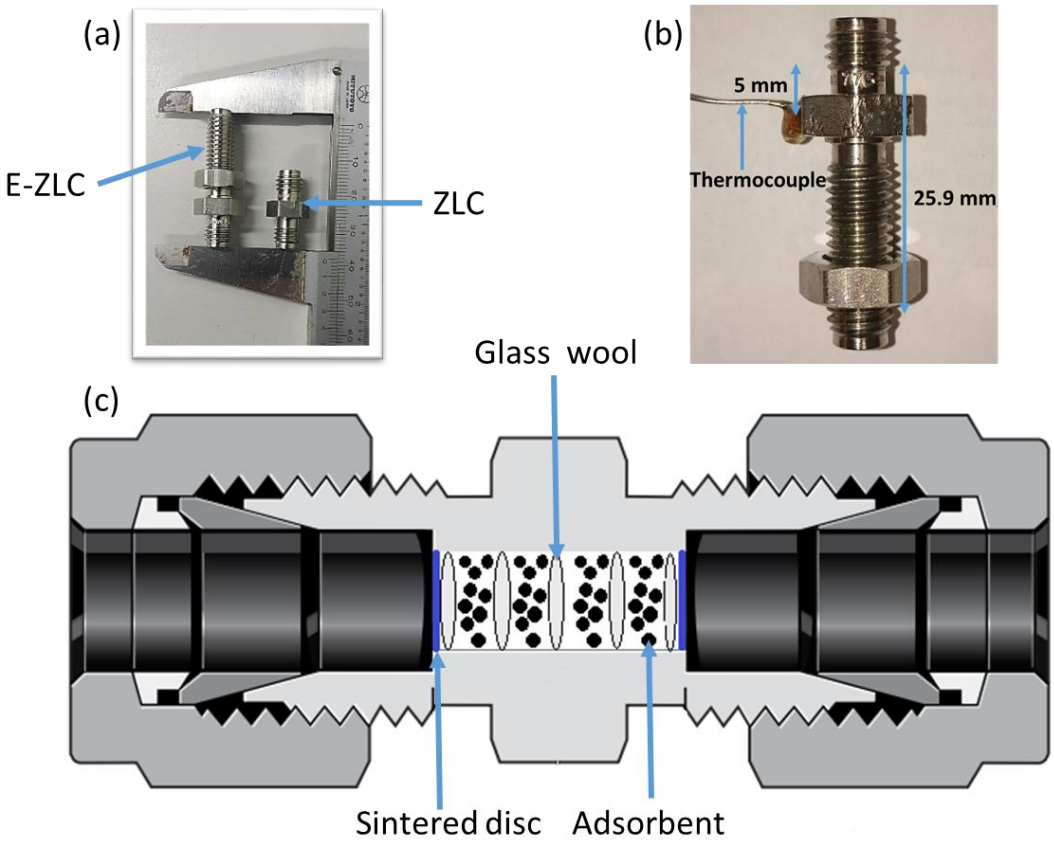

Figure 3.3: (a) Relative scale of E-ZLC and ZLC, (b) EZLC with thermocouple (c) Packing of zero-length column

3.2.4.4 Detector

The gas composition is sampled with a bench-top Ametek Dycor Dymaxion mass spectrometer after the ZLC. A small diameter silica capillary is used to sample the centre of the gas stream. The capillary is heated to 180°C with a heating jacket to prevent condensation in the capillary. Using a mass-spectrometer as a detector adds versatility to the system as multiple components can be monitored simultaneously. This allows binary mixtures to be investigated. The signal from the mass spectrometer (σ_t) is normalised with the input composition (σ_0) and the baseline (σ_∞) using equation 3.15. The response ($\frac{c}{c_0}$) is plotted vs time. An additional plot of ($\frac{c}{c_0}$) *vs* the product of time and the flow rate (Ft) can prove useful in determining the controlling mechanism.

$$\frac{c}{c_0} = \frac{\sigma_t - \sigma_\infty}{\sigma_0 - \sigma_\infty} \quad (3.15)$$

As an alternative to a mass spectrometer, a thermal conductivity detector (TCD) can be used. This was used on the trace gas chromatography system (trace-GC). However, limitations of a TCD prevent the analysis of multi-component mixtures. In addition for flammable components a flame ionisation detector (FID) can be used.

3.3 Extended zero-length column (breakthrough)

The extended zero-length column (E-ZLC) allows breakthrough experiments to be carried out on larger amounts of sample than previously possible with the standard ZLC experiment. The column is a 1/8" bulkhead union with the same internal radius as the standard ZLC (1.1 mm) and is approximately three times the length (25.9 mm). The longer column allows a clear separation of two components to be investigated. The advantages of the E-ZLC over a more traditional larger breakthrough column are that it requires less equilibration time at low flow rates, due to lower sample mass, therefore less gas is required and the time required for complete desorption is shorter. As will be seen in chapter 6 the adsorption column also remains effectively isothermal throughout the experiment.

To validate the isothermal nature of the E-ZLC a modified system was developed. A small hole was drilled in the bulkhead and a 0.5 mm diameter thermocouple was inserted into the centre of the column and glued in place with epoxy resin. This enabled the temperature inside the adsorption column to be monitored throughout the experiment. The temperature profile of the adsorption column could then be compared to the temperature profile predicted by Cysim (see section 3.4). One disadvantage of sealing the thermocouple in place with epoxy resin is that epoxy resin degrades at elevated temperature. Therefore to allow a full *in-situ* regeneration of the adsorption

column an additional adsorption column using Swagelok connections is being designed and built.

3.4 Cysim – Adsorption simulator

The adsorption simulator Cysim was developed at the University of Edinburgh by D. Friedrich et al. [110] the simulator is incredibly flexible and enables virtually any combination of units (inc valves, columns, splitters, mixing tanks) to be combined to simulate an adsorption system. The mass balance and heat balance are accurately modelled, resulting in an accurate prediction of pressure, temperature and composition profiles of adsorption experiments. Through the Cysim simulator, a complete model can be implemented taking into account a wide variety of rate limiting mechanisms. The full model hierarchy is visualised in Figure 3.4.

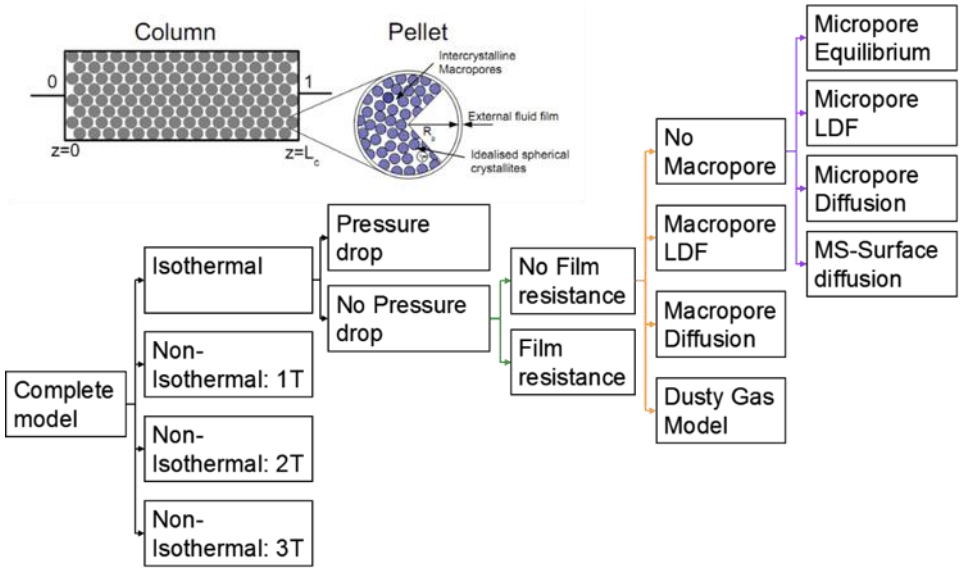

Figure 3.4: Available adsorption models implemented by Cysim. Courtesy of Daniel Friedrich.

Cysim has been utilized to model breakthrough experiments in the E-ZLC. Both the temperature profile of the bed and the concentration profile were simulated and compared to experimental data. The configuration of the units in the adsorption simulator was similar to that reported by Friedrich et al[111] in simulating the ZLC experiment. The only difference was that the length of the unit representing the

adsorption column was increased to represent the E-ZLC. The set-up of the units is shown in Figure 3.5.

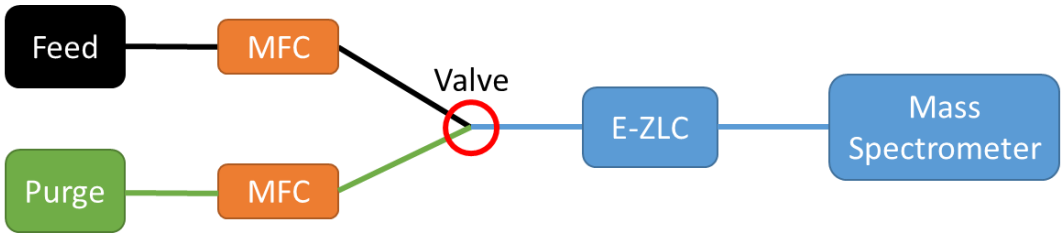

Figure 3.5: Schematic of adsorption units in Cysim simulation

The feed units set the gas composition in each of the lines. The mass flow controllers control the flow rate of each component. The valve controls which line the adsorption column is exposed to at a given experimental time and the E-ZLC column models the adsorbent. It was possible to model the detector's response by also treating the detector (mass spectrometer) as an adsorption column. The blank system responses were first fitted at each flow rate to ensure the simulation accurately predicted the profile of the detector. This increases the accuracy of the adsorption parameters by ensuring the contribution to the breakthrough profile was accurately modelled. The parameters that must be input to accurately model the adsorption column include: isotherm parameters for each gas (linear, single and dual site Langmuir can all be used) kinetic constants, axial dispersion and the heat transfer coefficients. In addition the void fraction of the bed, the heat capacity of the sample and the relative times of each adsorption step must be provided.

3.5 Volumetric system

Several different Quantachrome volumetric systems have been used in this work. They include a NOVA 3000, an autosorb IQ1 and an autosorb IQ2. All three systems collect volumetric isotherms. The NOVA 3000 is an older system and is limited to collecting N_2 isotherms at 77K. This provides useful information on the surface area and pore structure of the porous materials. The IQ1 and IQ2 are newer, more advanced systems and can collect isotherms for a wide variety of gases at various adsorption temperatures. They also have other features (e.g. chemisorption) that have not been used in this work. The IQ1/IQ2 systems have pressure transducers that are able to record data points at very low pressures, this can provide information on the pore size distribution in the micropore region, which is outside the capabilities of the NOVA3000. The IQ1 and the NOVA 3000 are shown in Figure 3.6.

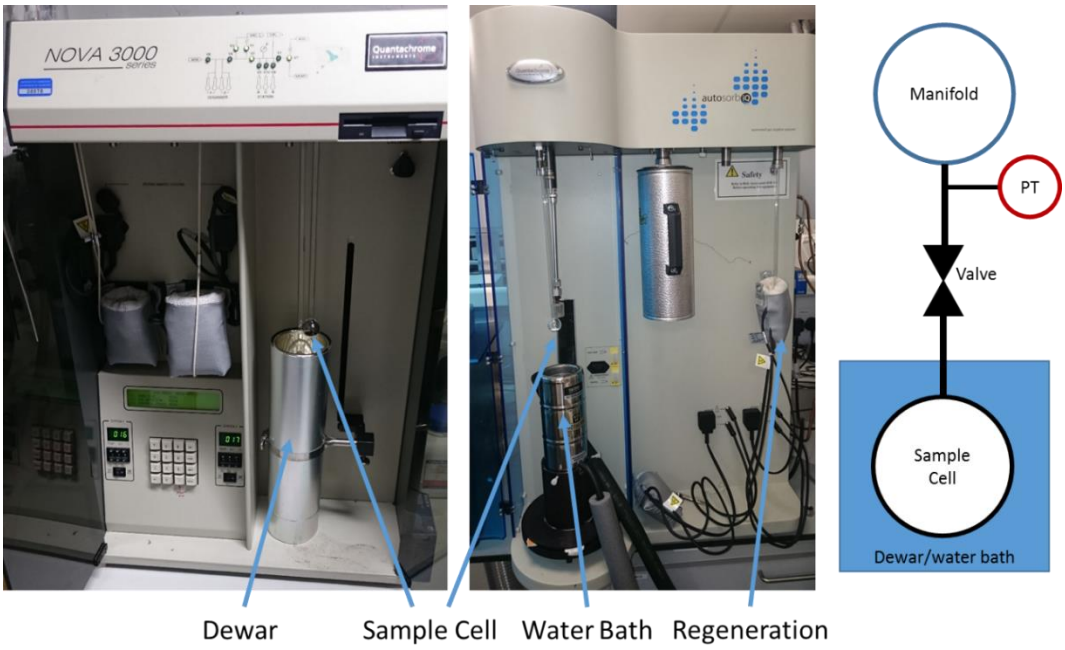

Figure 3.6: Top Schematic of volumetric system. LHS: Quantochrome Nova 3000, middle: Quantachrome IQ1 RHS: schematic

3.5.1 Background and theory

Each system contains a dosing volume (manifold) that is separated from the cell containing the sample by a valve along with one or a series of pressure transducers (Figure 3.6). In a standard experiment the manifold is first filled with a known number of moles of gas, which by opening the valve between the manifold and the sample cell is then exposed to the sample. The pressure change is then monitored. Further gas is then dosed to the sample until the user-requested pressure has been reached. The sample will equilibrate for a defined equilibration time before that point on the isotherm is recorded i.e. volume of gas dosed and the relative pressure. The next point on the isotherm will then be collected. Prior to the start of an experiment the sample volume is measured by dosing a known volume of nitrogen (NOVA3000) or helium(iQ1/iQ2) to the sample at room temperature and monitoring the pressure change. The sample cells in the NOVA3000 must be calibrated prior to sample measurement. It is assumed that there is negligible adsorption of He or N_2 at room temperature by the adsorbent. In addition for a kinetic experiment the change in pressure in the system, once the sample has been exposed to the adsorbate, can be monitored with respect to time in order that kinetic parameters can be extracted.

Isotherms can be collected at multiple temperatures and fitted with isotherm models in order to extract parameters to use in subsequent simulations. The single site and dual site Langmuir isotherms are commonly used, equations 3.16 and 3.17 respectively.

$$q^* = \frac{q_{s1} b_1 P x}{1 + b_1 P x} \tag{3.16}$$

$$q^* = \frac{q_{s1} b_1 P x}{1 + b_1 P x} + \frac{q_{s2} b_2 P x}{1 + b_2 P x} \tag{3.17}$$

With:

$$b_i = b_{0,i} \exp\left(-\frac{\Delta H_i}{\mathbf{R}T}\right) \text{ for } i = 1,2 \tag{3.18}$$

Where q_{s1} is the saturation capacity of site 1, b_1 is the equilibrium constant of site 1, P is the total pressure, x is the mole fraction **R** is the ideal gas constant and ΔH is the heat of adsorption. By fitting the isotherms at multiple temperatures, accurate parameters can be extracted. The majority of isotherm shapes can be assigned under the 1985 IUPAC classifications as shown in Figure 3.7.[112] Type I isotherms are characteristic of microporous adsorbents and type II and III are characteristic of nonporous/macroporous adsorbents with strong and weak adsorption site respectively. Type IV and V isotherms are indicative of mesoporous materials with strong and weak adsorption sites respectively whilst type VI is representative of layer by layer adsorption on a uniform surface.[113]

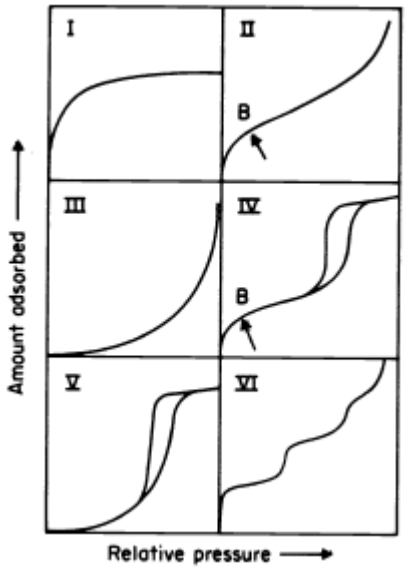

Figure 3.7: IUPAC classification of physisorption isotherms[112]

In addition, in 2015, an update to the original IUPAC classifications was proposed by Thommes et al. to account for the recent developments in material characterization.[113] Pores with a diameter of <2nm are considered micropores, 2-50 nm mesopores and >50nm are macropores.[112]

Volumetric isotherms at cryogenic conditions are a powerful tool to characterize the structure of adsorbents. Information can be extracted from the isotherms regarding the

surface area, pore volume and pore size distribution by applying theoretical models.[113] Typically the experiments are done at 77 K with nitrogen or 87 K with argon. BET theory is a widely used adsorption theory to quantify the surface area of a material and requires the BET equation 3.19 to be implemented.[114]

$$\frac{p/p_0}{q(1-p/p_0)} = \frac{1}{q_m C} + \frac{C-1}{q_m C}(p/p_0) \qquad (3.19)$$

Where q is the amount adsorbed at the relative pressure (p/p_0), C is the BET constant and q_m is the monolayer capacity. By plotting the left hand side of equation 3.19 vs p/p_0 then the monolayer capacity can be extracted from the slope and the intercept and converted to a surface area through equation 3.20.

$$S_{BET} = \frac{q_m N A_{CS}}{M m_s} \qquad (3.20)$$

Where N is Avogadro's number, A_{CS} is the cross sectional area of the adsorbate, M is the molar mass of the adsorbate and m_s is the sample mass. The BET measurement allows the surface area of adsorbents to be compared, however care must be taken to be sure calculations are carried out within the BET range, typically between P/P_0 values of 0.05 -0.3. Particular care must be taken with microporous adsorbents (Type I) where it may be impossible to separate the processes of monolayer/multilayer adsorption and micropore filling.[113] However, the apparent surface area of microporous materials can still be used as a useful tool to compare adsorbents.[113]

The total pore volume of a material can be estimated from the total number of moles adsorbed at a P/P_0 close to 1. At this point the assumption can be made that the micro and mesopores are filled with liquid adsorbate. The adsorbed amount q (in grams) can then be converted to the volume of liquid in the pore by:[115]

$$V_p = \frac{W_a}{\rho_l} \qquad (3.21)$$

Where ρ_l is the liquid density and V_p is the pore volume.

The pore size distributions calculated in this work were carried out using the DFT method that allows the pore size distribution to be calculated across the micro and mesoporous range. The method relies on simulated kernels of isotherms, to which the experimental data is then fitted. The kernels are calculated by molecular simulation and take into account density profiles of confined fluids and consider the adsorbate interactions on a molecular level.[113] Care must be taken when selecting the correct kernel to ensure the correct pore geometry (slit, cylindrical, spherical or hybrid) is selected because if the selected kernel does not accurately represent the adsorbent a significant error in the calculated pore size distribution can result.[113, 116] The pore size distribution calculations were implemented with Quantachrome's ASiQwin software version 3.01.

3.5.2 Experimental procedure

In a typical volumetric adsorption experiment the adsorbent is first regenerated under vacuum at elevated temperature. In the case of the Quantachrome system this is done in the regeneration stations. The temperature of regeneration is sample dependent ranging from 50 °C for functionalized carbons to 350 °C for zeolites. The sample cell is backfilled with helium or nitrogen to enable the sample to be transferred to the analysis station. A stopper is used to prevent any unwanted adsorption from air. The sample is accurately weighed post-regeneration and the dry sample mass is used in all calculations. The sample is then attached to the analysis station where there is a circulating bath to control the temperature from approximately –20 to 60 °C or alternatively a Dewar for measurements under cryogenic conditions. The experimental parameters were set using Quantachromes automated software (version 3.01 or 1.11).

3.6 Infra-red spectroscopy

Fourier transform infrared (FT-IR) spectra of the materials were measured on a Smiths Illuminat IR microscope equipped with Smiths Detection ATR diamond coated objective (x36 magnification). IR spectral features of carbon materials exhibited low intensity (on the level of 0.01 absorption units) and for all spectra a baseline subtraction procedure was applied. The assignment of IR spectra was performed using the atlas of infrared characteristic group frequencies [117].

3.7 X-ray photoelectron spectroscopy (XPS)

XPS spectra were collected by Dr. Ron Brown using a VG Sigma Probe with a monochromated Al K-alpha source with a photon energy of 1486.7 eV. Small pieces of material of approximately 1 mm thick were prepared on carbon tape prior to analysis.

4 Covalent grafting of MWCNTs and porous carbons

Carbon materials have been used as adsorbents in separation processes for decades, they have numerous advantages over other types of adsorbent including high stability and low cost. However, in general, at the low partial pressures of interest for carbon capture the carbon surfaces have a low affinity for CO_2. It is therefore necessary to chemically functionalise the surface to enhance the carbon adsorbents' selectivity towards CO_2. The addition of amine moieties introduces a basic group to the surface that can selectively interact with the acidic CO_2. There are a variety of different routes that can be taken to functionalise the surface including wet chemistry, plasma treatment and impregnation. A full discussion of related materials reported in the literature can be found in section 2.3.2. However, of particular relevance Lu et al. reported the grafting of monoethanolamine, NH_3, ethylenediamine, polyethyleneamine and (3-aminopropyl)triethoxysilane (APTES) to the surface of MWCNTs and an activated carbon.[87, 118] A maximum enhancement of approximately 7 % and 80 % in the CO_2 capacity at 10% CO_2 for APTES grafted activated carbon and MWCNT was reported.[118] Su et al. also reported CNTs functionalized with APTES with a CO_2 capacity of 2.45 mmol g^{-1} although the large weight percentage of APTES (45%) in this case would suggest that the material was a composite as opposed to individual groups grafted to the surface of the CNT.[88] In terms of grafting to activated carbon Houshmand et al. grafted EDA and DETA to a microporous activated carbon and found in terms of the adsorption per unit mass that the grafting had a detrimental effect on the capacity.[89] The conclusion was reached that the grafting of the amines blocked the microporous structure and that a mesoporous carbon may be a more suitable support upon which to graft amines.

In this chapter amine groups were introduced to the surface by direct covalent functionalization. The advantages of grafting amine groups to the surface include relatively high thermal and cyclic stability.[56] The two starting materials of interest in this study were activated carbon and multi-walled carbon nanotubes (MWCNTs). For MWCNTs some examples of potential synthetic routes, which can also be applied to

activated carbons, are shown in Figure 4.1a. Multi-walled carbon nanotubes and porous activated carbons were both investigated as suitable starting materials for synthetic functionalisation. MWCNTs were chosen over single walled carbon nanotubes because they are cheaper and in general contain a larger number of defects in the carbon lattice for sidewall functionalisation. For the investigations the general two-step functionalisation procedure in Figure 4.1b was followed.

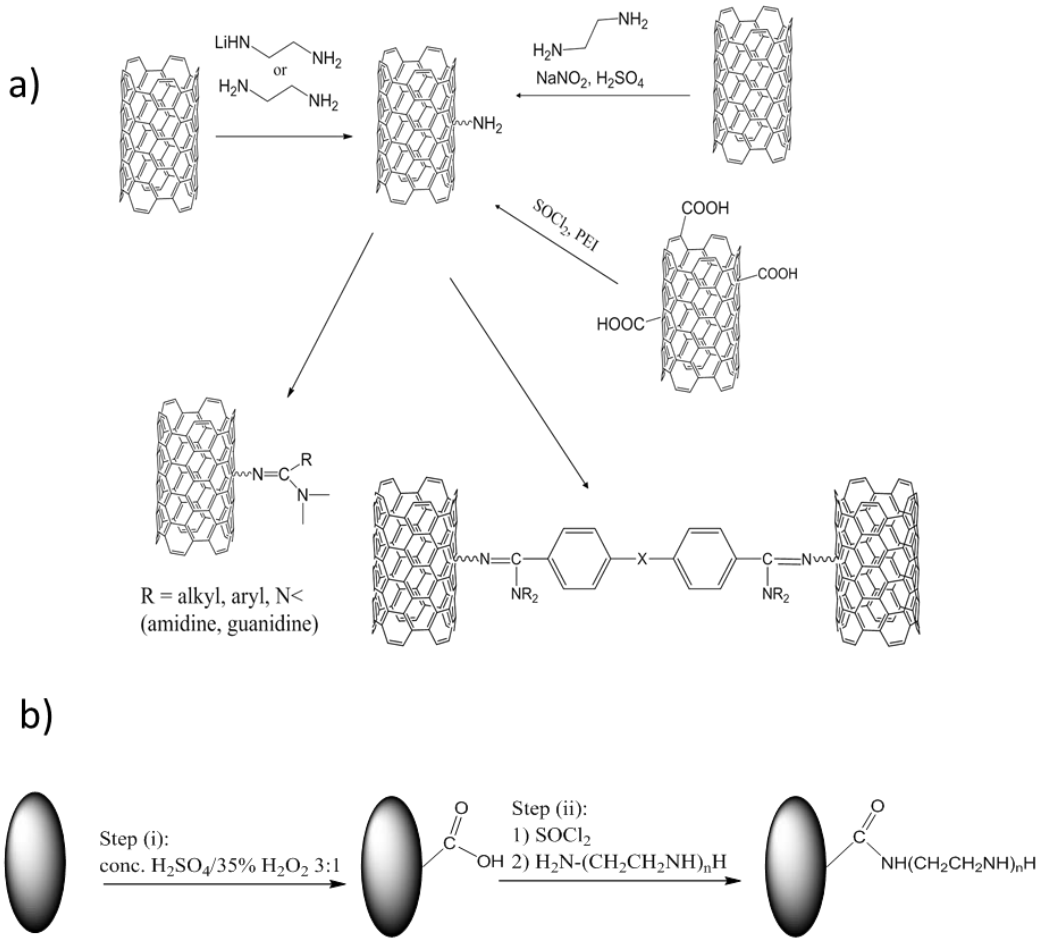

Figure 4.1: (a) Synthetic routes to carbon nanotube functionalisation. (b) Two-step synthetic covalent functionalisation procedure

4.1 Experimental- Chemical grafting and synthesis of carbon materials

4.1.1 Carbon materials

The multi-walled carbon nanotubes (MWCNT) were provided by Thomas Swann & Co. Ltd. The MWCNTs have a length and diameter of up to 10 μm and 8-10 nm respectively with, on average, 5-8 walls.

A second carbon material (further denoted as meso-AC) was synthesised using a templating method with a carbon precursor on mesoporous silicagel, similar to the method reported by Bohme et al.[119]. Typically, ~3g of dry sucrose, 2.5 g of silicagel, 20 ml of distilled water and 200 μl of conc. sulphuric acid (96%) were stirred on a hotplate at a temperature of 50-60 °C until all the water had evaporated. The homogeneous dry dark mixture was heated in an oven at 100 °C for 4 h and then 160 °C for 5h. The resulting 'caramel' was annealed at 900 °C in an Ar atmosphere for 5h. The resultant carbon-silica composite was treated with 30% KOH solution at 70 °C overnight and the product was isolated by filtration. Typically the yield of carbon material was 1-1.1 g. XPS analysis showed no presence of Si in the product. Further analysis and characterization of the pore structure of meso-AC and micro-AC was carried out in section 5.2.1.

4.1.2 Amines

The amines that were grafted in this study all had the general form $H(HNCH_2CH_2)_nNH_2$. 1,2-diaminoethane anhydrous, laboratory grade reagent (further denoted as EDA, n=1) was purchased from Fisher Scientific; diethylenetriamine (DETA, n=2), 99% and polyethyleneimine with molecular weight 600 (PEI600, n=13.5), branched, 99% were purchased from Alfa Aesar; triethylenetetramine (TETA, n=3), tech. grade, 60% of linear isomer was purchased from Acros Organics.

4.1.3 Functionalisation method

The surface of the carbon was modified by a two-step functionalisation process as illustrated in Figure 4.1b. The same procedure was followed for both activated carbon and MWCNTs

Step (i) – Oxidation:

Approximately 500 mg of carbon material was dispersed under stirring in 100 cm^3 of conc. sulphuric acid (95%). Then 30 cm^3 of a 35 % solution of hydrogen peroxide was added under cooling so that the temperature of the reactor did not exceed 20 °C. Strong gassing was observed during the addition of the hydrogen peroxide. The reaction mixture was heated at 70 °C for 5h. The oxidised carbon material was isolated by filtration, washed with water, a sat. solution of sodium hydrocarbonate, water, a 3% solution of HCl, water and then methanol.

Step (ii) – Amine grafting:

Approximately 100 mg of oxidized carbon material was added to 6 cm^3 of thionyl chloride (82.7 mmol) and 90 µl of dimethylformamide. It was refluxed for >12h in a nitrogen atmosphere. The carbon material was isolated by filtration through a PTFE membrane, and the excess $SOCl_2$ was washed out with dry dichloromethane. This material was then dispersed in 50 ml of dry dichloromethane and added to a solution of 3 g of the amine of interest (50 mmol EDA/29 mmol DETA/20.5 mmol TETA/5 mmol PEI600) in 80 ml of dry dichloromethane. The mixture was then refluxed for 2 days. The product was isolated by filtration, washed with water, sat. solution of sodium hydrocarbonate, water and methanol.

4.2 Results

4.2.1 Surface characterisation: XPS, IR and N_2 adsorption

The surface composition of all the synthesised materials was first investigated by x-ray photoelectron spectroscopy (XPS). In Figure 4.2 the XPS spectra along with the calculated atomic composition of the surface are presented. It can be clearly seen that the nitrogen content of the surface compared to the original oxidized material has increased significantly.

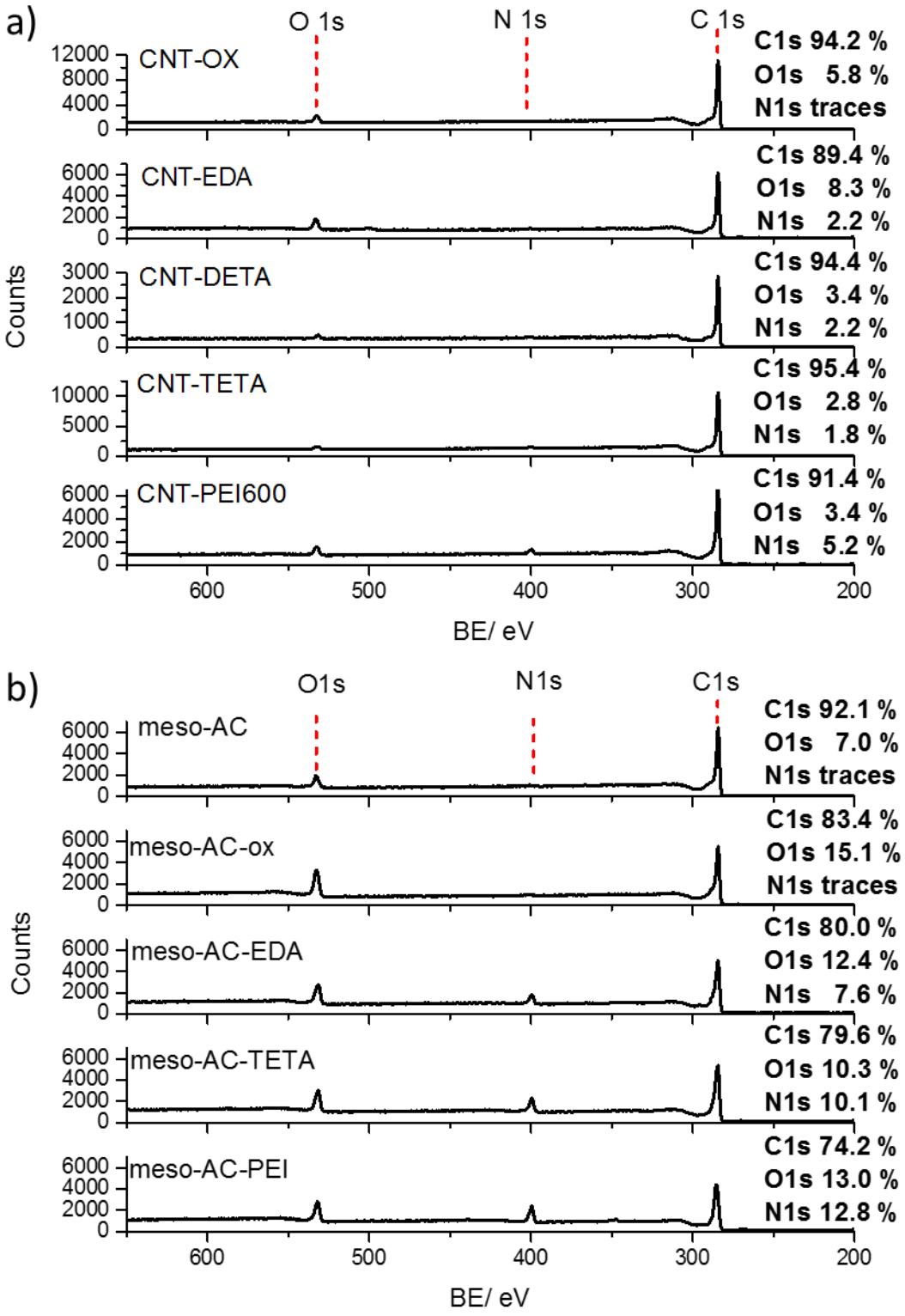

Figure 4.2: XPS spectra of covalently grafted carbon materials. a) MWCNTs, b) meso-AC

In the case of meso-AC, the relative atomic % of nitrogen present on the surface increases as the chain length of the polyamine increases. This was to be expected because with the longer chain polyamines each successful covalent functionalisation results in the incorporation of a greater number of nitrogen atoms. In the case of the CNT's the attempts to functionalise the surface only resulted in a maximum atomic percentage of 5.2% nitrogen. A discrepancy was observed in the case of CNT-EDA where a higher atomic percentage of oxygen was recorded than in the starting oxidized material (CNT-OX).

In order to further assess the success of the functionalization, the yield of surface carbonyl groups that had been functionalized with amine in each case was calculated. First the number of carboxyl groups (COOH) on the surface of the CNTs and meso-AC was calculated. Oxidation of multi-walled carbon nanotubes with H_2O_2/H_2SO_4 (piranha) along with other oxidation methods (HNO_3, NH_4OH/H_2O_2 and plasma) have been reported to create a mixture of oxygen containing groups, including alcohol, carbonyl and carboxyl functionalities.[120, 121] Peak fitting was carried out on the XPS data in Figure 4.3 in an attempt to quantify the number of carboxyl sites on the surface. However, the binding energies of the oxygen containing functional groups are very close together in the C1s and O1s spectra and the measured spectra are relatively featureless. The use of peak fitting can lead to misleading and ambiguous quantification of the functional groups present on the surface.[121, 122] The functional groups cannot be quantified with confidence by XPS alone due to the lack of distinct peaks in the spectra of CNT-OX and meso-AC-OX (Figure 4.3). As a result, in order to compare the relative yield of the second stage of the functionalization (amine grafting) for each of the different amines, it was assumed that all the atomic oxygen on the surface was present in carboxyl groups that were available to react with amine. This enables the conversion rate of carboxyl to amine for the polyamines of different chain length to be compared. However, it should be noted that Datsyuk et al. reported that only approximately 30% of the oxygen content was incorporated in carboxyl functional groups when piranha solution was used as the oxidizing agent.[120] Therefore the real conversion yield of carbonyl to amine groups would be significantly higher than those reported below.

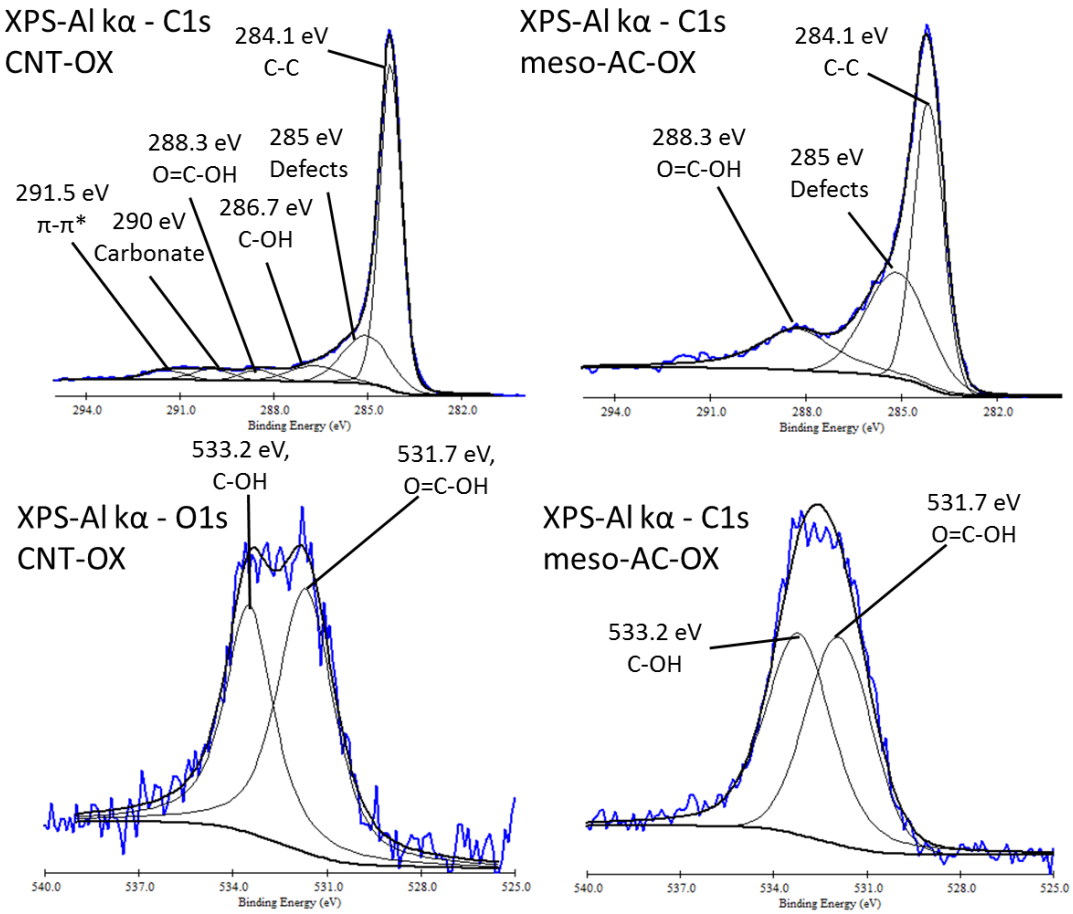

Figure 4.3: XPS peak fitting of C1s and O1s of CNT-OX (LHS) and meso-AC (RHS). Shirley baseline used, mixed Lorentzian-Gaussian peaks. Peak assignment from Ref([120, 123, 124])

From XPS the atomic composition at the surface has been calculated. In order to calculate the number of surface functional groups per 100 carbon surface atoms a series of calculations were carried out. Each COOH group on the surface contains two oxygen atoms and one carbon atom, in order to calculate the atomic percentage of carbon not incorporated in COOH groups ($\%C_{surface}$), assuming all oxygen measured was in that form, the following equation was applied:

$$\%C_{surface} = \%C - \frac{\%O}{2} \qquad (4.1)$$

Where %C is the total atomic percentage of carbon and %O is the total atomic percentage of oxygen. The number of COOH groups per 100 surface carbon atoms (N_{COOH}) was then calculated with the following equation:

$$N_{COOH} = \frac{100}{\%C_{surface}} \times \frac{\%O}{2} \quad (4.2)$$

For the amine functionalized materials, to calculate the number of amine groups per 100 carbon atoms of surface (N_{amine}) the following procedure was followed. Hydrogen atoms are not detected by XPS so are not included in the atomic composition. First the atomic percentage of the carbon atoms that were not included in the amine functional group or the remaining carboxyl groups was calculated.

$$\%C_{surface} = \%C - \left(\frac{\%N}{n+1}\right) \times (2n+1) - \frac{\%O - \frac{\%N}{n+1}}{2} \quad (4.3)$$

Where n is the number of monomers in the polyamine with the general formula $H(HNCH_2CH_2)_nNH_2$ and %N is the atomic percentage of nitrogen. In equation 4.3, the second term accounts for contribution of the carbon in the amine chain along with the carbon in the amide that binds to the surface (Figure 4.1b). The third term accounts for carbon that is present in unreacted carboxyl groups. The number of amine groups per 100 carbon surface atoms was then calculated with the following equation:

$$N_{amine} = \frac{100}{\%C_{surface}} \times \left(\frac{\%N}{n+1}\right) \quad (4.4)$$

The conversion percentage of carboxyl groups to amine functional groups (%Yield) was then calculated:

$$\%Yield = \frac{N_{amine}}{N_{COOH}} \times 100 \quad (4.5)$$

The results were summarized in Table 4.1 and it can be clearly seen that as the length of the polyamine chain increases the conversion of carbonyl groups to amide groups

decreases. The larger molecules are less reactive and hence fewer of the available groups are functionalised.

Table 4.1: XPS results and calculation of %Yield in converting carboxyl groups to amine functionalities on the surface of CNTs and meso-AC (AC).

	%C	%O	%N	n	$\%C_{Surface}$	N_{COOH}*	N_{amine}*	%Yield	$\%M_{\uparrow}$[b]	$\%M_{\uparrow}$[c]
CNT	98	2	0	-	97	1.0[a]	-	-	-	-
CNT-OX	94.2	5.8	0	-	91.3	3.2[a]	-	-	-	-7.2
CNT-EDA	89.4	8.3	2.2	1	82.6	-	1.34	42.3	4.2	4.7
CNT-DETA	94.4	3.4	2.2	2	89.1	-	0.84	26.4	5.3	10.6
CNT-TETA	95.4	2.8	1.8	3	90.5	-	0.49	15.5	4.7	2.3
CNT-PEI600	91.4	3.4	5.2	13.5	79.2	-	0.45	14.2	19.5	8.7
AC	92.1	7	-	-	88.6	4.0[a]	-	-	-	-
AC-OX	83.4	15.1	-	-	75.9	10.0[a]	-	-	-	-7.8
AC-EDA	80	12.4	7.6	1	67.1	-	5.7	56.9	14.4	0
AC-TETA	79.6	10.3	10.1	3	64.6	-	4.0	39.3	30.4	14
AC-PEI600	74.2	13	12.8	13.5	61.8	-	1.4	14.4	50.4	12.5

* number of groups per 100 atoms of carbon surface
[a] Calculated with equation 3.2
[b] Percentage mass increase predicted from XPS using equation 4.6
[c] Experimental measured percentage mass increase

From the calculations of the %Yield it was possible to calculate a corresponding expected mass increase after the synthesis ($\%M_{\uparrow}$) using the following equation:

$$\%M_{\uparrow} = \frac{\%\text{Yield} \times N_{COOH}(MW_{amine} - MW_{water})}{100MW_{C} + N_{COOH}MW_{COOH}} \quad (4.6)$$

Where MW is the molecular weight of the various components. When the amine reacts with the COOH group water is lost as a byproduct. Considering that the synthetic procedure involved two filtration steps with small quantities of sample lost at each stage the predicted percentage mass increase of the CNT samples was in good agreement with the percentage weight change measured experimentally. The exception was CNT-DETA where the experimental mass increase was greater than

expected, it is probable that residual solvent or water from the atmosphere remained on the sample when the material was weighed post synthesis.

The predicted % mass increase for the meso-AC series of samples was significantly higher in all cases than the experimentally obtained result. This can be understood by considering the nature of the XPS technique and the meso-AC material. The penetration depth of XPS is typically ~10 nm, therefore for CNTs the atomic percentages can be considered to represent the bulk composition of the material. The meso-AC particles are of a size that is >>10 nm and therefore the XPS data only provides the composition of the surface and not the bulk of the material. As a significantly large fraction of the meso-AC is made of bulk carbon the overall mass fraction of carboxyl and amine groups is lower than calculated from the XPS data. Therefore, the calculations carried out above, significantly over predict the percentage mass increase.

The above XPS data shows that polyamines have been attached to the surface of the carbon materials and are in a good qualitative agreement with the IR data (Figure 4.4). In the spectra of all the grafted species a new band at 1645 cm^{-1} was observed, which corresponds to N-H bending vibrations.[117] The intensity of this band is stronger for TETA and PEI600 grafted meso-AC which indicated the bigger mass fraction of amino groups in these species. Additionally the band at 1450 cm^{-1} (CH_2 scissoring vibration) appeared in the spectra of grafted materials, the biggest intensity being observed for meso-AC-PEI600 sample. The intensity of the C=O stretching band at 1710 cm^{-1} decreased in all amide samples. The measured absorbance of the CNTs was so low that it was difficult to clearly distinguish the features.

Clearly the external surface of the meso-AC has been successfully functionalized with amine groups. To investigate the effect of the grafting on the pore morphology, nitrogen adsorption experiments were carried out at 77 K. The isotherms can be seen in Figure 4.5.

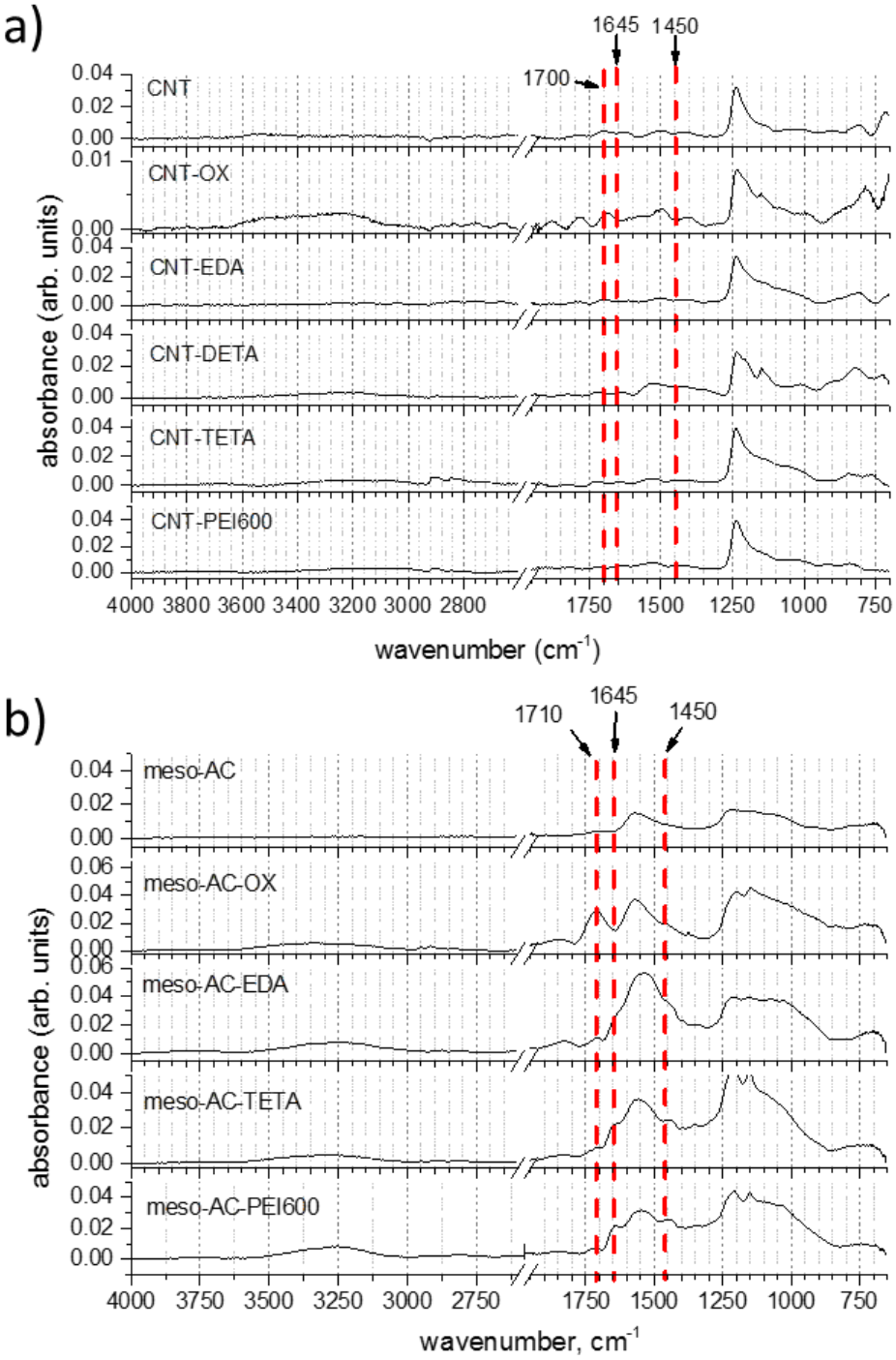

Figure 4.4: IR spectra of (a) grafted CNTs and (b) grafted meso-AC recorded by ATR FTIR spectroscopy.

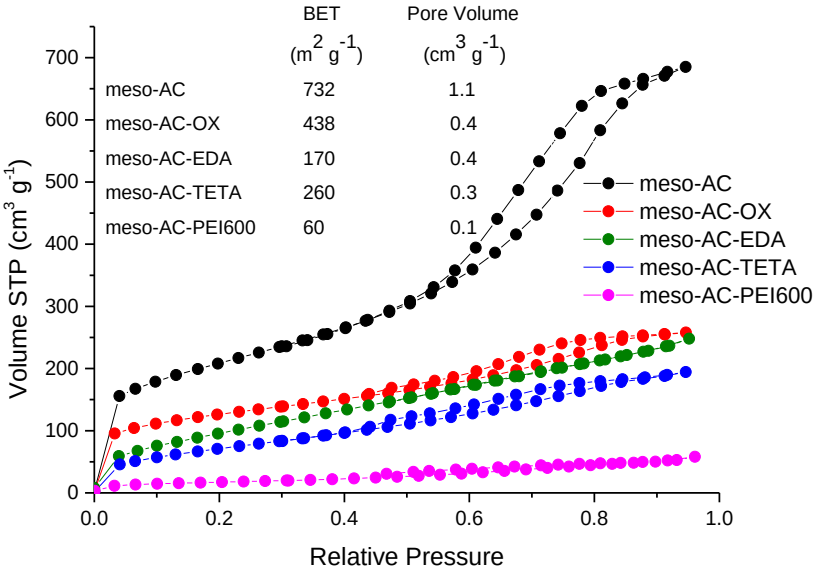

Figure 4.5: Nitrogen isotherms at 77K, amine grafted meso-AC

The oxidation step destroys the pore structure of the meso-AC greatly reducing the available pore volume and the BET surface area (Figure 4.5). A further decrease in accessible pore volume and surface area was measured when the meso-AC-OX was functionalized with the amine. This provides further evidence that the surface of the carbon was functionalized and in the case of PEI600 that a significant amount of PEI was present on the carbon as the pore volume was either blocked or filled by the polymer.

To further investigate the functionalization of the CNTs, laser ablation mass spectrometry was performed. In Figure 4.6 the mass spectrum of the oxidized carbon nanotubes has a clear peak pattern every twelve mass units, corresponding to fragments of the carbon nanotube structure. When the functionalized carbon nanotubes were tested a more complex peak pattern was recorded. The additional peak structure around the peaks of the carbon fragments originates from the amine and is a clear indicator that amine moieties have been successfully grafted to the surface. The additional peak structure was most clearly observed for the larger molecular weight polyamines (PEI600, PEI10K and PEI750K) which was in agreement with the XPS

result for CNT-PEI600 which had the highest recorded atomic percentage of nitrogen containing groups. Peaks have been assigned to nitrogen containing groups in the mass spectrum for CNT-TETA as shown in Figure 4.6c.

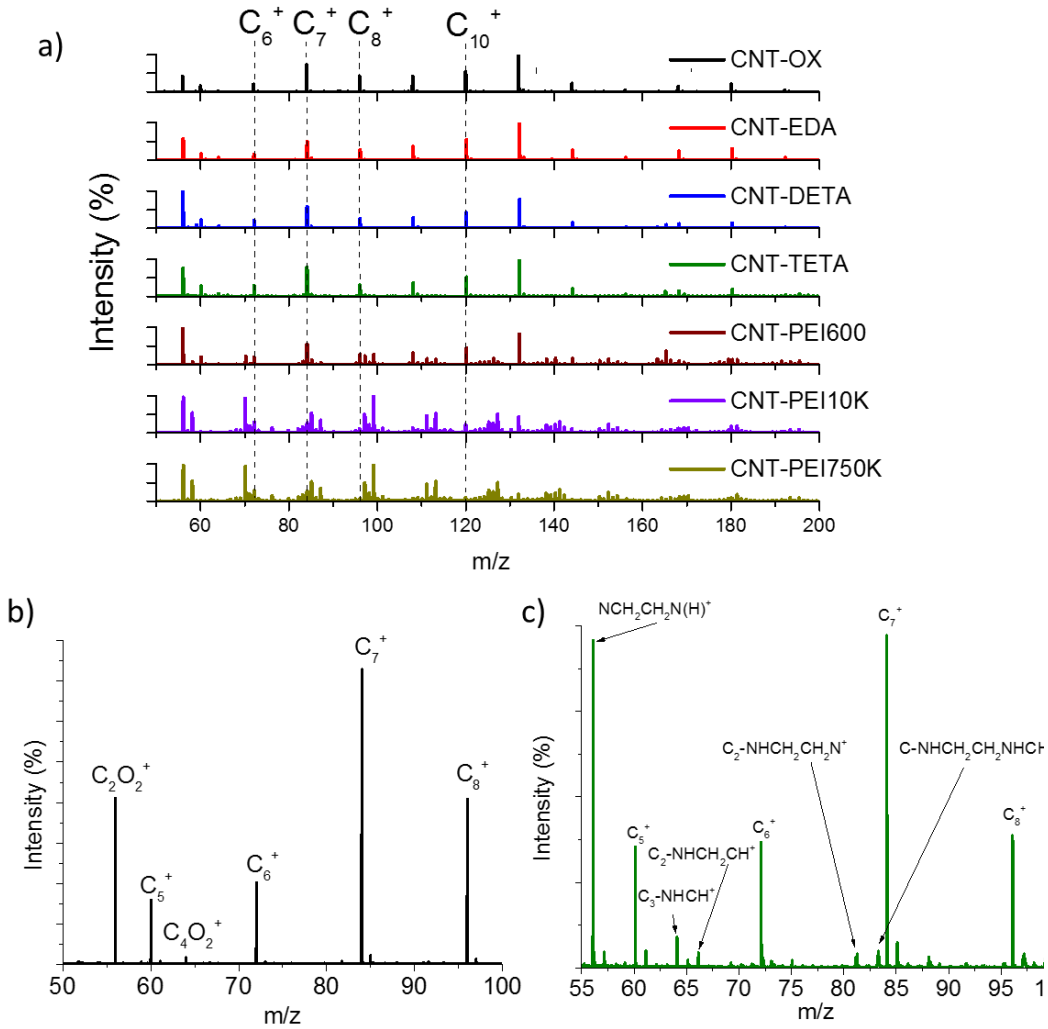

Figure 4.6: Laser ablation mass spectrometry (positive mode) of functionalised carbon nanotubes a) combined functionalised CNT's mass spectrums, b) expanded oxidised CNT mass spectrum, c) expanded TETA functionalised mass spectrum

Two mass spectra of two additional materials, CNT-PEI10K and CNT-PEI750K have also been shown in Figure 4.6, although due to the substantial size of the polymer it was difficult to determine whether the polymer was grafted to the surface or whether the polymer chain simply wrapped around the CNT surface.

From the analysis carried out above it was clear to see that both the surface of the CNTs and the meso-AC have been successfully functionalized by the two step wet synthetic process detailed in Figure 4.1. The introduction of the basic amine groups should enable the selective capture of the slightly acidic CO_2 at low partial pressures. The materials were ranked in terms of their effectiveness to adsorb CO_2 and discussed in the next section.

4.2.2 Ranking of CO_2 capacity for carbon capture

The CO_2 capacity of the grafted materials was first investigated by the zero-length column experiment. The ranking of the materials was carried out at a CO_2 partial pressure of 0.1 bar and at several different temperatures. The blank response of the system was first measured at the flow rate of interest in order to quantify the volume of the system and accurately calculate the capacity. The capacity was calculated by integrating the area between the sample response curve and the blank response and dividing by the sample mass, as detailed in Section 3.2.1.

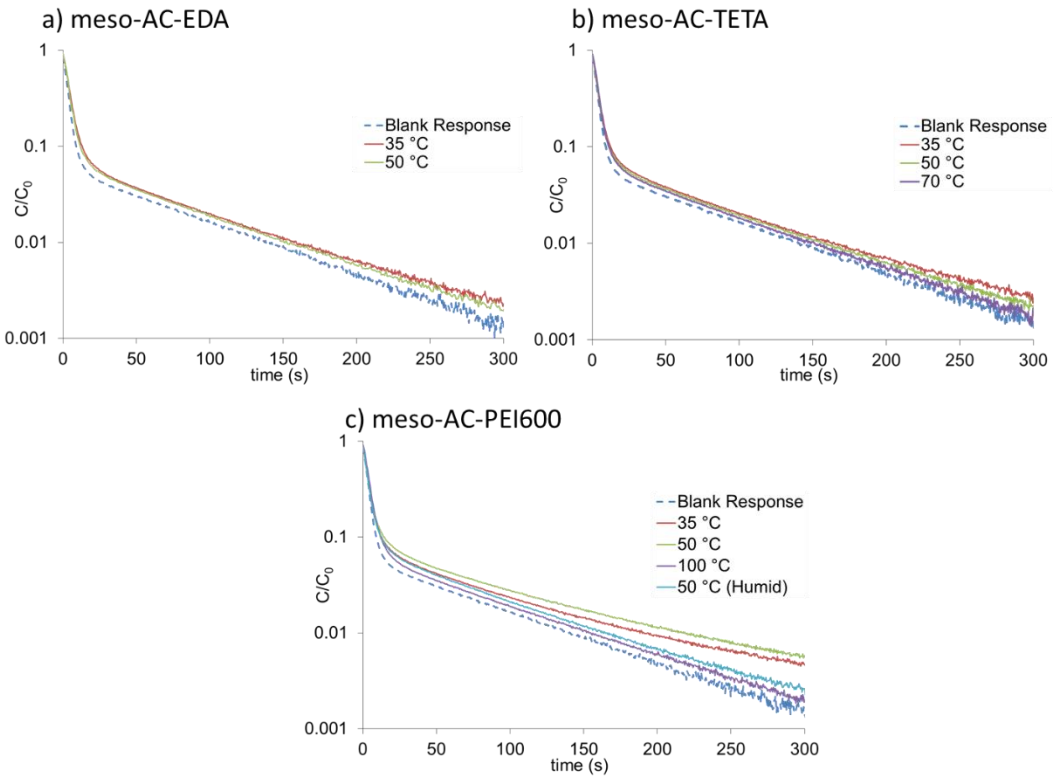

Figure 4.7: ZLC experimental curves of amine grafted meso-AC. 0.1 bar CO_2 0.9 bar He, 5.6 cm^3 min^{-1}, various temperatures. Humid conditions: 5000 ppm H_2O 0.1 bar CO_2, 0.9 bar He

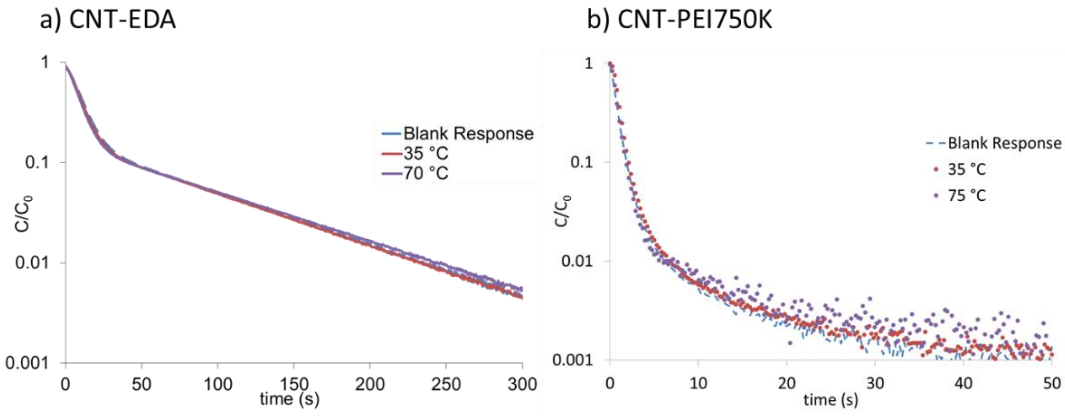

Figure 4.8: ZLC experimental curves of amine grafted CNTs at 0.1 bar CO_2, 0.9 bar He with a helium purge, various temperatures. a) CNT-EDA, 2 cm^3 min^{-1}, 1.6 mg. b) CNT-PEI750K, 10 cm^3 min^{-1}, 8.6 mg.

The ZLC desorption curves for functionalized meso-AC can be seen in Figure 4.7. The capacity of the sample is calculated from the area between the sample response curve and the blank system response. For all temperatures and samples tested the sample response curves are very close to the blank system response. This is indicative of a sample with a very low CO_2 capacity. The calculated capacities are tabulated in Table 4.2 where it can be seen that the CO_2 capacities are less than 0.35 mmol g^{-1} at all the temperatures tested. The only sample where the desorption curve was starting to significantly move away from the blank response was meso-AC-PEI600, where at low concentrations at 35 and 50 °C a slower decay in the gas phase concentration was recorded. This would suggest that a small amount of CO_2 was adsorbed on strong adsorption sites. These results were disappointing as there was no significant improvement in the total CO_2 capacity when the raw, unmodified activated carbon was taken as a benchmark (0.30 mmol g^{-1} at 35 °C). The meso-AC-PEI600 material was also tested under humid conditions (5000 ppm H_2O) as this has been widely documented to significantly enhance the CO_2 capacity.[20] The CO_2 capacity under humid conditions was half that which was measured under dry conditions, this would suggest that a physical adsorption process is dominating with the water competing with the CO_2 for the available adsorption sites. Two of the functionalized CNT materials (CNT-EDA and CNT-750K) were also tested (Figure 4.8) and again the desorption curve was very close to the blank response of the system and the CNT materials appeared to have virtually no CO_2 capacity.

Table 4.2: CO_2 capacities of amine grafted carbon materials at various temperatures

	Temperature (°C)	Capacity (mmol g^{-1})
meso-AC	35	0.30[a]
	50	0.23[a]
	75	0.15[a]
meso-AC-EDA	35	0.17
	50	0.15
meso-AC-TETA	35	0.15
	50	0.12
	70	0.15
meso-AC-PEI600	35	0.26
	50	0.32
	50 (humid)[b]	0.16
	100	0.16
CNT-EDA	35	0.00
	70	0.00
CNT-PEI750K	35	0.00
	75	0.00

[a]Measured by TGA (Section 5.2.3, Figure 5.9)
[b]Humid conditions 5000 ppm H_2O

To understand the low CO_2 uptake capacity recorded, the number of moles of nitrogen atoms on the surface per kg of adsorbent for each functionalized material was calculated as follows:

$$\text{mol(N)} = \frac{\left(\%M_{\uparrow}/_{100}\right)}{(\text{MW}_{\text{amine}}-1)} \times (n+1) \times 1000 \qquad (4.7)$$

Where the first term calculates the number of amine molecules in one gram of adsorbent and the second term considers the number of nitrogen atoms in each amine molecule. Assuming that two NH/NH_2 groups are required to react with one CO_2

molecule under dry conditions as shown in Figure 2.3 then the number of active sites available for CO_2 adsorption can be calculated as 0.5*mol(N). The results of the calculation are shown in Figure 4.9. In all cases, the CNTs have less than 2.5 mmol g^{-1} active sites available for CO_2 adsorption. The calculated number of sites available on the EDA, DETA and TETA functionalized tubes was so low that a significant uptake of CO_2 during the adsorption step could not be expected. This conclusion is in agreement with the experimental ZLC measurements carried out on CNT-EDA (Figure 4.8). The CNT-PEI material had greater promise with 2.3 mmol g^{-1} of active sites available for adsorption, however as will be discussed in greater detail in section 5.2.3, the efficiency of utilization of the active sites in the amine is dependent on the morphology of the support and the type of amine. For PEI600 the ratio of CO_2 adsorbed $q(CO_2)$ to the number of the active sites (0.5*mol(*N*)) was calculated to be ~0.2. Therefore the CO_2 capacity of CNT-PEI600 would not be competitive for carbon capture compared to other adsorbents reported in the literature.

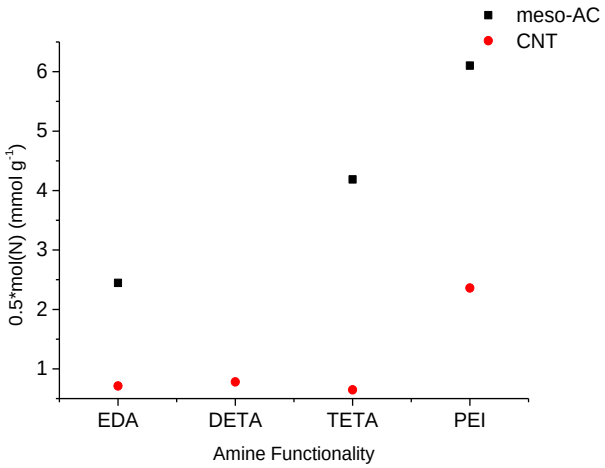

Figure 4.9: Number of active sites (0.5* mol(N)) available for CO_2 adsorption calculated from the surface atomic composition as measured by XPS

For meso-AC functionalized materials on the surface the number of available active sites appears more promising, with an increase in the number of active sites for the higher molecular weight amine. The surface to volume ratio of the meso-AC is large with a BET surface area of 732 m^2 g^{-1}, however despite this, XPS only measures the

composition of the material to a depth of approximately 10 nm and the composition of the bulk carbon is not accounted for. Therefore, due to the contribution of the bulk carbon within the activated carbon the number of active sites per gram was significantly less than the number calculated. It was therefore possible to conclude that not enough active sites had been created on the surface of the functionalized materials to significantly enhance the CO_2 uptake of the adsorbents.

In the calculation of the number of active sites per gram of adsorbent (Figure 4.9) there are two principle sources of error. First, as previously mentioned, for the meso-AC, XPS only measures the surface composition and not the bulk, which potentially results in an overestimation of the relative number of active sites. Secondly, there is an associated error in the quantitative analysis of surface composition through the XPS technique. The quantification of the uncertainty is discussed in the review by Powell et al.[125]. It was concluded that it can be extremely challenging to quantify the magnitude of the uncertainty because it depends on numerous factors including sampling conditions and homogeneity of the surface. However, XPS is generally accepted to provide a good quantitative estimation of the surface composition of the material.

4.2.3 The effect of CO_2 adsorption on the resistivity of functionalized carbon nanotubes

It was apparent that with the current density of functional groups grafted to the surface of the CNTs that the materials were not going to be competitive adsorbents for carbon capture. However, CNTs have widely documented and interesting electrical properties.[126-128] The resistivity of CNTs both single walled and multi-walled has been reported to change on exposure to different gas environments.[129-131] As a result CNTs have the potential to be used as novel gas sensors.[128] There are a wide variety of studies investigating the effect of functionalization on the gas sensing properties of carbon nanotubes for a variety of different gases.[132, 133] Functionalisation whether covalent or

non-covalent can enhance the sensitivity and selectivity of the device. For example, Star et al. reported the fabrication of a nanotube field effect transistor (FET) where the CNTs are non-covalently coated with PEI and starch polymers.[134] Through a doping mechanism the conductance of the FET was reported to change at CO_2 concentrations as low as 0.05%. SWCNTs covalently functionalized with poly(m-aminobenzene sulfonic acid) were reported to be sensitive to ammonia at 5 ppm.[135] In addition, Anoshkin et al. demonstrated that the creation of defects on the CNT surface greatly enhances the sensitivity of the device towards ethanol vapour. [136]

The change in resistivity of the CNTs produced in this work on exposure to an atmosphere containing CO_2 was investigated using the four probe Van der Pauw technique. The sensitivity with respect to the degree of functionalization was investigated.

4.2.3.1 Resistivity measurements: Van der Pauw technique

Resistivity measurements were carried out using the Van der Pauw four probe technique. The Van der Pauw technique[137] enables the sheet resistance of the material to be measured whilst minimizing any error that arises from contact resistance. A current, up to 1 mA, was applied between two electrodes along one edge whilst the voltage is simultaneously measured between the two electrodes along the opposite edge. This procedure was then repeated by changing the two electrodes through which the current is applied, as detailed in Figure 4.10. In this way the resistance along the horizontal (R_H) and vertical (R_V) edges of the sample can be calculated. The Van der Pauw equation (equation 4.8) was then used to calculate the sheet resistivity (R_s). As can be seen in Figure 4.10 R_H and R_V were measured along both edges, the average values of R_H and R_V were used to calculate the sheet resistivity.

$$e^{-\pi R_V/R_S} + e^{-\pi R_H/R_S} = 1 \qquad (4.8)$$

The sheet resistivity was measured under both nitrogen and carbon dioxide gas environments. Additional measurements where a constant current was applied along one edge and the voltage with respect to time was measured across the opposite edge were carried out. The resistivity with respect to time was then calculated and in this way the dynamic response of the system to a change in gas environment could be investigated.

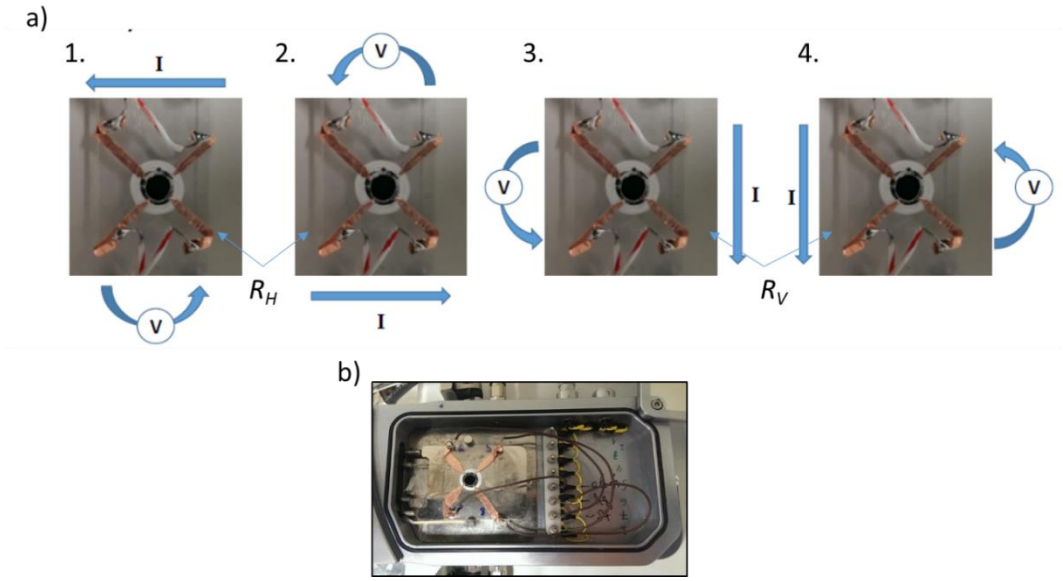

Figure 4.10: Measurement of sheet resistance. a) Steps 1 and 2 measure resistance along horizontal edge (R_H). 3 and 4 resistance along the vertical edge (R_V). b) Sample inside LTS350 Linkam chamber.

To carry out the measurements, bucky paper films of CNTs were produced by dispersing, via sonication, CNTs in dimethylformamide, and then collecting the material on a PTFE filter prior to vacuum drying. The films were then secured between two glass slides, one of which had a 6 mm hole to expose the surface of the film to the gas environment. The electrodes were then placed with equal spacing around the edge of the film as depicted in Figure 4.10. The electrode contact area was minimized to reduce contact resistance. The sample was placed in a LTS350 Linkam chamber which

was used to control the gas environment. The chamber was sealed and various compositions of gases could be flowed through the chamber using mass flow controllers. The chamber was equilibrated at the concentration of interest for 15 minutes prior to the measurement of the sheet resistivity. The stage in the chamber and hence the sample was heated at 90 °C under nitrogen flow prior to any resistivity measurements in order to remove any adsorbed species.

4.2.3.2 Results: change in CNT resistivity upon exposure to CO_2

The percentage change in sheet resistivity (ΔR) was calculated for a series of functionalized films upon exposure to CO_2 by

$$\Delta R = \frac{R_{S,CO_2} - R_{S,N_2}}{R_{S,N_2}} \times 100 \qquad (4.9)$$

The results are visualized in Figure 4.11 where it can be seen that the response of the amine functionalized CNTs was greater than for the raw and oxidized carbon nanotubes. The greatest change of 1.2 % in the sheet resistance was observed for CNTs functionalized with PEI with a molecular weight of 10,000. Raw resistivity values can be found in the appendix in Table A.1.

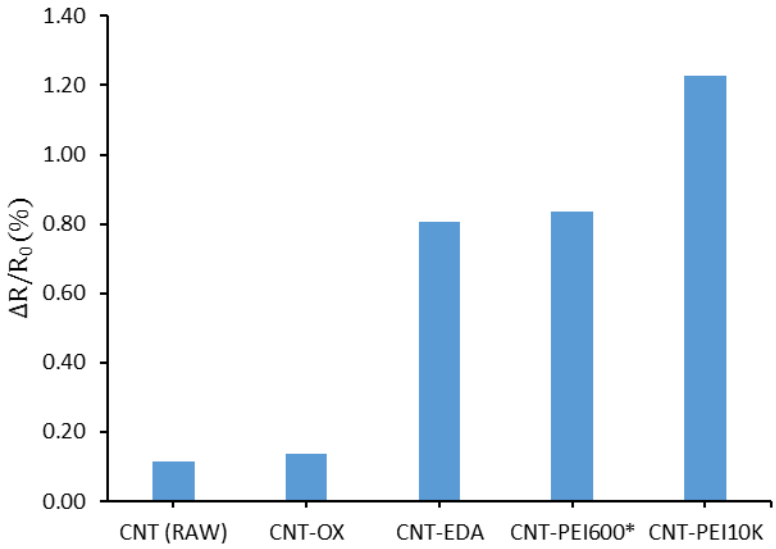

Figure 4.11: Change in sheet resistivity on exposure to 100% CO_2. *Sample exposed to 50:50 mixture of CO_2 and nitrogen

It should be noted that the measured values of sheet resistivity were highly dependent on the regeneration conditions. The presence of adsorbed species (H_2O, CO_2) had a large effect on the conductivity of the films, with the calculated resistivity of the films varying from day to day. In future work, greater control of the humidity of the chamber

and regeneration conditions would be required to ensure reproducibility. In addition, it is possible that the morphology of the films is changing throughout the measurements, through localized heating, resulting in a change in the measured conductivity.[138] Despite this a change in the resistivity for all the amine functionalised films was observed on the introduction of CO_2.

The next step was to test the response of a film at a variety of concentrations. For this CNT-PEI10K was chosen because it had the largest percentage change in sheet resistivity on exposure to pure CO_2. The sheet resistivity was measured at 0, 4, 10, 33, 50 and 66 percent CO_2 and the percentage change in sheet resistivity with respect to CO_2 concentration is shown in Figure 4.12. The sheet resistivity varied linearly with CO_2 concentration, although the magnitude of the measured change at a given concentration was variable over multiple measurements. The probable source of the variation between the measurements is the incomplete regeneration of the films with adsorbed water or CO_2 present on the sample prior to the start of the measurement. The linear response is a promising characteristic for CO_2 sensor applications.

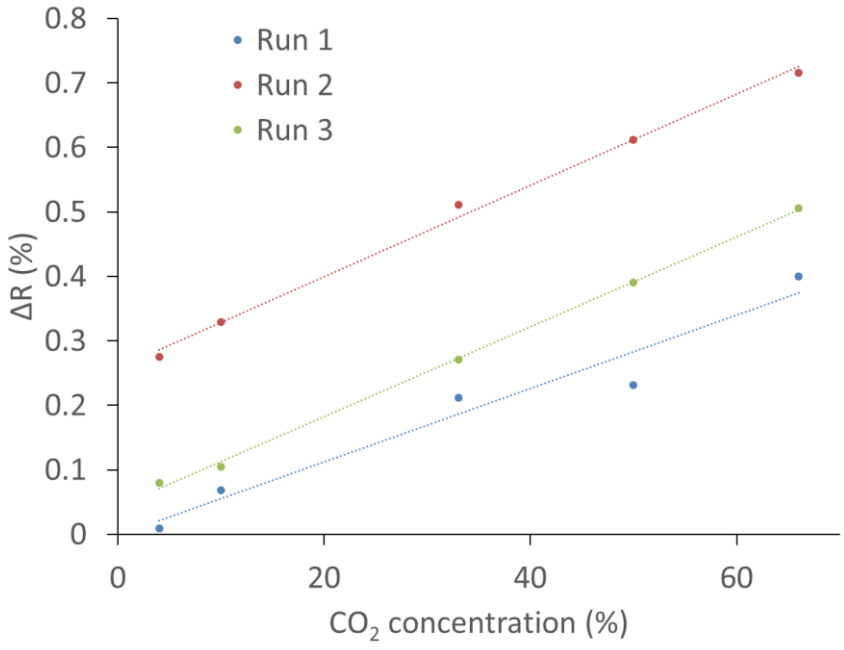

Figure 4.12: Sheet resistivity of CNT-PEI10K with respect to CO_2 concentration.

For a CO_2 sensor the response with respect to time is an important parameter for many applications. The CNT-PEI10K film was exposed to 66 % CO_2 and then purged with nitrogen over three cycles. It can be seen that the resistivity of the CNT film changes rapidly upon exposure to CO_2 and returns to close to the baseline value of a pure nitrogen atmosphere within 5 minutes.

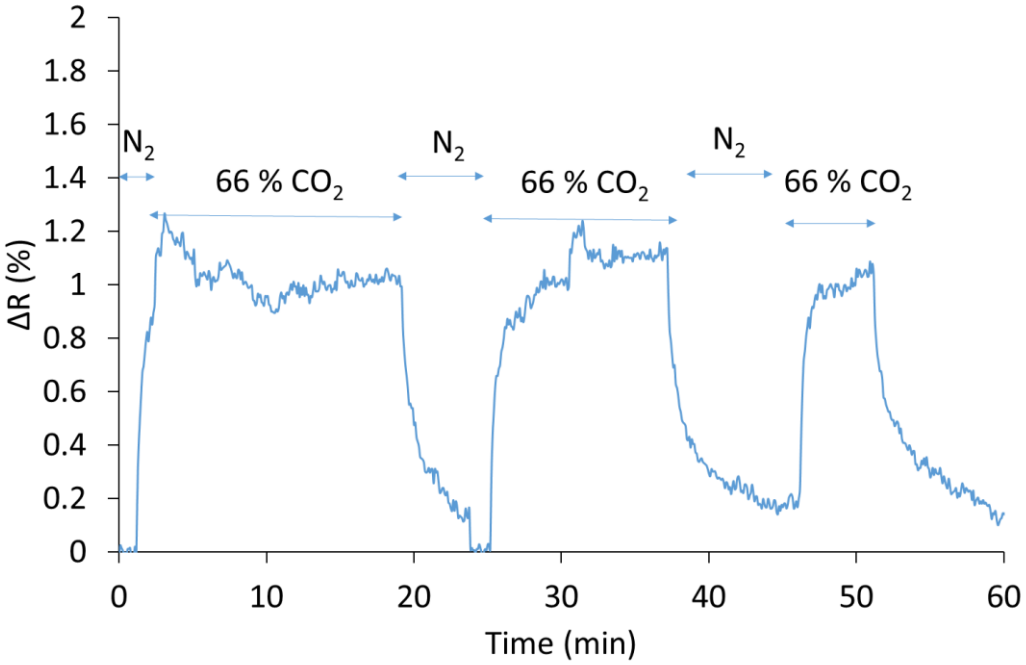

Figure 4.13: % Change of resistivity of CNT-PEI10K film with respect to time

The main purpose of the resistivity measurements was to prove that the amine functionalized carbon nanotubes interact to a greater extent with CO_2 than the non-functionalized tubes. This was indeed the case as shown in Figure 4.11, however in order to fully characterize the CNT thin films as CO_2 sensors further work is required in terms of device design and measurement conditions in order to fully characterize the materials and ensure that reproducible results are obtained. The main commercial CO_2 sensors use infrared absorption to detect the CO_2, however novel, small, low power, wireless devices based on CNTs could have applications in biological and industrial environments.[128, 134] A field effect transistor device with SWCNT could

potentially have higher sensitivity and reliability as a result of the semiconducting properties of the SWCNTs. Functionalisation of the SWCNT could provide selectivity to sense the gas species of interest. The resistivity measurements prove that there is an enhanced interaction of CO_2 with the CNTs as a result of functionalisation, however as previously discussed there are not enough active sites for the materials to make competitive adsorbents for carbon capture in their current form.

4.3 Conclusions

Both CNTs and mesoporous activated carbon have been grafted with amine functionalities in an attempt to enhance their selectivity towards CO_2. The CO_2 uptake capacity of the materials was ranked by the ZLC technique at a partial pressure of 0.1 bar CO_2. However results have shown that not enough active sites were created on the surface of the materials to dramatically enhance the CO_2 uptake of the materials compared to their unmodified forms. The resistivity of the CNTs was seen to change as a function of the CO_2 concentration providing evidence that the materials do interact with CO_2 but not at the levels required for a competitive carbon capture adsorbent. Future work could involve a different synthetic methodology to create more functional groups on the carbon surface. At the first stage of the procedure oxidation with a mixture of HNO_3 or $KMnO_4$ has been shown to create a larger number of carboxyl groups on the surface of CNTs with > 8 atomic percent of covalently attached oxygen reported.[120, 121] This would provide the anchoring point for the addition of a greater number of amine functionalities at the second stage. However, the CO_2 capacity of the functionalized CNTs is so low it is doubtful that even the approximate factor of two increase in the number of a viable anchoring sites would result in a competitive adsorbent for carbon capture. For a competitive separation process an adsorbent with a working capacity of 1 mmol g^{-1} is required.[9] As a result of the low number of active sites created on the surface, the materials reported in this chapter are a long way from achieving this. Therefore, the next progression was to incorporate more amine active sites into the solid adsorbents via wet impregnation. The results of which are reported in the following chapter.

5 Physical impregnation of activated carbon by amines

In order to incorporate a greater number of amine groups into the carbon substrate, the approach of physical wet impregnation was adopted. This method has been widely documented in the literature as an approach to incorporate amines into both porous silica and carbon structures. This chapter is based on the work published in the journal Microporous and Mesoporous materials in 2015[139] along with some additional material. As previously discussed in the introduction, section 2.3.2 surface modification of activated carbon with adsorbed organic basic moieties was reported to improve the selectivity of activated carbon and improve the total capacity with respect to CO_2 due to the change of the CO_2 adsorption mechanism from physisorption to chemisorption[56, 71-74]. This should ensure CO_2 uptake even from CO_2 dilute gas mixtures (i.e. flue gas). However, literature results vary significantly depending on the amine/carbon substrate and the conditions and procedure used to calculate the CO_2 capacity. For example, recent results show a capacity of up to 1.5 mmol g^{-1} for monoethanolamine [72] and 1.1 mmol g^{-1} for polyethylenimine (PEI) impregnated microporous activated carbons[140]. For mesoporous carbon containing PEI, Wang et al reported a CO_2 capacity of up to 5 mmol g^{-1} at a high CO_2 partial pressure[73].

In an attempt to further understand the effect of wet impregnation of carbon by amines on the CO_2 adsorption properties, this chapter directly and systematically compares the incorporation of amine molecules with various molecular weights into two carbons with different pore structures. The effect of the different weight loadings of amine on the available pore volume, surface area and pore size distribution to determine the relationship between the CO_2 uptake and the morphology of the amine containing activated carbon was investigated. The discussion is then advanced to examine how efficiently the active sites are utilized on the support and how the molecular weight of the amine impacts on its reactivity towards CO_2.

A further mesoporous carbon was then synthesised by Rachel Rayne (master's student 2014/15) with a larger total pore volume. This enabled a larger volume of amine to be

incorporated per gram of material. The kinetics of the amine:CO_2 reaction in the long-time region were investigated at different amine loadings. All CO_2 measurements in this chapter were carried out at a 0.1 bar partial pressure of CO_2. This is within the range of partial pressures that are found in the flue gas of fossil fuel power stations and was used as a benchmark.

5.1 Experimental

5.1.1 Materials

1,2-Diaminoethane anhydrous, laboratory grade reagent (further denoted as EDA) was purchased from Fisher Scientific; diethylenetriamine (DETA), 99% and polyethyleneimine with molecular weight 600 (PEI600), branched, 99% were purchased from Alfa Aesar; triethylenetetramine (TETA), tech. grade, 60% of linear isomer was purchased from Acros Organics. EDA, DETA and PEI600 were used for preparation of impregnated porous carbons without additional purification; TETA was additionally purified by vacuum distillation (b.p. 118 °C/7 mbar) before use.

Granular activated carbon (SRD 10061) was provided by Calgon Carbon. This material exhibited a microporous structure (see Table 5.1) and is denoted as micro-AC. Two other activated carbon materials (further denoted as meso-AC and meso-AC2) were synthesized as detailed in section 4.1.1. The meso-AC material was synthesized from a silica gel with an average pore size of 60 Å, whilst for meso-AC2 the silica precursor had an average pore size of 150 Å. SEM images of the surface of the three different carbon materials are shown in Figure 5.1. Differences between the surfaces of the three activated carbon materials were observed. Large pores can be clearly seen in the meso-AC2 (Figure 5.1c) material with no visible pore structure observed in the micro-AC due to the small average pore size of the micro-AC (<2 nm). As detailed below, the meso-AC has pores with diameters in the range of 4-10 nm, with some larger pores visible in the SEM image.

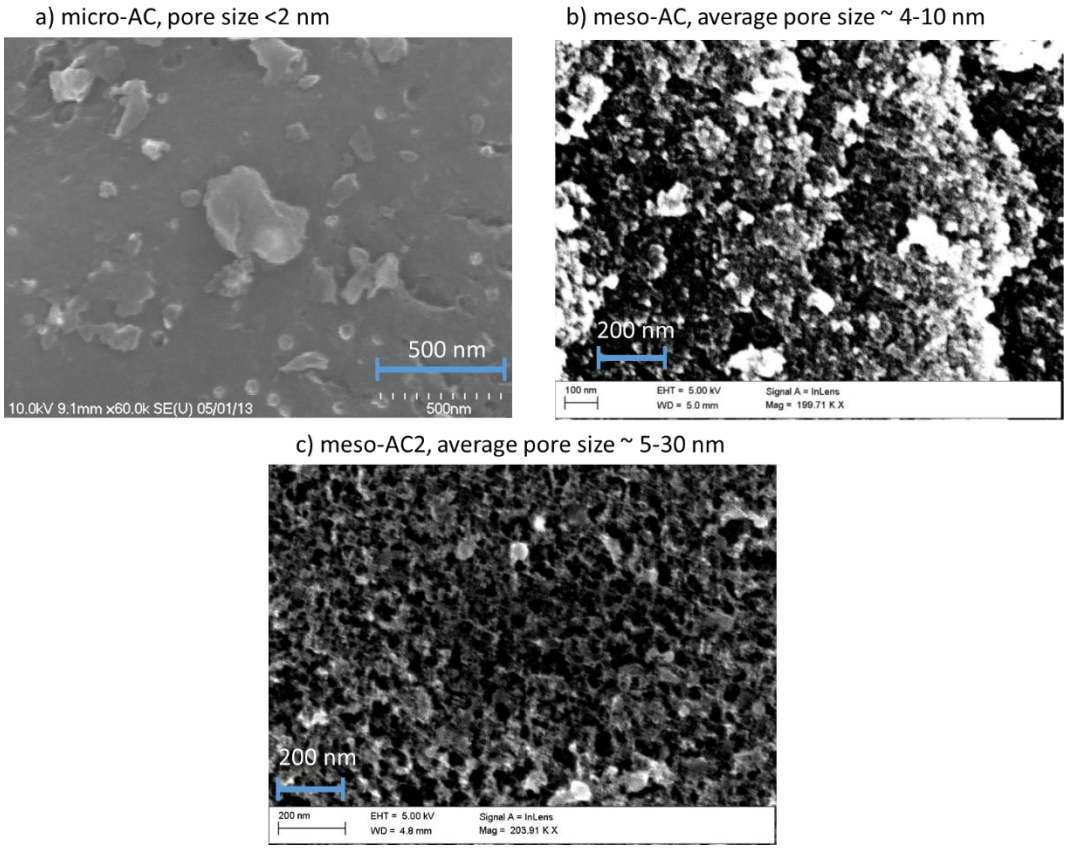

Figure 5.1: SEM images of the surface of activated carbons

Before the impregnation with amine, the carbon materials were heat treated at 100-120 °C under vacuum for 4-5 h. This was to ensure the removal of water from the pores before impregnation. If the heat treatment was not carried out it was observed that the stability of the materials impregnated with lower molecular weight amines was reduced.

5.1.2 Impregnation of carbon materials

Typically, 70-100 mg of carbon material was dispersed in 5 ml of dry dichloromethane and the calculated appropriate amount of amine (10/30/50/70 parts of amine with respect to 100 parts w/w of dried carbon material) was added to this dispersion. The dispersion was sonicated in a bath for 5-10 min and then left for a few hours; after that the dichloromethane was removed using a rotary evaporator, the product being carbon

powder. The resulting weight of the products was in good agreement with the expected yields.

The following species of impregnated carbon materials were prepared and studied by nitrogen adsorption (the number after the sample name corresponds to the weight parts of amine with respect to 100 parts of carbon material): micro-AC, micro-AC-EDA(10), micro-AC-EDA(30), micro-AC-DETA(10), micro-AC-DETA(30), micro-AC-TETA(10), micro-AC-TETA(30), micro-AC-TETA(50), micro-AC-TETA(70), micro-AC-PEI600(10), micro-AC-PEI600(30), meso-AC, meso-AC-EDA(10), meso-AC-DETA(10), meso-AC-TETA(10), meso-AC-TETA(30), meso-AC-TETA(50), meso-AC-TETA(70), meso-AC-PEI600(10). The surface properties of the prepared impregnated carbon materials are summarized in Table 5.1. For CO_2 capture an additional series of various loadings of meso-AC-PEI600 was prepared.

Table 5.1: Overview of surface properties of the studied materials

Sample name	BET surface area (m^2/g)	Pore volume (cc/g) NLDFT (slit/cyl)			V_{carbon}[a] (cc/g)	V_{amine}[b] (cc/g)	$V_{free} = V_{carbon} - V_{amine}$ (cc/g)[c]	blocked volume (%)[d]
		Total (V_{meas})	Micro (<2 nm)	Meso (>2 nm)				
micro-AC	1336	0.68	0.59	0.085	0.68	0	0.68	0
micro-AC-TETA(10)	954	0.50	0.42	0.079	0.61	0.093	0.52	5
micro-AC-TETA(30)	220	0.11	0.093	0.018	0.52	0.24	0.28	61
micro-AC-TETA(50)	24	0.017	0.007	0.010	0.45	0.34	0.11	85
micro-AC-TETA(70)	7	0.014	0	0.014	0.40	0.42	-0.022	-
micro-AC-EDA(10)	1022	0.53	0.43	0.094	0.61	0.10	0.51	-2
micro-AC-DETA(10)	938	0.48	0.38	0.097	0.61	0.095	0.52	7.5
micro-AC-PEI600(10)	1017	0.53	0.45	0.076	0.61	0.087	0.53	0
micro-AC-EDA(30)	265	0.14	0.09	0.043	0.52	0.26	0.26	48
micro-AC-DETA(30)	318	0.17	0.11	0.060	0.52	0.24	0.28	41
micro-AC-PEI600(30)	519	0.27	0.20	0.065	0.52	0.22	0.30	11
meso-AC	817	1.1	0.086	0.98	1.1	0	1.1	0
meso-AC-TETA(10)	510	0.75	0.029	0.72	0.97	0.093	0.87	14
meso-AC-TETA(30)	274	0.46	0	0.46	0.82	0.24	0.58	20
meso-AC-TETA(50)	162	0.30	0	0.30	0.71	0.34	0.37	18
meso-AC-TETA(70)	93	0.19	0	0.19	0.62	0.42	0.21	9
meso-AC-EDA(10)	589	0.84	0.051	0.79	0.97	0.10	0.87	3
meso-AC-DETA(10)	518	0.77	0.028	0.74	0.97	0.095	0.87	12
meso-AC-PEI600(10)	541	0.79	0.024	0.77	0.97	0.087	0.88	10

[a] in impregnated materials the mass fraction of activated carbon was not equal to 100%. Therefore, the pore volume of the carbon per gram of impregnated material (V_{carbon}) is equal to the mass fraction of the carbon support in the composite multiplied by the pore volume per gram of unmodified carbon.

[b] - the volume of added amine in a gram of impregnated material

[c] - see section 3.1 for details

[d] - $[1-V_{meas}/(V_{carbon}-V_{amine})]*100\%$, for detail see section 3.1

5.1.3 Characterisation of adsorbents

As detailed in section 3.5, N_2 adsorption isotherms were measured at 77 K on a Quantachrome NOVA 3000 instrument. All samples were regenerated in a degas station under vacuum (< 1 mbar) at up to 75 °C to remove any adsorbed species prior to analysis. The exceptions were micro-AC-EDA(10) and meso-AC-EDA(10) that were regenerated at 40 °C (<1 mbar) and micro-AC-EDA(30) that was regenerated at 70 °C (250 mbar) in order to avoid the evaporation of the EDA. This could have resulted in incomplete removal of solvent and other species from the adsorbent.

Quantachrome AsiQwin (version 3.01) software was used to calculate micro- and mesopore volume, surface area and pore size distribution (PSD) data on the basis of experimentally obtained adsorption/desorption isotherms. The estimation of micro/mesopore volume for both carbon materials was performed using the non-local density functional theory (NLDFT) for N_2 adsorption at 77 K on carbon with the kernel optimized for a mixed hybrid slit/cylindrical pore geometry. This kernel assumes a slit-pore geometry for the micropores and a cylindrical pore model to describe correctly the adsorption/condensation mechanism in the mesopores (e.g. Refs. [141, 142]). It has been reported that choosing the wrong pore geometry would result in poor DFT fitting results, and thus would lead to incorrect values of the PSD and pore volume being calculated [116]. Therefore, this particular DFT kernel was chosen because it exhibited (i) the smallest fit error of DFT calculated isotherm to the experimental isotherm for pristine and low-loading impregnated carbon materials, and (ii) it provided a good match between DFT calculated total surface area and BET surface area values.

5.2 Results and discussion

5.2.1 Effect of amine loading on the pore structure of carbon materials

Nitrogen adsorption measurements on the starting carbon micro-AC and meso-AC materials produced adsorption isotherms of different type (Figure 5.2a, b). The adsorption isotherm of micro-AC is clearly a Type I isotherm according to IUPAC classification, typical for a microporous material[112]. In contrast, the isotherm for meso-AC is a characteristic Type IV isotherm typical of a mesoporous material. The micro-AC material contained mainly micropores (pore width <2 nm), and *ca* 95% of the total pore volume is provided by pores that are <2.5 nm in diameter (Figure 5.2c). For the meso-AC material, 92% of pore volume falls within the pore size range of 3 -11 nm, with a PSD mean value at 5.6 nm. This corresponds well to the PSD (pore size range 4-11.5 nm) of the template silica gel determined by the NLDFT kernel for cylindrical pores (Figure 5.2d). As a result of the contrasting pore structures, micro-AC and meso-AC allow a systematic comparison of the influence of the pore structure on the effect of impregnation on the adsorption properties.

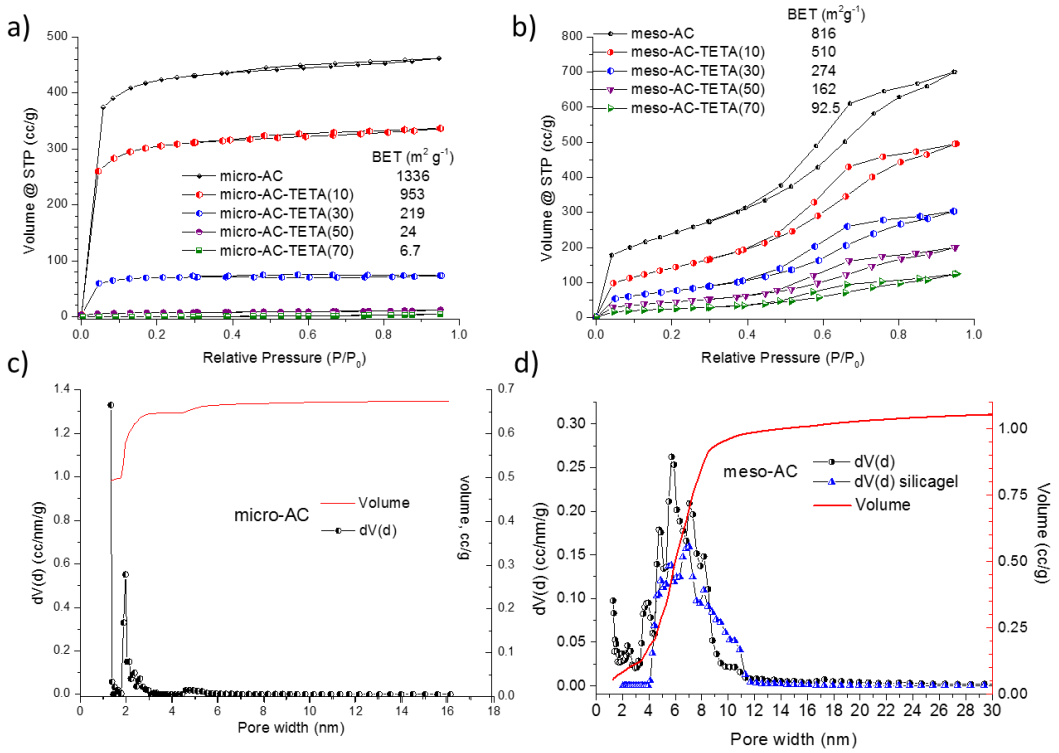

Figure 5.2: N_2 adsorption isotherms and pore size distributions, 77 K. (a) micro-AC impregnated with various weight loadings of TETA. (b) meso-AC impregnated with various weight loadings of TETA (c) Pore size distribution of micro-AC (d) Pore size distribution of meso-AC and silica gel

The aim of the impregnation was to introduce as many basic amino groups to the carbon support as possible. Among polyamines with general formula $H(HNCH_2CH_2)_nNH_2$, EDA has the highest relative content of basic amino groups, which are considered to be responsible for increasing uptake of CO_2. However, EDA is a volatile species with a vapour pressure of 13 mbar at 20 °C which is a value that is 27 and 100 times higher than for DETA and TETA respectively. Therefore for initial studies TETA was chosen as the candidate for impregnation.

The success of the impregnation with TETA was proved by monitoring the weight increase of the material and by infra-red spectroscopy (Figure 5.3). As the amine loading increases the relative intensity of the bands at 1648 cm^{-1}, N-H bending, and 1437 cm^{-1}, CH_2 scissoring, increase. The weak peaks at 1360 cm^{-1}, which appear in

the impregnated samples with high amine loading, may be attributed to carbamate salt formation in air [143].

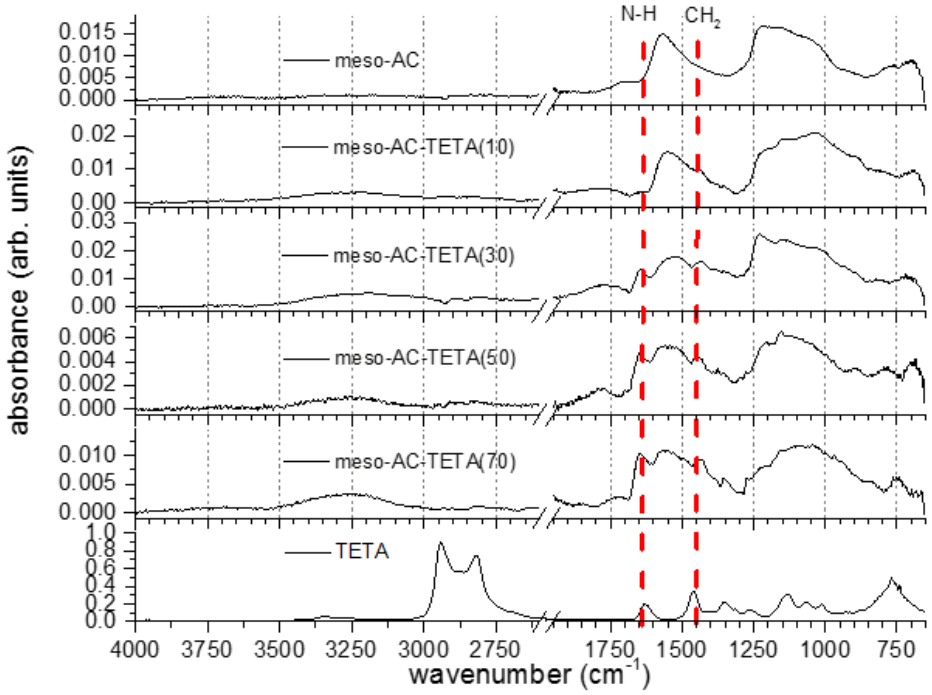

Figure 5.3: ATR FTIR spectra of the synthesized meso-AC material and meso-AC-TETA impregnated species. TETA spectrum is from NIST database[144]

In general the impregnation of both micro-AC and meso-AC materials with different amounts of TETA resulted in a loading dependent decrease of the pore volume and surface area (see Table 5.1). There was no effect on the type of N_2 adsorption isotherms which remained as Type I isotherms for the micro-AC series and Type IV isotherms for the meso-AC series of impregnated materials (Figure 5.2a, b). micro-AC materials that were impregnated with a large loading of amine (micro-AC-TETA(50) and micro-AC-TETA(70)) had very low values of BET surface area and total pore volume.

The volume of added amine in the impregnated samples did not exceed the available pore volume of the carbon content in the impregnated materials, except for the micro-AC-TETA(70) sample, where the volume of added amine was roughly equal to the pore volume of micro-AC (Table 5.1). If the extreme assumption is made that the

impregnation mechanism consists of a complete and uniform pore filling[43] of the carbon material, then the expected volume available for nitrogen adsorption (V_{free}) should be equal to the difference between the total pore volume of the starting (non-impregnated) material (V_{carbon}) and the volume of the added amine (V_{TETA}) as shown in eq. 5.1:

$$V_{free} = V_{carbon} - V_{TETA} \quad (5.1)$$

However, the calculated values of the total volume from the experimental N_2 adsorption isotherms are significantly lower than the value of V_{free}, calculated from eq. 5.1 (Figure 5.5). This observation implies that part of the pore volume is not filled with amine, but is blocked, and this fraction of the pore volume/surface is inaccessible to nitrogen during the adsorption measurement, consistent with the results of Sanz et al.[145] for mesoporous silicas where the impregnation with amines does not necessarily result in a uniform pore filling. Therefore, the blocked volume in the examined impregnated materials can be defined as the difference between V_{free} and the measured total pore volume after impregnation (V_{meas}). Quantification of the extent of pore blocking was performed by normalization of the blocked pore volume to the expected volume V_{free}. So, the value of 'blocking' caused by the impregnation of porous material (or % blocking, equal to 'blocking'*100%) may be expressed as shown in eq. 5.2:

$$'\text{blocking}' = \frac{V_{free} - V_{meas}}{V_{free}} = 1 - \frac{Vmeas}{V_{carbon} - V_{TETA}} \quad (5.2)$$

where the term $V_{meas}/(V_{carbon} - V_{TETA})$ shows the efficiency of nitrogen permeability to the available adsorption sites in the pores. Note that these considerations can only be applied to positive values of V_{free}. They cannot be applied in the case of a very low measured pore volume that could be the result of either complete pore filling with an excessive volume of impregnating species (0 or negative V_{free} values, micro-AC-TETA(70)) or the formation of a shell around the surface of the adsorbent that is non-permeable to the nitrogen at 77 K. In the latter case, the material can be considered to be non-porous and its surface area and volume would derive from the particle size and

interstitial voids (micro-AC-TETA(50)). For such a material an increase of amine loading, in practice, would not change the measured BET surface area and total pore volume, but would change significantly the V_{free} value and would give misleading estimates of 'blocking' values.

In micro-AC materials the initial impregnation resulted only in insignificant pore blocking (5% in micro-AC-TETA(10) sample). An increase in the amine loading led to a dramatic decrease in the pore volume that was accessible to the nitrogen gas in the volumetric experiment and resulted in 61% of blocking for micro-AC-TETA(30). Loading of larger volumes of amine onto micro-AC resulted in practically complete pore blocking. The values of surface area and total pore volume for micro-AC-TETA(50) and micro-AC-TETA(70) samples are remarkably similar, suggesting, as discussed above, that the impregnation of the microporous material resulted in the complete enveloping of the porous particles without penetrating further into the internal pore space.

Thus, the general scenario of impregnation of micro-AC material with TETA suggests that a significant part of the available pore volume is blocked instead of being filled, i.e. the amine first occupies the outer layer of the micropores in the micro-AC particles and does not penetrate into the deeper internal pore space, as shown in Figure 5.4.

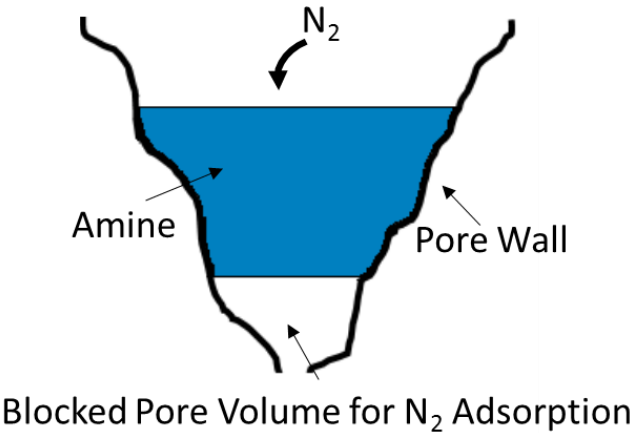

Figure 5.4: Schematic illustrating potential pore blocking mechanism

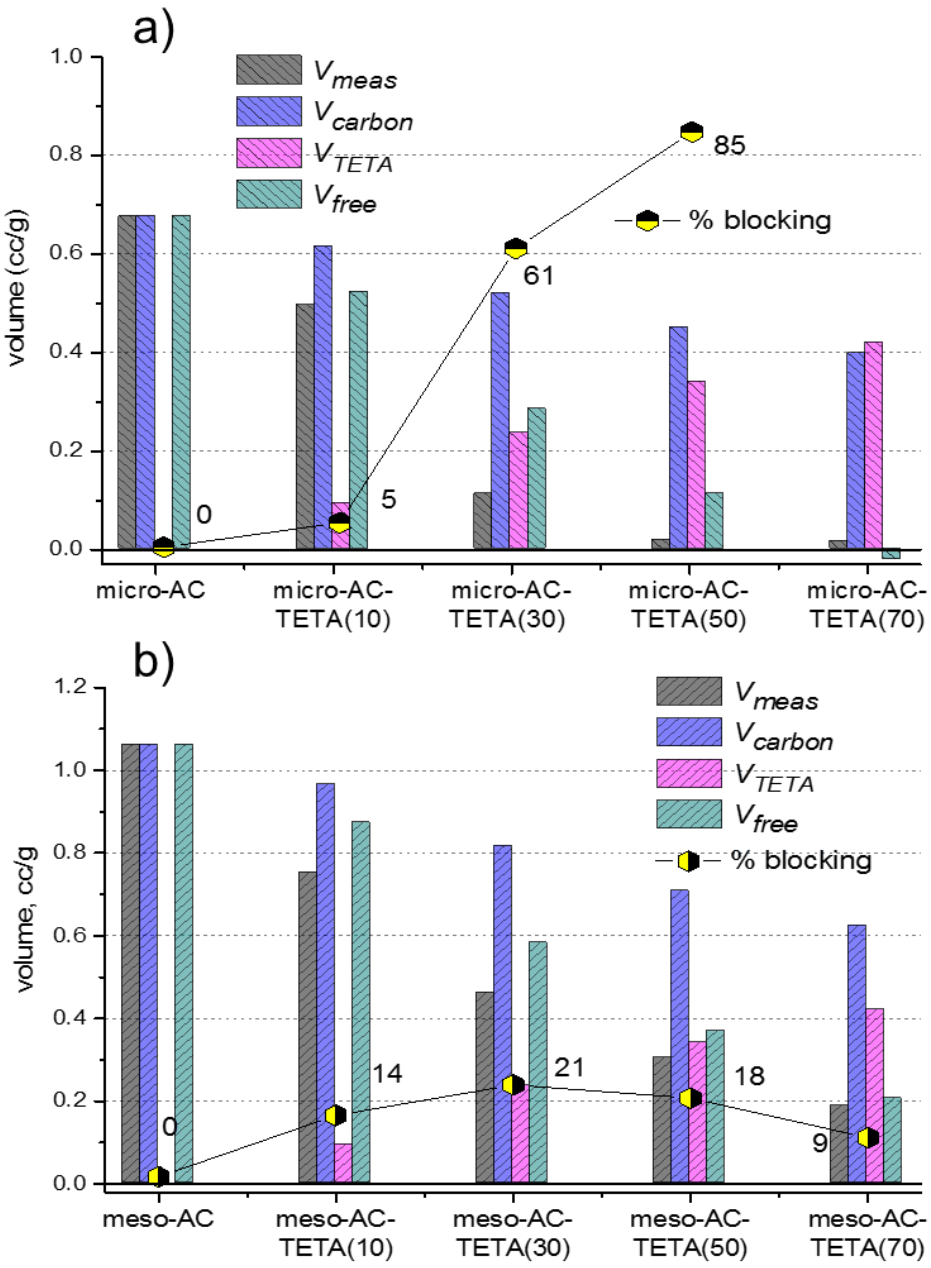

Figure 5.5: Comparison of the total pore volume of carbons loaded with TETA. (a) micro-AC-TETA series, (b) meso-AC-TETA series. Vmeas: total pore volume calculated by DFT; V_{carbon} : volume of carbon support taking into account mass fraction of impregnated amine; VTETA: volume of TETA added; V_{free} : expected volume available after impregnation; % blocking: ratio $(V_{free}-V_{meas})/V_{free}$ *100

Table 5.2: Relative pore volume in the investigated samples (normalized to the volume of micro- and mesopores in original micro-AC/meso-AC materials)

Sample name	V_{micro}/V_{meso} (cc/g)	norm V_{micro}	norm V_{meso}
micro-AC	0.59/0.085	1	1
micro-AC-TETA(10)	0.42/0.079	0.71	0.93
micro-AC-TETA(30)	0.093/0.018	0.16	0.22
micro-AC-TETA(50)	0.007/0.010	0.01	0.12
micro-AC-TETA(70)	0/0.014	0.00	0.17
meso-AC	0.086/0.98	1	1
meso-AC-TETA(10)	0.029/0.72	0.34	0.74
meso-AC-TETA(30)	0/0.46	0.00	0.47
meso-AC-TETA(50)	0/0.30	0.00	0.31
meso-AC-TETA(70)	0/0.19	0.00	0.19

With meso-AC material there was a gradual decrease in the surface area and pore volume as more amine was loaded onto the material (Table 5.1). In contrast to the micro-AC case only a small level of pore blocking was observed through the whole range of amine loading, with a maximum pore blocking value of 21% for meso-AC-TETA(30) (Figure 5.5b).

DFT analysis of adsorption isotherms for both kinds of studied materials indicates that the normalized micropore volume available for nitrogen adsorption drops faster than the mesopore volume with an increase of the amine loading (Table 5.2). It can be seen that $V_{micro}>V_{meso}$ for the micro-AC series (except micro-AC-TETA(50) and micro-AC-TETA(70) where the pore volume is negligible) and $V_{micro}<V_{meso}$ for all loadings of the meso-AC series.

For mostly micro-AC, in agreement with the pore blocking model, there is a sharp initial drop in the accessible micropores with increasing TETA loading from 0 to 30%, where the difference between V_{free} and V_{meas} was largest. With an increase of amine loading from 50% to 70% the relative volume of available micropores tends to zero, and the difference between V_{meas} and V_{free} decreases, indicating that an excess of amine

is located on the outer surface of the micro-AC particles. With meso-AC, DFT pore volume analysis calculates a three times reduction in the available micropore volume for 10% of amine loading, and there is no measured micropore volume at higher amine loadings. This may suggest that the initial adsorption of amine results in some of the micropore content being blocked. In the case of meso-AC there is less of a contribution from pore blockage and the amine distributes more evenly throughout the material, filling the small mesopores first. The latter assumption concerning the predominant filling/blocking of small pores is supported by PSD analysis of the TETA impregnated meso-AC series, where the minimal mesopore size is shifted from <2.5 nm for the original meso-AC material to 4.5 nm for the meso-AC TETA(50) and meso-AC TETA(70) species (Figure 5.6).

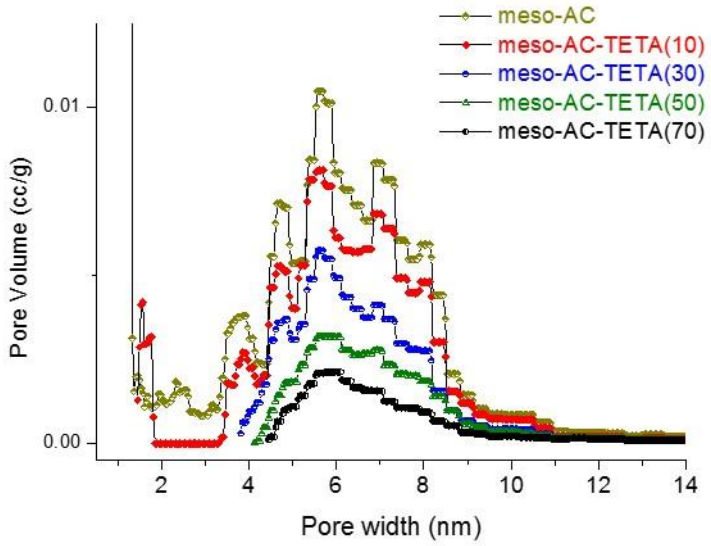

Figure 5.6: Pore size distribution of meso-AC impregnated with TETA. Calculated using NLDFT pore size distribution analysis.

All these findings imply that in the case of the wet impregnation procedure when small polyamine species are used, the amine molecules form droplet-like aggregates which do not penetrate deep inside the micropores. With an increase of amine loading the impregnating amine forms a continuous layer on the carbon surface and fills the mesopores. Thus, to ensure a more homogeneous distribution of amine across the surface of the material, supports with mesoporous structure are preferential.

5.2.2 Comparison of different amines at low loadings. EDA, DETA, TETA, PEI600

In order to check the proposed impregnation scenario we have studied the surface properties of micro-AC and meso-AC materials impregnated with a few polyamines of different size but with the same general formula H-(NH-CH_2CH_2)$_n$-NH_2: ethylenediamine (EDA, n=1), diethylenetriamine (DETA, n=2), triethylenetetramine (TETA, n=3) and branched polyethyleneimine with average molecular weight of 600 Da (PEI600, n=13-14). The molecular volumes of amines obtained from liquid densities, along with the calculated volumes and the adsorption cross sectional areas of the amines are shown in Table 5.3.

Table 5.3: Sizes of amine molecules

amine	Molecular volume, (Å^3)*		Calculated cross-sectional surface area, (Å^2)
	from molar volume of liquid	calculated for the given shape using bond lengths/angles & vdW constants	
EDA	111	106, (cylinder *l*=5.4 Å, *d*=5 Å)	27
DETA	180	178.5 (cylinder *l*=9.1 Å, *d*=5 Å)	45.5
TETA linear (60%)	247.5	250 (cylinder *l*=12.75 Å, *d*=5 Å)	64
TETA branched (40%)	248.5	245 (disc *d*=7.9 Å, *h*=5 Å)	49
PEI600 branched	950	950 (sphere, *d*=12.2 Å)	116.5

*Molecular volumes for the molecules were estimated on the basis of their liquid densities. For estimation of areas occupied by polyamines the molecular volumes were calculated for cylindrical (linear species), disc and sphere (for branched species) geometries using the values of bond lengths of 1.53 Å for C-C bond, 1.47 Å for C-N bond, 1.09 Å for C-H bond, 1.01 Å for N-H bond, tetrahedral bond angle of 109^o for all bonds and 1.2 Å for van der Waals' radius of hydrogen atom; *d* stands for diameter, *l*- length and *h* - height.

Impregnation of micro-AC material with 10% loading of different polyamines (EDA, DETA and PEI-600) showed results that were similar to those observed for micro-AC-TETA(10) (Figure 5.7), i.e. all the materials exhibited Type I nitrogen adsorption isotherms, and pore blocking values varied in the range 0-7.5%. The pore blocking

values for micro-AC-DETA(10) and micro-AC-TETA(10) samples were calculated to be 7.5 and 5% respectively. The low value of pore blocking for micro-AC-EDA(10) sample is due to the difficulty encountered in controlling the amount of EDA in the sample. EDA has a relatively high vapour pressure and was evaporated during the regeneration step prior to the N_2 adsorption measurement. The low value of pore blocking for the micro-AC-PEI600(10) sample cannot be explained by amine leaching as in the case of lower molecular weight amines, and thus required further elucidation. Therefore a series of the micro-AC samples impregnated with an amine weight loading of 30% were prepared and studied.

An increase of amine loading leads to a significant difference in N_2 adsorption behaviour between the micro-AC species impregnated with lower molecular weight amines (EDA, DETA and TETA) and the micro-AC impregnated with PEI-600. For lower amines the blocking values were in the range 40-60% (Table 5.1). The trend in the change of the pore blocking values shows that the impregnation with EDA and DETA provides slightly less pore blocking than TETA. The higher value of pore blocking for micro-AC-EDA(30) in comparison to micro-AC-DETA(30) is likely to be the result of the different regeneration conditions used (see section 5.1.3).

In contrast to the case of micro-AC impregnation with smaller amines, micro-AC-PEI600(30) showed a pore blocking value of only 11%. This agrees with the results of low pore blocking observed for micro-AC-PEI600(10).

The calculated cross-sectional surface areas of the amines used are 27 $Å^2$ for EDA, 45.5 $Å^2$ for DETA, 70 $Å^2$ for TETA and 116.5 $Å^2$ for PEI600 (which is equivalent to a diameter of ~1.2 nm for the spherical conformation of the PEI600 molecule). According to PSD in the original micro-AC material, 75% of the available volume is due to pores with diameters <1.25 nm. Thus, as discussed for impregnation of micro-AC with TETA, the lower amines (EDA, DETA and TETA) can fill the pores on the outer surface of the micro-AC particles and do not penetrate deeper inside the micropores. In contrast, PEI molecules are larger and do not fit into the majority of the

pores on the outer micro-AC particle surface, thus leaving micropores still available for nitrogen adsorption.

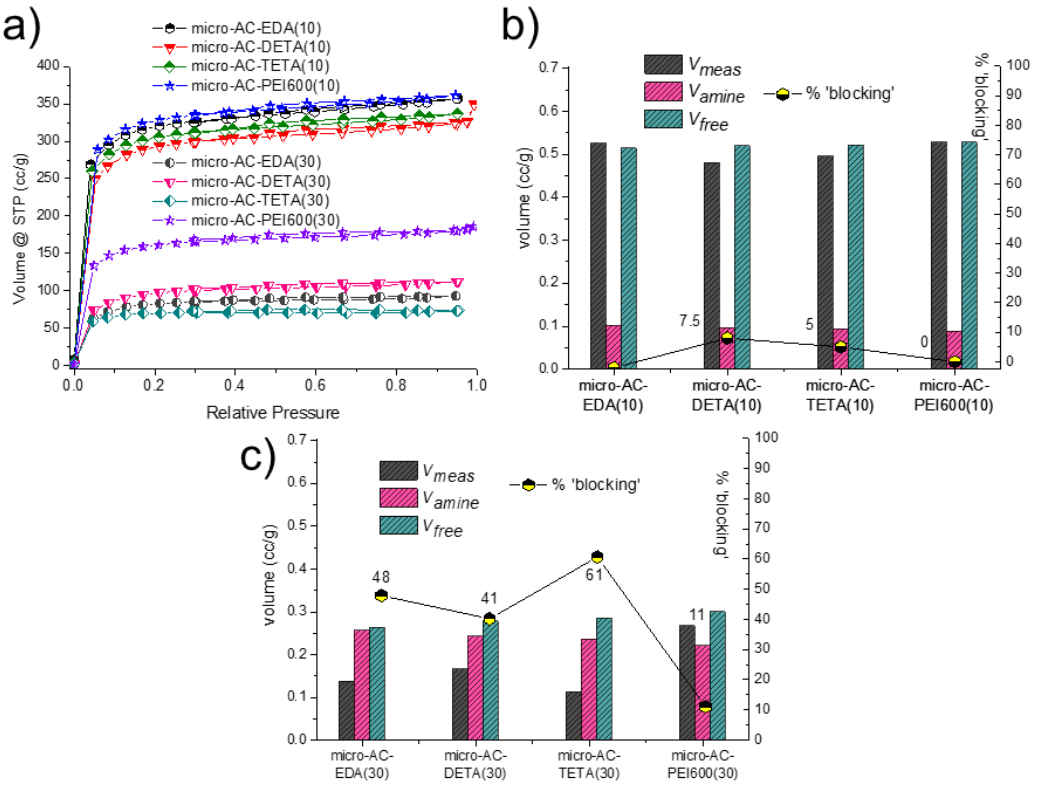

Figure 5.7: Impregnation of micro-AC with polyamines of different molecular weights. (a) N_2 adsorption isotherms of micro-AC weight loaded with 10 and 30% polyamine. NLDFT determined pore volume (V_{meas}), expected available volume (V_{free}) and % pore blocking for (b) micro-AC-amine(10) and (c) micro-AC-amine(30)

Impregnation of the meso-AC material with 10% of amine resulted in materials with very similar adsorption properties (Figure 5.8), with similar pore blocking values of 10 -13.5 % except for the EDA case. Similar to the case of micro-AC-EDA(10), the pore blocking value of 3% for meso-AC-EDA(10) could be a consequence of the regeneration regime used (40 °C/<1 mbar), which may have led to a partial evaporation of amine.

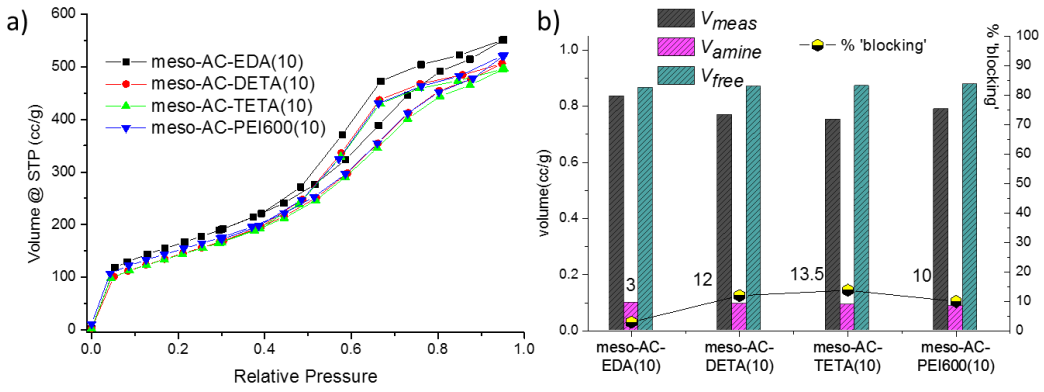

Figure 5.8: Impregnation of meso-AC with polyamines of different molecular weights. (a) N2 adsorption isotherms of micro-AC weight loaded with 10%. (b) NLDFT determined pore volume (Vmeas), expected available volume (V_{free}) and % pore blocking for meso-AC-amine(10)

Therefore, for microporous species the size of the amine is critical for successfully loading the support. In the case of meso-AC very little difference was observed on loading the different polyamines onto the carbon support as all molecules can fit into the mesoporous pores.

5.2.3 Ranking of impregnated materials as candidates for CO_2 adsorbents

The CO_2 capture was studied first on both microporous and mesoporous carbon materials with various TETA loadings. Due to leaching of TETA from the support during cyclic experiments at 75 °C (not observed during vacuum regeneration for N_2 adsorption measurements) the investigations were then extended to carbons loaded with PEI600.

The temperature dependence of the adsorption process was investigated by performing an adsorption/desorption cycle on two different materials at three different temperatures. The CO_2 adsorption curves for the unmodified micro-AC support are shown in Figure 5.9a. The trend in the capacity (q) with temperature follows the trend of a physisorption process with a decrease in q for an increase in temperature. In

contrast, from Figure 5.9c it can be seen that there was a minimum energy required for the chemical reaction between the amine and CO_2 to occur. At all temperatures, there was a fast initial uptake of CO_2 followed by a second slower process. At the lower temperatures of 35 °C and 50 °C the kinetics of the reaction/transport to the active sites was slow (Figure 5.9c). This resulted in the equilibrium capacity not being reached over the 5 hour timescale of the experiment. The optimum (highest) CO_2 capacity within the timescale of the experiment was observed at 75 °C. However, at this temperature, significant leaching of amine from the carbon support was observed over the course of the experiment.

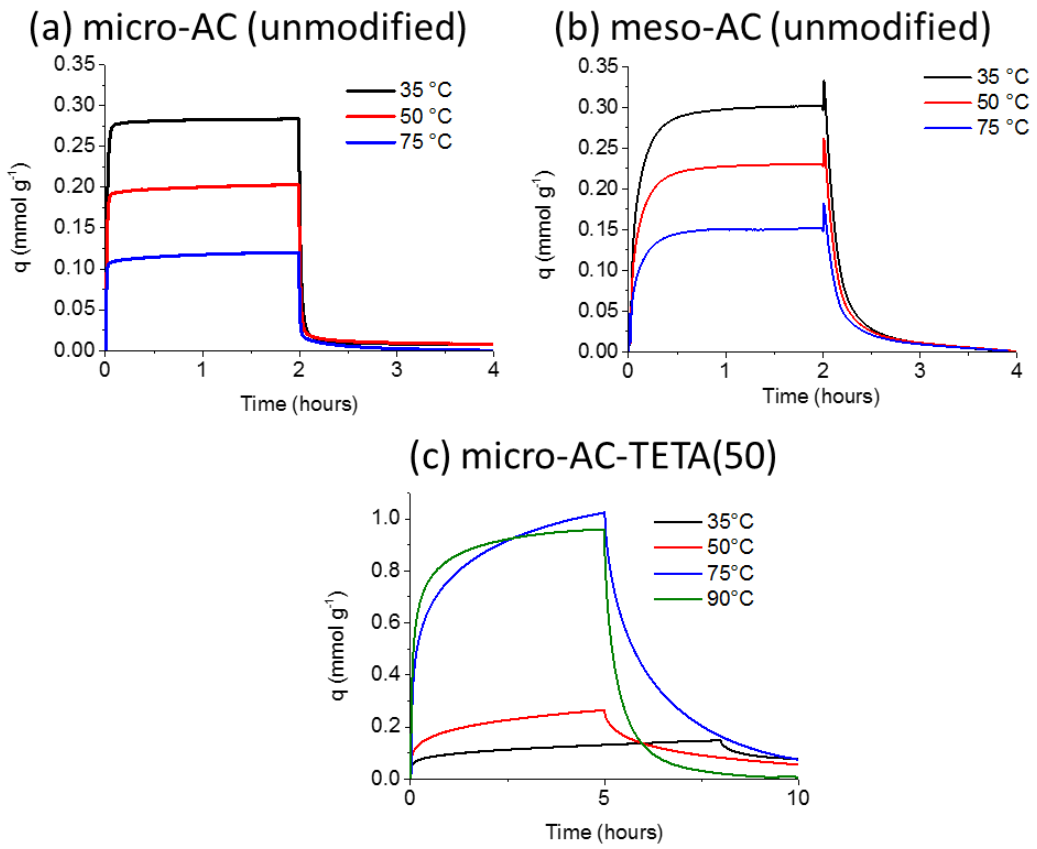

Figure 5.9: CO_2 uptake curves at various temperatures measured by thermal gravimetric analysis

From the TGA-DSC experiment the heat of adsorption (ΔH_{ADS}) and the heat of desorption (ΔH_{DES}) of the process could also be calculated from the heat flow, measured by the DSC using equation 5.3. Here q is the amount of adsorbed CO_2 in moles and t is time in seconds.

$$\Delta H = \frac{\int_{t0}^{t} Heat\ flow\ \mathrm{d}t}{q_t - q_{t_0}} \qquad (5.3)$$

Processes with values of ΔH that are less than 50 kJ mol^{-1} are considered to be physisorption and values that are greater than 50 kJ mol^{-1} are considered to be chemisorption [20].The values of ΔH_{ADS} and ΔH_{DES}, for the unmodified carbon support were approximately ±28 kJ mol^{-1}, at all the temperatures measured. This clearly indicated that the uptake mechanism was a physisorption process. All the impregnated materials measured had a calculated heat of adsorption of around 90 ± 10 kJ mol^{-1} (Table 5.4). The calculated values of ΔH_{ADS} and ΔH_{DES} were in agreement to within ±2 kJ mol^{-1}. Examples of experimental heat flow curves can be seen in section 5.2.4. It was concluded that a chemisorption process was the dominating mechanism of adsorption for the impregnated materials.

Table 5.4: Heat of CO_2 adsorption ΔH_{ADS} and ΔH_{DES} of several materials at different temperatures

	Temperature/ °C	$-\Delta H_{ADS}$ kJ mol^{-1}	ΔH_{DES} kJ mol^{-1}
micro-AC	35	28.0	26.2
	50	27.8	26.3
	75	28.5	28.6
micro-AC-TETA(50)	35	97.4	98.0
	50	88.9	88.7
	75	90.9	90.7
	90	90.5	91.1
meso-AC-TETA(30)	75	87.8	85.7
meso-AC-TETA(50)	75	91.2	91.3
meso-AC-PEI600(100)	75	92.5	92.4

To investigate the relationship between the amine loading and the CO_2 capacity of the materials, a range of samples were tested at 75 °C. It can be seen in Table 5.5 that there was a significant improvement in the CO_2 capacity for all materials loaded with amine compared to the unmodified carbon support. For the micro-AC material there appears to be an optimum loading of amine that achieves the maximum CO_2 capacity per unit mass of adsorbent. As discussed earlier this is likely to be a consequence of pore blockage and transport limitations of the CO_2 in accessing the active sites for higher loadings.

Table 5.5: CO_2 capacities of the materials with various loadings of amine at 75 °C after 5 hours of adsorption. The efficiency of the amine utilization is calculated as the ratio of the moles of CO_2 up taken by the adsorbent to the number of moles of amino groups available for adsorption, $q(CO_2)$: [0.5*mol(*N*)].

	$q(CO_2)$ (mmol g^{-1})	mol(*N*) (mmol g^{-1})	$q(CO_2)$: [0.5*mol(*N*)]
meso-AC-TETA(10)	0.24	2.49	0.19
meso-AC-TETA(30)	1.15	6.32	0.36
meso-AC-TETA(50)	1.67	9.11	0.37
meso-AC-TETA(50), run 2	1.33	9.11	0.29
meso-AC-TETA(75)	1.85	11.7	0.32
meso-AC-PEI600(20)	0.28	4.05	0.14
meso-AC-PEI600(40)	0.68	6.94	0.20
meso-AC-PEI600(60)	0.98	9.10	0.22
meso-AC-PEI600(75)	1.30	10.4	0.25
meso-AC-PEI600(100)	1.40	12.1	0.23
micro-AC-TETA(10)	0.20	2.49	0.16
micro-AC-TETA(30)	0.57	6.32	0.18
micro-AC-TETA(50)	1.05	9.11	0.23
micro-AC-TETA(65)	0.43	10.8	0.08

Figure 5.10 shows a comparison between the CO_2 uptake at 75 °C for various amine-loaded carbons. It can be seen for both the micro-AC and meso-AC supports that as a larger amount of amine is loaded onto the support there is an increase in the uptake of CO_2. For micro-AC this is true up to an optimal loading point beyond which there is a drop in the CO_2 uptake. In this material the pores are partly filled with amine and it would appear that transport of the CO_2 to all the active sites was limited. With the higher loaded micro-ACs (micro-AC-TETA(50), micro-AC-TETA(75)) it was clear that over the course of the 5 hour experiment an equilibrium state had not been reached between the gas phase and the adsorbed phase. The materials were still

adsorbing CO_2. The fast initial uptake was attributed to the fast interaction between the CO_2 and the readily accessible active sites of the amine on the surface. As micro-AC-TETA(50) and micro-AC-TETA(75) have very low BET surface area it is reasonable to assume that the number of active sites exposed directly to the CO_2 in the gas phase is low. We can hypothesize that the second, slower stage of the adsorption process, is a result of the reduction in concentration of available amino groups in the outer layer of amine and there is slow transport of the CO_2 through this layer to the available active sites provided by the amine in the internal pores. Alternatively this could be a secondary reaction between the basic groups and the CO_2, e.g. urea formation[60, 146, 147]. The results of further studies into the kinetics of the reaction are carried out in section 6.2.

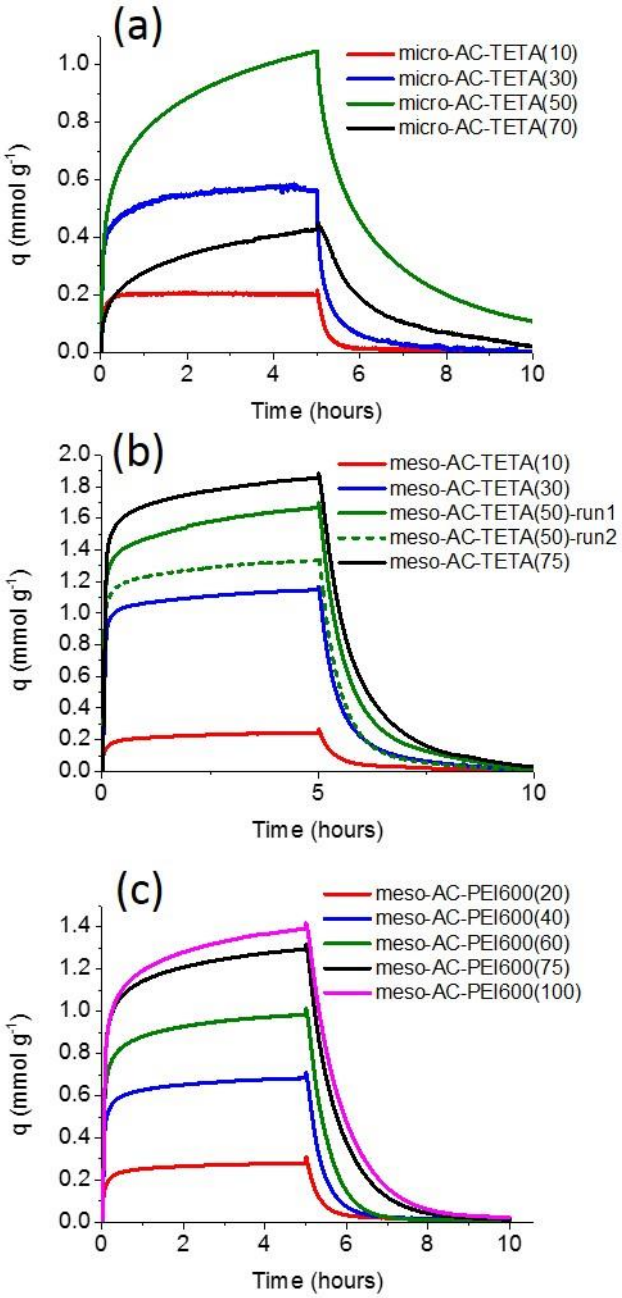

Figure 5.10: (a) Experimental uptake curves of micro-AC with various loadings of TETA. (b) Experimental uptake curves of meso-AC with various loadings of TETA. (c) TGA uptake curves of meso-AC with various weight loadings of PEI600 Measured at 75 °C, 0.1 bar CO_2, 0.9 bar He.

To estimate how efficiently the amine loaded onto the carbon support was being utilized, the ratio between the moles of CO_2 molecules adsorbed per gram, $q(CO_2)$, and

the number of moles of amino groups present in the support per gram, mol(*N*), was calculated. Primary, secondary and tertiary amine groups are all present in the TETA and PEI600 that were used. The generally accepted interactions between CO_2 and amino groups with and without water present are shown in Figure 2.3.

In a dry process two amino groups are required to interact with one CO_2 molecule. As a dry gas stream was used in these experiments then in order for the number of amino groups to correspond to the number of active sites available for reaction with CO_2, the value of mol(*N*) should be halved. Therefore, a value of one for [$q(CO_2)$: (0.5* mol(*N*)] would correspond to the maximum loading of the CO_2 on the adsorbent by the proposed mechanism. It can be seen in Table 5.5 that for the micro-AC material the ratio [$q(CO_2)$: 0.5* mo*l(N)*] is low. This implies that the active sites were not being used efficiently for carbon capture. It should be noted that if further time was given for the equilibrium point to be reached then the efficiency of site utilization would increase. However, the time for the experiment is already relatively long and this further capacity could not be practically utilized in an industrial carbon capture process.

In the case of the meso-AC loaded with TETA, there was an observed increase in CO_2 uptake as the loading increased. Compared to the micro-AC material the overall uptake of CO_2 for comparative loading of TETA was higher in all cases. As discussed earlier the average pore size in meso-AC is larger than in micro-AC and hence a larger number of amine active sites were accessible on the surface for CO_2 adsorption. This resulted in a more significant CO_2 uptake and a more efficient utilization of the available CO_2 active sites as shown in Table 5.5. The active sites become less accessible to the CO_2 as the amine loads onto the surface of the carbon in multiple layers. However, the amine is more efficiently utilized in all the meso-AC material than in the micro-AC materials.

As can be seen in Table 5.5, the primary factor in the CO_2 capacity is the amount of loaded amine on the substrate despite a significant decrease in available surface area

and pore volume. However, the structure of the support is also important in providing a favourable distribution of the amine across the support surface.

Throughout regeneration and the CO_2 measurement it was apparent that TETA was leaching from the support. This effect was highlighted further by meso-AC-TETA(50) where a second run of the experiment was performed, shown in Figure 5.10b, a significant drop in the uptake capacity of 20% was observed in the second cycle. Alongside amine leaching it is possible that the active sites are deactivating through the formation of carboxylate/carbamate/urea species. This effect was investigated by Tanthana et al.[45] through an infra-red spectroscopy study. The rate of amine leaching was lower at lower loadings. This was likely to be a result of more favourable surface interactions between the TETA and the carbon support, than between TETA molecules. As follows from Figure 5.6, smaller pores are filled first, the smaller pores will adsorb the amine more strongly than larger ones. This is discussed in more detail in section 5.2.4, concerning the cyclic experiments.

During cycling, leaching of TETA from the carbon substrate was observed, this was similar to published results for silicas impregnated with tetraethylenepentamine (TEPA).[59, 148] For this reason higher molecular weight PEI600 was tested on the carbon support at various loadings. As can be seen in Figure 5.10c and Table 5.5 the trend in the CO_2 adsorption uptake is similar to that of the TETA loaded substrates. However, the ratio $q(CO_2)$: [0.5*mol(N)] is lower than in the case of TETA. This was to be expected as PEI600 is a larger molecule, with more sterically hindered amino groups, and is hence less reactive with CO_2. There is therefore a trade-off between the stability of the amine on the carbon support and the reactivity towards the CO_2 gas.

5.2.4 CO_2 cyclic adsorption experiments

In order to assess the potential of the impregnated materials over several adsorption desorption steps, cyclic experiments were carried out on two materials. meso-AC-TETA(30) was selected, as during the earlier single cycle measurements the leaching of TETA from the carbon support was lower than for TETA-50 and 75 and it had a higher capacity than meso-AC-TETA(10). meso-AC-PEI600(100) was subjected to a cyclic test as it had the highest capacity of the materials impregnated with polyethyleneimine. The experiments were conducted at 75 °C over 16 hours with 4 adsorption and 4 desorption cycles. As shown in Figure 5.11a, meso-AC-PEI600(100) was stable over the 4 ADS/DES cycles. There was a CO_2 uptake of 1.22 mmol $g^{-1}$and a reproducible heat flow for each ADS/DES cycle. In the case of meso-AC-TETA(30) (Figure 5.11b) there was a slow leaching of TETA from the support. This resulted in a reduced uptake of 9 % between the 1^{st} and 4^{th} adsorption cycle. This degradation in the material means that it would have to be regularly replaced if it was used in a carbon capture process. As a result the support impregnated with the heavier PEI600 is more suitable despite the less efficient utilization of the NH sites.

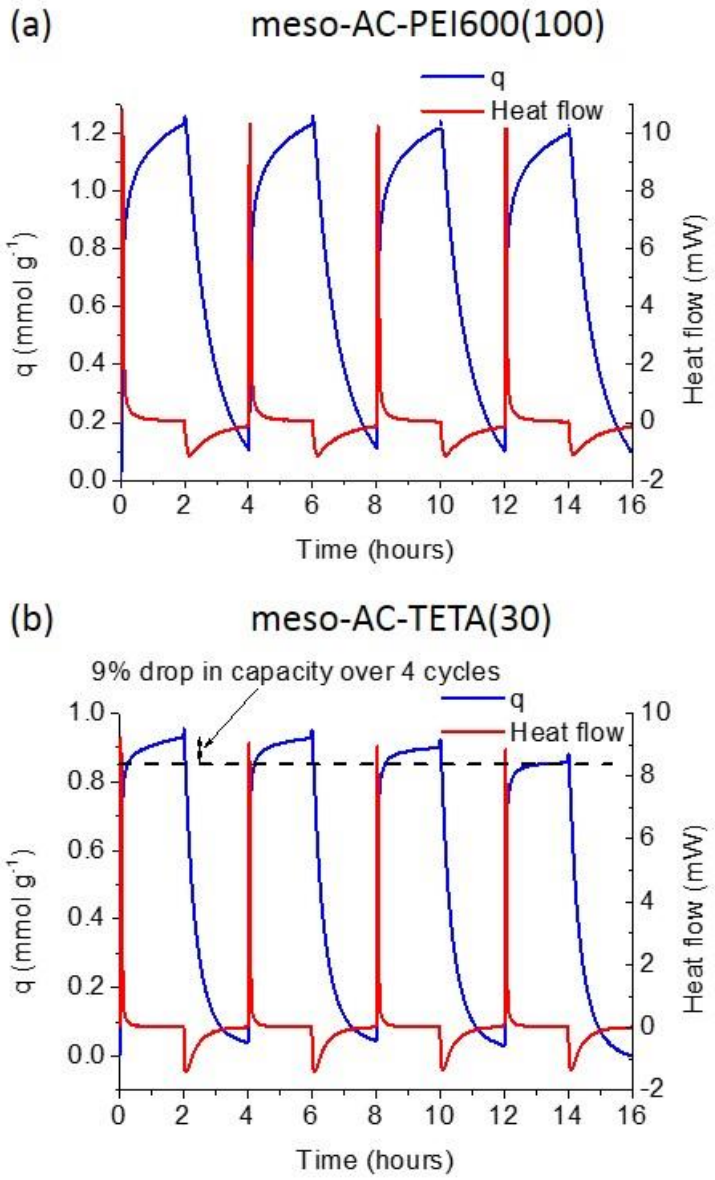

Figure 5.11: Cyclic experiments- 2 hours adsorption of CO_2 at 0.1 bar, 0.9 bar He, followed by desorption under pure helium flow. Four cycles, flow rate remains constant throughout the experiment. Temperature: 75 °C. (a) meso-AC-PEI600(100), (b) meso-AC-TETA(30)

5.2.5 Larger pore volume carbon

In the previous sections, it was seen that mesoporous carbon materials provide a more suitable support for amine impregnation with a more efficient CO_2:amine interaction and the ability to load larger polyamines that exhibit higher stability. In an attempt to increase the CO_2 capacity of the materials further, a mesoporous activated carbon with a larger total pore volume was synthesised (meso-AC2). The synthesis method was the same as reported in section 4.1.1 however a silica with a larger average pore size of 150 Å was used as a template in order to produce materials with a larger total pore volume to incorporate a greater weight percentage of PEI. The resulting carbon (meso-AC2) had a larger total pore volume of 3.1 $cm^3\ g^{-1}$ and a BET surface area of 1254 $m^2\ g^{-1}$ compared to a pore volume of 1.1 $cm^3\ g^{-1}$ and a BET surface area of 817 $m^2\ g^{-1}$ for the previously reported material. This allowed a PEI weight percentage of 73% (meso-AC2-PEI600(270)) compared to a previously reported maximum of 54% (meso-AC-PEI600(100)) to be impregnated into the activated carbon. The nitrogen isotherms at 77 K along with the pore size distributions of the silica template meso-AC2 with and without PEI impregnation are shown in Figure - A.1. Initial adsorption measurements were carried out on the material (meso-AC2-PEI600(270)) at 35 °C, however as can be seen in the zero-length column experiments in Figure 5.12a, the uptake of CO_2 after an adsorption time of three hour was low at only 0.17 mmol g^{-1}. The capacity increased significantly to 2.07 mmol g^{-1} at 75 °C after three hours of adsorption. The higher temperature increases the kinetics of the chemisorption enabling more CO_2 to adsorb and desorb within the time frame of the experiment. The higher required operating temperature for the amine impregnated carbons will influence the design of the separation process. For example, the flue gas will not need to be cooled prior to the separation process.

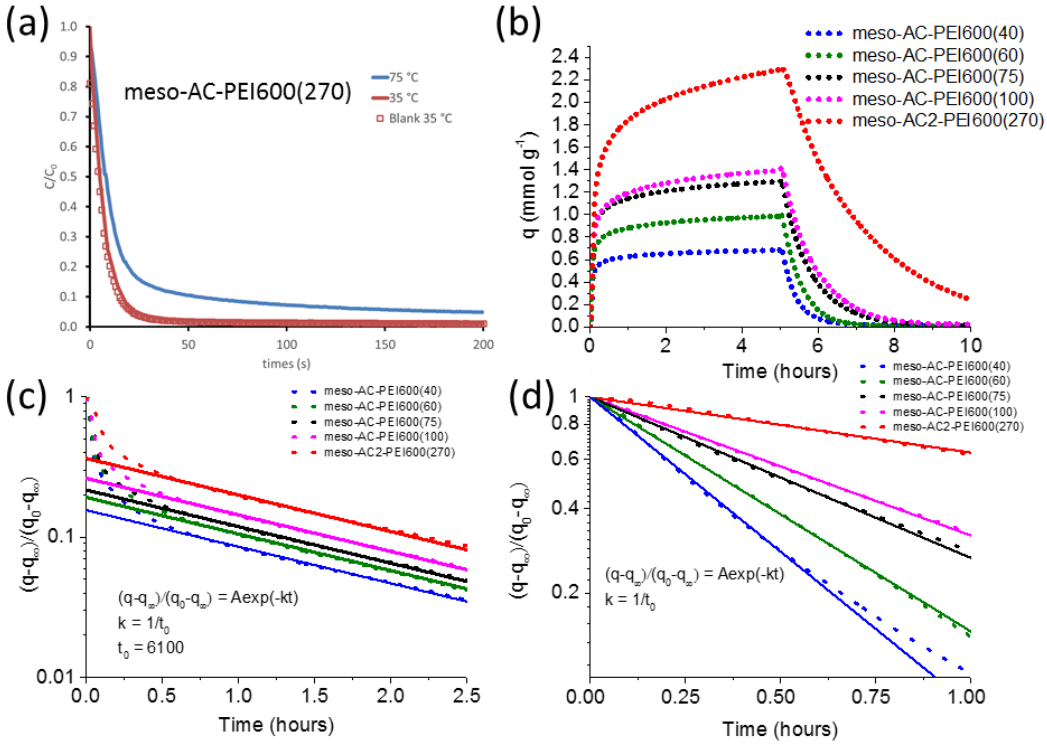

Figure 5.12: (a) ZLC response of amine modified activated carbon at 35 °C and 75°C, 5.4 mg of sample, blank system response shown as unfilled squares. Thermal gravimetric analysis of impregnated activated carbons. (b) CO_2 adsorption and desorption on activated carbons with various loadings of PEI600. 5 hour adsorption step at 75 °C, 5 cm^3 min^{-1} CO_2, 45 cm^3 min^{-1}; desorption 50 cm^3 min^{-1} (c) Normalised adsorption step, $\frac{q-q_\infty}{q_0-q_\infty}$ where q_0 and q_∞ are the initial value and final value of the adsorbed amount respectively, plotted on a semi-log plot. Solid line shows long-time asymptote. (d) Normalised desorption step, on a semi-log plot. Solid line is the exponential fit.

Due to the slow kinetics, further measurements were carried out by thermal gravimetric analysis at 75 °C on a larger sample mass (~50 mg). Over a five hour adsorption step, meso-AC2-PEI600(270) had a CO_2 uptake of 2.3 mmol g^{-1} (Figure 5.12b), this was higher than the previously reported impregnated carbons, included in Figure 5.12b for comparison.[139] Further optimization of the pore structure including an increase in the total pore volume, to enable a higher amount of amine to be impregnated along with an ordered pore structure, to increase the efficiency of the interaction between CO_2 and the amine should allow even higher capacities to be

reached. In addition, the thermal gravimetric system allows the heat of adsorption to be measured via differential scanning calorimetry. The heat of adsorption for the chemisorption process between the CO_2 and the amine was found to be ~90 kJ mol^{-1}.[139]

The time constant of the adsorption step was investigated by thermal gravimetric analysis for different loadings of PEI600 in an attempt to understand the reaction kinetics at 75 °C. The experimental data for the adsorption step was normalised using $\frac{q-q_\infty}{q_0-q_\infty}$, i.e. the initial ($q_0$) and final ($q_\infty$) value of the adsorbed amounts. The plots of $\frac{q-q_\infty}{q_0-q_\infty}$ vs time on a semi-log plot are shown for various loadings of PEI in Figure 5.12c. It can be seen that in the long-time region the response of each sample approaches an exponential decay. The time constant (t_0) is approximately 6080 seconds for all the different loadings of PEI. As the slope was independent of the amount of amine loaded on the sample this gradual uptake of CO_2 can be attributed to the amine. It was likely that this kinetically limited uptake was a result of the dissolution of the CO_2 into the liquid amine, in a similar manner to the mechanism proposed by Zhao et al for impregnated mesoporous silicas.[149] The transport to the remaining active sites through the liquid amine would appear to be rate limiting at higher loadings. During desorption, the lower the amine loading the faster the desorption process occurs (Figure 5.12d). When there is less amine in the pores a larger percentage of the amine is exposed to the gas environment. This results in a faster release of the adsorbed CO_2 with the time constants shown in Table 5.6.

Table 5.6: Time constants from TGA experiments for meso-AC impregnated with PEI600

	Adsorption Step		Desorption Step	
	t_0 (s)	Error* (s)	t_0 (s)	Error* (s)
meso-AC-PEI600(40)			1400	∓70
meso-AC-PEI600(60)			1860	∓40
meso-AC-PEI600(75)	6100	∓400	2700	∓70
meso-AC-PEI600(100)			3130	∓70
meso-AC2-PEI600(270)			7900	∓500

*Error bounds calculated from range of t_0 values that resulted in a reasonable fit of the experimental data

The cyclic uptake at 75 °C, 0.1 bar CO_2 of meso-AC2-PEI600(270) was measured by thermal gravimetric analysis. The result in Figure 5.13 clearly shows a significant uptake of CO_2 within the 2 hour adsorption step. It was also clear that the material requires a significant time to fully desorb under helium flow. A temperature swing desorption step would significantly reduce the regeneration time, making the material a viable candidate for carbon capture due to the potentially high working capacity.

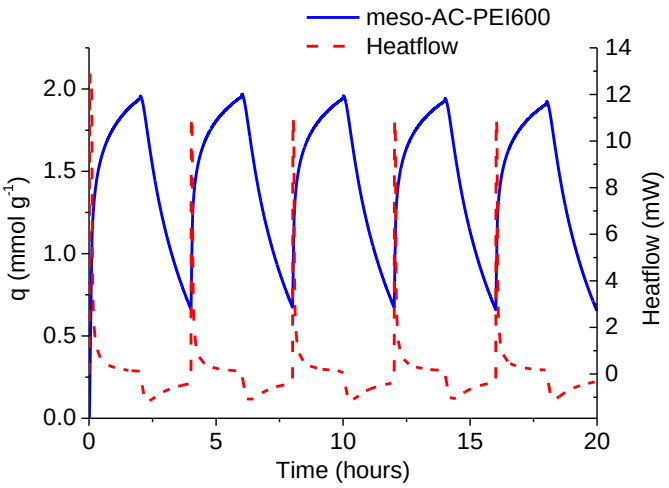

Figure 5.13: Cyclic uptake of CO_2 measured by thermogravimetric analysis. Adsorption steps 5 cm^3 min^{-1} CO_2 and 45 cm^3 min^{-1} He, 75 °C. Desorption steps: 50 cm^3 min^{-1}, 75 °C.

5.2.6 Effect of water on CO_2 capacity of amine impregnated materials

The presence of water vapour has been reported to both increase and decrease the CO_2 capacity depending on the experimental conditions.[20, 47] Stoichiometrically, under dry conditions, 1 mole of CO_2 can react with 2 moles of amine groups whereas in the presence of water 1 mole of CO_2 can react with 1 mole of amine groups as discussed in section 2.3. Measurements were carried out using the E-ZLC technique on a meso-AC carbon impregnated with polyethyleneimine of a molecular weight 1200, meso-AC-PEI1200(200), at a weight fraction of 67 %. The breakthrough experiments were carried out at 75 °C under two different sets of conditions. First measurements were carried out under dry conditions with a feed composition of 10 % CO_2 and 90% N_2 and purged with N_2 then a second set of experiments were carried out with 2000 ppm of water vapour added to the feed composition. Results can be seen in Figure 5.14.

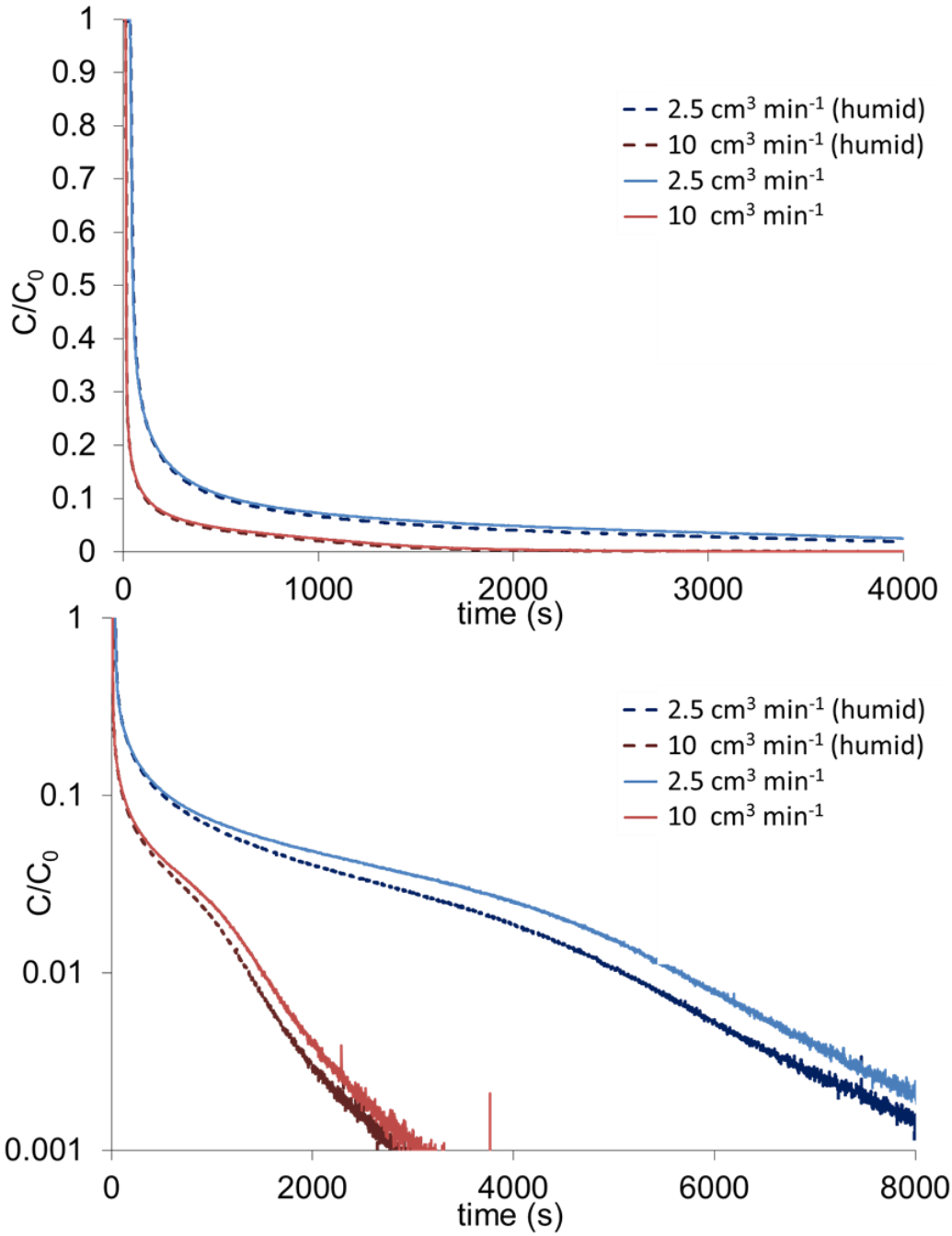

Figure 5.14: E-ZLC meso-AC2-PEI1200-200 at 75 °C and 2.5 and 10 cm^3 min^{-1}. Top: linear scale, bottom: semi-log plot. Dry conditions – Adsorption: 10% CO_2 90 % Nitrogen, Desorption: 100% N_2 Humid: 10% CO_2 89.8% N_2 and 0.2% H_2O. Adsorption time 1 hour.

The area under the curve corresponds to the CO_2 uptake capacity and a small change in capacity was observed between dry (1.9 mmol g^{-1}) and humid (1.7 mmol g^{-1}). The

measurements were carried out on consecutive days and it is unclear if this change in capacity is a direct effect of the water or a small degradation of the sample. The sample was regenerated at 100 °C overnight. However, there was no significant increase in the capacity at the conditions investigated in the presence of water. This finding is in agreement with reports that water improves cyclic stability rather than greatly enhancing the capacity.[47, 60] The change in capacity was seen in the long time region of the desorption curve. This would suggest that some of the strong adsorption sites that adsorb CO_2 at low partial pressures were no longer available. In the semi-log plot in Figure 5.14 an interesting double curvature was observed. The mechanism responsible for this feature appears to be the same in both dry and humid conditions. The source of this feature will be investigated further with the fitting of a detailed model in chapter 6 to experiments on the ZLC.

5.3 Conclusions

The structural properties of activated carbon material were studied as supports for impregnation with low molecular weight polyamines by volumetric nitrogen adsorption. Microporous materials showed a tendency for some of the free pore volume to be inaccessible (blocked) for nitrogen adsorption even at a low weight loading of polyamines. Mesoporous materials in contrast appeared to be more suited to impregnation with polyamines with a low level of blocked pore volume.

A series of materials were tested at a CO_2 partial pressure of 0.1 bar. On the addition of polyamines to both types of raw carbon material, the adsorption mechanism changed from a physisorption to a chemisorption process. All impregnated materials tested exhibited an enhanced affinity towards CO_2. The relative improvements compared to the starting micro-AC are highlighted in Figure 5.15.

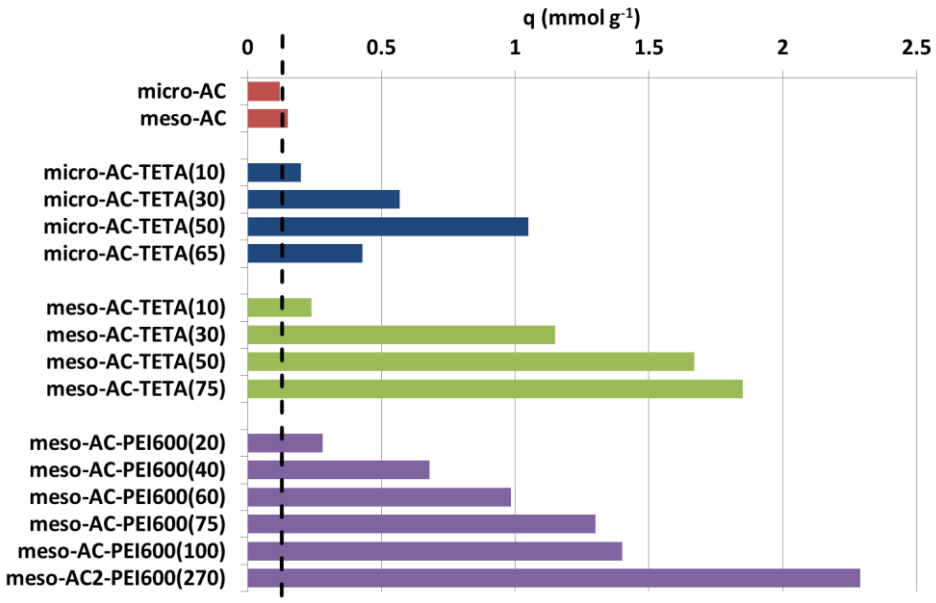

Figure 5.15: Summary chart showing uptake capacity of micro-AC and meso-AC porous carbons loaded with various quantities of polyethyleneimine derivatives.

It was apparent that the value of the CO_2 capacity was dependent on the structure of the carbon support, the amount of loaded amine and the type of amine. It was

hypothesized that better mass transport to the active sites was possible when the material loaded had larger mesopores as opposed to small micropores, where access to the active sites in the inner pores was easily hindered. For micro-AC there was an optimum amine loading beyond which the CO_2 capacity was lower. In the case of the meso-AC series there was a gradual increase in the CO_2 capacity as a larger amount of amine was loaded onto the support. It can be concluded that microporous supports are not ideal candidates for impregnation with amines. This is supported by the mixed results achieved by those attempting such work in the literature[73, 78]. It was suggested that as a greater volume of amine was loaded onto the carbon support, transport to the active sites was limited due to a blocking effect where the CO_2 had difficulty accessing the active sites. These findings support the conclusions from recent studies of PEI impregnated silica materials. [55]

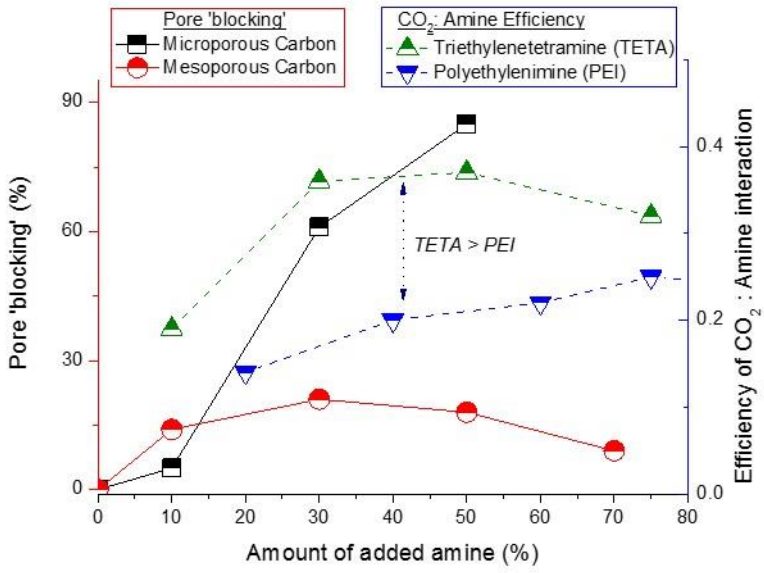

Figure 5.16: Summary % Pore blocking and efficiency of CO_2 interaction with amine. Triangles – Efficiency of CO_2: amine interaction. Squares and circles pore 'blocking'

The efficiency of the reaction of CO_2 with amine was relatively constant within each meso-AC and micro-AC series. However, the TETA impregnated meso-AC series interacted more efficiently with CO_2 (*ca.* 0.4 CO_2 molecules per 2 nitrogen atoms) compared to the micro-AC-TETA series (*ca.* 0.2 CO_2 molecules per 2 nitrogen atoms).

It was also observed that at the same mass loading, smaller polyamines (TETA) are more reactive towards CO_2 than the larger less volatile alternatives (PEI600), i.e. the efficiency of amino group utilization in the meso-AC-TETA series is higher than for the meso-AC-PEI600 series. These results are summarized in Figure 5.16. However, there was a pay-off in terms of stability and at high loading a drastic drop off in capacity was observed from the first to subsequent capture/regeneration cycles. Initial investigations into the kinetics of the reaction were investigated by thermal gravimetric analysis, which showed a slow second process in the long time region. Further investigations into reaction kinetics in the form of a detailed model are carried out in chapter 6.

6 ZLC experiments: A kinetic model

To investigate the amine:CO_2 reaction kinetics, the ZLC and E-ZLC techniques were used. It has been established through TGA experiments (section 5.2.3) that the amine:CO_2 reaction has a very high heat of adsorption (~90 kJ mol^{-1}). It was therefore possible that even with the very small amount of adsorbent used in the ZLC experiments that the system may not operate under isothermal conditions. A typical ZLC experiment under isothermal conditions reduces to a simple exponential decay in the long time region. An example from the literature[108], with 13 X as the adsorbent is shown in Figure 6.1. The adsorbent 13 X has a heat of adsorption greater than 40 kJ mol^{-1} for CO_2 which is significantly less than for the functionalised carbons. However, the temperature change of the ZLC during desorption is dependent on both the heat of adsorption and the adsorption rate. The heat balance may be defined by the following equation.[150]

$$C_s \frac{dT}{dt} = \frac{dq}{dt}(-\Delta H) + h\frac{A}{V_s}(T_0 - T) \qquad (6.1)$$

Where A is the cross sectional area of the solid, V_s is the volume of the solid, T_0 is the constant oven temperature, h is the heat transfer coefficient and C_s is the volumetric heat capacity of the material. The rate of adsorption/desorption of CO_2 on 13X is significantly faster than CO_2 on amine functionalized carbons. Therefore, even though the heat of adsorption is lower for 13X than amine functionalized carbons, the power generated ($\frac{dq}{dt}(-\Delta H)$) and the resultant temperature change of the system should be of a comparable order of magnitude. As a result, commercial zeolite 13X was used to characterize the heat transfer properties of the system.

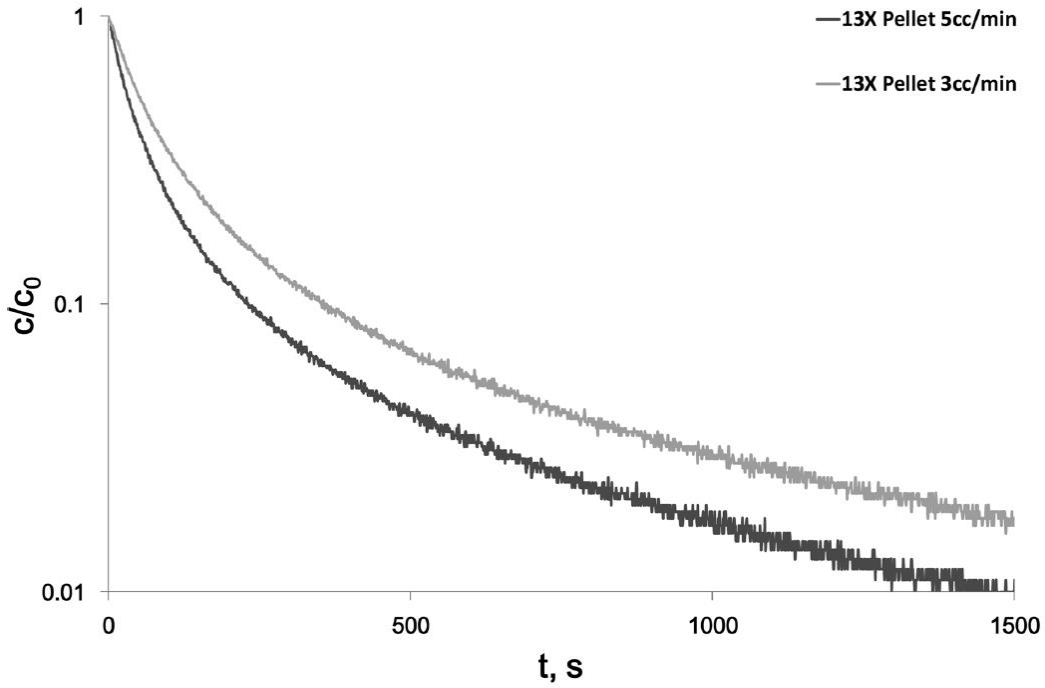

Figure 6.1: ZLC desorption curves of a 13 X pellet 38 °C at two different flow rates 5 and 3 cm^3 min^{-1} Adsorption at 0.1 bar CO_2 in helium.[108]

The non-isothermal ZLC response has been modelled by Brandani et al.[150], however to date, the resulting double curvature has not been seen experimentally. An example of the theoretical non-isothermal desorption curves can be seen in Figure 6.2. It can be seen that under non-isothermal conditions an interesting double curvature in the response was predicted. This can be explained by the fact that under certain combinations of model parameters[150] the heat transfer rate is limited and a low temperature plateau is obtained at which the heat convected into the system balances the heat necessary for desorption. As the adsorbed phase is depleted the system then moves back to the original temperature of the oven and the final exponential decay has the same slope as the isothermal case.

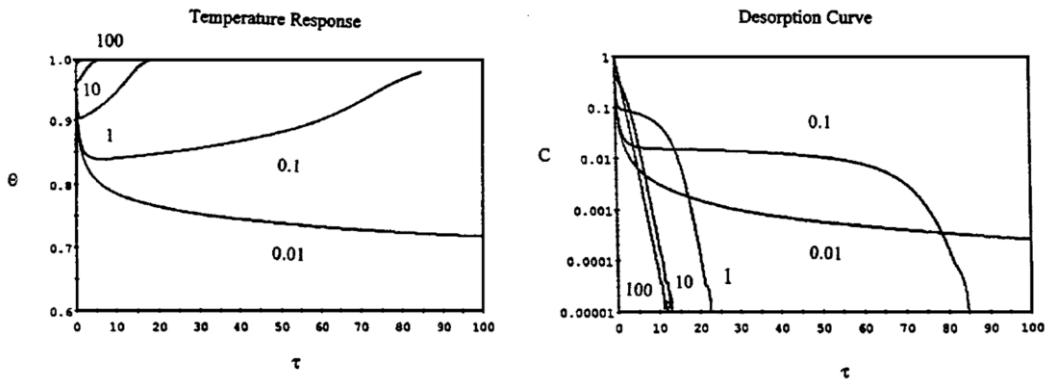

Figure 6.2: Theoretical non-isothermal ZLC desorption curves with increasing heat transfer resistance. Θ is dimensionless temperature, C is dimensionless concentration. Parameter shown is γ which is related to the heat transfer, ranging from γ= 100 (nearly isothermal) to γ = 0.01 (adiabatic).[150]

The parameter γ in the model (Figure 6.2), is a measure of the ratio of the time constants of heat transfer and convection and is defined as follows:

$$\gamma = \left(\frac{3h/C_S R}{F/K_0 V_S}\right) \tag{6.2}$$

Where R is the radius of the particle and K_0 is the henry law constant at the initial equilibrium temperature. The parameter γ alongside two other parameters α, the dimensionless adiabatic temperature change, and δ the dimensionless heat of adsorption, combine to give the parameter ($\alpha\delta/\gamma$) governing the isothermality of the system. For powder samples R is small and therefore γ is large and in general the system is nearly always isothermal. This is more obvious when one considers that for small particles the Nusselt number is approximately 2 and the parameter γ will become inversely proportional to the square of R and hence for small particles $\alpha\delta/\gamma$ becomes small.[150]

The breakthrough curves that were run with the E-ZLC for meso-AC2-PEI1200(200) are shown in Figure 5.14 with further examples shown in Figure 6.3. An interesting double curvature in the concentration profile was observed. It was unclear whether this

feature was a heat effect or an interesting response from the reaction kinetics between CO_2 and amine.

In this chapter, the source of the double curvature was investigated further. Although the tested amine-impregnated samples were powders, first experimental evidence was collected to establish whether the E-ZLC was operating at close to isothermal conditions. Therefore, a thermocouple was inserted into the E-ZLC and the temperature within the adsorption column was measured throughout the experiment. The experimental temperature profile within the E-ZLC was then modelled using Cysim. The column was first characterized with the commercial adsorbent 13 X and the heat transfer coefficients within the experimental set-up were established. Measurements were then carried out on the impregnated carbons and the experimental temperature profile within the adsorbent bed was monitored throughout the experiment to determine that the experiments were being conducted under near isothermal conditions.

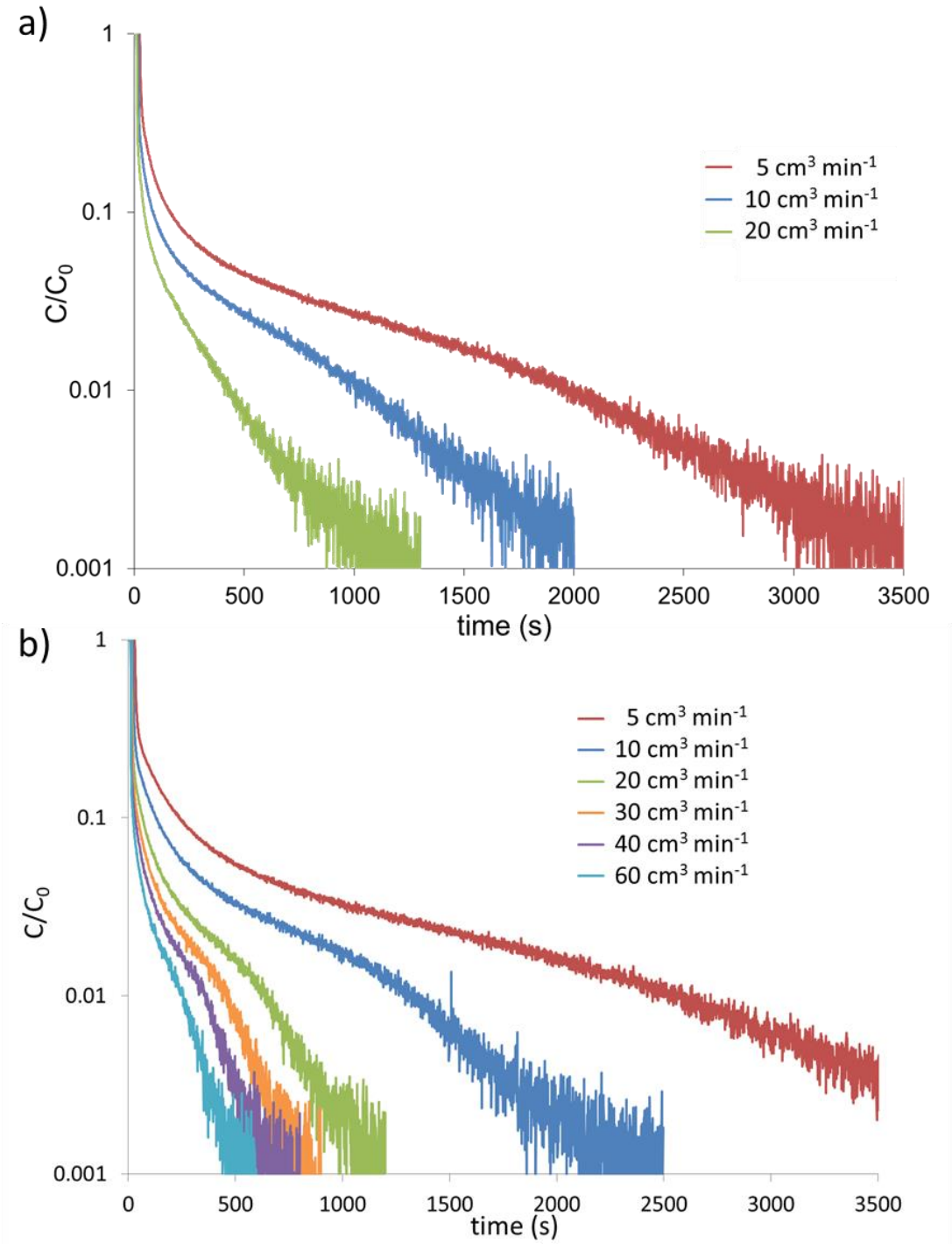

Figure 6.3: E-ZLC experiments on impregnated carbons that show double curvature in the concentration profile during desorption. a) meso-AC-PEI600(120), 30.04 mg, q = 1.1 mmol g^{-1} Conditions: 75 °C; 10% CO_2, 90% He; He purge b) meso-AC-PEI600(170), 24.7 mg, q = 1.8 mmol g^{-1} Conditions: 75 °C, 10% CO_2, 89.7% He, 0.3% H_2O; He purge

To complete the analysis, of the reaction kinetics between the amine and CO_2, experiments were carried out using the ZLC technique. The ZLC technique enabled a simple model to be developed that accounted for the chemical reaction that occurs in the adsorbed phase between the CO_2 and amine.

6.1 Temperature profile of the adsorbent bed during E-ZLC breakthrough experiments

The extended zero-length (E-ZLC) column is approximately three times the length of the ZLC at 25.9 mm and is housed in a 1/8 inch Swagelok bulkhead connector (shown in Figure 6.4), allowing the use of the same set-up developed for the traditional ZLC experiment. This allows more sample to be packed in the adsorption column to achieve a clear separation of components in a binary mixture and the binary adsorption selectivity to be determined. Examples of binary breakthrough curves, for the separation of biogas, are reported and discussed in chapter 7. The advantage of the E-ZLC over a larger more traditional breakthrough column (~5 g) is that a relatively small amount of sample is required (~50 mg) and the column can still be considered isothermal. To assess whether the system was in fact isothermal, a thermocouple was inserted into the centre of the E-ZLC and sealed in place with epoxy resin.

6.1.1 13X breakthrough experiments

Breakthrough experiments on commercial zeolite 13X were carried out to determine the temperature profile within the column. To ensure the sample was well packed around the thermocouple, pellets of 13X were broken up prior to being packed. The thermocouple was positioned 5 mm from the end of the column in the gas phase.

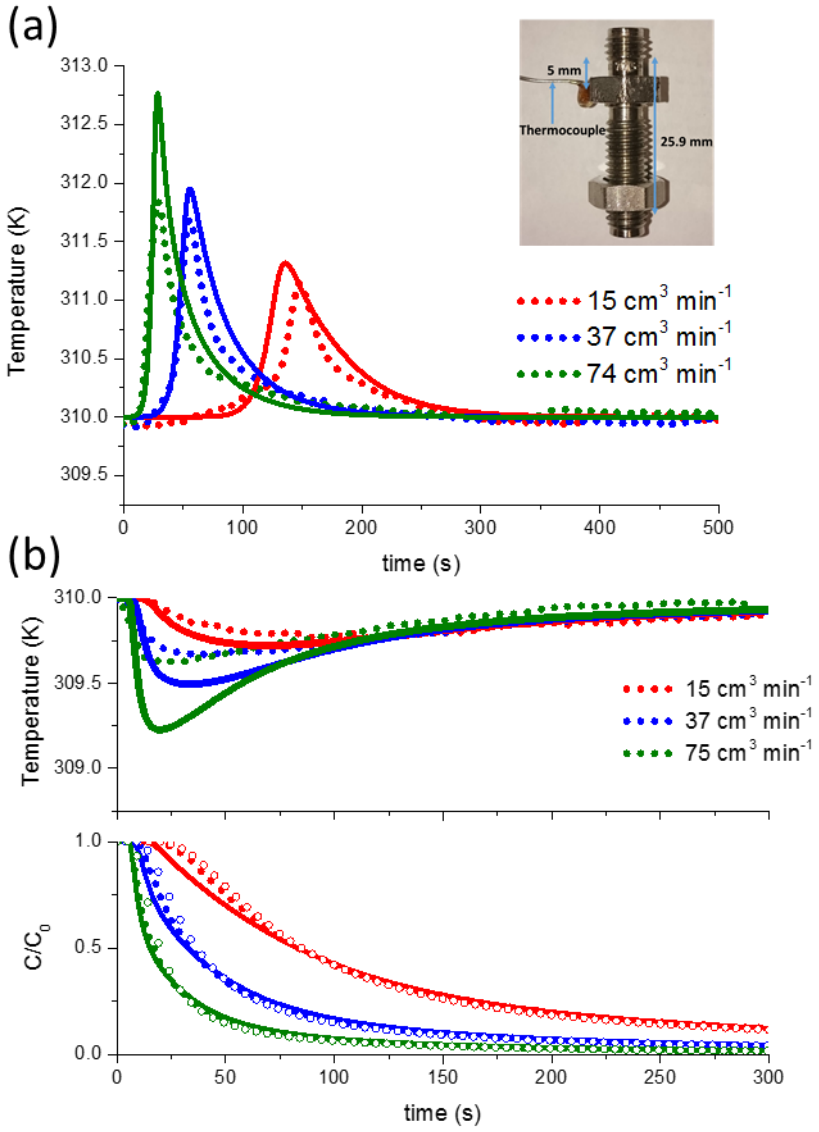

Figure 6.4: Breakthrough curves zeolite 13X, (63.75 mg, 310K, Feed: 0.1 bar CO_2, 0.9 bar N_2 Purge: N_2)

(a) Experimental temperature profile during adsorption and E-ZLC.
(b) Desorption temperature and CO_2 profiles with isothermal and non-isothermal Cysim fits. Experimental data – dots, non-isothermal Cysim simulation solid lines, isothermal Cysim fit open dots.

From Figure 6.4a an experimental spike in the temperature of up to 2.5 K was observed during the adsorption step. The temperature spike was larger at higher inlet flow rate and the bed returned to an isothermal state within 3 minutes as the heat was quickly

dissipated to the system. Due to the small diameter of the adsorption column there was a high rate of heat transfer out of the column, this resulted in a small change in the gas phase temperature.

A much smaller temperature change was observed in the desorption experiments, which is consistent with the fact that under non-linear conditions, desorption is slower than adsorption. Therefore the desorption experiments are closer to isothermal behaviour and require fewer parameters to be modelled. The isotherm parameters were independently collected at three different temperatures on a Quantachrome Autosorb IQ1 volumetric system (Figure 6.5). A dual site Langmuir isotherm was used to fit the CO_2 isotherms at three different temperatures simultaneously and the same saturation capacities were used to regress the N_2 data to ensure thermodynamic consistency. The resulting isotherm parameters were used in the simulation. In addition, the blank system desorption profile was modelled, with Cysim, to account for the response of the detector. The blank experimental curves along with the associated fittings can be found in Figure - A.2.

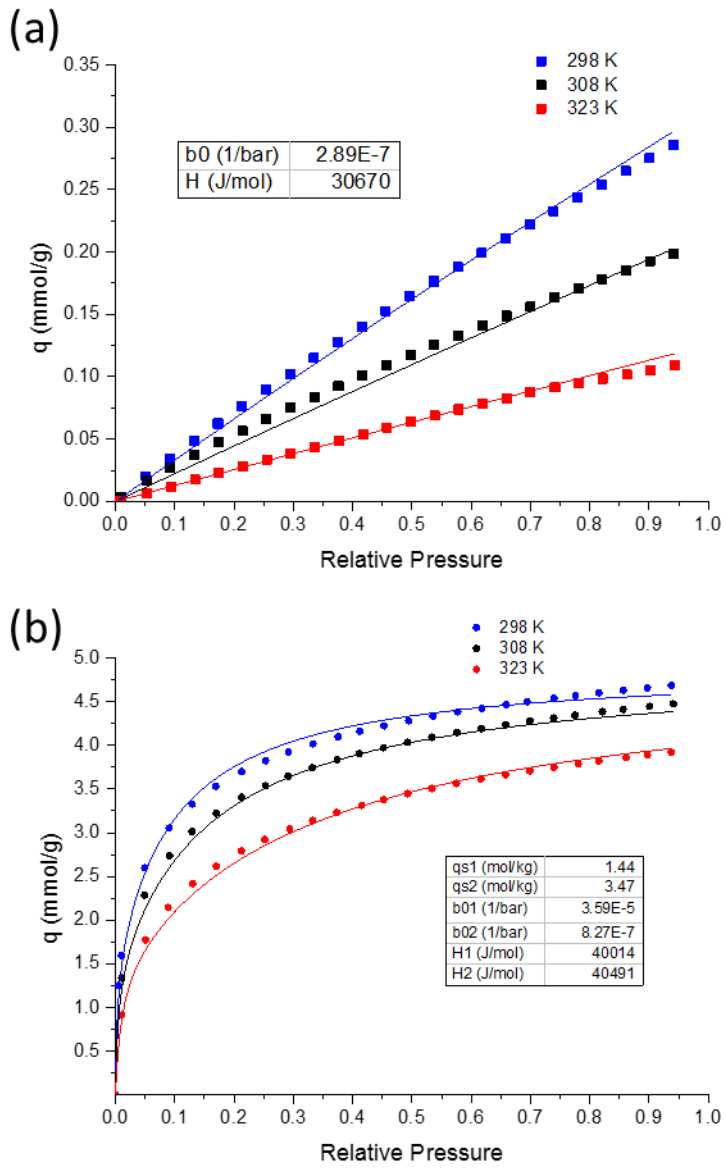

Figure 6.5: (a) N_2 isotherms on 13X measured at 298, 308 and 323K. The same values of qs1 and qs2 as for CO_2 were used to fit the nitrogen isotherms (b) CO_2 isotherms on 4 mm 13X pellets measured at multiple 298, 308 and 323K. Solid line is the fitted dual site Langmuir with the parameters shown in the inset table

The desorption breakthrough profile was modelled using both an isothermal and a non-isothermal model in Cysim. In the case of the non-isothermal model, the heat transfer coefficient that represents the heat transfer from the fluid phase to the column wall was adjusted to match the experimentally observed temperature profile. The two other

coefficients that govern the heat transfer from the pellet to the fluid and the column wall to the oven were estimated via simple experiments and through relationships from the literature which are discussed in Appendix B. A reasonable fit was achieved between the predicted fluid phase temperature and the experiment, Figure 6.4b, considering that a shielded thermocouple was used and the heat transfer dynamics of the thermocouple were not included in the model. As the temperature change of the fluid, during desorption, was less than one degree it was possible to consider the bed to be isothermal. A comparison of the predicted breakthrough profile for the isothermal and non-isothermal case is shown in Figure 6.4b, confirming that the system is sufficiently close to isothermal behavior. There were small simulated differences in the CO_2 profile at short times. At 74 cm^3 min^{-1}, where the largest change in temperature was observed, the non-isothermal model provided a more accurate prediction of the experimental breakthrough profile than the isothermal case. However in the long-time region there was no noticeable difference between the adsorption models and both accurately represented the data, confirming the validity of the mass transfer kinetic parameters.

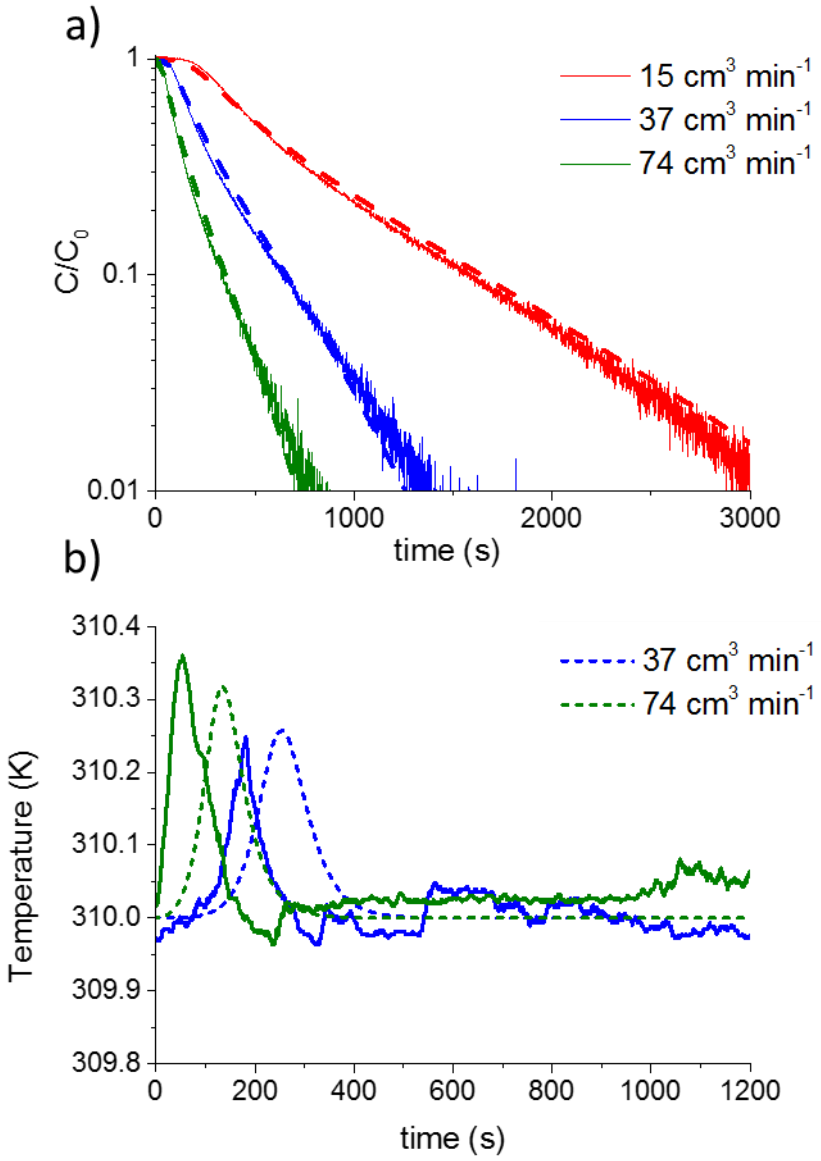

Figure 6.6: E-ZLC breakthrough curves, Zeolite 13X (63.75 mg). Conditions: 310 K, Adsorption – 1% CO_2, 99% N_2; Desorption – 100% N_2. a) Desorption curves, b) Adsorption temperature profile Solid line experimental data, Dashed line Cysim simulation, non-isothermal model.

In addition, experiments were run at a CO_2 concentration of 1% during the adsorption step. In Figure 6.6a it can be seen that the experimental desorption concentration profile was accurately simulated by the simulation. In addition a very small spike in the temperature was recorded during the adsorption step of less than 0.4 K. The simulation produced an accurate prediction of the temperature spike when the very

small magnitude of the temperature change is taken into consideration. The slight shift in the position of the peak can be accounted for by an inaccurate modelling of the axial heat transfer or a small error in the experimental flow rate during the adsorption step.

In conclusion, the temperature profile of the E-ZLC has been investigated and it was clear that during breakthrough experiments with 13 X, the adsorption column can be considered to be isothermal with a temperature change of less than 1 °C during desorption. The adsorption simulator was able to accurately predict the concentration and temperature profiles of the column.

6.1.2 Amine-impregnated carbons breakthrough experiments

The amine-impregnated carbons have a significantly higher CO_2 heat of adsorption than 13 X (13X: ~40 KJ mol^{-1}, meso-AC-amine: ~90 kJ mol^{-1}). Therefore it was plausible, that although the E-ZLC could be considered isothermal for 13 X breakthrough experiments, that non-isothermal effects could be present in breakthrough experiments carried out on amine impregnated carbons. The larger amount of heat generated per adsorbed CO_2 molecule results in a larger amount of energy being transferred to the system. However, as previously discussed, the rate of uptake is slower for the amine impregnated carbons, therefore the heat is generated over a longer time period resulting in a smaller temperature change. In addition, in general, at a CO_2 concentration of 10% the total uptake of CO_2 by the amine-impregnated sample is less than by 13X, therefore it was likely that the total amount of heat generated by the amine samples during the breakthrough experiments will be at a comparable level to 13X. To validate that the breakthrough experiments on amine impregnated samples were indeed carried out under isothermal conditions, experiments were carried out with a thermocouple *in situ*.

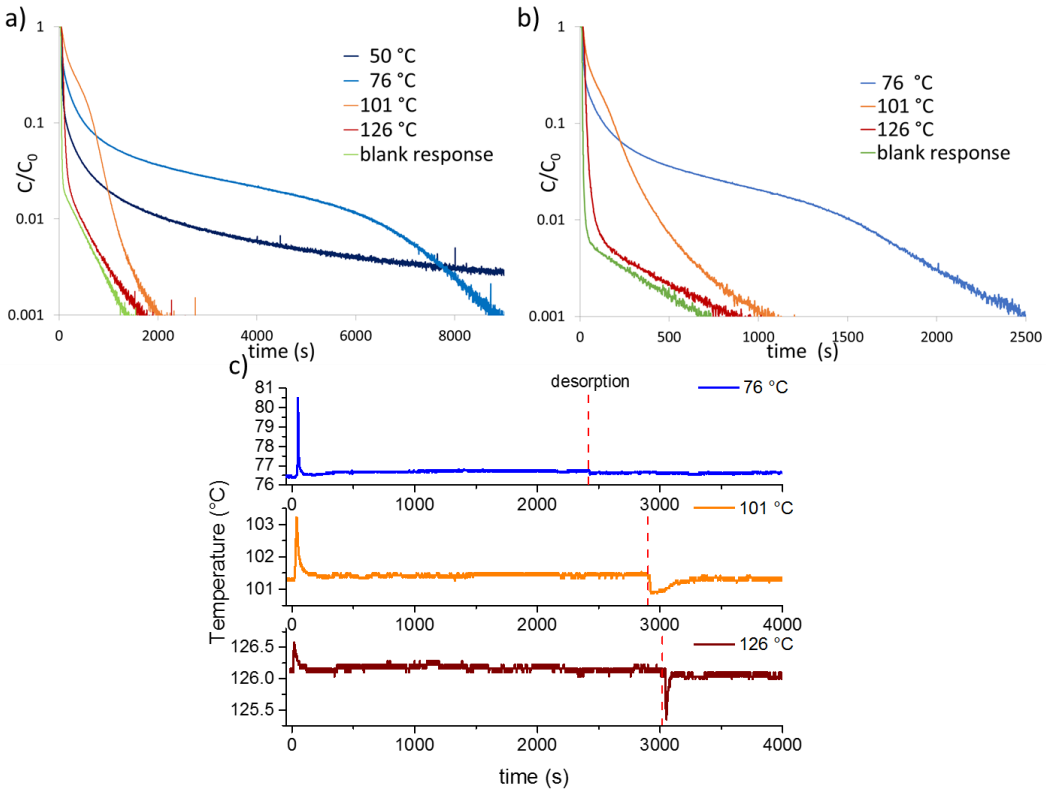

Figure 6.7: meso-AC2-PEI1200-200 E-ZLC desorption curves at various temperatures; Adsorption – 10% CO_2, 90% N_2; Desorption – 100% N_2; 24.2 mg. Plotted on semi-log scale to emphasize the desorption profile a) 2.5 cm^3 min^{-1} b) 10 cm^3 min^{-1} c) Experimental temperature profiles during experiments at 10 cm^3 min^{-1}, t = 0 s is the start of the adsorption step

From Figure 6.7a,b the interesting desorption profile was evident during experiments carried out at 76 and 101 °C. The CO_2 capacity at each temperature, calculated from the area under the curve is tabulated in Table 6.1. The lower amount of CO_2 adsorbed on the sample at 50 °C and 126 °C results in no feature being present in the desorption profile.

Table 6.1: CO_2 capacity of meso-AC2-PEI1200-200 at various temperatures and 0.1 bar CO_2 measured by E-ZLC breakthrough experiments

Temperature (°C)	Capacity (mmol g^{-1})
50	1.08
76	1.90
101	1.75
126	0.35

In Figure 6.7c, the temperature profiles at the various different temperatures are reported. During the adsorption step at 76 °C a temperature spike of 4 °C was observed, however the heat was rapidly dissipated to the system and the column returned to isothermal conditions. The magnitude of the temperature change during desorption at 76 and 101 °C was much smaller than during the adsorption step. At 101 °C the temperature of the column dropped by less than 0.5 °C for around 350 s. It would therefore appear that during the desorption step the change in temperature within the column was minimal. The measured experimental temperature was likely to be a combination of both the gas phase and solid phase temperature and was dependent on the packing of the adsorbent particles around the thermocouple. The particle size of the meso-AC was small (<150 micron) facilitating the heat transfer from the solid phase to the gas phase. It was therefore concluded that the interesting desorption profile was not due to a heat effect. In order to investigate the profile further, the ZLC technique was used, where with an even smaller sample mass required (< 5 mg), the experiments can be conducted under isothermal conditions.

6.2 Reaction kinetics of CO_2 adsorption on amine-impregnated carbons

In this section ZLC experiments have been carried out on mesoporous activated carbon samples that have been impregnated with amine. Polyethylenimine was chosen as the amine for these studies due to its low volatility and cyclic stability enabling multiple measurements to be carried out on the same sample. First, experimental ZLC results are presented at a variety of temperatures and flow rates. Secondly, a model was developed for the ZLC that attempts to account for the chemical reaction between CO_2 and amine in the adsorbed phase.

6.2.1 ZLC experimental data – PEI impregnated carbon

ZLC experiments were carried out on two samples. Polyethylenimine of two different molecular weights was investigated. First, meso-AC2-PEI600(270), molecular weight of 600, was tested at 75 °C with the results at two flow rates shown in Figure 6.8. The double curvature in the desorption data was clearly still present. The response in the long time region shows a clear kinetic effect as the concentration profiles, at the two different flow rates, do not overlap in the plot of C/C_0 *vs* the product of flow rate and time (Ft).

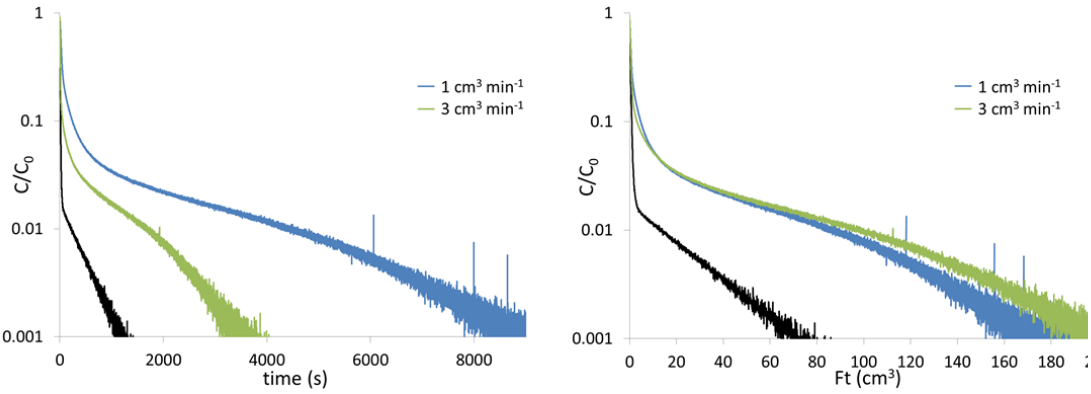

Figure 6.8: ZLC experiments at 75 °C on meso-AC2-PEI600(270), sample mass – 5 mg, q = 2.07 mmol g^{-1}, 3 hour adsorption time. LHS: semi-log plot vs time, RHS semi-log plot vs the product of flowrate and time. Conditions: Adsorption – 10% CO_2, 90% N_2; Desorption 100% N_2. System blank response at 3 cm^3 min^{-1} shown in black.

As a direct comparison a sample was impregnated with polyethyleneimine with a molecular weight of 1200. The sample was tested at 60, 75 and 90 °C and at 1, 2 and 3 cm^3 min^{-1}. The response curves can be found in Figure 6.9. The double curvature was again evident in the desorption profiles particularly at 75 and 90 °C. In addition, the process was clearly under kinetic control at all temperatures with the desorption profiles not overlapping in the *Ft* plots.

As has been seen previously through the TGA studies carried out in chapter 5 there is a period of rapid initial uptake of CO_2 by the amine-impregnated samples followed by a second slower adsorption process. As a result, even at 75/90 °C the samples take a very long time to reach their equilibrium capacity. The amount adsorbed by the samples was therefore dependent on the adsorption time in agreement with previous results. The amount adsorbed obviously directly effects the desorption profile. The various adsorption times for the ZLC experiments along with the associated capacity were tabulated in Table 6.2. The adsorption time for the measurement at 90 °C and 3 cm^3 was 20 minutes shorter than the other flow rates measured at that temperature. The lower adsorbed amount was clearly seen in the *Ft* plot (Figure 6.9c) where the area under the curve is visibly smaller for 3 cm^3 min^{-1} than the other flow rates. In

addition at 75 °C when the adsorption time was increased from 45 to 120 minutes the CO_2 capacity of the material increased by ~10%.

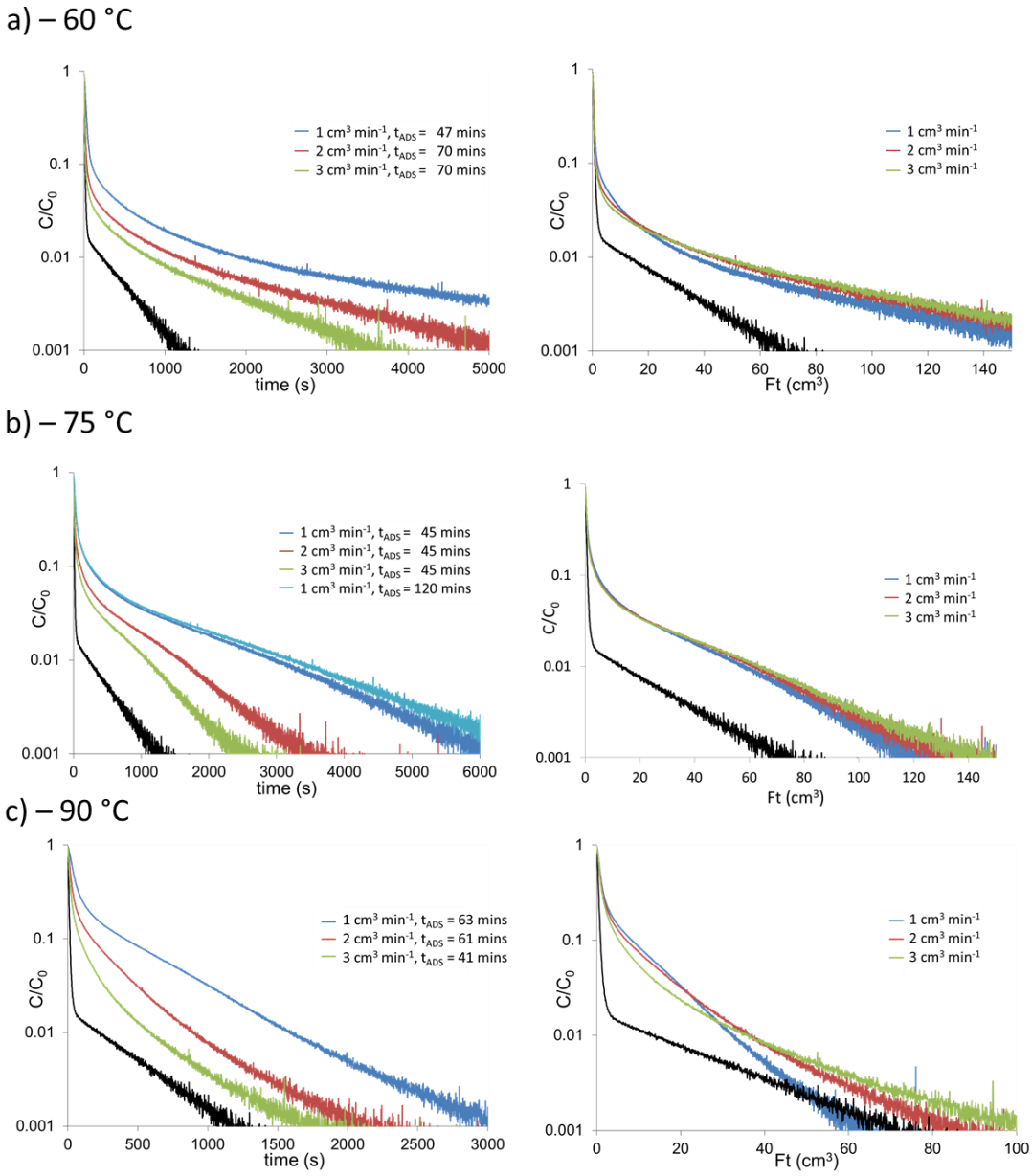

Figure 6.9: ZLC experiments meso-AC2-PEI1200(200) at various different temperatures, 4 mg. LHS: C/C_0 vs t, RHS: C/C_0 vs Ft. Conditions: Adsorption – 10% CO_2, 90% N_2; Desorption 100% N_2. t_{ADS} is the time of the adsorption step. System blank response at 3 cm^3 min^{-1} shown in black.

Table 6.2: CO_2 adsorbed amounts alongside adsorption time at 0.1 bar CO_2 partial pressure and various flow rates (F). Results calculated from ZLC experiments shown in Figure 6.8 and Figure 6.9. t_{ADS} is the adsorption time

		Temperature					
		60 °C		75 °C		90 °C	
	F ($cm^3\ min^{-1}$)	t_{ADS} (min)	q ($mmol\ g^{-1}$)	t_{ADS} (min)	q ($mmol\ g^{-1}$)	t_{ADS} (min)	q ($mmol\ g^{-1}$)
meso-AC2-PEI1200(200)	1	47	1.13	45	1.90	63	1.85
	1			120	2.10		
	2	70	1.24	45	1.91	61	1.83
	3	70	1.29	45	1.95	41	1.33
meso-AC2-PEI600(270)	1			180	2.01		
	3			180	2.07		

As previously discussed, due to the long equilibration times, it is challenging to establish the true equilibrium capacity of the impregnated materials. In the next section a kinetic model was developed in an attempt to explain the interesting double curvature observed in the concentration profile and to quantify some kinetic constants for the reaction between the polyamine and the CO_2.

6.2.2 Reaction kinetics – a theoretical ZLC model

The chemical reaction between CO_2 and amines has been studied for decades with a wide variety of kinetic data presented in the literature.[151, 152] A recent review into the kinetics of the reaction between amine and CO_2 in aqueous solutions was carried out by Couchaux et al. where they compared the apparent first order constants measured by different groups using the stopped-flow technique for a wide variety of amines.[153] From this study it is clear that the rate constants and the order of reaction with respect to the amine vary significantly with amine type and their study does not consider the reversibility of the reaction. In the literature three main mechanisms have been proposed for the reaction of CO_2 and amine. They are the zwitterion mechanism, the

termolecular mechanism and the base-catalyzed hydration mechanism.[153, 154] The zwitterion mechanism is detailed below, where the amine (AmH) first reacts with the CO_2 to form a zwitterion as an intermediate.

$$CO_2 + AmH \underset{k_{-1}}{\overset{k_1}{\rightleftarrows}} AmH^+COO^- \quad (6.3)$$

The zwitterion is then deprotonated by a base (B) which could potentially be another amine group.

$$AmH^+COO^- + B \overset{k_b}{\rightarrow} AmCOO^- + BH^+ \quad (6.4)$$

In the termolecular mechanism the amine reacts simultaneously with both CO_2 and a base to form a carbamate.

$$CO_2 + AmH \cdots B \underset{k_{-1}}{\overset{k_1}{\rightleftarrows}} AmCOO^- + BH^+ \quad (6.5)$$

And finally the base-catalyzed hydration mechanism has been proposed for the reaction of tertiary amines with CO_2.

$$R_3N + H_2O + CO_2 \underset{k_{-1}}{\overset{k_1}{\rightleftarrows}} R_3N^+H + HCO_3^- \quad (6.6)$$

Vaidya et al. concluded that in the literature, the reaction of primary, secondary and sterically hindered amines with CO_2 was in general described with the zwitterion mechanism and that the reaction of CO_2 with tertiary amines is usually attributed to the base-catalyzed hydration mechanism.[154]

Although studies of the reaction mechanism between amine and CO_2 in solution is a useful starting point, the reaction kinetics that occurs in the adsorbed phase is likely to be significantly different due to surface effects and the absence of a solvent. The

majority of kinetic studies consider the process as irreversible, whereas in an adsorption column in order to accurately simulate multiple cycles it is necessary to simulate the kinetics as a dynamic reversible process. Several studies have attempted to model the reaction kinetics in the adsorbed phase. Serna-Guerrero et al. investigated Langergen's pseudo first and second order models along with an Avrami kinetic model to fit experimental breakthrough curves collected on amine functionalized mesoporous silica.[155, 156] In addition, Jones and co-workers used similar models along with LDF resistances to model breakthrough curves on functionalized silicas.[157] Experimentally, they observed a sharp initial breakthrough of CO_2 followed by a long tail in the concentration profile.[158] It was concluded that the long tail in the breakthrough experiments was a result of the slow diffusion of the CO_2 through the polymer phase of the adsorbent as opposed to non-isothermal behavior in the adsorption column.[158] However, as pointed out by Ebner et al. none of these models consider the desorption kinetics of the reaction.[159] Ebner et al. have proposed a kinetic model which takes a mechanistic approach to studying the reaction kinetics between the amine and the CO_2. Five different models are proposed, with each implementing a different combination of reactions which occur in series or parallel to model the chemical process. The models are compared to thermogravimetric experimental data at a variety of temperatures and pressure in order to validate the model and the parameters. Their optimum model has three reactions taking place in parallel and requires 20 parameters to be fitted. This does however allow curves to be predicted for a wide range of temperatures and pressures. With such a large number of fitting parameters, it is reasonable that a good fit to the experimental data is achieved. A similar approach is adopted in this work where both the forward and backward reaction are considered to enable the full process to be modelled but with fewer fitted parameters.

The zero length column technique has been widely used to investigate diffusion in zeolites and a wide variety of kinetic models have been developed as discussed in section 3.2.2. In this work the model of the ZLC has been expanded to account for a chemical reaction within the adsorbed phase. The reaction between CO_2 and amine is used as an example in this case, however in principle the model could be adapted to

consider any reaction that occurs in the adsorbed phase. The fluid mass balance of the ZLC is given in equation 6.7.

$$V_g \frac{dc_f}{dt} + k_{LDF} A\left(K_{eq} c_f - q\right) = F c_{in} - F c_f \quad (6.7)$$

With

$$K_{eq} = \frac{q_0}{c_0} \quad (6.8)$$

Where V_s is the volume of the solid, V_g is the volume of the fluid phase, F is the flow rate, q the adsorbed phase concentration, c_{in} is the gas concentration at the inlet, k_{LDF} is the linear driving force coefficient from the gas phase to the physically adsorbed phase and c_f the gas phase concentration in the column. In a standard ZLC experiment, the rate of change of the physically adsorbed amount (q) in the case of a linear equilibrium isotherm is governed by equation 6.9.

$$\frac{dq}{dt} = \frac{1}{V_s} k_{LDF} A\left(K_{eq} c_f - q\right) \quad (6.9)$$

In the case of interest, a PEI-impregnated carbon, very little of the CO_2 is physically adsorbed, with the majority of the CO_2 reacting with the basic amine groups. This is due to the amine filling the pore volume of the carbon support and blocking the surface sites for physical adsorption. In this model it was therefore assumed that the CO_2 is rapidly physically adsorbed and then reacts from the physically adsorbed phase to a chemically bound state. There is therefore an additional flux from the physically adsorbed phase to the chemisorbed phase and equation 6.9 can be expanded to equation 6.10.

$$\frac{1}{V_s} k_{LDF} A\left(K_{eq} c_f - q\right) = \frac{dq}{dt} + \frac{da_1}{dt} \quad (6.10)$$

Where a_1 is the concentration of amine salt formed by the reaction of CO_2 and free amine. Depending on the proposed reaction mechanism there could be any number of

products formed from the reaction in the adsorbed phase. For example, if there were two possible reactions that occurred in parallel in the adsorbed phase, then they could be modelled by expanding equation 6.10 to account for the formation of a secondary product (equation 6.11)

$$\frac{1}{V_s} k_{LDF} A\left(K_{eq} c_f - q\right) = \frac{dq}{dt} + \frac{da_1}{dt} + \frac{da_2}{dt} \quad (6.11)$$

Where a_2 is an alternative reaction product. As PEI is a large complex polymer there are three different types of amine group, primary, secondary and tertiary. In principle all of these groups can react with CO_2 via a different mechanism and at a different reaction rate. It is therefore plausible that multiple reactions could be occurring in series or in parallel during the adsorption step. To keep the number of fitted parameters to a minimum and reduce the complexity of the model the simplest case with one possible reaction will be considered in this study. The overall reversible reaction that was considered is:

$$CO_2 + a_1^* \underset{k_{1A}}{\overset{k_{1D}}{\longleftrightarrow}} a_1 \quad (6.12)$$

Where a_1^* is the number of available amine adsorption sites, a_1 is the product (carbamate salt) and k_{1A}/k_{1D} are the rate constants for adsorption and desorption respectively. The rate expression for this simplest case the salt was formulated with the flexibility to consider different orders of reaction with respect to the individual components. The rate equation with respect to the formation of the salt (a_1) is given by equations 6.13.

$$\frac{da_1}{dt} = k_{1A} q^m (a_1^* - a_1)^n - k_{1D} (a_1)^p \quad (6.13)$$

$$a_1^* = a_{Tot} * x \quad (6.14)$$

Where, a_1^* is the number of accessible amine sites, a_{Tot} is the total number of amine sites, x is the fraction of amine sites that are accessible and m,n,p are the order of reaction with respect to CO_2, amine and the amine salt respectively.

Therefore, three governing differential equations for the fluid phase (equation 6.7), the physically adsorbed phase (equation 6.10) and the chemisorbed phase (equation 6.13) have been established.

A diagrammatic representation of the various mass balances is presented in Figure 6.10. On top of modelling the processes in the adsorption column, it was also necessary to model the blank detector response of the ZLC system. The detector response was modelled in a similar way to that which was used in the Cysim simulations presented in section 6.1.1. An additional adsorption phase was used after the adsorption column, governed by the equations presented in Figure 6.10, to account for the detector response. The fitting of the blank response, where no adsorption occurs in the adsorption column, can be found in appendix A5.

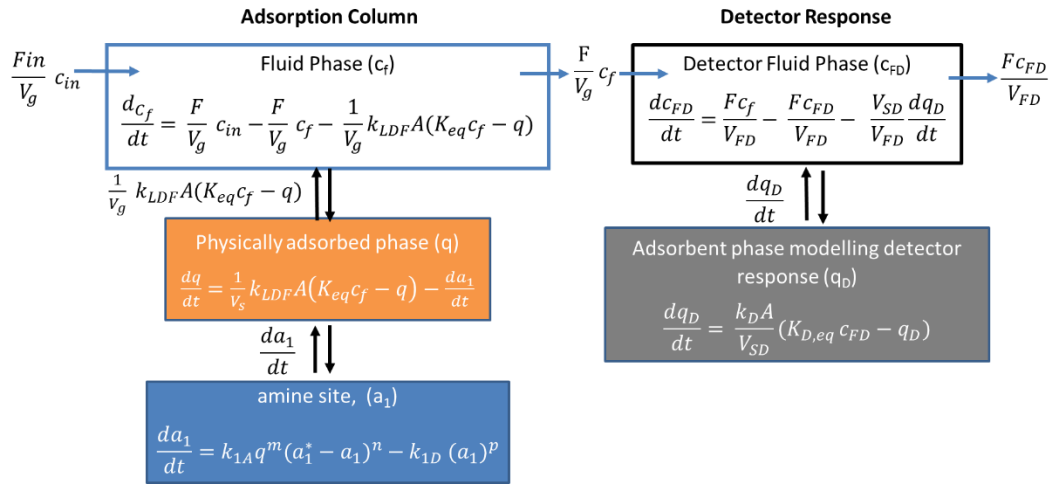

Figure 6.10: Mass balances in the various phases of the adsorption column along with the relevant fluxes between the phases.

The three governing equations (6.7, 6.10 and 6.13) were normalised as follows for implementation in Matlab. The equations were normalised with

$C_f = \frac{c_f}{c_0}$, $C_{in} = \frac{c_{in}}{c_0}$, $Q = \frac{q}{q_0}$ and $A_1 = \frac{a_1}{a_{1,0}}$

Where c_0 is the initial concentration of CO_2, q_0 is the equilibrium adsorbed amount of CO_2 in the physically adsorbed phase and $a_{1,0}$ is the equilibrium adsorbed amount in the chemisorbed phase. Therefore equation 6.7 becomes

$$\frac{dC_f}{dt} = \frac{F}{V_g} C_{in} - \frac{F}{V_g} C_f - \frac{q_0}{c_0}\frac{A}{V_g} k_{LDF}(C_f - Q) \quad (6.15)$$

The normalization of equation 6.10 with the substitution of equation 6.8 becomes

$$\frac{dQ}{dt} = \frac{1}{V_s} k_{LDF} A(C_f - Q) - \frac{a_{01}}{q_0}\frac{dA_1}{dt} \quad (6.16)$$

And finally equation 6.13 becomes

$$\frac{dA_1}{dt} = \frac{k_{1A}}{a_{01}}(Qq_0)^m(a_1^* - a_{1,0}A_1)^n - \frac{k_{1D}}{a_{1,0}}(a_{1,0}A_1)^p \quad (6.17)$$

In this model, the forward reaction can be dependent on the concentration of CO_2 and the concentration of accessible amine. The backward reaction is dependent on the concentration of amine salt. As it is an equilibrium process, at equilibrium the rate of the forward reaction equals the rate of the backward reaction and:

$$\frac{da_1}{dt} = 0, \text{ and } A_1 = 1, Q = 1 \quad (6.18)$$

Therefore at equilibrium

$$\frac{k_{1A}}{k_{1D}} = \frac{(a_{01})^p}{(q)^m(a_1^* - a_1)^n} = K_1 \quad (6.19)$$

The equilibrium parameter K_1 governs how far the equilibrium lies to the products or the reactants. As a result of the equilibrium condition, the value of k_{1A} and k_{1D} are

intrinsically linked. Therefore if k_{1A} is a fitted parameter then k_{1D} is derived. The number of accessible amine sites (a_1^*) is also an unknown and is calculated from the specified value of K_1 through the relationship in equation 6.18. The order of reaction with respect to each component can be varied to fit the experimental data. The amount adsorbed in the physically adsorbed phase is assumed to be small and the transport kinetics into that phase are fast, i.e. the reaction of CO_2 with amine is the rate determining step. All other parameters are known and fixed.

In order that the equilibrium constant (K_1) is unitless the concentrations of the reactants and products were divided by standard concentrations a_1^θ, $a_1^{*\theta}$ and q^θ which were equal to 1 mol m^{-3}. For example equation 6.19 becomes:

$$\frac{k_{1A}}{k_{1D}} = \frac{\left(\frac{a_{01}}{a_1^\theta}\right)^p}{\left(\frac{q}{q^\theta}\right)^m \left(\frac{a_1^*}{a_1^{*\theta}} - \frac{a_1}{a_1^\theta}\right)^n} = K_1 \qquad (6.20)$$

These terms have been omitted from the equations for simplicity.

To check that the model had been implemented correctly in Matlab adsorption (C_{in}=1) and desorption curves (C_{in}=0) were simulated with no adsorption in the chemisorbed phase. This limiting case with the adsorption process controlled by the linear driving force parameter (k_{LDF}) produced an adsorption profile which when plotted as 1-C/C_0 vs time overlapped with the desorption profile of the same process plotted as C/C_0 vs time. This symmetrical behavior is characteristic of a linear ZLC experiment. The simulated curves including the detector response can be seen in Figure 6.11.

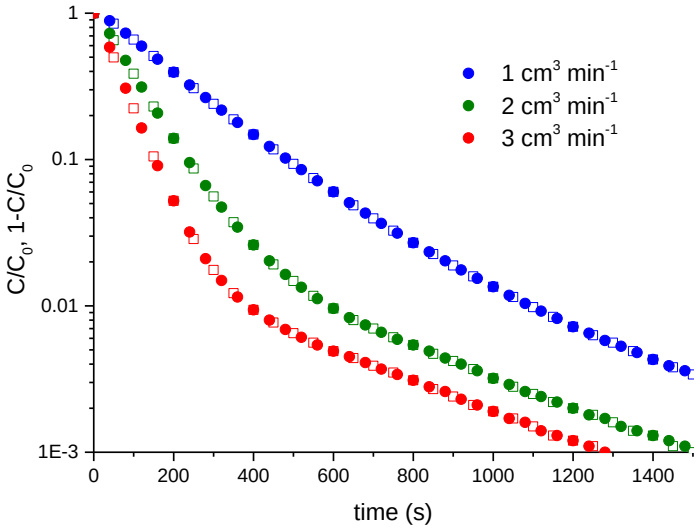

Figure 6.11: Theoretical adsorption and desorption curves with no chemisorption. Adsorption (solid circles) initial conditions: C_f =1, Q=1, C_{in} = 1, plot of 1-C/C_0 vs time. Desorption (unfilled squares) initial conditions: C_f =0, Q=0, C_{in} = 0, plot of C/C_0 vs time.

In order to examine the shape of the model response, when the reaction in the adsorbed phase was considered, some theoretical curves have been generated for certain model parameters. K_1 governs the equilibrium relationship of the reaction and was varied in magnitude from a value 0.01 to 100. The rate constant k_{1A} governs the rate of the forward reaction and theoretical curves were generated with values of k_{1A} spanning 3 orders of magnitude. From these two fixed inputs and the relationship detailed in equations 6.18 the associated values of k_{1D}, a_1^* were calculated. All other inputs were kept constant throughout. The simulated theoretical curves are shown in Figure 6.12 with various combinations of reaction order for the various components.

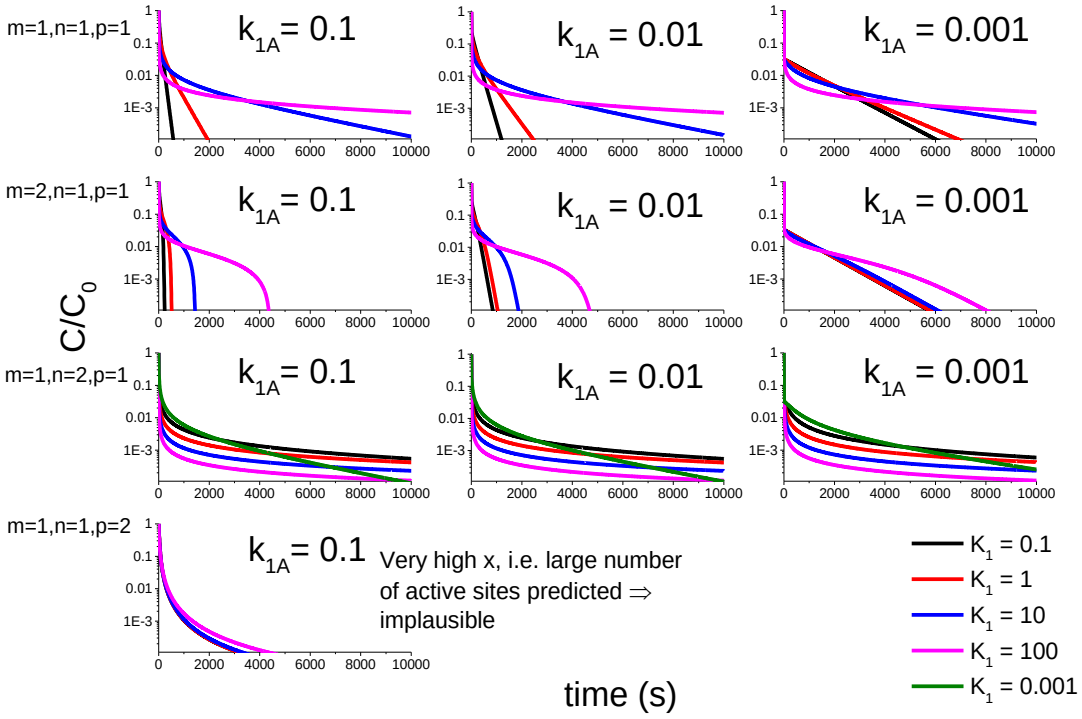

Figure 6.12: Model 1-Effect of equilibrium constant (K_1) and rate constant k_{1A}

a_{tot} =10, F=2.5 cc min^{-1} Initial values: $a_{1,0}$ = 1, q_0=0.01, c_0=0.1.

From Figure 6.12 it can be clearly seen that only if the rate of reaction was considered second order with respect to the concentration of CO_2 did the desorption curve exhibit a double curvature in the concentration profile. Using the same model, theoretical desorption curves were generated assuming fractional order kinetics for each of the components and are shown in Figure 6.13.

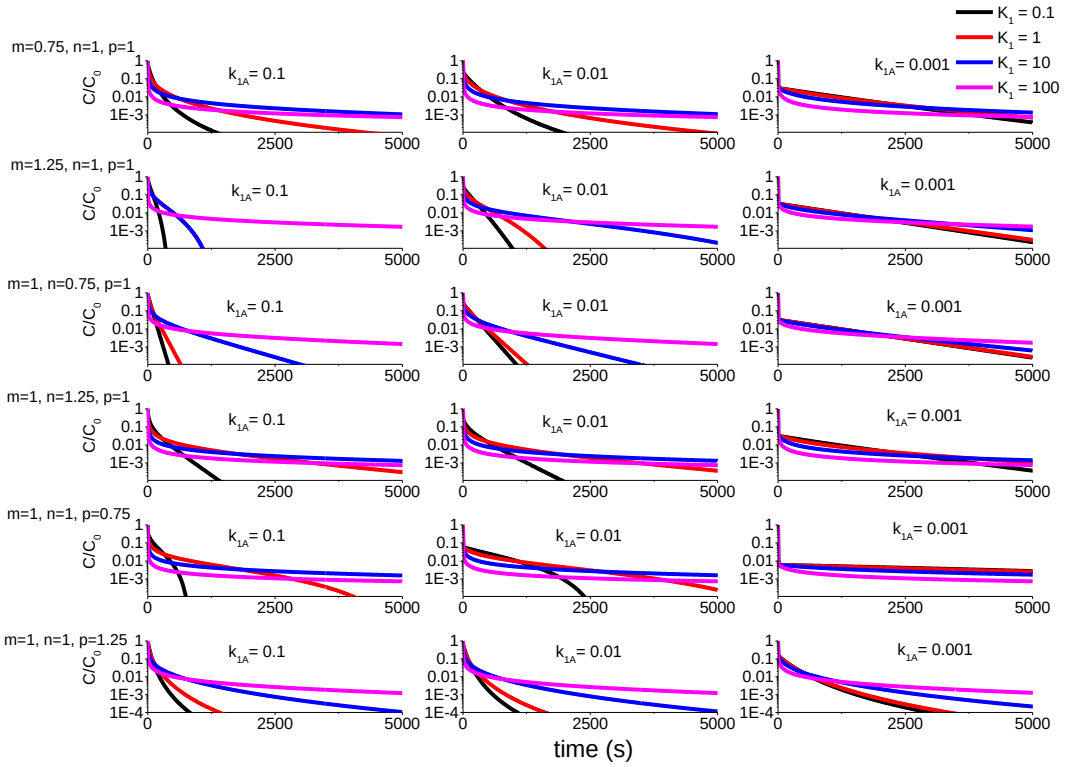

Figure 6.13: Fractional order kinetics, theoretical curves. The equilibrium constant (K_1) and rate constant k_{1A} were varied. a_{tot} =10, F=2.5 cm^3 min^{-1} Initial values: $a_{1,0}$ = 1, q_0=0.01, c_0=0.1.

From Figure 6.13 it was observed that a fractional order with respect to the CO_2 and the amine under certain conditions produced a desorption profile with a double curvature. A second order or fractional process with respect to the CO_2 does not make sense mechanistically because it would suggest that the rate of reaction was dependent on two CO_2 molecules. However, if the zwitterion mechanism is considered, which is the generally accepted mechanism for primary and secondary amines in solution,[154] the dissociation of the salt could be dependent on both parts of the salt and it is probable that there is a complex mechanism. It is therefore not implausible that there could be a fractional dependence on the concentration of the salt. As the polyethylenimine within the activated carbon contains a large number of primary and secondary groups a fractional order with respect to the salt formed between the

reaction of CO_2 and amine was used in an attempt to model the double curvature observed in the concentration profile.

6.2.3 ZLC – reaction model fitting experimental data

The model considering the reaction in the adsorbed phase was used to fit the experimental data. It was seen in section 6.2.1 that when the equilibration time of the sample was increased by nearly a factor of three at 75 °C that the adsorbed amount of CO_2 only increased by ~10%. As the amount of adsorbed CO_2 changes so slowly it was possible to consider the sample to be in a state close to equilibrium, i.e.

$$\frac{da_1}{dt} \sim 0$$

However, in this case, it is important to note that because the samples do not start at equilibrium, a pseudo equilibrium constant is calculated by the model.

The differential equations (6.14-6.16) were solved using Matlab and parameter values of K_1 and k_{1D} were chosen to fit the experimental data with the following initial conditions for the desorption step:

$C_f = 1$, $Q = 1$, $A_1 = 1$ and $C_{in} = 1$

The total adsorbed amount (q^*) at the start of the desorption step was equal to the sum of the adsorbed amount in the physically adsorbed (q_0) and chemically adsorbed phase ($a_{1,0}$) (equation 6.21).

$$q^* = q_0 + a_{1,0} \qquad (6.21)$$

The total adsorbed amount was calculated from the integration of the desorption curve with the majority of the capacity attributed to the chemisorbed phase ($a_{1,0}$)

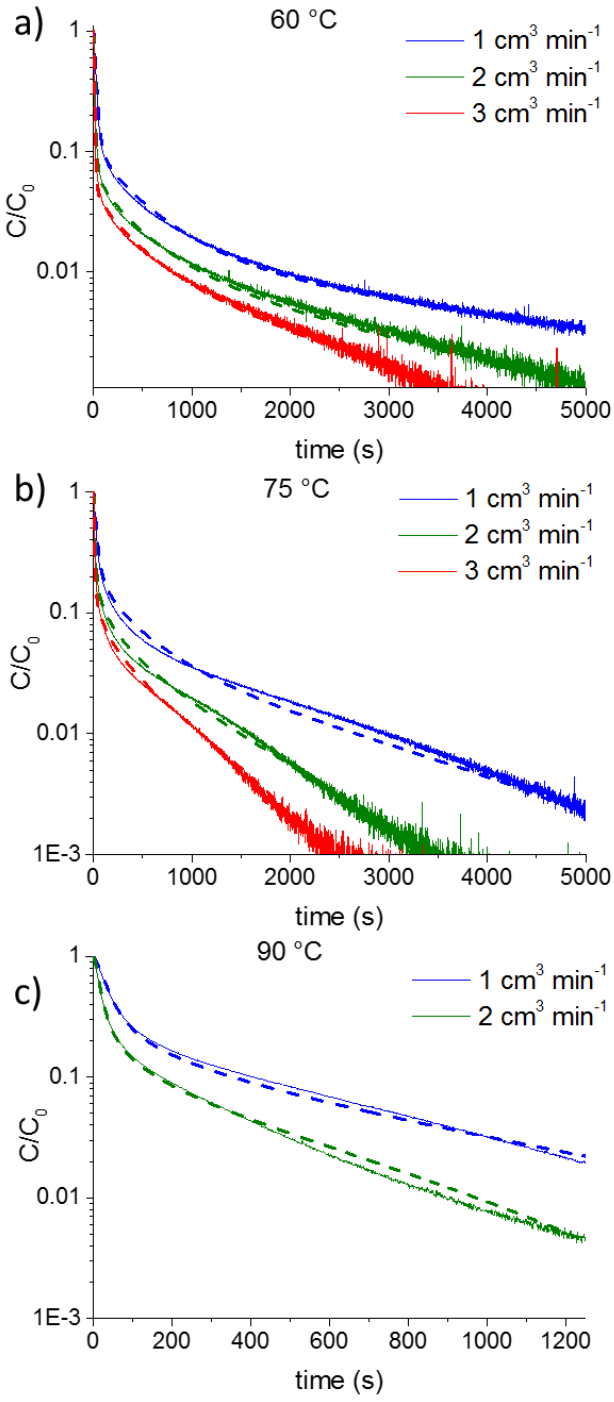

Figure 6.14: ZLC experiments meso-AC2-PEI1200(200) with model prediction (a) 60 °C k_{1D} = 0.01 s^{-1}, K_1 = 0.4, $a_{1,0}$ =1.2 mmol g^{-1}, q_0 = 0.05 mmol g^{-1}, (b) 75 °C k_{1D} = 0.03 s^{-1}, K_1 = 0.09, $a_{1,0}$ =1.85 mmol g^{-1}, q_0 = 0.05 mmol g^{-1}, (c) 90 °C k_{1D} = 0.95 s^{-1}, K_1 = 0.0425, $a_{1,0}$ =1.78 mmol g^{-1}, q_0 = 0.05 mmol g^{-1}. m=1, n=1 and p=0.75 at all temperatures. Experimental (solid line), Model (dashed)

In Figure 6.14 it can be seen that a good agreement between the experimental and model response was achieved at three different temperatures. The model predicted the double curvature at 75 °C and with the change in the equilibrium parameter (K_1) at lower temperature the double curvature was not predicted, in agreement with the experimental data. In Figure 6.14c, the 3 cm^3 min^{-1} flow rate is not shown because the experimental saturation time was significantly different resulting in a lower adsorbed amount as shown in Table 6.2. The van't Hoff relationship equation (6.22) was then applied to the fitted equilibrium parameters (K_1):

$$\ln(K_1) = -\frac{\Delta H^{\theta}}{\mathbf{R}T} + \frac{\Delta S^{\theta}}{\mathbf{R}} \qquad (6.22)$$

Where T is the temperature in Kelvin. The plot of $\ln(K_1)$ vs $1000/T$ is shown in Figure 6.15 and from the slope the heat of adsorption was calculated to be 75 kJ mol^{-1}. In Figure 6.15, the slope corresponding to a heat of adsorption of 89 kJ mol^{-1} is also shown, and it can be seen that it is not very different from the trendline that was fitted to the model parameters and lies within the error bars. The error bars were calculated by investigating the range across which the model parameter K_1 could be varied and still provide a reasonable fit of the experimental data. Given the simplicity of the model and the pseudo nature of the equilibrium, the calculated heat of adsorption was in very good agreement with the heat of adsorption of 89 kJ mol^{-1} that was measured experimentally by thermal gravimetric analysis in section 5.2.3.

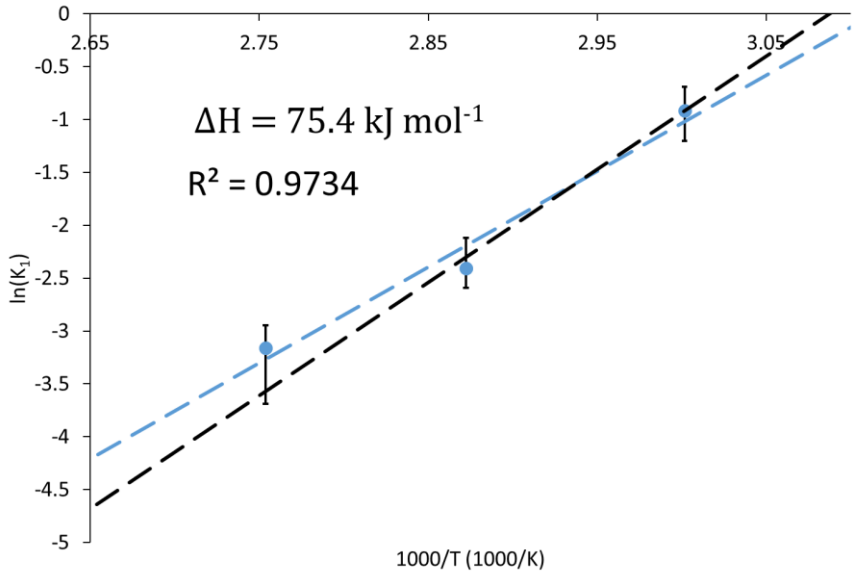

Figure 6.15: Van't Hoff plot of fitted parameters for meso-AC2-PEI1200(200), slope yields heat of adsorption. Trendline of fitted equilibrium parameters (Blue dashed). Black dashed line has a slope corresponding to a heat of adsorption of 89 kJ mol^{-1}. Error bars calculated from range of K_1 which provided a reasonable fit of experimental data.

The change in the total adsorbed phase concentration (q^*) with respect to time was predicted by the model for both the adsorption and desorption step (Figure 6.16). It was clearly seen that the model predicted much faster adsorption of CO_2 than desorption.

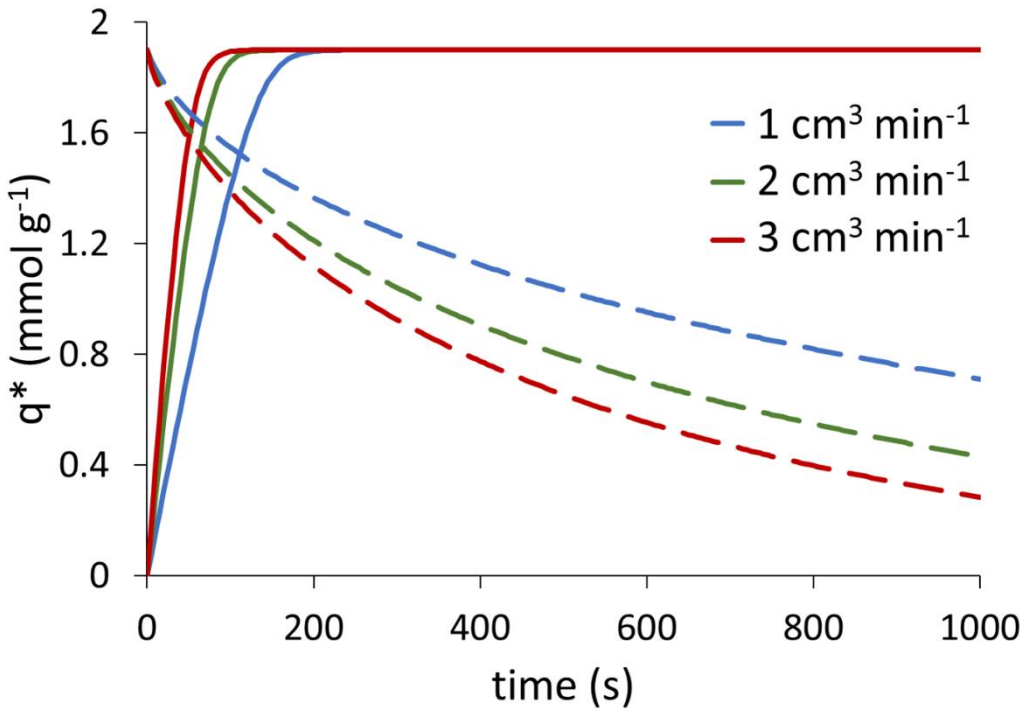

Figure 6.16: Model prediction of the total adsorbed phase concentration (q^*) with respect to time for fitted parameters at 75 °C. Adsorption – solid line, Desorption – (dashed line)

In addition the model was used to predict the gas phase concentration profile during the adsorption step (Figure 6.17). The time zero of the adsorption step was the valve switching time minus the number of seconds required for the CO_2 to breakthrough in the system blank response. In Figure 6.17, it was seen that the experimental CO_2 concentration profile remains at zero for a period of time at all flow rates. This, along with the model prediction of the adsorbed phase concentration in Figure 6.17, suggests that the adsorption kinetics are fast and the ZLC is behaving like an E-ZLC during the adsorption step. As a result, the simulated concentration profile assuming a well-mixed column shown in Figure 6.17 is not in very good agreement with the experimental data. However, it was seen that the rate of adsorption was significantly faster than desorption. This was in agreement with the temperature profile measured in the E-ZLC (Figure 6.7) where the spike in the column temperature was higher during the adsorption step than the desorption. The larger spike in temperature is indicative of a faster adsorption process as the change in temperature within the column is the product of both the rate of adsorption and the heat of adsorption (equation 6.1).

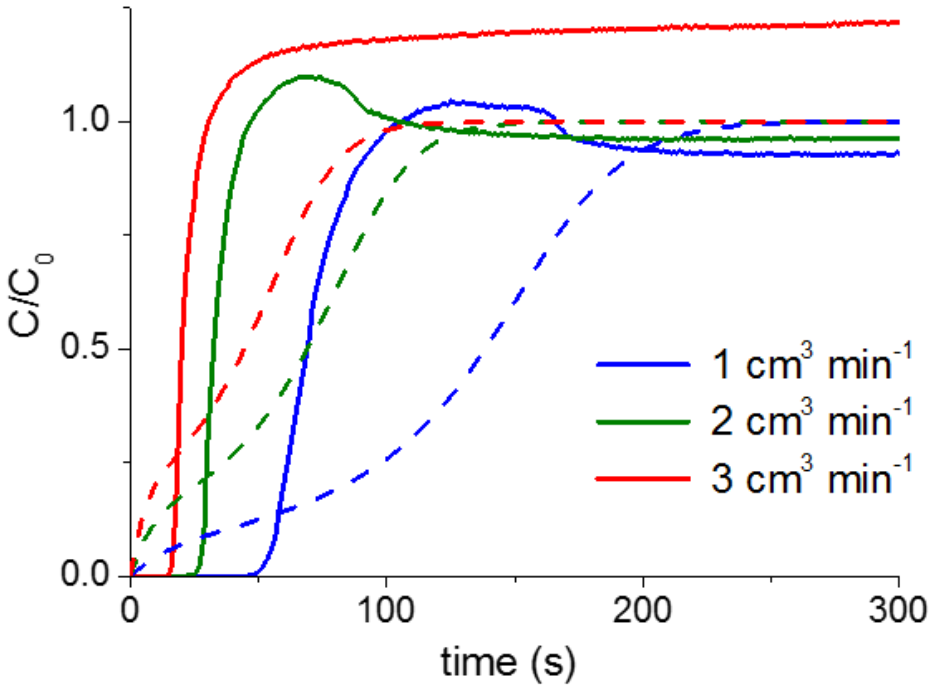

Figure 6.17: Adsorption step 75 °C, meso-AC2-PEI1200(200), experimental (solid line) , simulation (dashed line)

An additional reason for the poor correlation between the experimental concentration profile and the simulation in Figure 6.17 is because the mass spectrometer has a tendency to overshoot when measuring the gas phase composition in the adsorption step. This is possibly due to issues with the electronics of the sensor and when this occurs it was challenging to calculate the adsorbed amount from the adsorption step.

The agreement between the model and the desorption step and the fact that it qualitatively predicts correctly the much faster adsorption kinetics which result in a non-isothermal system (in adsorption) that behaves like an E-ZLC system, points to the fact that future work should be aimed at implementing the kinetic model in Cysim in order to be able to simulate both adsorption and desorption steps.

As polyethylenimine has three different types of amine groups, it is probable that several different reaction mechanisms are occurring. To fully establish the reaction mechanism may prove very challenging with numerous factors contributing to the overall rate. Fitting additional reaction pathways to this model with additional parameters would improve the quality of the fit but would probably not provide any further insight into the reaction mechanism. However, it can be concluded that the desorption of the CO_2 from the adsorbent is not governed by a first order kinetic process which is often assumed in the literature.[157-159]

6.3 Conclusions

In this chapter, the E-ZLC was introduced and fully characterized with respect to its heat transfer properties. It was seen that the E-ZLC operates at close to isothermal conditions throughout the experiment. The temperature profile, of the system was accurately modelled with Cysim. The isothermal nature of the system greatly simplifies the analysis of the breakthrough curves. The work was then advanced to investigate the reaction kinetics, using the ZLC technique, between CO_2 and amine in the adsorbed phase.

A theoretical model has been developed to consider the reaction of amine and CO_2 in the adsorbed phase. The mechanism is highly complex and the ZLC experiment enables the system to be studied at very low CO_2 partial pressures. At low CO_2 partial pressures a double curvature was observed in the gas phase concentration profile in the long time region which could not be explained by a first order kinetic process. This model can accurately simulate the desorption curve of a ZLC experiment where a reaction occurs in the adsorbed phase. The exact form of the rate equation cannot be determined by this technique alone, however, a feasible model has been proposed to accurately reproduce the experimental data. In this case a fractional order kinetic rate equation was required to simulate the experimental data and obtain the characteristic double curvature. Parameters are obtained for the reaction in the adsorbed phase which could be used to model CO_2 desorption in a carbon capture process.

The simple model proposed could be applied to other cases where chemical reactions occur on the surface of the adsorbent. The model could be used in future studies to determine rates of reaction along with mechanistic information about a process. In particular, if a product is formed (i.e. catalysis) and desorbed through the course of the reaction its concentration at the outlet could be monitored with the mass spectrometer.

Future work would include further experiments to fully validate the model on a number of different samples and extract further kinetic information about the process. As the

process is slow and doesn't reach a true equilibrium state within the time frame of the experiment, the model should be adapted so that it accurately predicts the desorption curves at short saturation times (e.g the partial loading experiment[102]). In addition, the model should be implemented in Cysim in order that the E-ZLC breakthrough curves can be simulated to further validate the parameters.

7 Biogas upgrading by 13X and functionalized activated carbon

With the world's ever increasing requirement for green clean energy, there is great potential to reduce carbon emissions through the optimization of current energy generation methods. One such green technology is the production of biogas through the fermentation of plant material, or waste, to produce a mixture of predominantly CO_2 and methane. Depending on the process used during production along with the type of fermented material, the composition of the produced gas can vary significantly. However, it is clear that from an anaerobic digester a significant portion of the produced gas is CO_2. In order to enhance the gas stream an adsorption process can be used to purify the individual components.[160] Purification of the gas mixtures to produce two high purity gas streams has the added benefit of producing a higher value product of close to pure methane along with a CO_2 stream that could potentially be sequestered, preventing the release of the CO_2 into the atmosphere and hence reducing the environmental impact of the process. This process is referred to as biogas upgrading and as a result of its green power generation credentials, the optimisation of the upgrading process has recently begun to attract interest as an area of research[160-162]. An integrated biomass carbon capture plant would result in a net decrease in the amount of CO_2 in the atmosphere.[163] The feedstock for the biomass plant first removes CO_2 from the atmosphere via photosynthesis and then through the subsequent treatment of the biogas the CO_2 is captured and stored prior to combustion of the methane. This results in a subsequent net removal of CO_2 from the atmosphere. In addition the CO_2 released during the combustion of the methane could be separated and stored, further enhancing the environmental credentials of a biogas upgrading process.

The optimum technology for biogas upgrading is highly dependent on the specific biogas process/plant. The biogas feedstock, the scale of the plant, and the acceptable concentration of impurities in the product streams are all important factors in selecting an upgrading technology. As of 2013 there were more than 220 commercial biogas

upgrading plants that used a variety of different technologies.[164] The main commercial technologies, up until 2008, were water scrubbing and pressure swing adsorption.[165, 166] However, in addition, other technologies have been investigated and in certain cases implemented. They include, cryogenic separation, chemical absorption, physical absorption and membrane separation[167, 168]. A review comparing the cost and investigating the appropriate utilisation of these and other technologies was carried out by Sun et al[169]. From this review it is clear that further work is required to establish the potential of the different techniques if the upgrading of biogas is going to become a more widespread large scale technology. There are also several recent reports that propose novel optimised systems to lower the cost of the separation. In 2015 Kim et al.[166] proposed a four column pressure swing adsorption process using a carbon molecular sieve as an adsorbent, that only had a selectivity for CO_2 over methane of 1.9. Grande et al. proposed a novel layered pressure swing adsorption system where a kinetic adsorbent such as a carbon molecular sieve was layered with an equilibrium adsorbent[170]. This set-up improved the productivity of the set-up and resulted in a potential size reduction of the separation unit by up to 60%.The selection of a novel adsorbent could significantly enhance the efficiency of an adsorption separation process.

However, there are few reports in the literature regarding the development of an optimum adsorbent material for biogas upgrading. The main materials used in PSA separation are zeolites and activated carbons. Alonso-Vicario et al. compared commercial zeolites 13X, 5A and natural clinoptilolite via breakthrough experiment and concluded that despite its lower CO_2 capacity the natural zeolite clinoptilolite was preferential as it was able to separate the CO_2 along with H_2S, that was present in their biogas stream, simultaneously from the methane.[171] Various activated carbons have been investigated for the separation of CO_2/CH_4 with a typical selectivity of around 2-4 depending on the material and the process conditions.[172, 173] Triamine grafted pore expanded silica was investigated as an adsorbent by Belmabkhout et al. who proposed that it had great potential to separate the acidic gases from methane with a high selectivity.[174] The design and selection of a suitable adsorbent could result in significant cost savings in the upgrading of biogas.

As has been discussed in previous chapters a large number of adsorbents have been proposed and developed to separate CO_2 from nitrogen for carbon capture and storage from fossil fuel powered power plants. It stands to reason that many of these materials may find useful application in a biogas upgrading process. The separation of CO_2/N_2 is fundamentally similar to CO_2/CH_4 and materials with the same properties and characteristics are required. In the case of biomass the partial pressure of CO_2 in the gas stream (~45 %) is significantly higher than the partial pressure typically found in the flue gas of a power station (4-20 %). The higher concentration of CO_2 increases the amount of CO_2 a physisorbent will selectively adsorb, with the net result being a decrease in the cost of the separation.

In this chapter the selectivity for CO_2 over methane of three different adsorbents was investigated. The three materials are commercial zeolite (13X), commercial microporous activated carbon (micro-AC) and an amine-impregnated activated carbon (meso-AC2-PEI). Despite a number of studies investigating amine-impregnated activated carbons for carbon capture and storage, to the author's knowledge there have been no reports to date investigating their potential for upgrading biogas. The three materials allow a direct comparison of the various advantages and disadvantages of using physical adsorption (13X, micro-AC) or chemical adsorption (meso-AC2-PEI) to separate the methane and the carbon dioxide.

7.1 Experimental – E-ZLC breakthrough experiments

Three E-ZLC were packed, one with commercial zeolite 13X (63.8 mg), the second with Calgon® microporous activated carbon (37.9 mg) and the other with a mesoporous activated carbon impregnated with PEI (MW 1200) (25.2 mg). The ratio of PEI to carbon support was two parts polymer to 1 part carbon. Due to the difference in density of the respective adsorbents the different mass of adsorbent packed in the column in each case should be noted.

Breakthrough experiments were run on the adsorbents; 13 X and micro-AC were run at 35°C and meso-AC2-PEI1200 was run at 75 °C. The impregnated material was run at 75 °C, because, as shown in chapter 5, in order to achieve a significant uptake of CO_2 within the time frame of the experiment the column must be run at elevated temperature. The physisorbents have higher capacity at a lower working temperature, this is an example that emphasizes the importance of process design and conditions being developed in parallel with the adsorbent. The composition of the feed gas was 45% CO_2 and 55% methane, nitrogen was used as a purge. The breakthrough experiments were conducted at multiple flow rates. The experimental breakthrough curves were then accurately modelled using Cysim and from the adsorbed phase concentration of each component at the start of the desorption step the binary selectivity for each adsorbent was calculated.

7.2 Results – 13 X, micro-AC and meso-AC-PEI1200 biogas breakthrough response

The adsorption breakthrough profiles of 13X, micro-AC and meso-AC-PEI1200 are shown in Figure 7.1 where the step change in concentration was from a pure N_2 purge to a mixture of 45% CO_2 and 55% methane.

The breakthrough experiments for biogas on 13X in Figure 7.1a show a clear separation of the CO_2 and methane. At a flow rate of 7.5 $cm^3\,min^{-1}$ the breakthrough times (with the breakthrough time of the blank response, 14 s, subtracted) are approximately 9 s and 84 s for methane and CO_2 respectively. The roll up of the methane was clearly observed, this is due to all the CO_2 being adsorbed by the 13X, therefore the concentration of the gas at the outlet prior to the breakthrough of CO_2 is that of pure methane. As the adsorption bed becomes saturated with CO_2, the CO_2 breaks through and the concentration of the methane returns to that of the feed concentration (C/C_0=1). The magnitude of the roll up was larger than expected and the signal from the mass spectrometer was not stable. The mass spectrometer over responded to the large step change in the gas phase concentration of methane as it broke through.

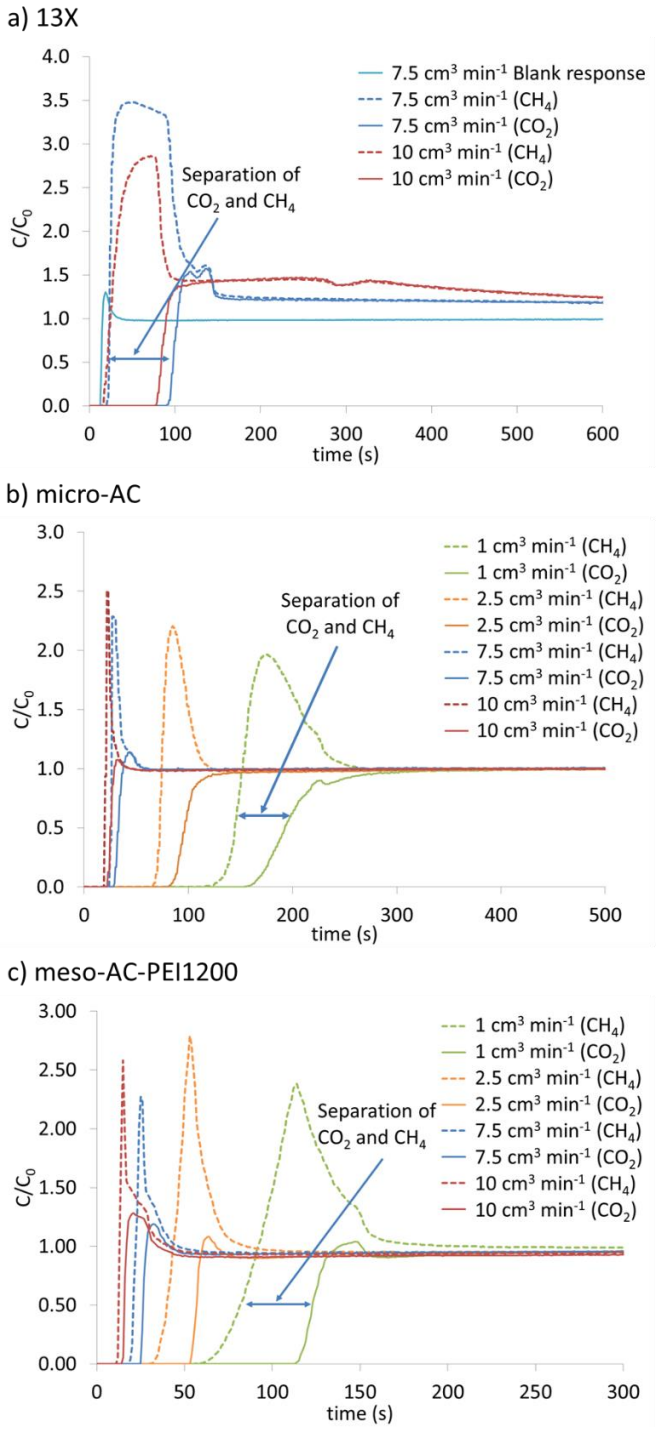

Figure 7.1: E-ZLC concentration profile during the adsorption step vs time (a) 13X, 35 °C, 63.8 mg (b) micro-AC, 35 °C, 37.9 mg (c) meso-AC2-PEI1200, 75 °C, 25.2 mg. Multiple flow rates, dashed line methane and solid line CO_2 concentration profile.

It can clearly be seen in Figure 7.1b,c that CO_2 and methane breakthrough at different moments for both micro-AC and meso-AC-PEI1200 and the materials can therefore be used to separate CO_2/CH_4. Therefore to compare the materials a more detailed analysis of the breakthrough curves was required. It would be appropriate to assess the selectivity of CO_2 over methane from the adsorption branch of the breakthrough experiment, however due to inconsistencies in the stability of the mass spectrometer signal during the adsorption experiments it was challenging to assess the true selectivity. In Figure 7.2 the desorption of CO_2 and methane from the saturated bed was evaluated at several different flow rates of a pure nitrogen purge. The signal from the mass spectrometer was smooth and the binary selectivity was evaluated for each material by fitting the experimental data with the adsorption simulator Cysim.

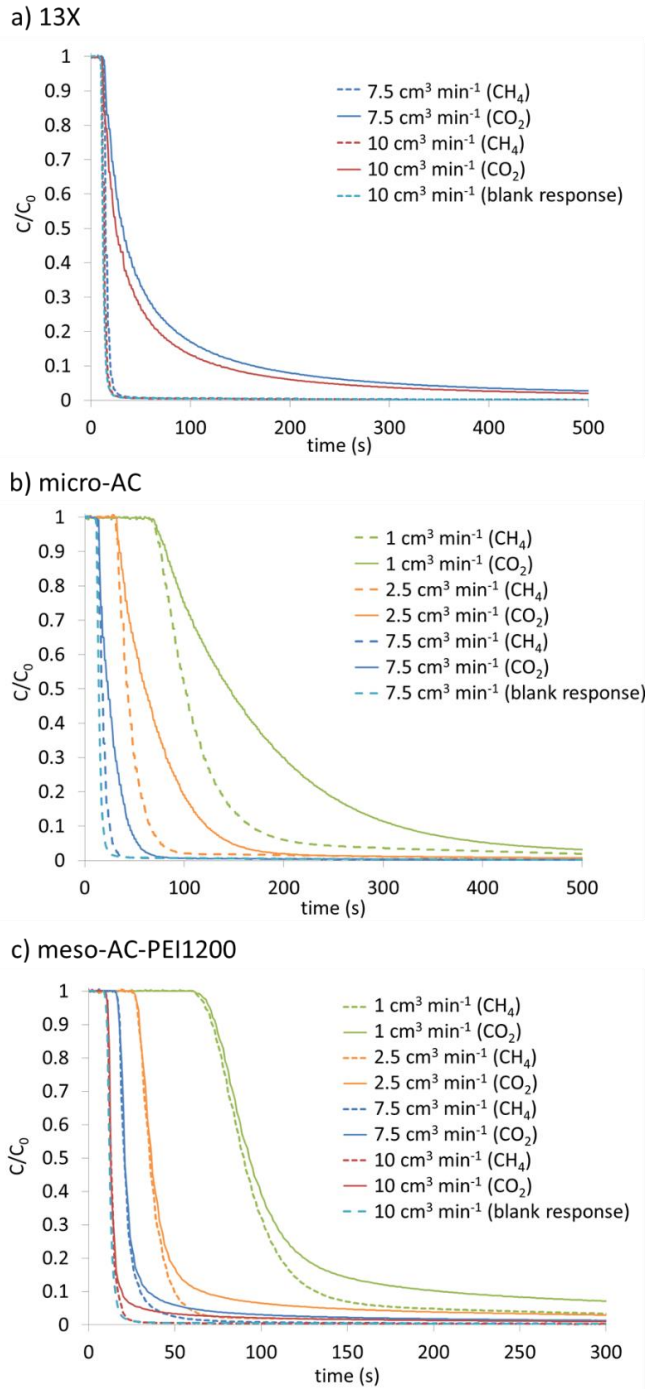

Figure 7.2: E-ZLC concentration profile during the desorption step vs time (a) 13X, 35 °C, 63.8 mg (b) micro-AC, 35 °C, 37.9 mg (c) meso-AC2-PEI1200, 75 °C, 25.2 mg. Multiple flow rates, dashed line methane and solid line CO_2 concentration profile. Adsorption: 45 % CO_2 55 % CH_4 Desorption 100% N_2

In Figure 7.2, it can be seen from the shape of the breakthrough profile that the desorption of the CO_2 from the impregnated meso-AC occurs at significantly lower pressure and at slower rate that the physisorbents micro-AC and 13X. In order to reduce the cycle time and rapidly desorb the CO_2 it is probable that the meso-AC-PEI1200 material would have to be integrated into a thermal swing adsorption process.

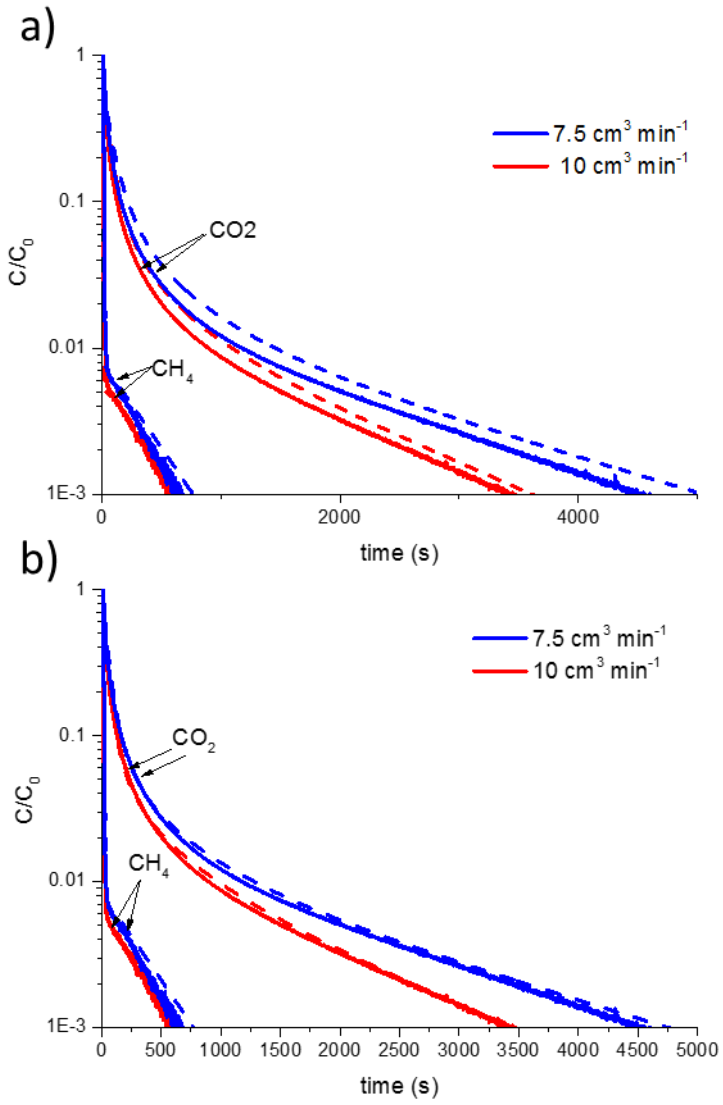

Figure 7.3: 13X breakthrough curves (desorption) plotted vs time on a semi-log plot with model predictions a) original isotherm parameters in agreement with volumetric system b) modified isotherm parameters to account for adsorbed H_2O. Experimental data solid line, simulation dashed line

As there was a large step change in the concentration of the gas phase the flow rate passing the detector was not constant and varies with time. Several methods have been suggested to correct the flow rate but are generally only valid for small step changes.[106] Therefore, the system was simulated using Cysim an in house developed process simulator, which corrects the flow rate and ensures that the mass balance closes.[110]

In Figure 7.3 the desorption curves for 13X can be seen along with the model prediction on a semi-log plot vs time. In the first case the isotherm parameters for 13 X were the same as previously used to fit the breakthrough experiments at 10% and 1% CO_2 in section 6.1.1. In addition the volumetric isotherms for 13X can be found in Figure 6.5. The model over-predicted the amount of CO_2 adsorbed on the solid, this was attributed to incomplete regeneration of the sample. This hypothesis was validated by regeneration of the sample after the measurements and a clear peak was seen in the signal for water (*m*/*z* 18) as shown in the appendix in Figure - A.4. The isotherm parameters were adjusted in order that the model fitted the experimental desorption data. It was interesting to note that even with a small volume of adsorbed water, 13X still selectively separated CO_2 and methane albeit with a lower total uptake of CO_2. A thermocouple was inserted into the column and sealed with epoxy resin as previously detailed. The limitations of the epoxy resin in terms of thermal stability prevented complete regeneration of the 13X. The development of a breakthrough column with integrated thermocouples to enable high temperature regeneration is under way and a picture of the first iteration of the design is shown in the appendix in Figure - A.5.

The parameters used to predict the experimental breakthrough response of all three sample are reported in Table 7.1. A dual site Langmuir isotherm was used to fit the 13X with the same saturation capacity (q_s) used for each gas, on each site, to ensure thermodynamic consistency. A single site Langmuir expression was used to fit the micro-AC and meso-AC2-PEI1200 samples. The experimental volumetric isotherms for CO_2 and N_2 on micro-AC, along with the Langmuir isotherm fits that were used in the simulations, can be seen in Figure 7.4. Volumetric isotherms could not be measured for meso-AC2-PEI1200(200) due to the amine potentially damaging the

system. The parameters were therefore solely established by fitting the breakthrough curves.

Table 7.1: Isotherm parameters used in Cysim simulations *modified isotherm parameters to account for adsorbed water on 13X

		qs_1 (mmol g^{-1})	qs_2 (mmol g^{-1})	$b_{1,0}$ (bar^{-1})	$b_{2,0}$ (bar^{-1})	ΔH_1 (J mol^{-1})	ΔH_2 (J mol^{-1})
13X (dry)	CO_2	1.44	3.47	3.59e-5	8.27e-7	40014	40484
	N_2	1.44	3.47	2.89e-7	2.89e-7	30670	30670
	CH_4	1.44	3.47	0.005	0.005	10000	10000
13X (modified)*	CO_2	1.44	3.47	3.59e-5	4.27e-7	40014	40484
	N_2	1.44	3.47	2.89e-7	2.89e-7	30670	30670
	CH_4	1.44	3.47	0.005	0.005	10000	10000
micro-AC	CO_2	4.7		2.12e-5		27000	
	N_2	4.7		5.07e-6		23964	
	CH_4	4.7		3.5e-4		17000	
Meso-AC2-PEI1200(200)	CO_2	1.74		3e-11		88000	
	N_2						
	CH_4	1.74		0.01		1450	

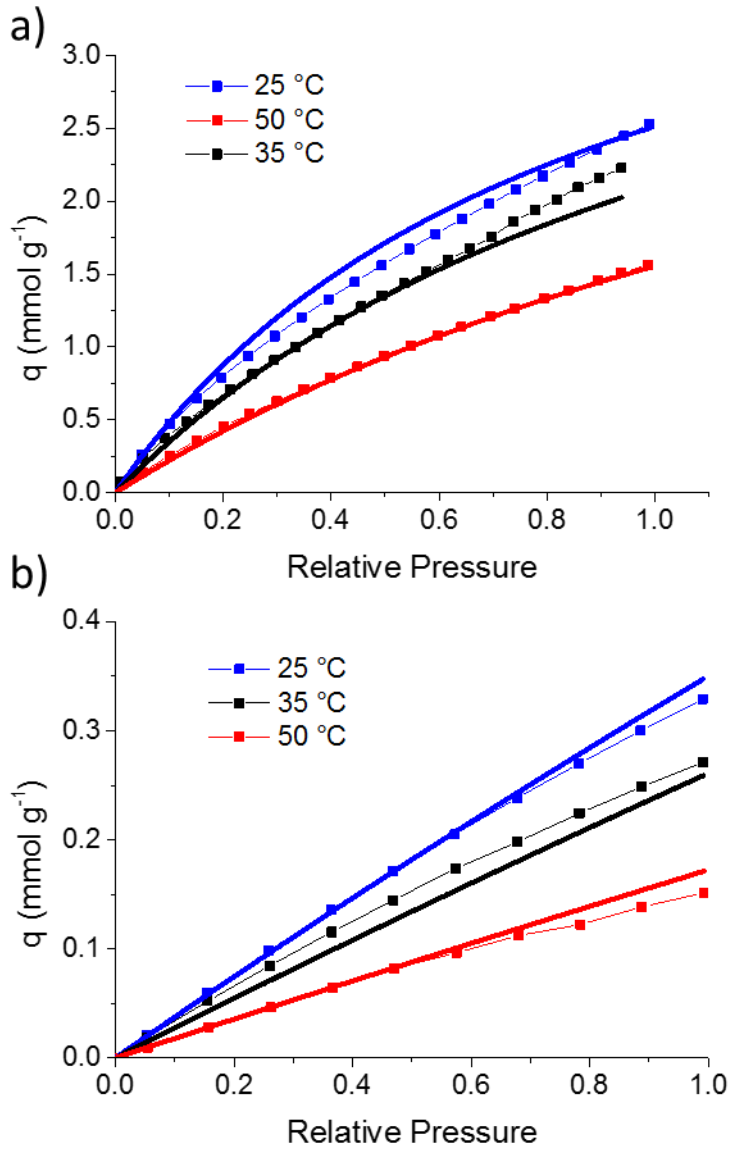

Figure 7.4: Micro-AC volumetric isotherms measured on iQ1 at multiple temperatures, 25 °C 35 °C and 50 °C along with Langmuir fitting (solid) line. Langmuir parameters in Table 7.1. a) CO_2 b) N_2

The experimental breakthrough desorption curves, along with the simulation from Cysim for each sample at two different flow rates are presented in Figure 7.5. The measurements were carried out at 35 °C for micro-AC and 13X and 75 °C for meso-AC-PEI1200(200) with N_2 as a purge gas. A clear separation of the components was observed with each sample adsorbing a significantly larger quantity of CO_2 than methane.

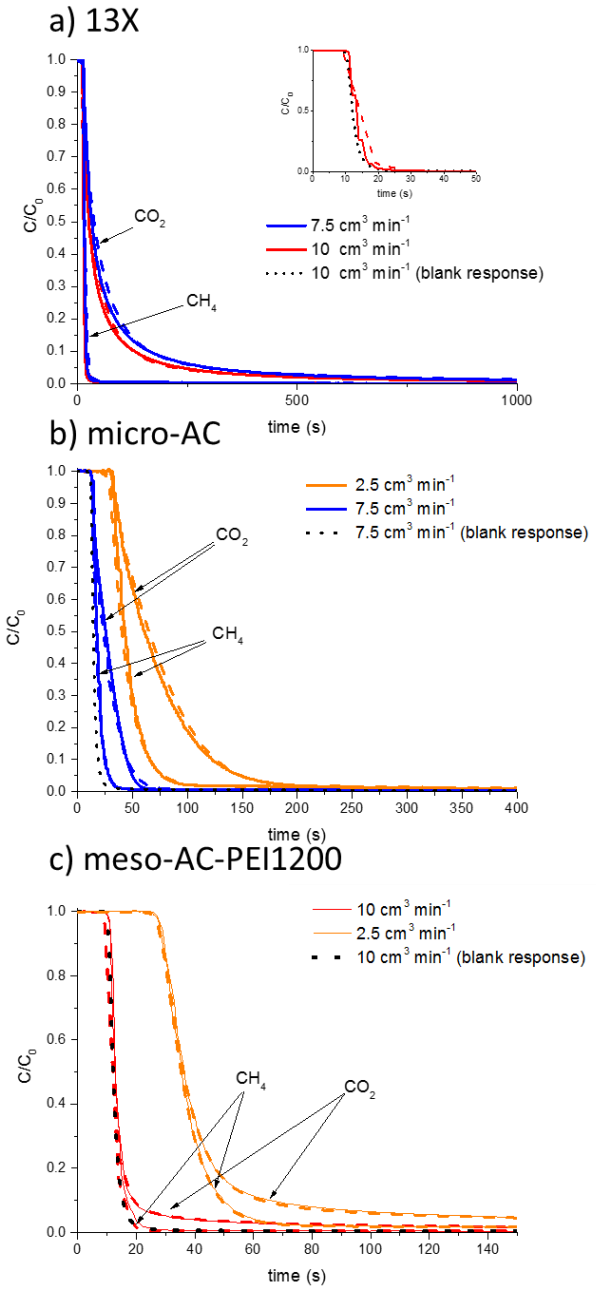

Figure 7.5: Breakthrough desorption curves at selected flow rates with Cysim simulations (a) 13X, 35 °C, 63.8 mg (b) micro-AC, 35 °C, 37.9 mg (c) meso-AC2-PEI1200, 75 °C, 25.2 mg. dashed line simulation and solid line experimental concentration profile. Adsorption: 45 % CO_2 55 % CH_4 Desorption 100% N_2. Black dots blank response at specified flow rate

In the case of amine-impregnated meso-AC and the 13X virtually no methane is adsorbed by the adsorbent. In the inset in Figure 7.5a and the main body of Figure 7.5c the concentration profile of the methane from the adsorption bed practically overlaps with the systems blank run response. The total uptake of CO_2 was less for the impregnated carbon sample than for 13X, however as was seen in previous experiments, the presence of water does not significantly hinder the uptake of CO_2 by amine-impregnated samples. This is advantageous as biogas often has a high water content.[175] The meso-AC-PEI1200 adsorbs more CO_2 per unit mass than the micro-AC. Of particular interest are the relative shapes of the adsorption profiles. The shape of the desorption curves are significantly different when physisorbents (13X and micro-AC) are compared to meso-AC-PEI. CO_2 is strongly bound to the amine, as demonstrated by the high heat of adsorption of approximately 90 kJ mol^{-1}. The CO_2 is therefore very favorably adsorbed, compared to the methane, and the majority of the CO_2 starts to desorb from the sample at a lower CO_2 partial pressure (low C/C_0) than is the case for 13X and micro-AC. The strong chemisorption between the amine and the CO_2 makes the adsorbent highly selective to CO_2 at low partial pressures. The relative adsorbed amounts of each component were extracted from the simulations and tabulated in Table 7.2 which enabled the selectivity of each material to be quantified.

Table 7.2: Selectivity of CO_2 over Methane from biogas gas stream for adsorbents *modified isotherm parameters to account for adsorbed water

	13X (dry)	13X* (modified)	Micro-AC	Meso-AC(2)-PEI1200-200
q_{CO_2}(mmol g^{-1})	3.79	3.25	1.07	1.73
q_{CH_4} (mmol g^{-1})	0.13	0.19	0.45	0.00
Selectivity	36	21	2.90	→∞

The selectivity of the two adsorbents with respect to CO_2 was calculated by following equation:

$$S_{ADS} = \frac{q_{CO_2}/q_{CH_4}}{\mathrm{P_{CO_2}}/\mathrm{P_{CH_4}}} \quad (7.1)$$

where $\mathrm{P_{CO_2}}$ is 0.45 and P_{CH_4} is 0.55.

As expected the selectivity of 13X is significantly higher than micro-AC due to the strong interactions between the CO_2 quadrupole and the zeolite surface. Under equilibrium conditions very little CH_4 was adsorbed by 13X. A very accurate fitting of the system blank and the sample data is required to extract the exact amount of methane that is adsorbed on 13X. The blank response of the system was fitted with Cysim prior to the sample fitting. The blank response curves at each flow rate along with their associated fit can be found in the appendix, Figure - A.3. A selectivity of 21 was calculated but the value of methane adsorbed was small, as a result a small error in the calculated adsorbed amount of methane can have a large impact on the calculated selectivity. The same can be said for the meso-AC-PEI1200 material where the methane concentration profile was so close to the system response that it wasn't possible to accurately extract the adsorbed amount. As a result the selectivity tended towards infinity. Both 13X and meso-AC-PEI1200 can be regarded as highly selective to CO_2 over methane. Silva et al. reported the experimental selectivity of 13X to range from 37 at low pressure (0.67 atm) and low temperature (313 K) to 5 at high temperature (423 K) in good agreement with the experimental selectivity of 21 calculated in this work.[176] Comparing the impregnated meso-AC to the raw micro-AC it can be seen that the functionalization enhanced the selectivity. The selectivity of the micro-AC is limited as unlike 13X and meso-AC-PEI1200 the material adsorbs a significant amount of methane as well as CO_2. Gil et al.[172] reported a selectivity factor of 3.2 for CO_2 over methane on a comparable microporous activated carbon which is in good agreement with the calculated selectivity of 2.9 for micro-AC. Raw activated carbons may have a disadvantage over zeolites in terms of selectivity, however, activated carbons are relatively cheap and stable over many cycles. The selectivity of

activated carbon was increased through the modification of the adsorbent with the polyamine. The basic amine groups preferentially chemisorbed a large fraction of CO_2 and, in addition, loading the pores with amine through a wet impregnation method has the added benefit of filling the pore volume of the activated carbon, greatly reducing the number of sites available for physical adsorption of methane. To facilitate the chemisorption and increase the reaction kinetics the process must be carried out at elevated temperature, again this greatly reduces the volume of adsorbed methane, further enhancing the selectivity of the modified activated carbon.

The temperature profile along the adsorption column was simulated and compared to the experimentally measured temperature 80 % of the way along the column (Figure 7.6). The simulated temperature was a close match to the experiment. The simulation predicted two temperature peaks, one associated with the breakthrough of methane and the other with the breakthrough of CO_2. Due to the low heat of adsorption of methane the associated temperature rise was predicted to be low and the experimental response was very close to the noise level. A very small peak was seen experimentally after 88 seconds, in good agreement with the simulation.

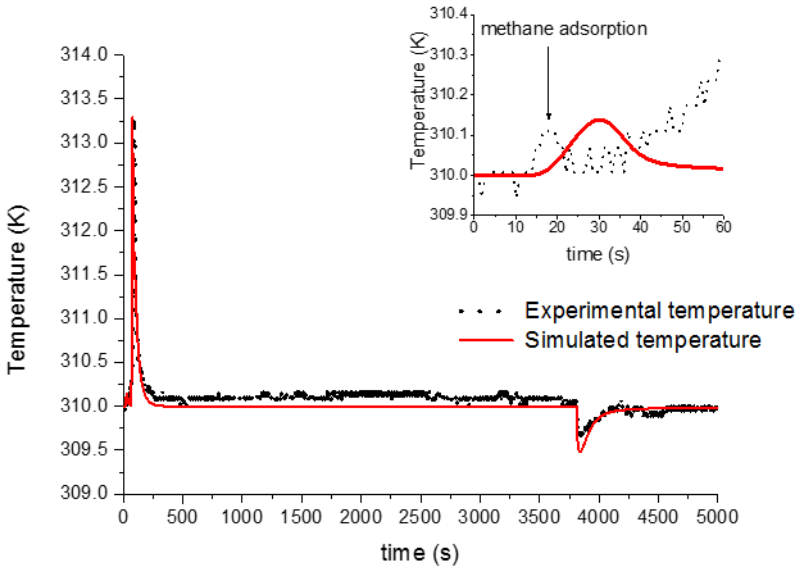

Figure 7.6: Temperature profile in 13X breakthrough column. Temperature measured by thermocouple inserted 80% along column and simulated by Cysim. Experiment at 7.5 cm^3 min^{-1}. Inset shows temperature spike as a result of methane adsorption.

For meso-AC-PEI1200 a very small experimental spike in the temperature was recorded despite the high heat of adsorption of CO_2 by amines. It would appear that the recorded experimental temperature profile is highly dependent on the packing of the adsorbent around the thermocouple and the small column rapidly dissipates any heat generated.

7.3 Conclusions

13X, micro-AC and meso-ACPEI1200 could be used to separate CO_2 from methane in a biogas upgrading adsorption process. Both meso-AC-PEI1200 and 13X have high selectivity adsorbing only small amounts of methane. Depending on the type of process, the biogas feedstock and the purity requirements of the product streams, all three adsorbents could be utilized to upgrade biogas.

Commercial zeolite 13X has a strong selectivity of up to 36 however in the presence of water the total uptake of CO_2 is reduced. It is therefore desirable to have dry feed gas. In contrast, water has been shown to have a negligible effect on the uptake of CO_2 by amine impregnated carbons and water can prevent the formation of urea.[60] This is an advantage as there would be no need to pre-dry the biogas prior to upgrading as from many feedstocks water is a significant component of the biogas. The operation temperature for the amine material is higher and the material has potential to be integrated into a temperature swing adsorption process. The material could be regenerated with excess heat from the biogas plant or through direct joule heating. However, due to the high input partial pressure of CO_2 it may prove that, for an efficient separation, the strong amine-CO_2 adsorption sites are not required. The high regeneration costs of a separation process may outweigh the advantage of the high selectivity of amine impregnated carbon. Process simulations would be required to fully assess the viability of the material.

As a larger number of biogas plants are introduced to the energy mix, novel materials will be required to upgrade the fuel to the required purities in the most economical manner possible. It is likely that one technology will not be satisfactory at every biogas site and the optimum technology will be dependent on the biogas feedstock and the local operating conditions. When combined with carbon capture and storage or CO_2 utilization, biogas upgrading has the potential to have a negative carbon dioxide output.

8 Carbon nanotube aerogels as amine supports

It was seen in Chapter 5 that with the incorporation of a higher weight percentage of amine that the CO_2 capacity of the materials increased. Carbon materials with mesopores acted as a more efficient support for amine-impregnation than materials with a predominately microporous structure. It was therefore logical to extend the study to investigate highly porous materials with a large total pore volume and a predominantly macroporous structure.

Sol-gel chemistry can produce cross linked organic gels which after drying and a thermal treatment produce carbon materials with hierarchical pore structures.[177, 178] Resorcinol and formaldehyde are commonly used precursors in the synthesis of carbon aerogels.[177] Building on this synthetic approach recent studies have reported the development of highly porous composite aerogels which incorporate CNTs or graphene into the structure.[179-182] Advantages of including CNTs/graphene can include enhanced electrical properties and a structure with greater mechanical stability.[179] Typically, CNTs or graphene/graphene oxide are dispersed in a solvent with a polymer, the mixture gelates and the solvent is removed supercritically or via a freeze drying process. This leaves a highly porous structure of CNTs/graphene that is reinforced with the polymer phase. Materials have been reported that are capable of supporting 8000 times their own weight.[180] It has been shown that MWCNT aerogels can be compressed down to 5% of their volume with rapid and complete recovery of the their original volume over numerous cycles.[183] A wide range of applications have been proposed for the carbon aerogels including gas sensing[183], catalyst supports[184] and energy storage[185, 186].

In addition, the aerogels have exhibited a strong adsorption capacity for organics, resulting in potential applications removing environmental contaminants, i.e. oil spill clean-up.[187-189] Carbon nanofiber aerogels have been reported to be capable of adsorbing a quantity of organics in the range of 51 to 139 times their own weight.[188] This implies that the porous aerogels have the potential to act as a support for a

significant quantity of amine and hence act as a selective adsorbent of carbon dioxide from a dilute gas stream.

In this chapter, a series of composite MWCNT and polyvinyl alcohol (PVA) aerogels are synthesized and their 3D structural and mechanical properties are investigated. The work presented on these materials, is still in its infancy, however the most promising candidate was impregnated with PEI at ~80 wt. % and its CO_2 adsorption properties were investigated.

8.1 Experimental – MWCNT/PVA aerogel synthesis

The procedure to prepare the aerogels was a modified version of the method reported by Bryning et al.[180] In this work, a surfactant was not used to disperse the CNTs and the PVA was crosslinked to further strengthen the aerogel. The typical procedure that was followed is detailed below.

MWCNTs were first oxidized, to remove any impurities from the surface, following the procedure detailed in section 4.1. The oxidized MWCNTs were then dispersed in water using tip sonication at a ratio of ~ 1 mg of tubes per 1 cm^3 of water. The oxygen functionalities on the surface facilitated the dispersion of the tubes. The dispersed MWCNTs were then combined with an aqueous solution of PVA (35 mg cm^{-3}). The specific volume of each solution was chosen to achieve the desired tubes to PVA mass ratio. Water was evaporated from the solutions until the materials were dispersed in the desired volume of water, then a crosslinking agent, glutaraldehyde (10-30 µl, 25 % aq. soln.) and HCl (20-60 µl, 2.5% aq. soln.) was added. The mixture was then frozen at –20 °C in a beaker with a diameter of ~20 mm and freeze-dried at a reduced pressure of 0.1 mbar for 3-5 days. The sample was then isolated and characterized. Aerogels were prepared with different MWCNT:PVA mass ratios (1:1, 1:2 and 1:3) in order to investigate the effect of the carbon nanotubes on the structural properties of the material. In addition, dispersions were prepared in three different volumes of water (2, 3 and 5 cm^3), prior to lyophilization, in order to prepare aerogel structures with different total volumes, which contain the same total mass of material.

8.2 Structural and mechanical properties of MWCNT/PVA aerogels

Table 8.1 details the various MWCNT:PVA ratios, volumes and masses of the aerogels that have been synthesized. Nine different aerogels were synthesized so that correlations in the material properties with respect to MWCNT content and relative volume could be established. The aerogels with a 1:1, 1:2 and 1:3 ratio of MWCNT:PVA have a dry mass of approximately 40, 60 and 80 mg respectively. During the synthesis the mass of MWCNTs was kept approximately constant at 20 mg whilst the taken quantity of PVA was varied in order to synthesize aerogels with the desired ratio.

Table 8.1: Summary of the key properties of the synthesised aerogels

Ratio MWCNT:PVA	Volume of water prior to freeze drying (cm^3)	Volume of aerogel, V_{aero}* (cm^3)	Mass, M (mg)	Density, $\frac{M}{V_{aero}}$ (mg cm^{-3})
1:1	2	1.7	41	24
	3	2.2	42	19
	5	3.0	42	14
1:2	2	1.3	61	47
	3	1.8	61	34
	5	2.7	62	23
1:3	2	1.1	82	75
	3	1.1	81	74
	5	2.7	81	30

*Calculated from measurement of height and diameter of aerogel assuming cylindrical shape

The synthesized aerogels retained the shape of the beaker used in the freeze-drying process and appeared to be relatively mechanically stable. The density of the aerogels was extremely low with calculated densities ranging from ~ 17 mg cm^{-3} to ~80 mg

cm^{-3}. A typical example of a synthesized aerogel balanced on a blade of grass to emphasize the lightness of the material is shown in Figure 8.1.

Figure 8.1: MWCNT/PVA aerogel balanced on vegetation

Initial investigations were carried out to determine the compressibility of the synthesized aerogels by applying various loads to the material and monitoring the relative extent of the compression. The different MWCNT:PVA ratio aerogels prepared in 5 cm^3 of water were comparable in terms of volume post synthesis. Therefore, a comparison of their compressibility was carried out. Weights ranging in mass from 5-50 grams were placed on top of the samples and the relative change in height of the materials was recorded by analysis of the photos in Figure 8.2a using the software ImageJ. The height of the sample was measured by counting the number of pixels form the top of the sample to the bottom and then the number of pixels was converted to mm using the ruler in the photos. From this analysis, it was seen that the higher the relative content of PVA the less compressible the aerogel was under load (Figure 8.2b). After the weights were removed from the sample a final photograph was taken after ~ 3 minutes to assess whether the sample returned to its original shape. It was seen that the samples regained almost their full height and it was probable that they would fully regain their original shape with a longer recovery time. The maximum

compression was seen when 50 g of mass was placed on top of the aerogel with a 1:1 ratio of MWCNT:PVA with the material reducing to 56% of its original height.

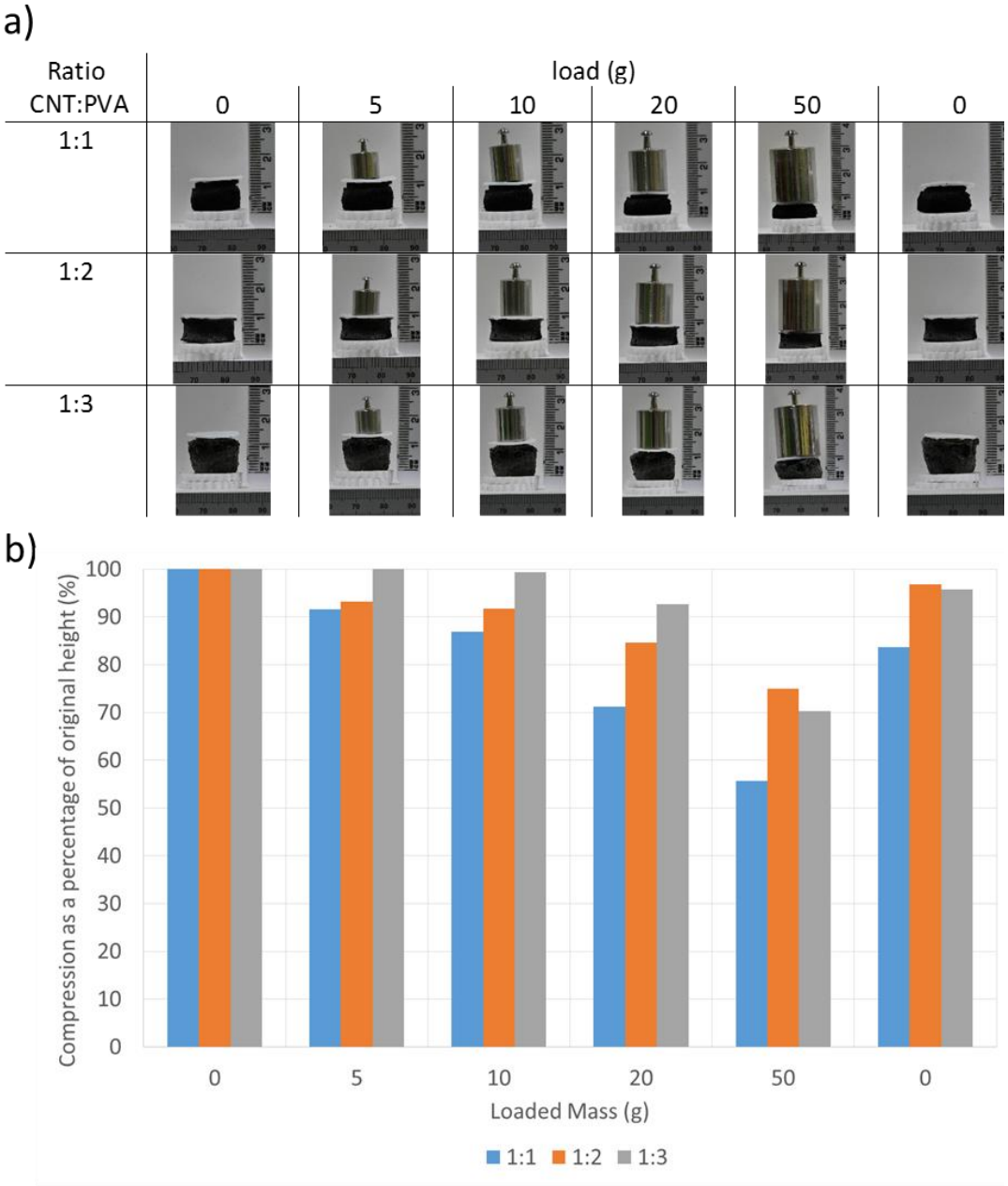

Figure 8.2: Aerogels under load, various MWCNT:PVA ratios, samples prepared in 5 cm^3 of water

The compressibility of the materials hints at their highly porous nature with further studies required to fully assess the mechanical properties of the material. The strength of the aerogels is emphasized by considering that they can support a weight that is 3

orders of magnitude greater than their own mass without falling apart. In the future, measurements of stress-strain and the Poisson ratio could yield further information regarding the aerogels' interesting structural properties.

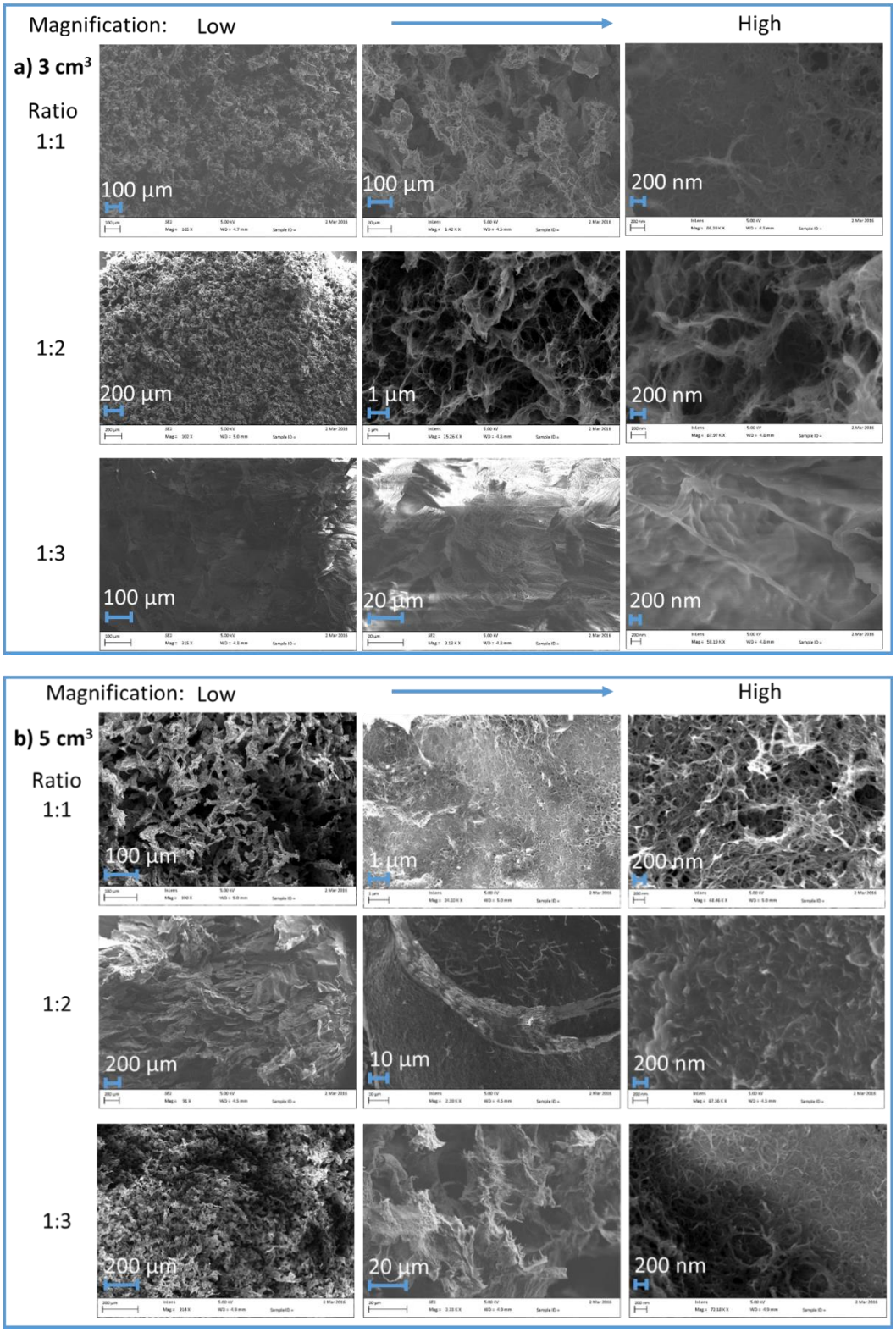

Figure 8.3: SEM images of internal pore structure of MWCNT/PVA composite aerogels. Aerogels prepared in a) 5cm^3 of water, b) 3cm^3 of water

The internal pore structure of the materials was visualized by scanning electron microscopy (SEM). A selection of images are presented in Figure 8.3. From the images, a macroporous structure was observed, with large pores distributed across the surface. At higher levels of magnification (Figure 8.3), it was possible to conclude that the MWCNTs were well distributed throughout the polymer phase. Comparing the 1:1 ratio samples prepared in different volumes of water it could be tentatively concluded that the sample prepared in 5 cm^3 of water appeared less dense with larger pores between the networked structure than the sample prepared in 3 cm^3. This was to be expected and is in agreement with the densities calculated in Table 8.1. A similar observation was made for the 1:3 ratio samples. However for 1:2, the images for the 5 cm^3 sample shows a structure which is less porous with sheet like features. It is possible that this is a result of incomplete freezing of the mixture prior to the vacuum drying step.

Before detailed conclusions are formulated regarding the structural properties of the individual aerogels, synthetic procedures must be repeated to ensure materials with reproducible properties can be produced.

8.3 CO_2 adsorption properties of amine-impregnated MWCNT/PVA aerogels

For an initial study the aerogel prepared in 5 cm^3 of water with a MWCNT:PEI ratio of 1:3 was impregnated with PEI with a molecular weight of 600. This particular aerogel sample was chosen due to its large total volume and high mechanical stability under load. A 7.5 mg piece of aerogel was impregnated with 30 mg of PEI, which corresponds to a loading of ~80 wt. %. The CO_2 capacity of the sample was measured with the ZLC technique and the result is shown in Figure 8.4.

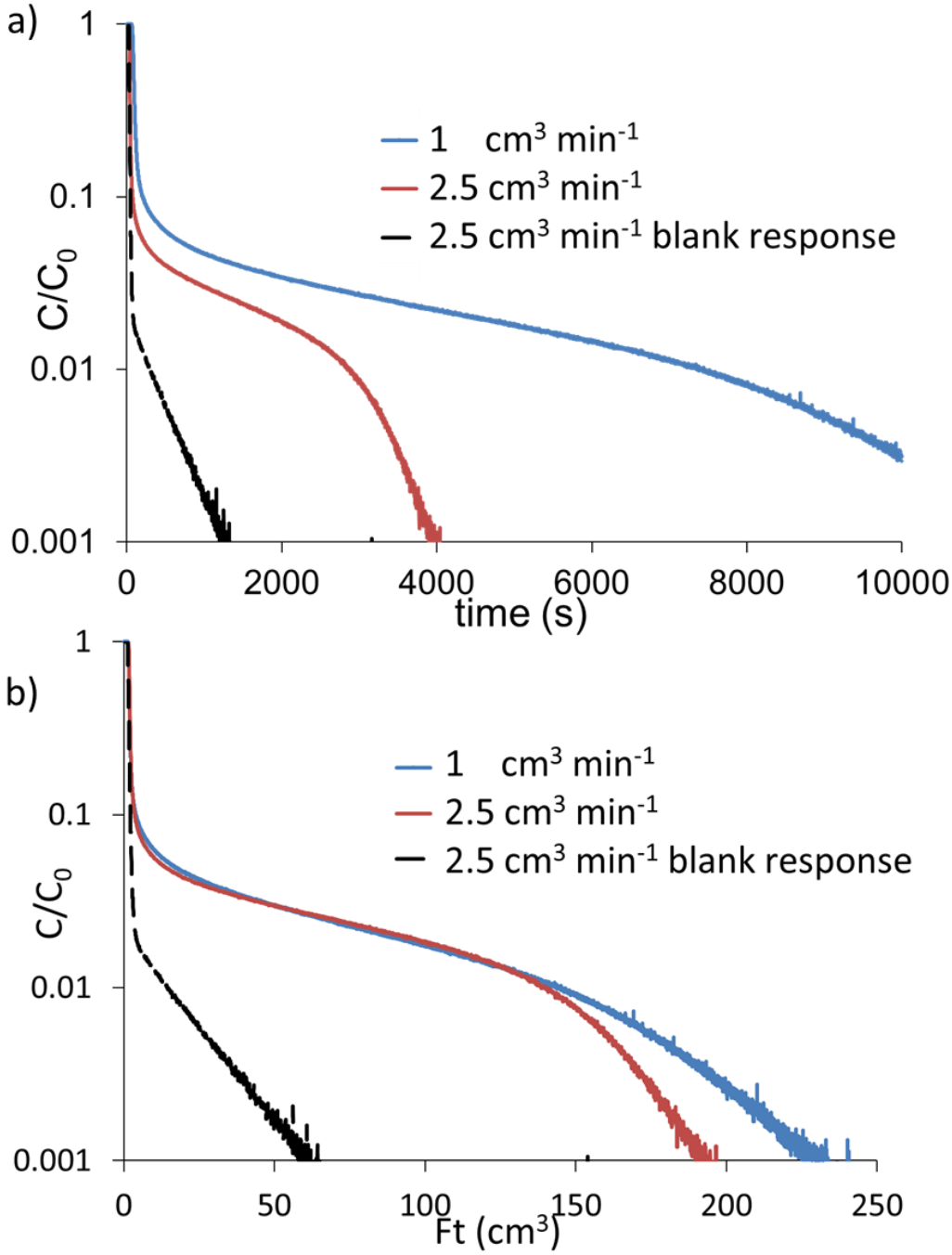

Figure 8.4: ZLC desorption curves of MWCNT:PVA (1:3) composite aerogel (5.6 mg) loaded with 80 wt. % PEI mw600. Measurements carried out at 75 °C. Adsorption: 10% CO_2: 90% N_2, Desorption: 100% N_2 Adsorption time – 1 cm^3 min^{-1}: 84 mins , 2.5 cm^3 min^{-1}: 32 mins., Capacity (mmol g^{-1}) – 1 cm^3 min^{-1}: 2.67, 2.5 cm^3 min^{-1}: 2.54

The measured CO_2 capacity of this sample was the highest of any of the materials reported in this work at approximately 2.7 mmol g^{-1}. The same analysis was carried out as in section 5.2.3 to calculate the efficiency of the CO_2 interaction with the available active sites. There were 19.5 mmol g^{-1} of nitrogen containing groups (mol(*N*)) in the material giving a $q(CO_2)$:0.5*mol(*N*) ratio of 0.28. The efficiency of interaction was at the top end of the values reported for the PEI impregnated meso-ACs reported in chapter 5. The low density of the aerogel potentially enables the impregnated amine to distribute throughout the materials volume. Therefore, if there is a thin layer of amine on the surface of the support then more active sites are exposed to the gas environment, improving the efficiency and kinetics of the process. A further study is required to investigate the correlation between the density of the aerogel loading of the amine and the efficiency of the CO_2: amine interaction. However, even if the efficiency increases with lower density aerogels there will come a point where the net gain from increase efficiency is outweighed by the detrimental effect of the increase in the adsorbent's volume. This is because, as the density of the aerogels decreases the adsorbed amount per unit volume of adsorbent will also decrease. If the density of adsorbent is too low then it will increase the required size of the separation unit in the carbon capture plant and hence reduce the efficiency of the overall process.

The ZLC desorption curves featured the same double curvature that was investigated in chapter 6 further validating the conclusion that the amine is the source of the double curvature not the support material.

8.4 Conclusions

It would appear that the composite MWCNT:PVA aerogels are promising candidates to act as supports for amine impregnation. The low density of the aerogels along with their highly porous structure allows the incorporation of a high weight percentage of amine that can interact efficiently with the CO_2. The electrical properties of the MWCNTs dispersed in the aerogel framework result in the possibility that the adsorbent could be regenerated by resistive heating.

In principle, the aerogel structures can be prepared in any type of mold, therefore they could be prepared in the form of a monolith. A monolith would greatly reduce the pressure drop along the column lowering the cost of the separation. In addition, a fabrication method to print 3D aerogels with periodic lattices of a predetermined structure has been reported.[190, 191] The flexibility of the aerogels in terms of their material properties makes them promising materials for application in a separation process.

Future work to characterize these MWCNT:PVA aerogels would include: full characterization of their mechanical and electrical properties; pore size analysis via mercury porosimetry; CO_2 adsorption properties as a function of density, amine loading and MWCNT content.

9 Conclusions and future work

In this work, a wide range of carbon materials were investigated as supports for amine moieties for application in a carbon capture process. The materials were first prepared and then ranked to assess their potential as CO_2 adsorbents using a variety of techniques including the zero-length column, thermal gravimetric analysis and breakthrough experiment. Materials were generally tested at a CO_2 partial pressure of 0.1 bar as this is representative of the conditions found in the flue gas of a fossil fuel powered power plant. Of particular interest in this study, was the development of adsorbents for carbon capture from gas fired power plants. The concentration of CO_2 in the flue gas of a gas fired power plant ranges from 4-8% and hence strong, highly selective adsorbents have been developed that exhibit a high uptake of CO_2 at low partial pressures. Strong selective adsorbents have a steep isotherm profile in the low pressure region and in order to achieve significant working capacities a rapid temperature swing adsorption process is required, where the adsorbent can be rapidly cycled through adsorption, regeneration and cooling steps. To develop a carbon adsorbent with competitive adsorption properties at low CO_2 partial pressure the surface must be functionalized to increase the materials affinity towards CO_2.

In this project, initial investigations were focused on the direct covalent grafting of amine groups to the surface of multi-walled carbon nanotubes and mesoporous carbon. Amine groups were successfully grafted to the surface. However, it was concluded that the density of the functional groups was not great enough to have a significant impact on the adsorbents' performance. The resistive properties of the MWCNTs were seen to change on exposure to CO_2, with an enhanced effect observed for the functionalized tubes. It would be interesting to extend this work to investigate the potential of the materials as novel CO_2 gas sensors.

To increase the number of functional amine groups incorporated in the carbon support, amine molecules were physically adsorbed within the porous carbon structure via wet impregnation. The materials were ranked in terms of CO_2 capacity by thermal

gravimetric analysis and a heat of adsorption, for the functionalized materials, of ~89 kJ mol^{-1}, indicative of a chemisorption process was measured. A microporous and a mesoporous activated carbon were compared and it was concluded that mesoporous carbons provided a more efficient support for the amine to interact with the CO_2. The CO_2 capacity increased as a higher weight percentage of amine was incorporated into the material. It was observed that at the same mass loading, lighter molecular weight polyamines interacted more efficiently with CO_2 than larger less volatile polyamines. However, there was a trade-off in terms of cyclic stability with the lower molecular weight amines exhibiting a drop off in performance over multiple cycles, hence the adsorbents became less desirable for application in a carbon capture process.

The work was then advanced to investigate the kinetics of the amine-impregnated materials via the ZLC technique. A novel double curvature was observed in the concentration profile of CO_2 at long times during the desorption step. The influence of heat effects was first excluded and then a detailed model was presented to consider the reaction between CO_2 and amine in the adsorbed phase. The mechanism of reaction between CO_2 and amine is highly complex and the double curvature in the response could not be explained by a linear first order process. A new ZLC column model was proposed that modelled a reaction in the adsorbed phase. A proposed model was shown to accurately model the experimental response with a fractional order rate equation. The sensitivity of the zero-length column technique enabled the system to be studied at low CO_2 partial pressure and the double curvature in the desorption profile to be observed. Future work will include the implementation of the model for the chemical reaction in the adsorbed phase in Cysim to enable both the adsorption and desorption experiments carried out by the E-ZLC breakthrough technique to be accurately modeled. Following the methodology presented in the AMP-Gas paper[13] a larger amount of adsorbent (~10g) should then be tested to further validate the model at a larger scale. The viability of using the model to predict the performance of the adsorbent in a large scale carbon capture process can then be assessed.

The novel E-ZLC breakthrough technique was introduced and the temperature profile within the column was fully characterized through the insertion of a thermocouple into

the gas phase. The temperature profile of the system was accurately modelled with the adsorption simulator, Cysim. It was concluded that the E-ZLC operates at near to isothermal conditions which greatly simplifies the analysis of the breakthrough experiments. The upgrading of biogas (45% CO_2:55% CH_4) was investigated with E-ZLC breakthrough experiments. Through fitting the experimental data with Cysim, binary selectivities of 21 and 2.9 for CO_2 over CH_4 were calculated for 13X and activated carbon respectively. It was seen that an impregnated mesoporous carbon was highly selective towards CO_2 with its binary selectivity tending towards infinity.

Finally, a novel series of low density MWCNT:PVA aerogels were reported with highly porous compressible structures. Aerogels were prepared with different densities and ratios of MWCNT to PVA. An initial impregnation of PEI at 80 wt. % was carried out and a CO_2 capacity of 2.7 mmol g^{-1} was measured at 75 °C and 0.1 bar which is comparable to commercial zeolite 13X. Future work includes the full characterization of these materials and a comparative study of the adsorption performance of these materials when the same weight percentages of polyamine is loaded into aerogels with different densities. The aerogels have great potential to incorporate a very high weight percentage of amine whilst maintaining pathways for efficient transport of CO_2 to the active sites.

This work has focused on the development of carbon based adsorbents functionalized with amines. A full range of materials has been investigated from microporous activated carbon through to low density macro porous carbon aerogels. For a competitive carbon capture process an adsorbent with working capacity of greater than 1 mmol g^{-1} is required.[9] The developed adsorbents exhibit competitive performance with regard to CO_2 uptake (> 2 mmol g^{-1}) from dilute gas streams and if operated under suitable conditions would operate with a viable working capacity. The materials have a strong affinity for CO_2 and relatively quick kinetics at elevated temperature, making them suitable adsorbents for a rapid temperature swing carbon capture process. In future projects, it is important to ensure that both the design of the adsorbents and the process are carried out together to ensure that the process conditions are optimized

to take full advantage of the adsorbents' properties and that the materials selected can be effective under process conditions.

Appendix A – Supplementary experimental data

A1. Sheet resistance of CNT films measured by the Van der Pauw technique

Table A.1: Measured sheet resistances of functionalised CNTs films under

* 50:50 CO_2/N_2 mixture

	Resistance, N_2 (Ω)	Resistance 100% CO_2 (Ω)	$\Delta R/R_0$ (%)
CNT (RAW)	8.78	8.79	0.11
CNT-OX	28.05	28.09	0.14
CNT-EDA	17.37	17.51	0.81
CNT-PEI600	75.32	75.95*	0.84
CNT-PEI10K	747.99	757.18	1.23

A2. Volumetric N_2 isotherms of mesoporous carbon

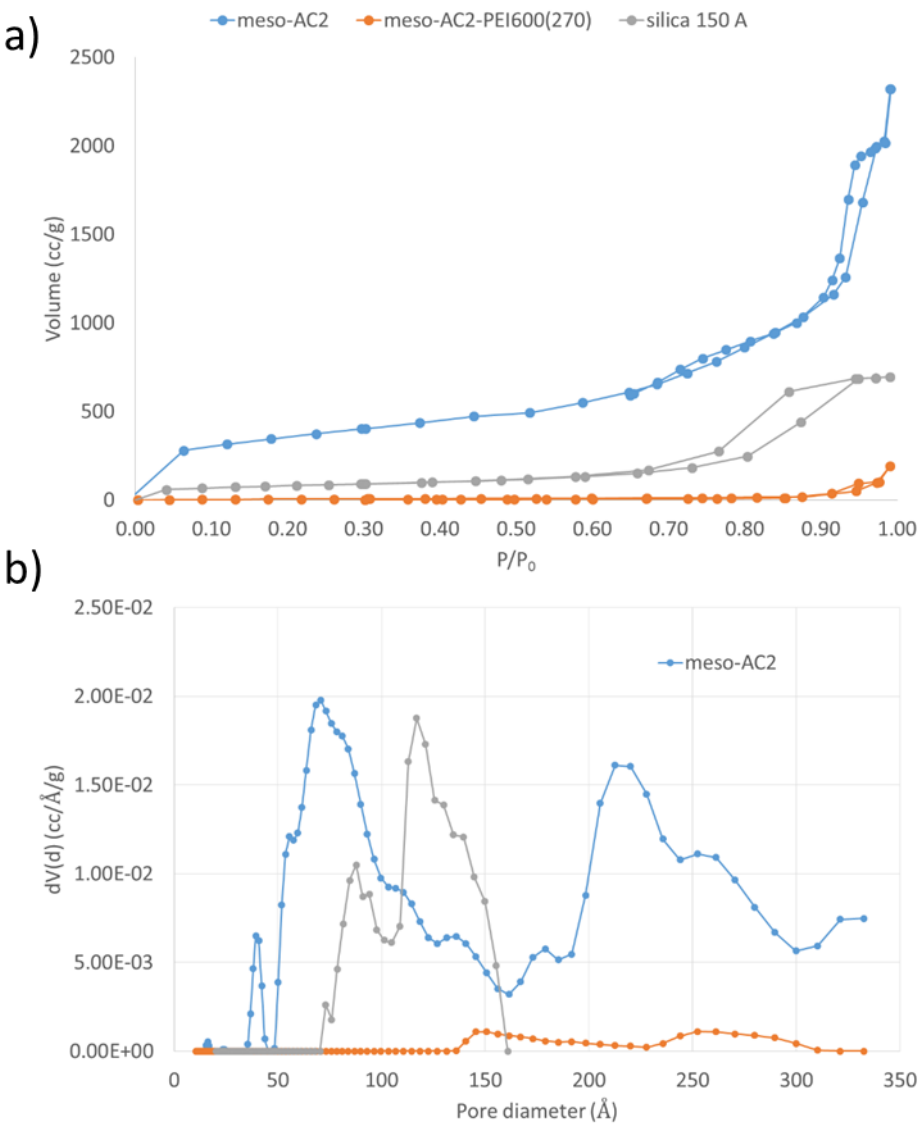

Figure - A.1: (a) Nitrogen isotherms 77K, (b) Pore size distribution Kernels: carbon slit/cylindrical QSDFT (adsorption), Silica cylindrical NLDFT (equilibrium)

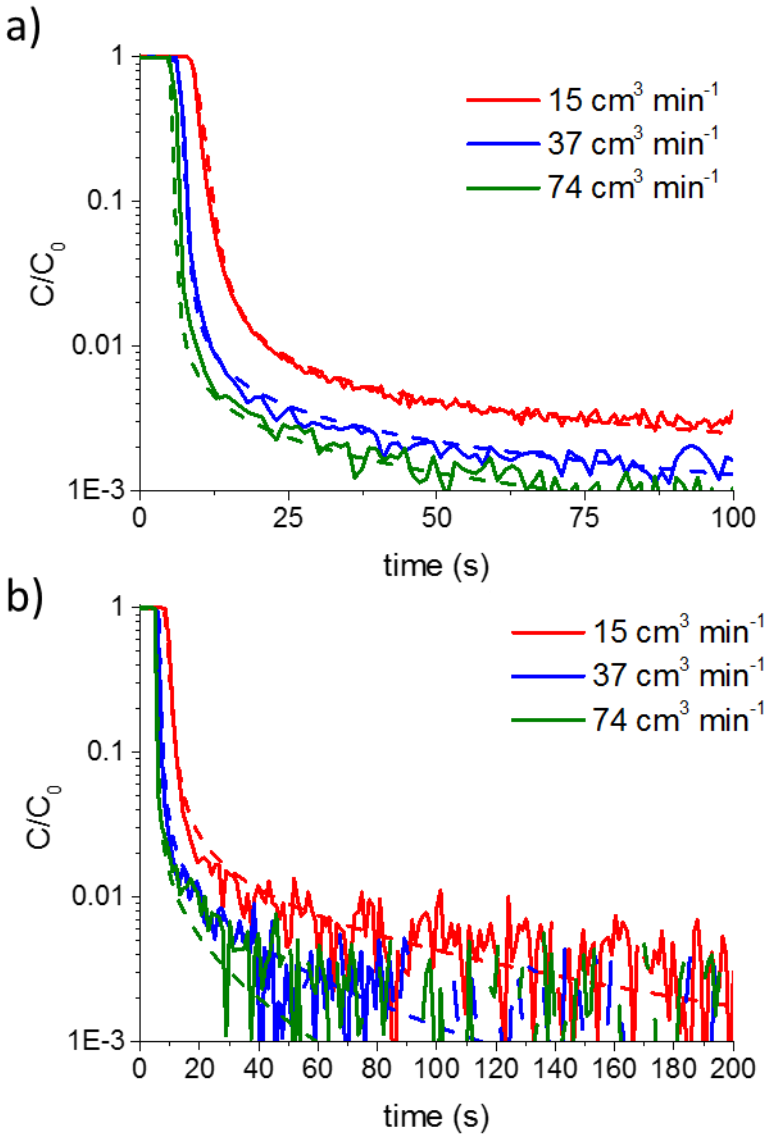

Figure - A.2: E-ZLC blank desorption experimental system response (solid line) with Cysim simulation (dashed line). a) Adsorption: 10% CO_2, 90% N_2; Desorption 100% N_2. b) Adsorption: 1% CO_2, 99% N_2; Desorption 100% N_2.

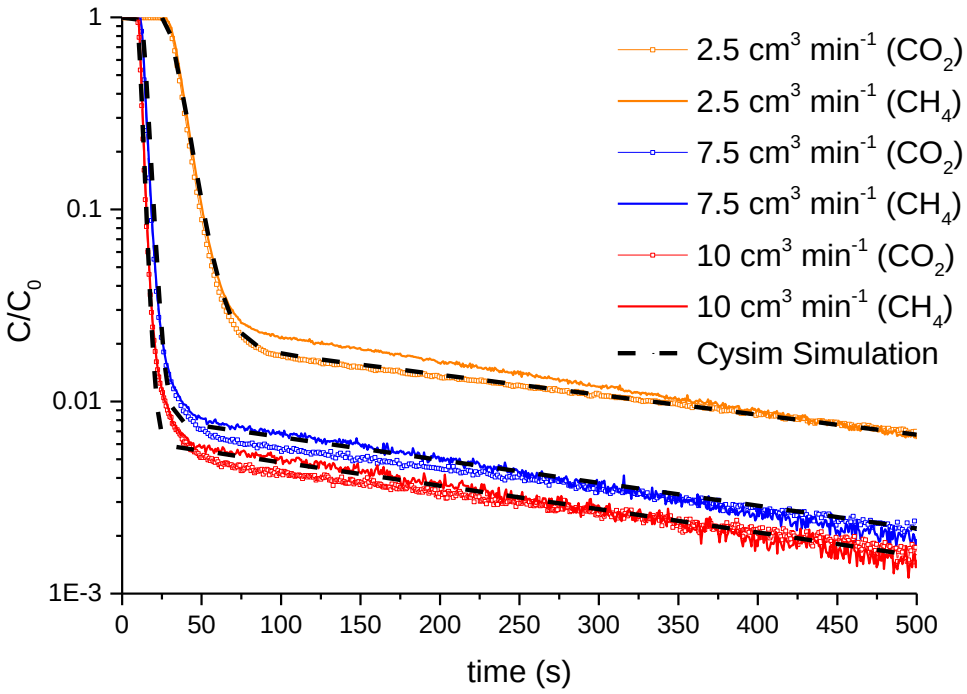

Figure - A.3: E-ZLC blank desorption experimental system response (solid line – CH_4, symbol – CO_2) with Cysim simulation (dashed black line). Adsorption: 45% CO_2, 55% CH_4; Desorption 100% N_2.

A4. Regeneration of 13X post biogas breakthrough experiments and new breakthrough column with thermocouples

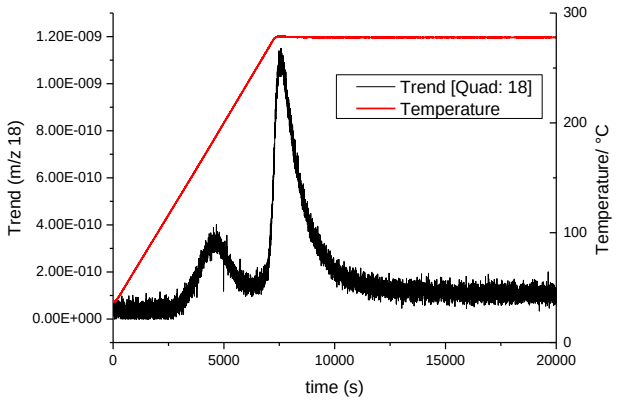

Figure - A.4: Regeneration of 13X post biogas measurements showing presence of adsorbed water on the adsorbent

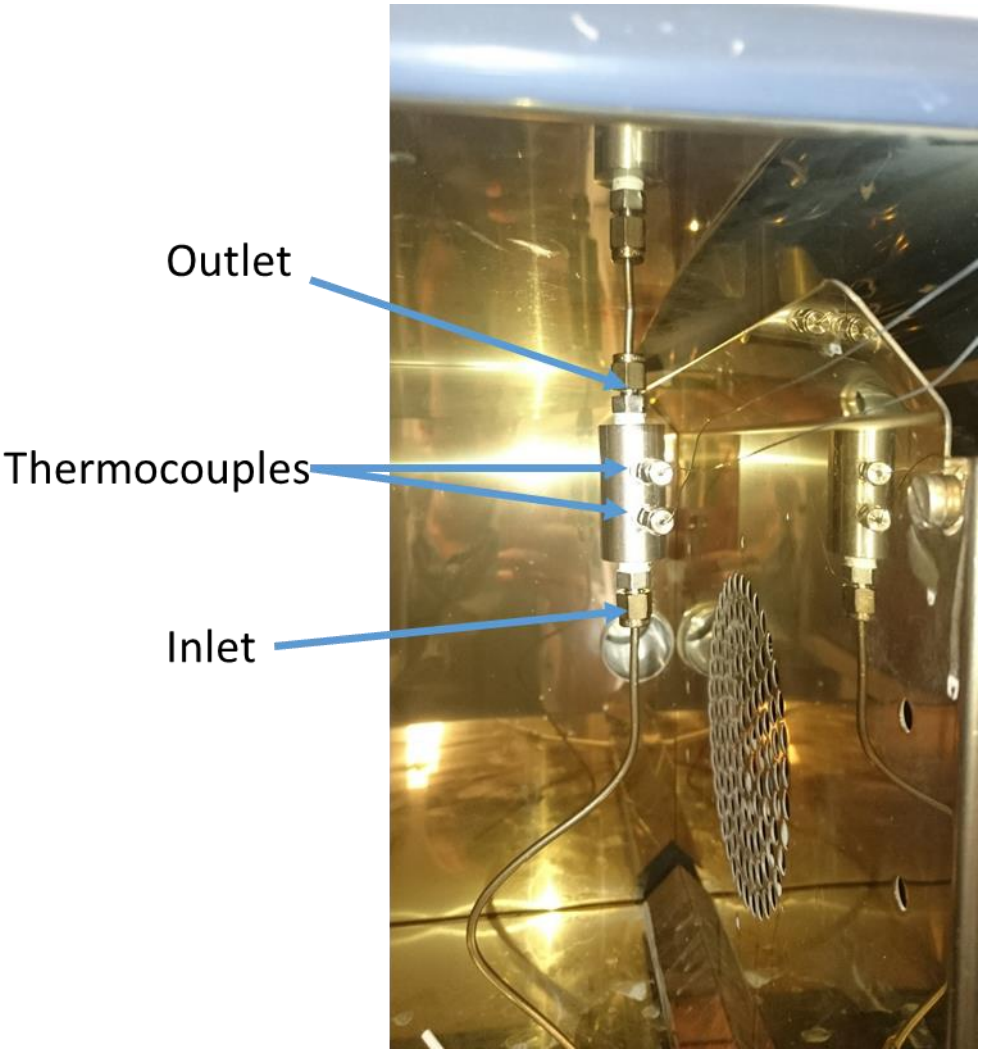

Figure - A.5: First iteration of breakthrough column designed with integrated thermocouples

A5. ZLC Blank response – kinetic model

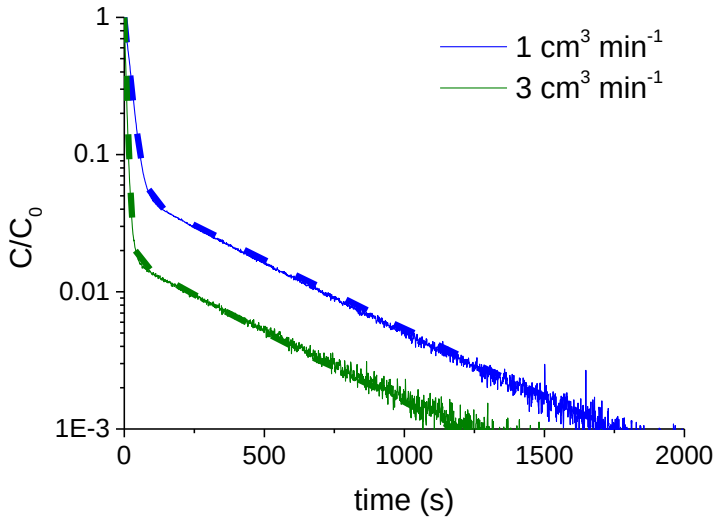

Figure - A.6: Experimental blank response of ZLC along with the simulated response generated with the equations defined in Figure 6.10. Experimental (solid line) Simulation (dashed line)

Appendix B – Heat transfer coefficients E-ZLC

In order to accurately model the temperature profile of the adsorption column it was necessary to determine as many of the heat transfer coefficients as possible. Relationships that calculate heat transfer coefficients in the literature have generally been developed for larger diameter columns and do not necessarily result in the calculation of an appropriate value for small laboratory columns.[12] The Cysim simulator requires three heat transfer coefficients to be specified. The external heat transfer coefficient (U) governs the heat transfer from the oven to the column wall, the second coefficient (h_w) governs the heat transfer from the wall to the fluid and the third coefficient (h_p) governs the heat transfer from the fluid to the pellet as depicted in Figure - B.1. The current model does not account for the heat transfer dynamics of the thermocouple.

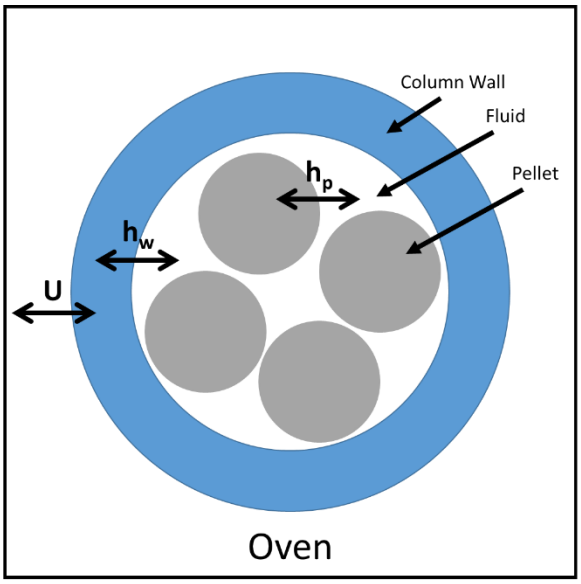

Figure - B.1: Schematic of heat transfer coefficients in E-ZLC

To quantify the external heat transfer coefficient, a simple experiment was carried out. The temperature of the ZLC oven was ramped from 35 °C to 120 °C and the temperature was monitored by two thermocouples. The first thermocouple was placed

in the gas phase of the oven right next to the external wall of the E-ZLC and the second was inside the E-ZLC in the gas phase. Two differential equations were proposed to model the heat transfer from the external gas phase of the oven to inside the column. The first differential equation (B.1) specifies the rate of change of the temperature of the column wall whilst the second equation (B.2) governs the rate of change of the temperature of the fluid.

$$\left(C_{p_w}\rho_w\right)\frac{\mathrm{d}T_w}{\mathrm{d}t} = \frac{h_w A_{cs}}{V_w}(T_f - T_w) - U\alpha\,(T_w - T_o) \quad \text{(B.1)}$$

$$\left(eC_{p_f}\rho_f + (1-e)C_{p_s}\rho_s\right)\frac{\mathrm{d}T_f}{\mathrm{d}t} = -\frac{h_w A_{cs}}{V_c}(T_f - T_w) - \frac{\nu A_c}{V_c}C_{p_f}\rho_f(T_f - T_{in}) \quad \text{(B.2)}$$

Where T_o, T_w, T_f and T_{in} are the temperature of the oven, column wall, fluid and the fluid temperature at the input of the column respectively. ν is the velocity of the gas. The remaining terms along with their relative values and units are defined in Table B.1. The first term in equation B.1 represents the heat transfer from the fluid to the column wall whilst the second term is the transfer from the oven to the column wall. The input T_o was the temperature measured in the oven next to the thermocouple. The first term in equation B.2 governs the heat transfer from the fluid to the column wall and the second term the change in the fluid temperature as a result of the input temperature of the fluid entering the column. In Figure - B.2 it can be seen that the temperature profile of the fluid within the column was independent of flow rate and the type of gas, therefore the second term in equation B.2 can be neglected.

Table B.1: Notation and definition of heat transfer parameters

	Definition	Values*	Units
$C_{p_{w,f,s}}$	Heat capacity (wall, fluid, solid)	500, N_2:1040, 920	J kg^{-1} K^{-1}
$\rho_{w,f,s}$	Density (wall, fluid, solid)	8000, N_2:1.25, 1053	kg m^{-3}
A_{CS}	Internal surface area of column	1.86e-4	m^2
A_c	Cross-sectional area of column	4.10e-6	m^2
V_c	Internal column volume	1.06e-7	m^3
V_w	Volume of column wall	2.03e-6	m^3
E	Void fraction of column	0.431	-
α	the ratio of the logarithmic mean surface area to volume of the column wall	158	m^{-1}

*Literature values from Chemical Handbook of Chemistry and Physics[192]

The equations were solved numerically to fit the experimental data and it was observed that for h_w values greater than 50 J m^{-2} s^{-1} K^{-1} the predicted temperature of the fluid and the column wall were similar. This implied that for the E-ZLC column there was rapid heat transfer between the fluid phase and the column wall. The differential equations were therefore solved to fit the external heat transfer coefficient (U) so that the model accurately predicted the experimental temperature (Figure - B.2). A high value of U of 550 J m^{-2} s^{-1} K^{-1} was calculated. The magnitude of the value was higher than expected as a result of the model not accurately representing the large external surface area, due to the thread on the E-ZLC, through the term α. The calculated value of the heat transfer coefficient was therefore inflated however the total contribution from α and U accurately models the heat transfer from the system.

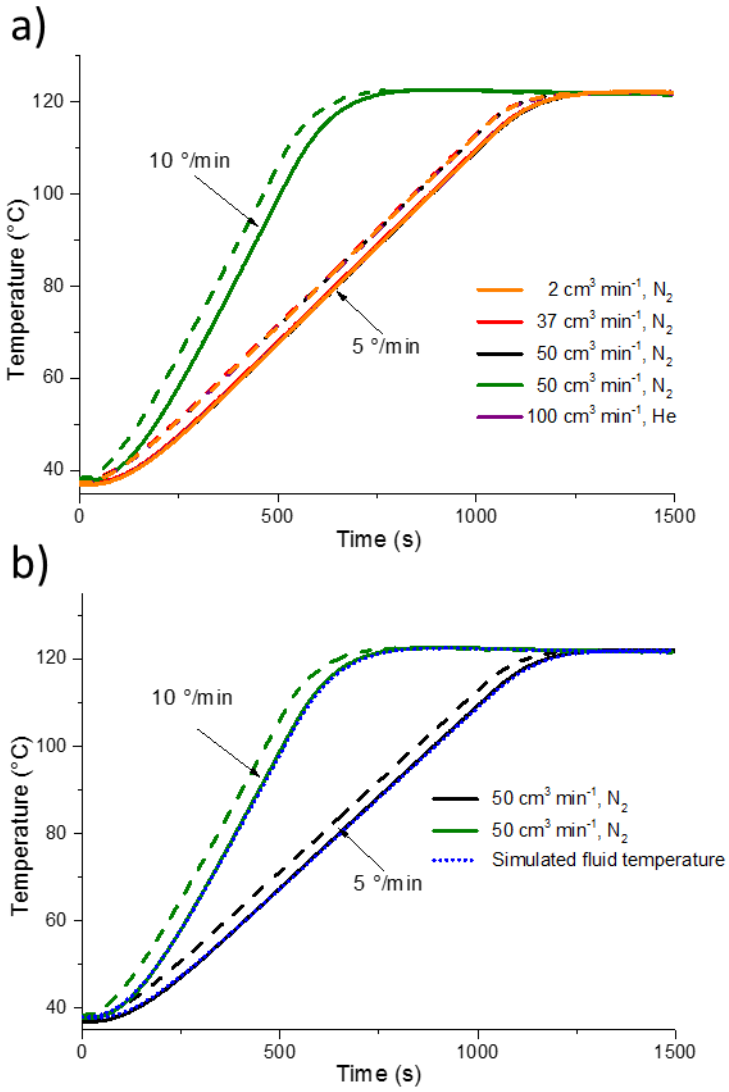

Figure - B.2: Temperature profile in system during ramping at two different ramp rates and various gas flow rates. Solid line temperature inside column, dashed line temperature in oven gas phase. a) Experimental data, b) Simulated fluid temperature with experimental data

The heat transfer coefficient from the pellet to the fluid was estimated from

$$h_p = \frac{kN_u}{2R_P} \qquad (6.3)$$

With the Nusselt number calculated from Wakao's correlation[193]

$$Nu = 2 + 1.1Pr^{1/3}\, Re^{0.6} \tag{6.4}$$

And the Reynolds number calculated by

$$Re = \frac{2R_p FMW}{\epsilon \pi R_c^2 \mu} \tag{6.5}$$

Where R_p and R_c are the radius of the pellet and column respectively. ϵ is the void fraction of the bed and $\mu$is the interstitial. For the range of flow rates studied the calculated value of h_p varied from 40 -190 J m^{-2} s^{-1} K^{-1}. A value of 60 J m^{-2} s^{-1} K^{-1} was used for the simulations because it fell within the calculated range and provided a good agreement with the experimental data.

The value of the heat transfer coefficient (h_w) from the wall to the fluid was fitted in order that simulated temperature in the fluid was in good agreement with the experimental data. As discussed in section 6.1.1 the E-ZLC operates at close to isothermal conditions due to the small diameter of the column and small sample mass, there was therefore rapid heat transfer out of the fluid phase.

Appendix C – The effect of pore structure on the CO_2 adsorption efficiency of polyamine impregnated porous carbons

J. A. Arran Gibson[a,b]*, Andrei V. Gromov[a], Stefano Brandani[b] and Eleanor E.B. Campbell[a,c]

[a] EaStCHEM, School of Chemistry, University of Edinburgh, Edinburgh, UK

[b] SCCS, School of Engineering, The University of Edinburgh, Edinburgh, UK

[c] Division of Quantum Phases and Devices, Konkuk University, Seoul 143-701, Korea

Appendix D – Adsorption Materials and Processes for Carbon Capture from Gas-Fired Power Plants (AMPGas)

J. A. Arran Gibson[1], Enzo Mangano[1], Elenica Shiko[1], Alex G. Greenaway[3], Andrei V. Gromov[2], Magdalena M. Lozinska[3], Daniel Friedrich[1], Eleanor E. B. Campbell[2,4], Paul A. Wright[3], Stefano Brandani[1*]

[1] School of Engineering, The University of Edinburgh, Edinburgh EH9 3FB, U.K.

[2] EaStCHEM, School of Chemistry, The University of Edinburgh, Edinburgh EH9 3FJ, U.K.

[3] EaStCHEM, School of Chemistry, University of St Andrews, St Andrews, Fife KY16 9ST, U.K.

[4] Division of Quantum Phases and Devices, School of Physics, Konkuk University, 143-701 Seoul, South Korea

10 References

1. P. Tans and R. Keeling, NOAA/ESRL and Scripps Institution of Oceanography www.esrl.noaa.gov/gmd/ccgg/trends/, 2015, vol. 2015.
2. N. Statistics, ed. D. o. E. C. Change, GOV.UK, 2015.
3. M. Blunt, F. J. Fayers and F. M. Orr Jr, *Energ Convers Manage*, 1993, **34**, 1197-1204.
4. R. M. Cuéllar-Franca and A. Azapagic, *Journal of CO2 Utilization*, 2015, **9**, 82-102.
5. K. M. K. Yu, I. Curcic, J. Gabriel and S. C. E. Tsang, *ChemSusChem*, 2008, **1**, 893-899.
6. X. Luo, M. Wang and J. Chen, *Fuel*, 2015, **151**, 110-117.
7. R. S. Haszeldine, *Science*, 2009, **325**, 1647-1652.
8. G. Scheffknecht, L. Al-Makhadmeh, U. Schnell and J. Maier, *Int. J. Greenh. Gas. Con.*, 2011, **5**, S16-S35.
9. J. C. Abanades, B. Arias, A. Lyngfelt, T. Mattisson, D. E. Wiley, H. Li, M. T. Ho, E. Mangano and S. Brandani, *Int. J. Greenh. Gas Con.*, 2015, **40**, 126-166.
10. D. M. Ruthven, S. Farooq and K. S. Knaebel, *Pressure swing adsorption*, VCH publishers New York, 1994.
11. S. Sircar, *Ind. Eng. Chem. Res.*, 2002, **41**, 1389-1392.
12. D. M. Ruthven, *Principles of adsorption and adsorption processes*, John Wiley & Sons, 1984.
13. J. A. A. Gibson, E. Mangano, E. Shiko, A. G. Greenaway, A. V. Gromov, M. M. Lozinska, D. Friedrich, E. E. B. Campbell, P. A. Wright and S. Brandani, *Ind. Eng. Chem. Res.*, 2016, **55**, 3840-3851.
14. A. Kodama, M. Goto, T. Hirose and T. Kuma, *J. Chem. Eng. Jpn.*, 1995, **28**, 19-24.
15. Inventys, http://www.inventysinc.com/wp-content/uploads/2012/02/Inventys-Brochure-Nov-2011-V8.pdf., 2011.
16. S.-H. Moon and J.-W. Shim, *J. Colloid. Interfac. Sci.*, 2006, **298**, 523-528.
17. T. S. Lee, J. H. Cho and S. H. Chi, *Build. Environ.*, 2015, **92**, 209-221.
18. N. Sipöcz and F. A. Tobiesen, *Int. J. Greenh. Gas. Con.*, 2012, **7**, 98-106.
19. K. Lindqvist, K. Jordal, G. Haugen, K. A. Hoff and R. Anantharaman, *Energy*, 2014, **78**, 758-767.
20. A. Samanta, A. Zhao, G. K. H. Shimizu, P. Sarkar and R. Gupta, *Ind. Eng. Chem. Res.*, 2012, **51**, 1438-1463.
21. S. Choi, J. H. Drese and C. W. Jones, *ChemSusChem*, 2009, **2**, 796-854.
22. M. M. Lozinska, E. Mangano, J. P. S. Mowat, A. M. Shepherd, R. F. Howe, S. P. Thompson, J. E. Parker, S. Brandani and P. A. Wright, *J. Am. Chem. Soc.*, 2012, **134**, 17628-17642.
23. M. M. Lozinska, J. P. S. Mowat, P. A. Wright, S. P. Thompson, J. L. Jorda, M. Palomino, S. Valencia and F. Rey, *Chem. Mater.*, 2014, **26**, 2052-2061.
24. D. Bonenfant, M. Kharoune, P. Niquette, M. Mimeault and R. Hausler, *Sci. Technol. Adv. Mat.*, 2008, **9**, 013007.

25. G. Greenaway Alex, J. Shin, A. Cox Paul, E. Shiko, P. Thompson Stephen, S. Brandani, B. Hong Suk and A. Wright Paul, *Z. Kristallogr.*, 2015, **230**, 223.
26. P. Guo, J. Shin, A. G. Greenaway, J. G. Min, J. Su, H. J. Choi, L. Liu, P. A. Cox, S. B. Hong, P. A. Wright and X. Zou, *Nature*, 2015, **524**, 74-78.
27. F. Brandani and D. M. Ruthven, *Ind. Eng. Chem. Res.*, 2004, **43**, 8339-8344.
28. E. Mangano, S. Brandani, M. C. Ferrari, H. Ahn, D. Friedrich, M. L. Lozinska, P. A. Wright, J. Kahr, R. Morris, M. Croad, N. McKeown, H. Shamsipour and P. Budd, *Energy Procedia*, 2013, **37**, 40-47.
29. J.-R. Li, Y. Ma, M. C. McCarthy, J. Sculley, J. Yu, H.-K. Jeong, P. B. Balbuena and H.-C. Zhou, *Coordin. Chem. Rev.*, 2011, **255**, 1791-1823.
30. J. P. S. Mowat, S. R. Miller, J. M. Griffin, V. R. Seymour, S. E. Ashbrook, S. P. Thompson, D. Fairen-Jimenez, A.-M. Banu, T. Düren and P. A. Wright, *Inorg. Chem.*, 2011, **50**, 10844-10858.
31. A. Greenaway, B. Gonzalez-Santiago, P. M. Donaldson, M. D. Frogley, G. Cinque, J. Sotelo, S. Moggach, E. Shiko, S. Brandani, R. F. Howe and P. A. Wright, *Angew. Chem. Int. Edit.*, 2014, **53**, 13483-13487.
32. R. S. Pillai, V. Benoit, A. Orsi, P. L. Llewellyn, P. A. Wright and G. Maurin, *J. Phys. Chem. C*, 2015.
33. A. Ö. Yazaydın, R. Q. Snurr, T.-H. Park, K. Koh, J. Liu, M. D. LeVan, A. I. Benin, P. Jakubczak, M. Lanuza, D. B. Galloway, J. J. Low and R. R. Willis, *J. Am. Chem. Soc.*, 2009, **131**, 18198-18199.
34. J. L. C. Rowsell and O. M. Yaghi, *Angew. Chem. Int. Edit.*, 2005, **44**, 4670-4679.
35. J.-R. Li, R. J. Kuppler and H.-C. Zhou, *Chem. Soc. Rev.*, 2009, **38**, 1477-1504.
36. F. X. L. i Xamena, A. Abad, A. Corma and H. Garcia, *J. Catal.*, 2007, **250**, 294-298.
37. L. E. Kreno, K. Leong, O. K. Farha, M. Allendorf, R. P. Van Duyne and J. T. Hupp, *Chem. Rev.*, 2011, **112**, 1105-1125.
38. R. Ben-Mansour, M. A. Habib, O. E. Bamidele, M. Basha, N. A. A. Qasem, A. Peedikakkal, T. Laoui and M. Ali, *Appl. Energ.*, 2016, **161**, 225-255.
39. W.-J. Son, J.-S. Choi and W.-S. Ahn, *Micropor. Mesopor. Mat.*, 2008, **113**, 31-40.
40. E. S. Sanz-Pérez, M. Olivares-Marín, A. Arencibia, R. Sanz, G. Calleja and M. M. Maroto-Valer, *Int. J. Greenh. Gas. Con.*, 2013, **17**, 366-375.
41. M. A. Alkhabbaz, R. Khunsupat and C. W. Jones, *Fuel*, 2014, **121**, 79-85.
42. G. Qi, Y. Wang, L. Estevez, X. Duan, N. Anako, A.-H. A. Park, W. Li, C. W. Jones and E. P. Giannelis, *Energ. Environ. Sci.*, 2011, **4**, 444-452.
43. X. Xu, C. Song, J. M. Andresen, B. G. Miller and A. W. Scaroni, *Micropor. Mesopor. Mat.*, 2003, **62**, 29-45.
44. M. U. Thi Le, S.-Y. Lee and S.-J. Park, *Int. J. Hydrogen Energ.*, 2014, **39**, 12340-12346.
45. J. Tanthana and S. S. C. Chuang, *ChemSusChem*, 2010, **3**, 957-964.
46. R. Sanz, G. Calleja, A. Arencibia and E. S. Sanz-Pérez, *Appl. Surf. Sci.*, 2010, **256**, 5323-5328.

47. D. J. N. Subagyono, M. Marshall, G. P. Knowles and A. L. Chaffee, *Micropor. Mesopor. Mat.*, 2014, **186**, 84-93.
48. X. Xu, C. Song, J. M. Andresen, B. G. Miller and A. W. Scaroni, *Energ. Fuel.*, 2002, **16**, 1463-1469.
49. J. Wei, L. Liao, Y. Xiao, P. Zhang and Y. Shi, *J. Environ. Sci.*, 2010, **22**, 1558-1563.
50. D. V. Quang, A. Dindi, A. V. Rayer, N. E. Hadri, A. Abdulkadir and M. R. M. Abu-Zahra, *Energy Procedia*, 2014, **63**, 2122-2128.
51. C.-H. Yu, C.-H. Huang and C.-S. Tan, *Aerosol Air Qual. Res.*, 2012, **12**, 745-769.
52. S.-H. Liu, C.-H. Wu, H.-K. Lee and S.-B. Liu, *Top. Catal.*, 2009, **53**, 210-217.
53. A. Heydari-Gorji, Y. Yang and A. Sayari, *Energ. Fuel.*, 2011, **25**, 4206-4210.
54. E. Vilarrasa-Garcia, E. M. O. Moya, J. A. Cecilia, C. L. Cavalcante Jr, J. Jiménez-Jiménez, D. C. S. Azevedo and E. Rodríguez-Castellón, *Micropor. Mesopor. Mat.*, 2015, **209**, 172-183.
55. D. Wang, X. Wang, X. Ma, E. Fillerup and C. Song, *Catal. Today*, 2014, **233**, 100-107.
56. Z. Chen, S. Deng, H. Wei, B. Wang, J. Huang and G. Yu, *Front. Environ. Sci. Eng.*, 2013, **7**, 326-340.
57. R. S. Franchi, P. J. E. Harlick and A. Sayari, *Ind. Eng. Chem. Res.*, 2005, **44**, 8007-8013.
58. Y. Han, G. Hwang, H. Kim, B. Z. Haznedaroglu and B. Lee, *Chem. Eng. J.*, 2015, **259**, 653-662.
59. C. Chen, S.-T. Yang, W.-S. Ahn and R. Ryoo, *Chem. Commun.*, 2009, 3627-3629.
60. A. Sayari and Y. Belmabkhout, *J. Am. Chem. Soc.*, 2010, **132**, 6312-6314.
61. A. Sayari, A. Heydari-Gorji and Y. Yang, *J. Am. Chem. Soc.*, 2012, **134**, 13834-13842.
62. V. Zelenak, D. Halamova, L. Gaberova, E. Bloch and P. Llewellyn, *Micropor. Mesopor. Mat.*, 2008, **116**, 358-364.
63. Y. Belmabkhout and A. Sayari, *Adsorption*, 2009, **15**, 318-328.
64. G. P. Knowles, S. W. Delaney and A. L. Chaffee, *Ind. Eng. Chem. Res.*, 2006, **45**, 2626-2633.
65. J. M. Dias, M. C. M. Alvim-Ferraz, M. F. Almeida, J. Rivera-Utrilla and M. Sánchez-Polo, *J. Environ. Manage.*, 2007, **85**, 833-846.
66. S. A. Dastgheib, T. Karanfil and W. Cheng, *Carbon*, 2004, **42**, 547-557.
67. D. Soares Maia, J. C. A. de Oliveira, J. Toso, K. Sapag, R. López, D. S. Azevedo, C. Cavalcante, Jr. and G. Zgrablich, *Adsorption*, 2011, **17**, 853-861.
68. H. Marsh and F. Rodríguez-Reinoso, in *Activated Carbon*, eds. H. Marsh and F. Rodríguez-Reinoso, Elsevier Science Ltd, Oxford, 2006, pp. 383-453.
69. N. Mohamad Nor, L. C. Lau, K. T. Lee and A. R. Mohamed, *Journal of Environmental Chemical Engineering*, 2013, **1**, 658-666.
70. M. Balsamo, T. Budinova, A. Erto, A. Lancia, B. Petrova, N. Petrov and B. Tsyntsarski, *Sep. Purif. Technol.*, 2013, **116**, 214-221.
71. C. S. Lee, Y. L. Ong, M. K. Aroua and W. M. A. W. Daud, *Chem. Eng. J.*, 2013, **219**, 558-564.

72. M. Maroto-Valer, Z. Lu, Y. Zhang and Z. Tang, *Waste Manage.*, 2008, **28**, 2320-2328.
73. J. Wang, H. Chen, H. Zhou, X. Liu, W. Qiao, D. Long and L. Ling, *J. Environ. Sci.*, 2013, **25**, 124-132.
74. C. S. Watana Kangwanwatanaa, Paitoon Tontiwachwuthikul, *Chem. Eng. Trans.*, 2013, **35**, 403-408.
75. H. J. Lim, K. Lee, Y. S. Cho, Y. S. Kim, T. Kim and C. R. Park, *Phys. Chem. Chem. Phys.*, 2014, **16**, 17466-17472.
76. C. M. Hansen, *Hansen Solubility Parameters: A User's Handbook, 2nd Edition*, 2007.
77. A. Subrenat, J. N. Baléo, P. Le Cloirec and P. E. Blanc, *Carbon*, 2001, **39**, 707-716.
78. M. K. Aroua, W. M. A. W. Daud, C. Y. Yin and D. Adinata, *Sep. Purif. Technol.*, 2008, **62**, 609-613.
79. J. Wang, M. Wang, B. Zhao, W. Qiao, D. Long and L. Ling, *Ind. Eng. Chem. Res.*, 2013, **52**, 5437-5444.
80. J. Wang, H. Huang, M. Wang, L. Yao, W. Qiao, D. Long and L. Ling, *Ind. Eng. Chem. Res.*, 2015, **54**, 5319-5327.
81. Z.-l. Liu, Y. Teng, K. Zhang, Y. Cao and W.-p. Pan, *Journal of Fuel Chemistry and Technology*, 2013, **41**, 469-475.
82. A. Grondein and D. Bélanger, *Fuel*, 2011, **90**, 2684-2693.
83. H. Yang, Y. Yuan and S. C. E. Tsang, *Chem. Eng. J.*, 2012, **185–186**, 374-379.
84. D.-I. Jang and S.-J. Park, *Bull. Korean Chem. Soc.*, 2011, **32**, 3377-3381.
85. Y. Du, Z. Du, W. Zou, H. Li, J. Mi and C. Zhang, *J. Colloid Interf. Sci.*, 2013, **409**, 123-128.
86. A. Houshmand, M. S. Shafeeyan, A. Arami-Niya and W. M. A. W. Daud, *J. Taiwan Inst. Chem. E.*, 2013, **44**, 774-779.
87. F. Su, C. Lu, W. Cnen, H. Bai and J. F. Hwang, *Sci. Total Environ.*, 2009, **407**, 3017-3023.
88. F. Su, C. Lu and H.-S. Chen, *Langmuir*, 2011, **27**, 8090-8098.
89. A. Houshmand, W. M. A. W. Daud, M.-G. Lee and M. S. Shafeeyan, *Water Air Soil Poll.*, 2011, **223**, 827-835.
90. S.-H. Chai, Z.-M. Liu, K. Huang, S. Tan and S. Dai, *Ind. Eng. Chem. Res.*, 2016, **55**, 7355-7361.
91. M. Wang, L. Yao, J. Wang, Z. Zhang, W. Qiao, D. Long and L. Ling, *Applied Energy*, 2016, **168**, 282-290.
92. Z. Liu, D. Pudasainee, Q. Liu and R. Gupta, *Sep. Purif. Technol.*, 2015, **156, Part 2**, 259-268.
93. M. B. Yue, Y. Chun, Y. Cao, X. Dong and J. H. Zhu, *Adv. Funct. Mater*, 2006, **16**, 1717-1722.
94. M. E. Boot-Handford, J. C. Abanades, E. J. Anthony, M. J. Blunt, S. Brandani, N. Mac Dowell, J. R. Fernandez, M.-C. Ferrari, R. Gross, J. P. Hallett, R. S. Haszeldine, P. Heptonstall, A. Lyngfelt, Z. Makuch, E. Mangano, R. T. J. Porter,

M. Pourkashanian, G. T. Rochelle, N. Shah, J. G. Yao and P. S. Fennell, *Energy Environ. Sci.*, 2014, **7**, 130-189.
95. M. Eic and D. M. Ruthven, *Zeolites*, 1988, **8**, 40-45.
96. S. Brandani and D. M. Ruthven, *Chem. Eng. Sci.*, 1995, **50**, 2055-2059.
97. S. Brandani, *Chem. Eng. Sci.* , 1998, **53**, 2791-2798.
98. S. Brandani, M. A. Jama and D. M. Ruthven, *Chem. Eng. Sci.*, 2000, **55**, 1205-1212.
99. X. Hu, E. Mangano, D. Friedrich, H. Ahn and S. Brandani, *Adsorption*, 2014, **20**, 121-135.
100. X. Hu, S. Brandani, A. I. Benin and R. R. Willis, *Ind. Eng. Chem. Res.*, 2015, **54**, 5777-5783.
101. C. L. Cavalcante, Jr. and D. M. Ruthven, *Ind. Eng. Chem. Res.*, 1995, **34**, 185-191.
102. S. Brandani and D. Ruthven, *Adsorption*, 1996, **2**, 133-143.
103. D. Ruthven and F. Brandani, *Adsorption*, 2005, **11**, 31-34.
104. S. Brandani, Z. Xu and D. Ruthven, *Microporous Mater.*, 1996, **7**, 323-331.
105. F. Brandani, D. Ruthven and C. G. Coe, *Ind. Eng. Chem. Res.*, 2003, **42**, 1451-1461.
106. H. Wang, S. Brandani, G. Lin and X. Hu, *Adsorption*, 2011, **17**, 687-694.
107. F. Brandani and D. Ruthven, *Ind. Eng. Chem. Res.*, 2003, **42**, 1462-1469.
108. X. Hu, S. Brandani, A. I. Benin and R. R. Willis, *Ind. Eng. Chem. Res.*, 2015, **54**, 6772-6780.
109. NIST, http://webbook.nist.gov/chemistry/fluid/, 2016.
110. D. Friedrich, M.-C. Ferrari and S. Brandani, *Ind. Eng. Chem. Res.*, 2013, **52**, 8897-8905.
111. D. Friedrich, E. Mangano and S. Brandani, *Chem. Eng. Sci.*, 2015, **126**, 616-624.
112. K. S. W. Sing, D. H. Everett, R. A. W. Haul, L. Moscou, R. A. Pierotti, J. Rouquerol and T. Siemieniewska, *Pure Appl. Chem.*, 1985, **57**, 603-619.
113. M. Thommes, K. Kaneko, A. V. Neimark, J. P. Olivier, F. Rodriguez-Reinoso, J. Rouquerol and K. S. Sing, *Pure Appl. Chem.*, 2015, **87**, 1051-1069.
114. S. Brunauer, P. H. Emmett and E. Teller, *J. Am. Chem. Soc.*, 1938, **60**, 309-319.
115. S. Lowell, J. E. Shields, M. A. Thomas and M. Thommes, *Characterization of porous solids and powders: surface area, pore size and density*, Springer Science & Business Media, 2012.
116. J. Landers, G. Y. Gor and A. V. Neimark, *Colloid Surface A*, 2013, **437**, 3-32.
117. G. Socrates, *Infrared and Raman Characteristic Groups Frequencies: Tables and Charts. Third Edition*, 2001.
118. C. Lu, H. Bai, B. Wu, F. Su and J. F. Hwang, *Energ. Fuel.*, 2008, **22**, 3050-3056.
119. K. Böhme, W.-D. Einicke and O. Klepel, *Carbon*, 2005, **43**, 1918-1925.
120. V. Datsyuk, M. Kalyva, K. Papagelis, J. Parthenios, D. Tasis, A. Siokou, I. Kallitsis and C. Galiotis, *Carbon*, 2008, **46**, 833-840.
121. K. A. Wepasnick, B. A. Smith, K. E. Schrote, H. K. Wilson, S. R. Diegelmann and D. H. Fairbrother, *Carbon*, 2011, **49**, 24-36.

122. T. Susi, T. Pichler and P. Ayala, *Beilstein Journal of Nanotechnology*, 2015, **6**, 177-192.
123. T. I. T. Okpalugo, P. Papakonstantinou, H. Murphy, J. McLaughlin and N. M. D. Brown, *Carbon*, 2005, **43**, 153-161.
124. http://www.lasurface.com/database/elementxps.php, 2016.
125. C. J. Powell and A. Jablonski, *J. Electron Spectrosc.*, 2010, **178–179**, 331-346.
126. M. V. Kharlamova, *Prog. Mater. Sci.*, 2016, **77**, 125-211.
127. C. Wang, K. Takei, T. Takahashi and A. Javey, *Chem. Soc. Rev.*, 2013, **42**, 2592-2609.
128. E. Llobet, *Sensor. Actuat. B-Chem.*, 2013, **179**, 32-45.
129. J. Kong, N. R. Franklin, C. Zhou, M. G. Chapline, S. Peng, K. Cho and H. Dai, *Science*, 2000, **287**, 622-625.
130. P. G. Collins, K. Bradley, M. Ishigami and A. Zettl, *Science*, 2000, **287**, 1801-1804.
131. O. K. Varghese, P. D. Kichambre, D. Gong, K. G. Ong, E. C. Dickey and C. A. Grimes, *Sensor. Actuat. B-Chem.*, 2001, **81**, 32-41.
132. T. Zhang, S. Mubeen, N. V. Myung and M. A. Deshusses, *Nanotechnology*, 2008, **19**, 332001.
133. P. Qi, O. Vermesh, M. Grecu, A. Javey, Q. Wang, H. Dai, S. Peng and K. Cho, *Nano Lett.*, 2003, **3**, 347-351.
134. A. Star, T. R. Han, V. Joshi, J. C. P. Gabriel and G. Grüner, *Adv. Mater.*, 2004, **16**, 2049-2052.
135. E. Bekyarova, M. Davis, T. Burch, M. E. Itkis, B. Zhao, S. Sunshine and R. C. Haddon, *J. Phys. Chem. B*, 2004, **108**, 19717-19720.
136. I. V. Anoshkin, A. G. Nasibulin, P. R. Mudimela, M. He, V. Ermolov and E. I. Kauppinen, *Nano Research*, 2012, **6**, 77-86.
137. L. J. Van der Pauw, *Philips Tech. Rev.*, 1958, **20**, 220-224.
138. T.-B. Song, Y. Chen, C.-H. Chung, Y. Yang, B. Bob, H.-S. Duan, G. Li, K.-N. Tu, Y. Huang and Y. Yang, *ACS nano*, 2014, **8**, 2804-2811.
139. J. A. A. Gibson, A. V. Gromov, S. Brandani and E. E. B. Campbell, *Micropor. Mesopor. Mat.*, 2015, **208**, 129-139.
140. A. Boonpoke, S. Chiarakorn, N. Laosiripojana, S. Towprayoon and A. Chidthaisong, *Korean J. Chem. Eng.*, 2012, **29**, 89-94.
141. J. P. Toso, J. C. A. Oliveira, D. A. Soares Maia, V. Cornette, R. H. López, D. C. S. Azevedo and G. Zgrablich, *Adsorption*, 2013, **19**, 601-609.
142. M. Thommes, K. A. Cychosz and A. V. Neimark, in *Novel Carbon Adsorbents*, ed. J. M. D. Tascón, Elsevier, Oxford, 2012, pp. 107-145.
143. E. Jo, Y. H. Jhon, S. B. Choi, J.-G. Shim, J.-H. Kim, J. H. Lee, I.-Y. Lee, K.-R. Jang and J. Kim, *Chem. Commun.*, 2010, **46**, 9158-9160.
144. NIST, http://webbook.nist.gov/cgi/cbook.cgi?ID=C112243&Mask=80#IR-Spec, 2016.
145. R. Sanz, G. Calleja, A. Arencibia and E. S. Sanz-Pérez, *Micropor. Mesopor. Mat.*, 2012, **158**, 309-317.

146. H. Ogura, K. Takeda, R. Tokue and T. Kobayashi, *Synthesis*, 1978, **1978**, 394-396.
147. C.-C. Tai, M. J. Huck, E. P. McKoon, T. Woo and P. G. Jessop, *J. Org. Chem.*, 2002, **67**, 9070-9072.
148. J. C. Hicks, J. H. Drese, D. J. Fauth, M. L. Gray, G. Qi and C. W. Jones, *J. Am. Chem. Soc.*, 2008, **130**, 2902-2903.
149. J. Zhao, F. Simeon, Y. Wang, G. Luo and T. A. Hatton, *RSC Advances*, 2012, **2**, 6509-6519.
150. S. Brandani, C. Cavalcante, A. Guimarães and D. Ruthven, *Adsorption*, 1998, **4**, 275-285.
151. R. J. Littel, G. F. Versteeg and W. P. M. Van Swaaij, *Chem. Eng. Sci.*, 1992, **47**, 2037-2045.
152. H. Hikita, S. Asai, H. Ishikawa and M. Honda, *Chem. Eng. J.*, 1977, **13**, 7-12.
153. G. Couchaux, D. Barth, M. Jacquin, A. Faraj and J. Grandjean, *Oil Gas Sci. Technol.*, 2014, **69**, 865-884.
154. P. D. Vaidya and E. Y. Kenig, *Chem. Eng. Technol.*, 2007, **30**, 1467-1474.
155. R. Serna-Guerrero, Y. Belmabkhout and A. Sayari, *Chem. Eng. J.*, 2010, **161**, 173-181.
156. R. Serna-Guerrero and A. Sayari, *Chem. Eng. J.*, 2010, **161**, 182-190.
157. P. Bollini, N. A. Brunelli, S. A. Didas and C. W. Jones, *Ind. Eng. Chem. Res.*, 2012, **51**, 15145-15152.
158. P. Bollini, N. A. Brunelli, S. A. Didas and C. W. Jones, *Ind. Eng. Chem. Res.* , 2012, **51**, 15153-15162.
159. A. Abdollahi-Govar, A. D. Ebner and J. A. Ritter, *Energ. Fuel.*, 2015, **29**, 4492-4502.
160. B. Wu, X. Zhang, Y. Xu, D. Bao and S. Zhang, *J. Clean. Prod.*, 2015, **101**, 251-261.
161. Z. Bacsik, O. Cheung, P. Vasiliev and N. Hedin, *Appl. Energ.*, 2016, **162**, 613-621.
162. J. Niesner, D. Jecha and P. Stehlík, *Chem. Eng. Trans.*, 2013, **35**, 517-522.
163. W. M. Budzianowski, *Renew. Sust. Energ. Rev.*, 2012, **16**, 6507-6521.
164. F. Bauer, C. Hulteberg, T. Persson and D. Tamm, *SGC Rapport*, 2013.
165. C. Yin, W. Sun, H. Yang and D. Zhang, *Chem. Eng. Sci.*, 2015, **135**, 100-108.
166. Y. J. Kim, Y. S. Nam and Y. T. Kang, *Energy*, 2015, **91**, 732-741.
167. B. Ozturk and F. Demirciyeva, *Chem. Eng. J.*, 2013, **222**, 209-217.
168. M. Scholz, M. Alders, T. Lohaus and M. Wessling, *J. Membrane Sci.*, 2015, **474**, 1-10.
169. Q. Sun, H. Li, J. Yan, L. Liu, Z. Yu and X. Yu, *Renew Sust. Energ. Rev.*, 2015, **51**, 521-532.
170. C. A. Grande and A. E. Rodrigues, *Ind. Eng. Chem. Res.*, 2007, **46**, 7844-7848.
171. A. Alonso-Vicario, J. R. Ochoa-Gómez, S. Gil-Río, O. Gómez-Jiménez-Aberasturi, C. A. Ramírez-López, J. Torrecilla-Soria and A. Domínguez, *Micropor. Mesopor. Mat.*, 2010, **134**, 100-107.

172. M. V. Gil, N. Álvarez-Gutiérrez, M. Martínez, F. Rubiera, C. Pevida and A. Morán, *Chem. Eng. J.*, 2015, **269**, 148-158.
173. D.-J. Seo, Z. Gou, H. Fujita, T. Fujii and A. Sakoda, *Renew Energ.*, 2016, **86**, 693-702.
174. Y. Belmabkhout, G. De Weireld and A. Sayari, *Langmuir*, 2009, **25**, 13275-13278.
175. E. Ryckebosch, M. Drouillon and H. Vervaeren, *Biomass and bioenergy*, 2011, **35**, 1633-1645.
176. J. A. C. Silva, A. F. Cunha, K. Schumann and A. E. Rodrigues, *Micropor. Mesopor. Mat.*, 2014, **187**, 100-107.
177. A. M. ElKhatat and S. A. Al-Muhtaseb, *Adv. Mater.*, 2011, **23**, 2887-2903.
178. M. Antonietti, N. Fechler and T.-P. Fellinger, *Chem. Mater.*, 2014, **26**, 196-210.
179. S. Nardecchia, D. Carriazo, M. L. Ferrer, M. C. Gutiérrez and F. del Monte, *Chem. Soc. Rev.*, 2013, **42**, 794-830.
180. M. B. Bryning, D. E. Milkie, M. F. Islam, L. A. Hough, J. M. Kikkawa and A. G. Yodh, *Adv. Mater.*, 2007, **19**, 661-664.
181. H. Sun, Z. Xu and C. Gao, *Adv. Mater.*, 2013, **25**, 2554-2560.
182. L. Dong, Q. Yang, C. Xu, Y. Li, D. Yang, F. Hou, H. Yin and F. Kang, *Carbon*, 2015, **90**, 164-171.
183. J. Zou, J. Liu, A. S. Karakoti, A. Kumar, D. Joung, Q. Li, S. I. Khondaker, S. Seal and L. Zhai, *ACS Nano*, 2010, **4**, 7293-7302.
184. C. Moreno-Castilla and F. Maldonado-Hódar, *Carbon*, 2005, **43**, 455-465.
185. E. Frackowiak and F. Béguin, *Carbon*, 2001, **39**, 937-950.
186. M. Mirzaeian and P. J. Hall, *Electrochimica Acta*, 2009, **54**, 7444-7451.
187. H. Bi, Z. Yin, X. Cao, X. Xie, C. Tan, X. Huang, B. Chen, F. Chen, Q. Yang, X. Bu, X. Lu, L. Sun and H. Zhang, *Adv. Mater.*, 2013, **25**, 5916-5921.
188. Z.-Y. Wu, C. Li, H.-W. Liang, Y.-N. Zhang, X. Wang, J.-F. Chen and S.-H. Yu, *Scientific Reports*, 2014, **4**, 4079.
189. S. Kabiri, D. N. H. Tran, T. Altalhi and D. Losic, *Carbon*, 2014, **80**, 523-533.
190. C. Zhu, T. Y.-J. Han, E. B. Duoss, A. M. Golobic, J. D. Kuntz, C. M. Spadaccini and M. A. Worsley, *Nat. Commun.*, 2015, **6**.
191. Q. Zhang, F. Zhang, S. P. Medarametla, H. Li, C. Zhou and D. Lin, *Small*, 2016, n/a-n/a.
192. W. M. Haynes, *CRC handbook of chemistry and physics*, CRC press, 2014.
193. N. Wakao, S. Kaguei and T. Funazkri, *Chem. Eng. Sci.*, 1979, **34**, 325-336.